

# **Improved Models of Electric Machines for Real-Time Digital Simulation**

By:

**Ali Banitalebi Dehkordi**

A Thesis

Submitted to the Faculty of Graduate Studies in Partial Fulfillment  
of the Requirements for the Degree of

**Doctor of Philosophy**

Department of Electrical and Computer Engineering  
University of Manitoba  
Winnipeg, Manitoba

© Copyright by Ali Banitalebi Dehkordi 2010

# Acknowledgments

I would like to express my gratitude to Professor Ani Gole, the supervisor of this thesis, for his support, encouragement, and guidance throughout all the stages of this research. Despite his busy schedule, Professor Gole always provided me with insightful comments and helpful discussions. I consider myself privileged to work with one of the leaders in the area of electromagnetic transient simulation programs. I am also grateful for the opportunities that he provided for me to work with the experts in the area of electric machines and electromagnetic transients programs.

I wish to express my sincere appreciation to Dr. Trevor Maguire for his assistance and technical support in real-time implementation of electric machine models, and providing insight regarding the operation of the real-time digital simulator (RTDS).

I would like to thank Dr. Prabhakar Neti for providing the FEM-based inductances of the laboratory synchronous machine and assisting in assembling the synchronous machine laboratory set-up.

I would also like to express my appreciation to Professor Robert Menzies for his guidance in the measurement procedure of the laboratory synchronous machine inductances. I always enjoyed our discussions regarding electric machines.

Financial support from the RTDS Technologies Inc., the Natural Sciences and Engineering Research Council (NSERC) of Canada, and the Mathematics of Information Technology and Complex Systems (MITACS) Internship Program is greatly appreciated.

I am also grateful to Mr. Erwin Dirks for his immense and high valued technical support during the laboratory experiments of this research.

During the progress of this research, I was kindly assisted by the following individuals:

- Mr. Garth Irwin from Electranix Corporation,
- Prof. Shaahin Filizadeh from the University of Manitoba
- Dr. Rohitha Jayasinghe, Dr. Dharshana Muthumuni, Mr. John Nordstrom, Mr. Juan Carlos Garcia, Mr. Farid Mosallat from the Manitoba HVDC Research Centre, and
- Dr. Ming Yu, Dr. Yi Zhang, Mr. In-Kwon Park, Ms. Heather Meiklejohn, Dr. Khosro Kabiri, Mr. Dean Ouellette, Mr. Shaun Warkentin, Ms. Christine Stuart-Edwards, and Mr. Gregory Jackson from the RTDS Technologies Inc.

Their support is greatly appreciated.

Finally, I would like to show my sincere gratitude towards Ms. Jillian Hoogland for her emotional support, kind words, and sensible advice during the progress of this thesis.



“Omar Khayyam”

## Abstract

This thesis advances the state of the art in modeling electric machines in electromagnetic transient simulation programs, particularly in real-time digital simulators. A new tool, developed in this thesis, expands the application of real-time digital simulators to closed-loop testing of protection relays designed to protect synchronous machines during internal faults.

To evaluate the inductances of synchronous machines, a winding function approach was developed in this thesis which is capable of taking into account both the actual distribution of windings and the shape of the pole-arc. Factors such as MMF drop in the iron and effects of slots are compensated by evaluating the effective permeance function of the machine using experimentally measured values of d-, q- and 0- axis inductances. In this winding function approach, the effects of magnetic saturation are also included by considering the actual distribution of magneto-motive force in each loading condition of the machine. The inductances of an experimental machine are evaluated using this approach and validated using the finite-element method and laboratory measurements. This thesis also proposes an embedded phase-domain approach for time-domain simulation of the machine model in electromagnetic transients programs. The approach significantly improves the numerical stability of the simulations. Special numerical techniques are introduced, which speed up the execution of the algorithm as needed for real-time simulation. The machine model is validated in healthy and faulted conditions using simulations and laboratory experiments. Effects of damper grid representation on simulating turn-to-turn faults are investigated. The capability of this new real-time synchronous machine model in closed-loop testing of synchronous machines ground-faults protection relays is clearly demonstrated.

# Table of Contents

<b>Acknowledgments</b> .....	<b>i</b>
<b>Abstract</b> .....	<b>iv</b>
<b>Table of Contents</b> .....	<b>v</b>
<b>List of Figures</b> .....	<b>viii</b>
<b>List of Tables</b> .....	<b>xiv</b>
<b>List of Symbols</b> .....	<b>xv</b>
<b>List of Abbreviations</b> .....	<b>xxi</b>
<b>Chapter 1: Introduction</b> .....	<b>1</b>
1.1 Power System Transient Simulation Tools .....	1
1.2 Closed-Loop Testing of Equipment Using Real-Time Simulation .....	2
1.3 Problem Motivation .....	4
1.4 Research Objectives of the Thesis .....	5
1.5 Thesis Organization .....	6
<b>Chapter 2: Background</b> .....	<b>9</b>
2.1 Electromagnetic Transients Programs .....	9
2.2 Approaches of Modeling Machines in Digital Electromagnetic Transient Simulation: Interface-Based & Embedded .....	13
2.3 Level of Detail in Existing Synchronous Machine Models in Digital Electromagnetic Transient Simulators .....	16
2.4 Real-Time Electromagnetic Transients Programs .....	17
<b>Chapter 3: Evaluation of Synchronous Machines Electric Parameters</b> .....	<b>21</b>
3.1 Time Domain Modeling of Electric Machines Using the Coupled Electric Circuit Approach .....	21
3.2 Dq0 Theory on Modeling Electric Machines .....	22

3.3	Application of the Finite Element Method in Obtaining the Inductances of Electric Machines.....	44
3.4	Application of the Modified Winding Function Approach for Obtaining the Inductances of Electric Machines .....	48
3.5	Chapter Contributions and Conclusions .....	70
<b>Chapter 4:</b>	<b>Inclusion of Saturation Effects in Evaluating Synchronous Machine Inductances .....</b>	<b>72</b>
4.1	Incorporation of Saturation in the Dq0 Approach .....	72
4.2	Modeling of Saturation in the FEM .....	80
4.3	Incorporation of Saturation in the MWFA.....	81
4.4	Chapter Contributions and Conclusions .....	88
<b>Chapter 5:</b>	<b>Development of an Embedded Approach for Time-Domain Simulation of Electric Machines in Electromagnetic Transients Programs .....</b>	<b>90</b>
5.1	Introduction.....	90
5.2	Traditional Approach of Interfacing Electric Machines in Electro-Magnetic Transient Programs .....	91
5.3	The Embedded Approach for Integrating Machine Models in Electro-Magnetic Transient Programs .....	97
5.4	Techniques for Speeding up the Procedure and Special Considerations for Real-Time Implementation of the Embedded Model.....	113
5.5	Electric Torque Calculation in ABC and DQ0 Frames and Interfacing External Mechanical and Control Systems .....	126
5.6	Chapter Contributions and Conclusions .....	129
<b>Chapter 6:</b>	<b>Validation of the New Embedded Phase-Domain Machine Model... 130</b>	
6.1	Embedded Phase-Domain Models Algebraically Equivalent to Dq0 Models.....	130
6.2	Validation of the MWFA-based Embedded Phase-Domain Machine Model .....	145
6.3	Chapter Contributions and Conclusions .....	172
<b>Chapter 7:</b>	<b>Application of the New Real-Time Model in Synchronous Generators Protection Studies.....</b>	<b>174</b>

7.1	Introduction .....	174
7.2	Differential Protection for Stator-Ground Faults .....	175
7.3	100% Stator-Ground Fault Protection Scheme .....	178
7.4	Chapter Contributions and Conclusions .....	189
<b>Chapter 8:</b>	<b>Conclusions and Future Directions .....</b>	<b>190</b>
8.1	Main Contributions of the Thesis.....	190
8.2	Summary of the Conclusions .....	191
8.3	Thesis Publications .....	195
8.4	Recommended Future Directions.....	196
<b>References:</b>	<b>.....</b>	<b>199</b>
<b>Appendix A:</b>	<b>Calculation of the Effective Permeance Function .....</b>	<b>205</b>
<b>Appendix B:</b>	<b>Numerical Stability of a Discretized System Using Rectangular and Trapezoidal Integration .....</b>	<b>209</b>
B.1	Stability of the System Using Rectangular Integration.....	210
B.2	Stability of the System Using Trapezoidal Integration .....	212
<b>Appendix C:</b>	<b>Electric Torque Calculation in Synchronous Machines .....</b>	<b>216</b>
<b>Appendix D:</b>	<b>Derivation of Synchronous Machines Saturation Factors.....</b>	<b>220</b>
D.1	Determination of the Constants $\alpha, k$ .....	223
D.2	Determination of the Saturation Factors Coefficients $a_{id}, a_{iq}$ .....	225



## List of Figures

Figure 2.1:	Norton equivalents in electromagnetic transients programs: (a) inductor, (b) capacitor.....	11
Figure 2.2:	Interfacing components to the network solution as a current source .....	14
Figure 3.1:	Diagram of an idealized synchronous machine.....	24
Figure 3.2:	Dq0 equivalent circuit of a synchronous machine: (a) d-axis, (b) q-axis, (c) 0-axis .....	33
Figure 3.3:	The B-H loop of a permanent magnet.....	35
Figure 3.4:	A simple rectangular magnet.....	37
Figure 3.5:	Equivalent circuits of a magnet: (a) magnetic circuit, (b) electric circuit. ....	38
Figure 3.6:	Simple structure of permanent magnet synchronous machine, (a) surface-mounted PMSM, (b) buried-magnet PMSM.....	38
Figure 3.7:	Dq0 equivalent circuit of a synchronous machine: (a) d-axis, (b) q-axis, (c) 0-axis. ....	40
Figure 3.8:	A triangular mesh pattern used to model a synchronous machine using FEM.....	45
Figure 3.9:	An elementary salient-pole synchronous machine with placements of the windings .....	51
Figure 3.10:	The Laboratory synchronous machine: (a) stator, (b) rotor .....	55
Figure 3.11:	Layout of the windings in the stator and rotor of the laboratory machine .....	55
Figure 3.12:	Rotor of the laboratory synchronous machine: (a) rotor cross-section, (b) rotor lamination. ....	57
Figure 3.13:	The air-gap function considering actual rotor pole-arc.....	57
Figure 3.14:	The turns function of the stator phase-A.....	58
Figure 3.15:	The turns function of the field winding.....	58
Figure 3.16:	The permeance functions considering different details ( $P_0 \cdots P_3$ ) .....	61
Figure 3.17:	The stator phase-A self inductance computed using permeance functions $P_0 \cdots P_3$ .....	62

Figure 3.18:	The mutual inductance between stator phase-A and phase-B computed using permeance functions $P_0 \cdots P_3$ .....	63
Figure 3.19:	Comparison of physical and effective permeance functions of the machine .....	66
Figure 3.20:	Stator inductances using $P_1(\phi_s, \theta_r)$ , $P_{eff}(\phi_s, \theta_r)$ and FEM, (a) self inductance of stator phase-A, (b) mutual inductances between stator phase-A and phase-B.....	67
Figure 3.21:	Stator inductances using $P_1(\phi_s, \theta_r)$ , $P_{eff}(\phi_s, \theta_r)$ and FEM. The permeance is adjusted using the $L_d$ , $L_q$ , $L_0$ from FEM (a) self inductance of stator phase-A, (b) mutual inductances between stator phase-A and phase-B. ..	68
Figure 3.22:	Inductances of sub-winding A2 using $P_1(\phi_s, \theta_r)$ , $P_{eff}(\phi_s, \theta_r)$ and measurement, (a) self inductance of A2, (b) mutual inductances between A2 and the field winding.....	69
Figure 4.1:	The effect of MMF distribution on saturated permeance function .....	76
Figure 4.2:	Variation of direct axis magnetization inductance with d- and q- axes magnetization currents .....	79
Figure 4.3:	Variation of quadrature axis magnetization inductance with d- and q- axes magnetization currents .....	79
Figure 4.4:	D- and Q-axis saturation curves generated from the open-circuit characteristics of the experimental machine .....	84
Figure 4.5:	Direct- and quadrature-axis saturation factors (Sd and Sq) of the experimental machine .....	84
Figure 4.6:	Change in the permeance function due to change in operating condition	86
Figure 4.7:	Change in the stator inductances due to saturation, (a) self inductance of stator phase-A, (b) mutual inductances between stator phase-A and phase-B. ....	87
Figure 4.8:	Procedure for computing machine inductances using MWFA .....	88
Figure 5.1:	Conceptual diagram of solving the machine equations.....	93
Figure 5.2:	Interfacing the machine model to the network solution.....	93
Figure 5.3:	Discretized equivalent circuit of a time-varying inductor: (a) for branch quantities, (b) for nodal quantities.....	100
Figure 5.4:	Modeling a time-varying inductor in PSCAD/EMTDC, three different ways.....	101

Figure 5.5:	Comparison of the simulated current and analytical solution of a time-varying inductor in the circuit shown in Figure 5.4 : (a) comparison, (b) error .....	103
Figure 5.6:	Simulated current of a time-varying inductor using the representation of a constant inductor and comparison with analytical solution .....	103
Figure 5.7:	Representing the machine as a set of time-varying mutually coupled inductances .....	104
Figure 5.8:	Discretized Norton equivalent circuit of the machine.....	108
Figure 5.9:	Test circuit for modeling a set of mutually coupled constant inductors .	110
Figure 5.10:	Comparison of the simulation results with analytical steady state solutions of the test circuit in Figure 5.9 .....	112
Figure 5.11:	Connection of winding nodes in an embedded model of a synchronous machine in electromagnetic transients programs .....	125
Figure 5.12:	Treatment of the equivalent admittance matrix of the machine for the node connection in Figure 5.11 .....	125
Figure 5.13:	Procedure for incorporating the embedded machine model into the network solution of RTDS .....	126
Figure 5.14:	Interfacing control and mechanical systems to the main network solution .....	128
Figure 6.1:	Short circuit currents in windings of the two synchronous machine models: a) stator phase A, b) field winding .....	132
Figure 6.2:	First ten cycles of the short circuit currents in stator phase A of the two synchronous machine models (curves are overlapping and indistinguishable.) .....	132
Figure 6.3:	Assumed saturation characteristics of the synchronous machine under study .....	133
Figure 6.4:	Transient behaviour of the synchronous machines during a step-increase in the field voltage, a) Phase A currents of the machines, b) Currents of the field windings c) Variation of d-axis magnetization inductance $L_{md}$ with time (curves are indistinguishable) . .....	135
Figure 6.5:	Test circuit for comparing the embedded and interfaced models of the PMSM .....	137
Figure 6.6:	Steady-state performances of the permanent magnet machines.....	138
Figure 6.7:	Steady state equivalent circuit for the PMSM.....	139

Figure 6.8:	Stator phase A short circuit currents of the PMSM models (the transient simulated curves for the two approaches lie exactly on each other).....	140
Figure 6.9:	Configuration of the embedded synchronous machine model developed in the RTDS environment.....	146
Figure 6.10:	Circuit diagram of the synchronous machine connected to an R-C load.	147
Figure 6.11:	Simulated variation of the total magnetizing currents along d and q-axis of the generator with R-C load switching: a) $i_{md}$ , b) $i_{mq}$ .....	148
Figure 6.12:	Experimental and simulated variation of the field current during the switching of the generator on the R-C load: a) experiment b) simulation incorporating saturation c) simulation ignoring saturation .....	149
Figure 6.13:	Experimental and simulated R-C switching transient ignoring saturation, a) phase-neutral voltage, b) phase current.....	151
Figure 6.14:	Experimental and simulated R-C switching transient including saturation, a) phase-neutral voltage, b) phase current.....	151
Figure 6.15:	Experimental and simulated steady-state waveforms with R-C load ignoring saturation, a) phase-neutral voltage, b) phase current .....	152
Figure 6.16:	Experimental and simulated steady-state waveforms with R-C load including saturation, a) phase-neutral voltage, b) phase current.....	152
Figure 6.17:	Experimental and simulated steady-state pre-switching (full-load) phase to neutral voltage: a) saturation modeled b) saturation ignored.....	154
Figure 6.18:	Steady-state experimental and simulated post-switching (0.36 pu load) phase to neutral voltage: a) saturation modeled b) saturation ignored....	154
Figure 6.19:	Experimental and simulated steady-state phase current waveforms with R-C load .....	156
Figure 6.20:	Simulated variation of total d and q-axis magnetizing currents of the generator with R-C load switching: a) $i_{md}$ , b) $i_{mq}$ .....	157
Figure 6.21:	Connection of the synchronous machine windings in the laboratory setup .....	158
Figure 6.22:	Experimental and simulated transients of a symmetrical three phase short circuit on the initially open circuited generator: a) phase-A current, b) field current.....	160
Figure 6.23:	Experimental and simulated transients of a terminal-to-neutral short circuit on the initially open circuited generator: a) phase-A current, b) field current.....	160

Figure 6.24:	Experimental transient currents of a short circuit on the stator winding A2: a) faulted winding A2, b) the field winding.....	162
Figure 6.25:	Simulated transient currents of a short circuit on the stator winding A2 using the new embedded phase-domain model: a) faulted winding A2, b) the field winding.....	162
Figure 6.26:	Direction of fluxes generated by the field winding and damper grid when only winding A2 is energized.....	164
Figure 6.27:	Diagram of the synchronous machine model with a detailed damper representation embedded in a stand-alone electromagnetic transients program .....	167
Figure 6.28:	Simulated transient currents of a short circuit on the stator winding A2 using the model with individual damper windings for each pole: a) faulted winding A2, b) the field winding .....	167
Figure 6.29:	Steady-state simulated waveforms of a short circuit on the stator winding A2 using the model with individual damper windings for each pole: a) the current in the faulted winding A2, b) currents of the d-axis damper windings (D1-D4) reflected to the stator side. ....	168
Figure 6.30:	Steady-state simulated currents of a terminal-to-neutral short circuit using the model with individual damper windings for each pole: a) phase current, b) currents of the d-axis damper windings (D1-D4) reflected to the stator side. (Curves are indistinguishable) .....	169
Figure 6.31:	Equivalent circuit of the rotor damper cage showing rotor loop currents and end ring currents .....	170
Figure 6.32:	Experimental and simulated currents of a short circuit on the stator winding A2 in the steady-state: a) simulated using a model with 4 d-axis and 4 q-axis damper winding, b) simulated using a model with damper grid modeled as a cage, c) Experiment .....	171
Figure 7.1:	Basic current differential scheme for the generator stator-ground fault protection.....	176
Figure 7.2:	Simulated transient currents of a stator-ground fault (node <i>AJ</i> -to-ground) with a grounding resistance of 5.3 Ohm, a) conventional representation of the damper grid as d- and q-axis windings, b) damper grid modeled as a cage.....	178
Figure 7.3:	Circuit diagram of a stator-ground fault in a synchronous machine .....	179
Figure 7.4:	Experimental and simulated voltage across the stator phase-A with the R-C load a) steady state waveform, b) harmonic spectrum (peak magnitude). ....	182

Figure 7.5:	Experimental and simulated voltage across the stator phase-A with the resistive load: a) steady state waveform, b) harmonic spectrum (peak magnitude).....	182
Figure 7.6:	RSCAD draft circuit used for the simulation of the 3 <sup>rd</sup> harmonic voltage .....	184
Figure 7.7:	Saturated inductances of faulted windings generated using MWFA, a) self inductances of windings A1 and A2, b) mutual inductances between the field winding and sub-windings A1 and A2.....	185
Figure 7.8:	Neutral voltage during a stator-ground fault a) ground fault on node NAJ, b) ground fault on terminal node NA1, c) ground fault on terminal node NA1 in a dq-based machine model. ....	186
Figure 7.9:	Neutral voltage 3 <sup>rd</sup> harmonic component as a function of active and reactive power loading .....	188
Figure 7.10:	Terminal voltage 3 <sup>rd</sup> harmonic component as a function of active and reactive power loading .....	188
Figure B.1:	Eigenvalue loci of matrix [A] and matrix [G] using rectangular integration .....	212
Figure B.2:	Eigenvalue loci of matrix [A] and matrix [G] using the trapezoidal integration.....	215
Figure D.1:	Unsaturated permeance function of a salient-pole synchronous machine .....	220

## List of Tables

TABLE 3.1: Specifications of the Laboratory Machine .....	56
TABLE 3.2: Permeance Functions of the Machine by Incorporating Different Details	60
TABLE 3.3: The Dq0 Parameters of the Laboratory Synchronous Machine .....	65
TABLE 6.1: The Dq Parameters of the Simulated Synchronous Machine.....	131
TABLE 6.2: The Dq Parameters of the Simulated PMSM .....	136
TABLE 6.3: Numerical Stability of Different Machine Models .....	144
TABLE 6.4: Specification of the Loads in Laboratory Experiments.....	147
TABLE C.1: Mechanical Torque Caused by Magnetic Coupling Field.....	216

## List of Symbols

$a_F$	Turns ratio of the field winding to the stator
$as$	Axis of stator phase A
$bs$	Axis of stator phase B
$B$	Flux density
$B_m$	Operating flux density of a magnet
$B_r$	Residual flux density of a magnetic material (remanence)
$[B_{abc-frame}]$	The inverse of the inductance matrix in abc frame
$[B_{dq-frame}]$	The inverse of the inductance matrix in dq frame
$cs$	Axis of stator phase C
$C_N$	Charging capacitance at a synchronous machine neutral
$C_T$	Charging capacitance at a synchronous machine terminals
$\delta$	Initial rotor angle of a synchronous generator
$\Delta t$	Simulation time-step
$\Delta t_c$	Critical time-step
$E_{fd0}$	Field voltage required for 1 pu open circuit terminal voltage in an unsaturated synchronous machine at rated speed
$\xi$	Angle of the total magnetomotive force
$fd$	Axis of the field winding or direct axis
$\mathcal{F}$	Magnetomotive force



$\mathcal{F}_{ag}$	Component of MMF corresponding to the air-gap line
$\mathcal{F}_{sat}$	Component of MMF contributing to saturation
$\mathcal{F}_m$	Magnetomotive force drop along a magnetic material
$g_L$	Conductance value associated with an inductor
$g_a$	Actual air-gap function
$g_c$	Air-gap function with circular approximation of pole-arc
$g_s$	Air-gap function generated by considering the effective depth of stator slots
$g^{-1}$	Inverse air-gap function
$[G_{eq}]$	Equivalent conductance matrix (for branch quantities)
$[G_{set}]$	Equivalent conductance matrix of a set of mutually coupled inductors
$H$	Magnetic field intensity
$H_c$	Coercive force
$H_m$	Operating magnetic field intensity of a magnet
$i_C$	Capacitor current
$i_L$	Inductor current
$i_{md}$	Total direct-axis magnetizing current
$i_{mq}$	Total quadrature-axis magnetizing current
$I_3$	The $3 \times 3$ identity matrix
$I_h$	History term
$\underline{I}_h$	Vector of history terms
$I_{mag}$	Magnitude of the total magnetomotive force

$k_B$	A constant that depends on the machine dimensions relating flux density and the total MMF
$l$	Rotor stack length
$l_c$	Characteristic inductance of a machine
$l_s$	Stator leakage inductance
$l_F$	Field leakage inductance
$L$	Inductance value
$L_d$	Direct-axis inductance
$L_D$	Self inductance of the d-axis damper winding
$L_F$	Self inductance of the field winding
$L_m$	Magnitude of the oscillating portion of the stator self inductances
$L_{md}$	Direct-axis magnetizing inductance
$L_{mq}$	Quadrature-axis magnetizing inductance
$L_q$	Quadrature-axis inductance
$L_Q$	Self inductance of the q-axis damper winding
$L_s$	Magnitude of the constant portion of the stator self inductances
$L_0$	Zero sequence inductance
$\lambda$	Eigenvalue of a matrix
$[L]$	Inductance matrix
$[L_{abc-frame}]$	Inductance matrix in abc frame
$[L_{dq-frame}]$	Inductance matrix in dq0 frame
$[L_{rr}]$	Matrix of rotor self inductances

$[L_{sr}]$	Matrix of mutual inductances between stator and rotor
$[L_{ss}]$	Matrix of stator self inductances
$M_j$	Modified winding function of the winding $j$
$M_D$	Peak value of the mutual inductance between a stator winding and the d-axis damper winding
$M_F$	Peak value of the mutual inductance between a stator winding and the field winding
$M_Q$	Peak value of the mutual inductance between a stator winding and the q-axis damper winding
$M_s$	Magnitude of the constant portion of the stator mutual inductances
$\mu$	Permeability of a magnetic material
$\mu_0$	Permeability of free space
$\mu_r$	Relative permeability of a magnetic material
$n_j$	Turns function of the winding $j$
$N$	Number of machine windings
$\omega_r$	Rotor speed
$p$	number of synchronous machine pole-pairs
$P$	Park's transformation
$\phi_s$	Angular positions with respect to the stator axis ( $as$ )
$\phi_r$	Angular positions with respect to the rotor axis ( $fd$ )
$\Phi_{A2}$	Flux generated by sub-winding A2
$\Phi_{f1}$	Flux generated by the pole 1 coil of the field winding
$\Phi_m$	Magnetic flux of a magnet

$\Phi_0$	Magnetic flux at the knee point of the saturation characteristics
$\Psi$	Flux linkage
$\Psi_{at}$	Total air-gap flux linkage
$\Psi_{md}$	Direct-axis magnetizing flux linkage
$\Psi_{mq}$	Quadrature-axis magnetizing flux linkage
$\underline{\Psi}$	Vector of flux linkages
$r$	Rotor radius
$r_D$	D-axis damper winding resistance
$r_F$	Field winding resistance
$r_Q$	Q-axis damper winding resistance
$r_s$	Stator resistance
$[R]$	Resistance matrix
$[R_{abc-frame}]$	Resistance matrix in abc frame
$[R_{dq-frame}]$	Resistance matrix in dq0 frame
$[R_{eq}]$	Equivalent discretized resistance matrix
$R_N$	Synchronous machine grounding resistance
$\mathcal{R}_m$	Reluctance of a magnet
P	Permeance function
$P_{eff}$	Effective permeance function
$S_d$	Saturation factor of the pole-face area
$S_q$	Saturation factor of the interpole area
$t$	Time

$T_a$	Armature time constant
$T_d'$	Direct-axis unsaturated transient short-circuit time constant
$T_e$	Electric torque
$\theta_r$	Rotor position
$\xi$	Angle of the total magnetomotive force
$X_{md}$	Direct-axis magnetizing reactance
$X_{mq}$	Quadrature-axis magnetizing reactance
$v_d$	D-axis component of voltage
$v_q$	Q-axis component of voltage
$v_0$	0-sequence component of voltage
$v_C$	Capacitor voltage
$v_L$	Inductor voltage
$v_N$	Neutral-ground voltage of a machine
$v_T$	Terminal-ground voltage of a machine
$V_{N3}$	Magnitude of the third harmonic voltage in the neutral
$V_{T3}$	Magnitude of the third harmonic voltage in the terminal
$W_m'$	Magnetic co-energy
$[Y]$	Nodal admittance matrix of a network
$\otimes$	Reference direction of the current is into the plane of the paper
$\odot$	Reference direction of the current is out of the plane of the paper

## List of Abbreviations

dq0	Direct, Quadrature, and 0-(axes)
DTNA	Digital Transient Network Analyzer
EMTP	Electro-Magnetic Transient Program
FACTS	Flexible Alternating Current Transmission System
FEM	Finite Element Method
HVDC	High-Voltage Direct Current
KVL	Kirchhoff's Voltage Law
LU	Lower/ Upper
MMF	Magneto-Motive Force
MWFA	Modified Winding Function Approach
PM	Permanent Magnet
PMSM	Permanent Magnet Synchronous Machine
pu	Per-Unit
RMS	Root Mean Square
TNA	Transient Network Analyzer
VSC	Voltage Source Converter
WFA	Winding Function Approach

# Chapter 1: Introduction

---

The background of power system transient simulation tools and the significance of real-time digital simulators in closed-loop testing of equipment are briefly covered in this chapter. The chapter also introduces the advantages and limitations of conventional synchronous machine models in electromagnetic transients programs.

The need for a detailed and numerically stable synchronous machine model for off-line and real-time electromagnetic transients programs is introduced. This model considers details such as the geometry and winding distribution of the machine, and it can simulate the behaviour of the machine during internal faults.

## 1.1 Power System Transient Simulation Tools

Modern electric power networks, which carry out the tasks of generation, transmission, and distribution of electric energy, are considered to be amongst the largest and most sophisticated systems in the world [1]. These are large-scale, nonlinear systems that demonstrate complicated dynamic behavior. This arises from the fact that such systems usually contain a large number of both linear and nonlinear elements, different types and layers of controls, and in an increasing number of cases, power electronic equipment used for purposes such as real and reactive power control and voltage regulation [1]. Electric machines play an important role in the operation of a power system with their capacity of converting the energy from mechanical form to electrical form and vice versa. Synchronous generators are the main source of generating electricity in the power system network, and induction machines dominate the energy consumption

sector. Modern transportation systems employ the advanced technology of electric machine drives to provide fast and environmentally friendly service to the public.

The analysis, design, and operation of such complex systems require various types of advanced tools and techniques to be employed. Power system simulation software consists of tools that can be used for both the analysis and design of power networks. In these tools, mathematical equations of the system are formed and solved using numerical methods. Thereby, they provide a sound understanding of the behavior of the system without recourse too costly or even destructive laboratory or field experiments.

Electromagnetic transient simulation programs are simulation tools that precisely analyze the performance of power systems in the time-domain. In these programs, time domain differential equations of the system, including individual elements, electric machines, controls, semiconductor switches, etc., are set up and solved using numerical integration methods, such as the trapezoidal rule [2]. Electromagnetic transient simulation programs or EMTP-type programs are used in a wide range of applications such as the tuning of power system controls, study of stress on components during transients, harmonic analysis and power quality studies [3]-[5].

## **1.2 Closed-Loop Testing of Equipment Using Real-Time Simulation**

If an electromagnetic transient simulation program can be run in real-time, i.e. the simulation results are synchronized with the real world phenomenon, then it is possible to interface actual equipment with the simulator and verify its performance under real-world conditions. Real-time simulation is needed for rigorous closed loop testing and correction of any potential problems such as harmonic injection and resonance of power electronic controllers and the power system. Closed-loop testing is characterized by taking output



signals from the simulation, and using them as input signals to a device under test. The output from the device under test is then fed back into the simulation, thereby affecting the simulation. This type of testing most closely resembles the actual performance of the device in service. However, it often requires the exchange of hundreds of input and output signals. The simulator's hardware architecture must facilitate handling these input and output requirements. A need therefore exists to develop techniques for accurate and efficient real-time simulation of systems containing power system components and power electronic apparatus. Since a real-time simulator is designed to operate essentially forever, developing numerically stable routines for these simulators is crucial.

RTDS<sup>®</sup> is the first real-time digital simulator for the power industry which was originally developed by the Manitoba HVDC Research Centre. This research is done under the sponsorship and guidance of RTDS Technologies Inc. Therefore, most of the simulations and the results obtained there-from are influenced by the capabilities and limitations of the RTDS simulator. The RTDS simulator can be used to mimic the physical system and provide the full system response during closed-loop testing. Closed loop testing not only tests the functionality and setting of particular devices, but also tests the system's reaction to the operation of that device. This provides a realistic testing environment for testing the system, the device, and the interaction between the two. As well, using an RTDS simulator for closed-loop testing enables a large number of contingency tests to be run either with or without user interaction. Many of these contingencies could not be performed by any other means or would not be permitted on the real system [6].

### 1.3 Problem Motivation

Existing models of synchronous machines in electromagnetic transients programs use the *dq0* theory to express the physical behavior of the machine in terms of mathematical equations. These equations are usually implemented in electromagnetic transients programs using the *interface-based* approach by solving machine equations in *dq0* frame and injecting machine currents into the network as current sources. The main assumption in the *dq0* theory is that the eigenvalues of the inductance matrix of a machine are unvarying as the rotor position changes. These models are widely used as the algorithm is fast; also electric utilities usually have access to the *dq0* parameters of their synchronous generators. These models, however, are not capable of correctly predicting the transient performance of the synchronous machines in irregular conditions such as during the presence of *internal faults* or rotor eccentricity. Furthermore, these models cannot account for the effects of non-sinusoidal distribution of the windings and permeance in synchronous machines. This is due to the fact that some fundamental assumptions of the *dq0* theory may not be applied in these situations.

There are some *phase-domain* machine models which have been previously developed for electromagnetic transients programs [7], [8]. In these models, the inductance matrix in the phase-domain is directly derived from the *dq0* inductance matrix using an algebraic transformation. Hence, their simulation results will be no different than the results from the interfaced models. The differences arise when the *numerical stability* and *computational burden* of the two approaches are compared.

## 1.4 Research Objectives of the Thesis

The main objective of this research is to develop a detailed and *numerically stable* synchronous machine model for *electromagnetic transients programs* which accounts for fine details of machine physical characteristics such as the *winding distribution*, *rotor geometry* and *operating-point dependent saturation*. This model is capable of properly representing winding- and permeance-related *time harmonics*, and predicting the transient behaviour of synchronous machines in conditions such as *internal faults*. Implementation of this model in a *real-time digital simulator* RTDS<sup>TM</sup> has created a unique tool for *closed-loop testing* of *relays* designed to protect the synchronous machines during internal faults. Also, this detailed model can be a reference for assessing the accuracy of more simple models, i.e. it can identify the effects of including each detail on the simulation results and the cost in execution time for considering finer details.

In this thesis, a winding function approach is developed which altogether takes into account details such as pattern of *winding distribution*, actual *rotor geometry*, and effects of *iron saturation* to generate the differential equations of the machine in a form appropriate for a coupled electric circuit approach. To improve the numerical stability of the time-domain simulation which is critical, particularly for *real-time digital simulation*, the model is implemented as an *embedded phase-domain* machine model. In this thesis, matters regarding the numerical stability of existing models of synchronous machines are also addressed.

This machine model is implemented in a *real-time* electromagnetic transients program (RTDS<sup>TM</sup>); and is capable of correctly simulating the transient performance of

synchronous machines in conditions such as *stator internal faults*. Thus, this tool has a unique feature of being used for closed-loop testing of relays designed to protect the synchronous machines from internal faults. Some of the applications of this model in synchronous generators protection schemes are also investigated in this thesis.

## 1.5 Thesis Organization

As stated, the main objective of this research is to develop a detailed synchronous machine model for a real-time digital simulator which is capable of properly representing winding- and permeance-related time harmonics, and predicting the transient behaviour of synchronous machines in conditions such as internal faults.

Following this introductory chapter, Chapter 2 introduces some basic theoretical background of electromagnetic transient simulation programs and also the significance of real-time digital simulation and its application. The chapter starts with the application of trapezoidal integration in Dommel's method of nodal analysis for electromagnetic transient phenomena. It also demonstrates the method of modeling simple elements such as inductors and capacitors in transient simulation programs. Furthermore, Chapter 2 introduces the method of interfacing more sophisticated power system components such as electric machines and power electronic sub-networks, its advantages and shortcomings. Further, the limitations of existing synchronous machine models for EMTP-type programs in representing the effects of non-sinusoidally distributed windings and their inability of modeling internal faults is explained.

Later in Chapter 2, real time digital simulation and its application is introduced. The structure (hardware and software) of RTDS, a widely used real-time digital simulator for the power industry, is presented. Finally the constraints of modeling in real-time such as

the limited amount of time for computation and communication, and the importance of numerical stability are discussed.

Chapter 3 identifies the “coupled electric circuit approach” as a suitable method for time-domain simulation of electric machines in electromagnetic transients programs. Various methods of evaluating the phase-domain inductance matrix of a synchronous machine (dq0 theory, finite element, and winding function approach) are also explained in Chapter 3. The relative merits of each of these approaches as to the level of modeling detail and accuracy of results are discussed. Chapter 3 also presents the *proposed contributions and adjustments* of this thesis to the winding function approach, and uses this method to evaluate the inductances of an experimental synchronous machine. The computed inductances are validated using the finite element approach and laboratory experiments.

Chapter 4 reviews methods of saturation treatment for calculating inductances and then proposes a new approach to accurately incorporate saturation effects in the Modified Winding Function Approach (MWFA). In this method effects of change in the operating point on the saturated values of inductances are taken into account.

Chapter 5 is devoted to time-domain simulation of electric machines in electromagnetic transients programs. The traditional approach of interfacing machine models into electromagnetic transients programs is explained briefly. Subsequently, Chapter 5 *presents* a detailed procedure for the development of an *embedded approach* for incorporating machine models into electromagnetic transients programs. This is one of the *contributions* of this thesis. Chapter 5 also *proposes* additional *numerical and*

*analytical techniques* for speeding up the above procedure. These improvements are sometimes *critical* for *real-time digital simulation*.

In Chapter 6, the new embedded synchronous machine model is *validated* through *simulations* and *laboratory experiments*. Through comparison with simulation results, the capability of the new model in correctly solving the differential equations of synchronous machines is verified. Later in Chapter 6, comparison with the results of laboratory experiments shows that the new model correctly represents winding- and permeance-related *time-harmonics* in the voltage and current signals of the machine. *Limitations* of this real-time synchronous machine model in simulating *some internal faults* are also explained in this chapter.

Chapter 7 presents some applications for this new machine model. The capabilities of this model in testing the *relays* designed to protect synchronous machines during *stator-ground faults* are demonstrated.

Finally, Chapter 8 provides a summary of this thesis and identifies the contributions made by the author. It also suggests future work and possible extension of the thesis.

This thesis ends with the list of references cited throughout the thesis and appendices which clarify some numerical, electromagnetic and electromechanical concepts.

# **Chapter 2: Background**

---

This chapter provides a brief history of electromagnetic transient simulation programs as well as the basic theoretical background of these programs. The chapter introduces real-time digital simulation, the basic structure of an RTDS simulator and the constraints of performing transient simulation in real-time.

## **2.1 Electromagnetic Transients Programs**

Electromagnetic transients programs, known as EMTP-type programs, are widely accepted tools for simulating power system transient phenomena [2]. These programs typically model the power system components in full detail and are able to simulate fast electromagnetic transients in power networks. The EMTP-type programs are powerful tools to simulate and analyze power system equipment and circuits in the time domain. In addition to transient studies, the increasing number of non-linear controllers and fast switching components puts a greater emphasis on the application of electromagnetic transient analysis in the steady-state; this is because continuous switching transients cause significant waveform distortion.

The Electro-Magnetic Transient Program (EMTP) was developed in Bonneville Power Administration (BPA), based on a proposed algorithm [2], to simulate the transient phenomena in single- and multi-phase networks. This program is considered to be the foundation of the majority of modern electromagnetic transients programs. The program uses trapezoidal integration to transform inductive and capacitive differential equations

into equivalent admittances and current sources in the discrete format. The procedure of discretizing the differential equation of such elements is explained as follows:

The differential equation of an inductor with the value of  $L$  is shown in (2.1).

$$v_L(t) = L \frac{d}{dt} i_L(t) \quad (2.1)$$

Equation (2.1) is integrated for the time interval of  $[t - \Delta t \quad t]$  as shown in (2.2):

$$\int_{t-\Delta t}^t v_L(t) dt = L \int_{t-\Delta t}^t \frac{d}{dt} i_L(t) dt \quad (2.2)$$

The integral in the right side of (2.2) has an analytical solution, and the one in the left side of (2.2) is numerically evaluated using the trapezoidal rule of integration as shown in (2.3).

$$\frac{1}{2} \Delta t (v_L(t) + v_L(t - \Delta t)) = L (i_L(t) - i_L(t - \Delta t)) \quad (2.3)$$

Equation (2.3) is the differential equation of the inductor in the discrete form. It shows the relationship between the inductor current and voltage at the present time-step ( $t$ ) and at the previous time step ( $t - \Delta t$ ). In (2.4),  $i_L(t)$ , the inductor current at the present time-step, is expressed in terms of other present and past quantities.

$$i_L(t) = g_L \cdot v_L(t) + I_{hL}(t - \Delta t) \quad (2.4)$$

where:

$$g_L = \frac{\Delta t}{2L} \quad \text{and} \quad I_h(t - \Delta t) = \frac{\Delta t}{2L} v_L(t - \Delta t) + i_L(t - \Delta t)$$

The term  $I_h$  is called **the history term**, because it is a function of past values of the current and voltage only. The term  $g_L$  is the **admittance value** of the inductor in discrete representation. This value is constant for non-varying inductors. This approach



transforms (2.4) to an equivalent circuit that consists of a resistor in parallel with a current source. This Norton equivalent [9] of the inductor in electromagnetic transients programs is shown in Figure 2.1-a, and is valid in any given time-step. This representation is employed later to calculate the voltage of the network nodes at the end of that time-step.

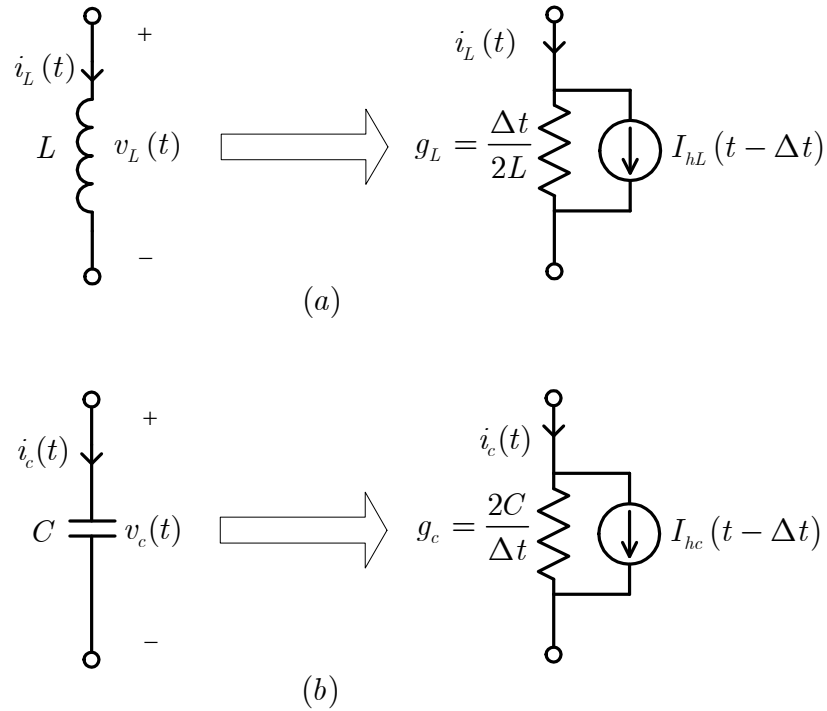


**Figure 2.1:** Norton equivalents in electromagnetic transients programs: (a) inductor, (b) capacitor

The differential equation of a capacitor (2.5) can be discretized in a similar manner as shown in (2.6):

$$i_C(t) = C \frac{d}{dt} v_C(t) \quad (2.5)$$

$$i_C(t) = g_C \cdot v_C(t) + I_{hC}(t - \Delta t)$$

where:

$$(2.6)$$

$$g_C = \frac{2C}{\Delta t} \quad \text{and} \quad I_{hC}(t - \Delta t) = -\frac{2C}{\Delta t} v_C(t - \Delta t) - i_C(t - \Delta t)$$

Figure 2.1-b shows the Norton equivalent of a capacitor in electromagnetic transients programs.

In electromagnetic transients programs, the above discretizing procedure is performed on every capacitive and inductive branch in the system. Other linear passive elements such as transformers, transmission lines, etc. can also be shown to be amenable to such a Norton equivalent representation. Once the network elements are reduced into such Norton equivalents, they can be represented by the set of linear equations using the standard nodal analysis method [2] as shown by (2.7). In this equation,  $[Y]$ ,  $\underline{V}(t)$  and  $\underline{I}_h(t - \Delta t)$  correspond to the nodal admittance matrix, node voltage vector, and injected node current vector respectively. In (2.7),  $\underline{I}(t)$  is the vector of excitation sources externally applied to the network. In the basic formulation, it is assumed that all such sources are current sources. The process of forming and solving this equation is generally called the **network solution**. In the network solution, the quantities on the right side are applied sources and history terms from previous time-steps, therefore they are known in the present time-step. By factorizing  $[Y]$ , (2.7) can be solved to yield the network node voltages in the present time-steps. This process is continued from time-step to time-step to evolve the time-domain solution of the network.

$$[Y] \cdot \underline{V}(t) = \underline{I}(t) - \underline{I}_h(t - \Delta t) \quad (2.7)$$

EMTP was one of the first electromagnetic transients programs capable of simulating transients in power systems [2]. It was suitable for modeling infrequent switching phenomenon in conventional power systems; however it was inefficient in modeling power electronic converters that need a large number of switching operations and

complex control systems. Hence, the EMTDC program [5] was developed with the capability of modeling large power electronic networks such as HVDC systems. This program relied on improved numerical methods facilitated by partitioning the network into smaller sub-networks and confining the switch branches to the lower portion of the  $[Y]$  matrix. When the status of the switch changed, it was thus only necessary to invert the matrices in the small sub-network resulting in considerable computational savings. It also had a more comprehensive library of control components necessary for power electronic device controls. In 1985, the Manitoba HVDC Research Centre validated EMTDC simulation with transient field data from Bipoles 1 and 2 of the Nelson River DC transmission system. In 1993, the Power System Computer Aided Design (PSCAD) package was combined with EMTDC to provide a graphical interface to assist users in setting up, running and analyzing simulations. The RTDS simulator evolved from EMTDC as a real-time implementation of the basic algorithm [10].

## **2.2 Approaches of Modeling Machines in Digital Electromagnetic Transient Simulation: Interface-Based & Embedded**

Sophisticated non-linear or time-varying components such as electric machines are usually integrated into the network solution of an electromagnetic transients program as a controlled current source. The electromagnetic transients program solves the circuit external to the component and communicates the voltages on the nodes of the component back to the component model. The component model in turn, uses these voltages as inputs and calculates the currents by solving the differential equations of that particular component. The computed currents are then injected back into the main network solution of the electromagnetic transients program. The network solution sees the externally

computed machine currents as an impressed current source. The machine model uses the network voltages computed by the external solver to calculate its currents. Note that the latest values available to each of the two solvers from the other are necessarily from the previous time-step. This one time-step delay between the solutions can be a source of errors or even numerical instabilities. The above procedure is repeated in each time-step. This is called the *interfaced-based* approach of modeling components. Figure 2.2 shows the manner in which a component is interfaced to the network solution as a current source.

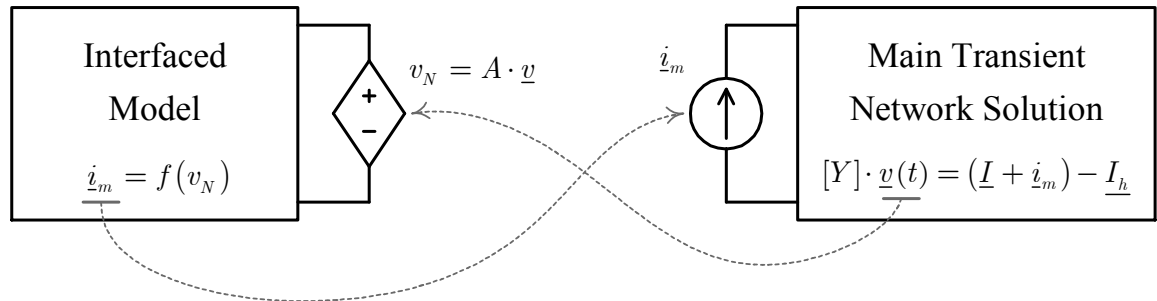


**Figure 2.2:** Interfacing components to the network solution as a current source

This technique allows smaller and more manageable sub-systems that can be easily simulated in parallel for real time purposes. The advantage of this approach in modeling electric machines is that the machine model is external to the network solution program, and the machine inductances are not included in the admittance matrix of the transient solution. Note that, unlike other elements, the machine rotates continuously, therefore its inductances are time-varying. Following the interfacing approach means that a new admittance matrix needs not to be calculated (and factorized) for each time-step in an electro-magnetic transient program.

This method has acceptable numerical stability and accuracy in conventional power system circuits with the operating frequency of 50-60 Hz and a simulation time-step of  $50 \mu s$  [11]. However, it shows numerical instability and inaccuracies in some cases, depending on the network configuration, system frequency and simulation time-step [12], [13]. The numerical performance can often be improved using projection methods that predict one time-step ahead node voltages from previous time-step values [14]. However, this is not always effective. The numerical performance is a critical matter in real-time simulation, because real-time digital simulators often operate for long periods of time (even continuous), and therefore there is a possibility of the constant accumulation of error as time progresses.

Another approach of integrating electric machines into electromagnetic transients programs is to involve the network solution engine in solving the mathematical equations of machines. In this approach, called *embedded* in this thesis, the time-varying inductances of machines are absorbed into the network solution in the manner of other passive elements such as capacitors, inductors and resistors. As before, in a manner similar to simple inductors and capacitors, the *trapezoidal integration* method [2] is applied to convert the *phase-domain* machine equations into Norton equivalents. Due to the avoidance of the time-step delay, the resulting machine model, referred to as the *embedded phase-domain*, is more stable than the interfaced-based model as will be shown in Chapter 5 of this thesis.

### **2.3 Level of Detail in Existing Synchronous Machine Models in Digital Electromagnetic Transient Simulators**

So far, the synchronous machine models implemented in electromagnetic transients programs use the dq0 theory [15], [16] to express the physical behaviour of the machines. In this theory, using the well known dq0 transformation, the machine variables in abc frame are transformed into a dq0 frame to eliminate the dependence of machine inductances on rotor position. This theory will be discussed in the following chapter.

The implementation of dq0-based machine models can be conducted either directly in dq0 frame by interfacing the machine model to electromagnetic transients programs [11], [17], or by transferring the variables back to abc frame and solving the machine equations in the phase-domain [7],[8]. Since the differential equations in both of the above approaches are algebraically equivalent, both models are expected to show identical transient behaviors [18],[19]. The models, however, may show different performances due to the individual numerical stability and accuracy behaviors of the selected approach [12], [19].

The advantage of the dq0-based formulation is its simplicity and the familiarity of dq0-based models amongst power system engineers. Also, the algorithm for implementing this model in electromagnetic transients programs is fast and efficient, particularly if the model is solved directly in dq0 domain and interfaced to the program.

One of the assumptions in this approach is that the machine windings are considered to be sinusoidally distributed and therefore the machine inductances have a particular sinusoidal form which does not contain space harmonics. Consequently, such models

cannot generate time-harmonics in the voltages and currents of the machine which otherwise exist as a result of space harmonics of the machine.

The other inadequacy of dq0 theory is that this theory is not valid if some structural asymmetries (e.g. internal faults or dynamic eccentricity) exist in the machine. Therefore, dq0-based models in electromagnetic transients programs are not suitable for such scenarios.

In the dq0 theory, machine equations in dq0 frame are interpreted as equivalent circuits on d-, q- and 0-axes. Each of the equivalent circuits on the d- and q-axes contains a magnetizing inductance called  $L_{md}$  and  $L_{mq}$  respectively. In dq0-based synchronous machine models, the values of  $L_{md}$  and  $L_{mq}$  are adjusted for the purpose of incorporating the effects of iron saturation. This approach is a macroscopic treatment of saturation which does not account for local saturation in the iron and distribution of magnetomotive force (MMF). Furthermore, the implementation of saturation in various electromagnetic transients programs is done in different manners, causing some discrepancies in the simulation results. This matter is addressed in Chapter 4 of this thesis.

## **2.4 Real-Time Electromagnetic Transients Programs**

Real time simulation was originally developed for the closed-loop testing of physical equipment that could be externally connected to the simulator. Electromagnetic transient simulation tools (excluding the fully digital offline simulators) can be classified into three main groups in accordance with their order of evolution [20].

1. Transient Network Analyzers (TNAs)

2. Analogue and Hybrid Simulators
3. Digital Transient Network Analyzers (DTNAs)

A TNA is a set of scaled down models of actual physical equipment operating at much lower levels of voltage and current [21]. The power system components, including generators, transformers, transmission lines, and power electronic converters are connected as in a real-network to assure real-time operation. TNAs are very expensive and difficult to build, but before the advent of computers, they were the only possible solution. A major problem with analogue TNAs is that parameter settings are implemented using potentiometers and other analogue means. This makes precise setting very difficult. Also component aging and other mechanical variations make it very challenging to precisely reproduce results from a study at much later dates.

Analogue electronic integrators, summers, and multipliers have been used in some analogue simulators to solve the equations describing a power system [22]. This approach helped in reducing the size and cost of the simulator. With the progress of digital computers, hybrid simulators were born. These simulators were combinations of passive physical equipment and digital computer models.

A digital simulator emulates a physical component by solving the mathematical equations which describe the behavior of the component. Electromagnetic transients programs such as EMTP and EMTDC are circuit oriented programs which utilize the nodal method of analysis for transient simulation [2].

Fast advancement in computer technology and parallel processing provided motivation for the development of fully real-time digital simulators which conquered the market of existing TNAs and hybrid simulators. Digital simulation overcomes the



shortcomings of the traditional analogue technology; it provides superior capabilities to analogue simulators; and it results in significant economies in operating costs and laboratory space over analogue technology. Digital simulators do not use physical miniaturizations of the system components. Component parameters and circuit configurations are instead, based on software models. Therefore, the models are not limited by the parameters of a single study. Digital simulation studies can be quickly and easily modified and there is minimal time involved to switch from one study to another [6]. Popular examples of real-time digital simulators are:

- RTDS<sup>TM</sup> ; initially designed by Manitoba HVDC Research Centre [6],
- Hypersim<sup>TM</sup> Simulator; initially designed by Hydro-Québec's Research Institute [23], and the
- Opal\_RT<sup>TM</sup> Simulator [24]

Major applications of real time simulators are power system protection (relay testing) [10] and testing of FACTS<sup>1</sup>, and HVDC<sup>2</sup> controllers [25]. They can also be used for analytical system studies and training of operators [6].

The simulator used in this thesis is the RTDS Simulator from RTDS Technologies Inc. [6]. It takes advantage of a custom parallel processing hardware architecture assembled in modular units called *racks*. Each rack contains slots (max. 20) and rail-mounted cards. A common communications backplane links all rack-mounted cards facilitating information exchange. Each rack's backplane functions independently so that communication of data can be done in parallel thereby reducing communication bottlenecks. The present generation of RTDS hardware, uses a GPC (Giga Processor

---

<sup>1</sup> Flexible Alternating Current Transmission System

<sup>2</sup> High-Voltage Direct Current

Card) [26] to perform the network solution. The computations required to model the user's power system components are performed on Triple Processor Cards (3PC) [26] or other GPC cards. The computed history terms and admittance values are then transferred through the backplane communication channels to the GPC card, which runs the network solver. The RTDS Simulator uses a graphical user interface, the RSCAD Software Suite. This software is the user's main interface with the RTDS hardware. The software contains several modules designed to allow the user to perform all of the necessary steps to prepare and run a simulation, and to analyze simulation output [6], [26].

As mentioned, computational time plays a very important role in modeling components for RTDS. Any model has to be implemented with a limited number of instructions in the range of the computational capacity of 3PC and GPC cards [6], [26] to ensure a real-time simulation. There are also limitations on the amount of data that can be transferred between different cards of the simulator [26]. Also, numerical instability is not acceptable since the simulation must be capable of being run on a continuous basis.

# Chapter 3: Evaluation of Synchronous Machines Electric Parameters

---

This chapter begins with the introduction of the *coupled electric circuit approach* as a suitable method for time-domain modeling of electric machines in electromagnetic transients programs. In this approach, the inductances of a machine are the input parameters which need to be evaluated before the simulation begins. In this chapter, different methods of evaluating inductances of synchronous machines (dq0 theory, finite element, and the winding function approach) are introduced. The relative merits of each of these approaches, based on the level of modeling detail and accuracy of results, are discussed. This chapter also *proposes* some *adjustments* to the winding function approach, which makes this method capable of taking into account the effects of *iron saturation* in different *loading conditions*. The computed inductances using this method are validated using the finite element approach and laboratory experiments.

## 3.1 Time Domain Modeling of Electric Machines Using the Coupled Electric Circuit Approach

The equivalent magnetic circuit approach [27],[28] and the coupled electric circuit approach are two widely used methods for time-domain modeling of electric machines. In the latter, a machine is modeled as a set of mutually-coupled time-varying inductances. This approach is more common in simulating the dynamic response of electric machines [7], [8], [11], [12], [17], [29] as it leads to a relatively small number of equations. In system level studies, machines are connected to a large external network; hence a fast, simple and yet sufficiently accurate machine model is needed for such studies. Thus, in

electromagnetic transients programs electric machines are modeled using the coupled electric circuit approach [7], [8], [11], [12], [17].

In this coupled electric circuit approach the relationship between voltages and currents of the windings of a machine are as in (3.1). Here,  $\underline{v}(t)$ ,  $\underline{i}(t)$  and  $\underline{\Psi}(t)$  are respectively vectors of voltages, currents and flux linkages for each of the windings in the machine. The resistance matrix  $[R]$  is a diagonal matrix containing resistances of the windings. The time-varying inductance matrix of the machine  $[L(t)] = [L(\theta(t), \underline{i}(t))]$  is the major factor in machine dynamic behaviour, which changes with rotor position and winding currents.

$$\underline{v}(t) = \frac{d}{dt} \underline{\Psi}(t) + [R] \underline{i}(t) = \frac{d}{dt} ([L(t)] \underline{i}(t)) + [R] \underline{i}(t) \quad (3.1)$$

In the following sub-sections, the principal methods of evaluating the inductance matrix of a synchronous machine are explained. Throughout this thesis, the positive sign is used for the inward flow of current into a coil as indicated in Figure 3.1 . Also, the positive torque corresponds to motoring operation of an electric machine (i.e. the torque generated by the machine is positive). Throughout this thesis, the per-unit bases for the voltage and current quantities of a machine are the rated line-neutral RMS voltage and the rated line RMS current of the machine respectively.

### 3.2 Dq0 Theory on Modeling Electric Machines

In this section, the dq0 theory is reviewed, and the manner in which this theory is used for modeling synchronous machines and permanent magnet synchronous machines is explained. *The following dq0 analysis is a summary of the comprehensive work conducted by previous authors.*

Equation (3.1) is the differential equation of an electric machine in the coupled electric circuit approach, which is often referred to as the phase-domain model of a machine. Some of the inductances of electric machines are functions of rotor position; therefore the inductance matrix of a machine is time-dependent. A change of variable is often employed to reduce the complexity of these differential equations. In the late 1920's, R. H. Park [15],[16] formulated a change in variables which effectively replaced the variables affiliated with the stator windings of a synchronous machine with variables associated with a fictitious windings rotating with the rotor. By transforming the stator variables to a frame of reference fixed in the rotor, he eliminated the dependence of synchronous machine inductance matrix on rotor position. The procedure of transforming inductances of a synchronous machine from the stator frame of reference to the rotor frame of reference is shown in the next section.

### 3.2.1 Application of Dq0 Theory in the Modeling of Synchronous Machines

The diagram of an *idealized two-pole synchronous machine* is shown in Figure 3.1. This type of representation is customary for the purpose of developing theories for electric machines [30]-[32]. The machine depicted in Figure 3.1 is a simplified form of a practical machine with three armature windings on the stator ( $a, b$  and  $c$ ) and one field winding on the rotor ( $F$ ). The axes  $as$ ,  $bs$ , and  $cs$  indicate the positive direction of the *magneto-motive force* (MMF) produced by phase-A, B, and C of the stator respectively. The *direct-axis* is the direction of MMF produced by the field winding. The angular velocity of the rotor, and the angular shift between the direct-axis and the axis of phase-A are designated by  $\omega_r$  and  $\theta_r$  respectively. The damper grid of a practical synchronous machine consists of many circuits carrying different currents and would require a large

number of coils for its representation. Nevertheless, for many applications it is sufficiently accurate to represent the damper circuit by only one or two damper windings ( $D$  and  $Q$ ) on each of the direct and quadrature axes [30]-[33].

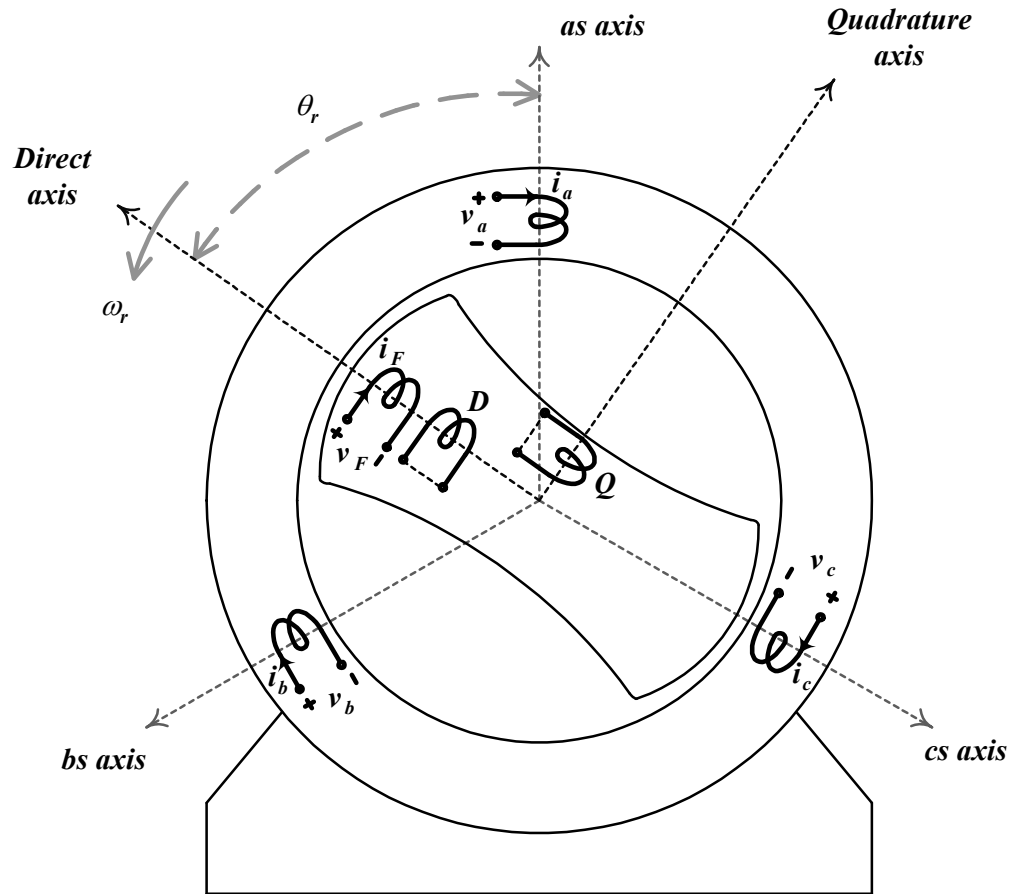


**Figure 3.1: Diagram of an idealized synchronous machine**

The set of differential equations for the machine in (3.1) is usually divided into flux linkage equations and voltage equations as respectively shown in (3.2) and (3.3). In (3.2)  $\Psi_a \cdots \Psi_Q$  and  $i_a \cdots i_Q$  are respectively flux linkages and currents of the machine windings. As shown in (3.3), the inductance matrix of the machine identifies the relationship between the flux linkages and currents. The synchronous machine inductance matrix can be divided into four sub-matrices: the inductance matrix of stator windings

shown by  $[L_{ss}]$ , the mutual inductances between stator and rotor windings included in  $[L_{sr}]$  and  $[L_{rs}]$ , and the inductance matrix of the rotor windings shown by  $[L_{rr}]$ .

$$\begin{array}{c}
 \begin{array}{c} \overbrace{\Psi_{abc}} \\ \Psi_a \\ \Psi_b \\ \Psi_c \end{array} \\
 \text{stator} \\
 \\
 \begin{array}{c} \overbrace{\Psi_{FDR}} \\ \Psi_F \\ \Psi_D \\ \Psi_Q \end{array} \\
 \text{rotor}
 \end{array}
 =
 \begin{array}{c}
 \begin{array}{c} \overbrace{[L_{ss}]} \\ L_{aa} \quad L_{ab} \quad L_{ac} \\ L_{ba} \quad L_{bb} \quad L_{bc} \\ L_{ca} \quad L_{cb} \quad L_{cc} \end{array} \\
 \\
 \begin{array}{c} \overbrace{[L_{rs}]=[L_{sr}]^T} \\ L_{Fa} \quad L_{Fb} \quad L_{Fc} \\ L_{Da} \quad L_{Db} \quad L_{Dc} \\ L_{Qa} \quad L_{Qb} \quad L_{Qc} \end{array} \\
 \\
 \begin{array}{c} \overbrace{[L_{rr}]} \\ L_{FF} \quad L_{FD} \quad L_{FQ} \\ L_{DF} \quad L_{DD} \quad L_{DQ} \\ L_{QF} \quad L_{QD} \quad L_{QQ} \end{array}
 \end{array}
 \begin{array}{c}
 \overbrace{i_{abc}} \\ i_a \\ i_b \\ i_c \\
 \\
 \overbrace{i_{FDR}} \\ i_F \\ i_D \\ i_Q
 \end{array}
 \quad (3.2)$$

$$\begin{array}{c}
 \overbrace{v_{abc}} \\ v_a \\ v_b \\ v_c \\
 \\
 \overbrace{v_{FDR}} \\ v_F \\ 0 \\ 0
 \end{array}
 =
 \begin{array}{c}
 \begin{array}{c} \overbrace{[r_s]} \\ r_s \quad 0 \quad 0 \\ 0 \quad r_s \quad 0 \\ 0 \quad 0 \quad r_s \end{array} \\
 \\
 \begin{array}{c} \overbrace{[r_r]} \\ r_F \quad 0 \quad 0 \\ 0 \quad r_D \quad 0 \\ 0 \quad 0 \quad r_Q \end{array}
 \end{array}
 \begin{array}{c}
 \begin{pmatrix} i_a \\ i_b \\ i_c \end{pmatrix} \\
 \begin{pmatrix} i_F \\ i_D \\ i_Q \end{pmatrix}
 \end{array}
 + \frac{d}{dt}
 \begin{array}{c}
 \begin{pmatrix} \Psi_a \\ \Psi_b \\ \Psi_c \end{pmatrix} \\
 \begin{pmatrix} \Psi_F \\ \Psi_D \\ \Psi_Q \end{pmatrix}
 \end{array}
 \quad (3.3)$$

From symmetry considerations, in a two-pole synchronous machine, in each complete rotation of the rotor, the stator inductances assume the same values twice. Therefore, stator inductances show a space variation of period equal to  $\pi$  and hence consist of a *constant value* and *even* space harmonics. Similarly, the values of mutual inductances between stator and rotor repeat *once* in every complete rotation of the rotor. These functions have the period of  $2\pi$  and consist of *odd* space harmonics. In the dq0 analysis, the space harmonics higher than the second space harmonic are ignored, therefore the functions shown in (3.4)-(3.10) are used to represent the inductances of a synchronous

machine (for an equivalent two-pole machine). This is tantamount to the assumption of windings with a perfectly sinusoidal distribution.

- **Stator inductances:**

Stator inductances show a space variation of frequency equal to twice the fundamental and hence, predominantly consist of a constant value and a second space harmonic. Stator self inductances of a synchronous machine are shown in (3.4). In this equation both  $L_s$  and  $L_m$  are constants and  $L_s > L_m \geq 0$  [32].

$$\begin{aligned} L_{aa}(\theta_r) &= L_s + L_m \cos 2(\theta_r) & \text{(H)} \\ L_{bb}(\theta_r) &= L_s + L_m \cos 2\left(\theta_r - \frac{2\pi}{3}\right) & \text{(H)} \\ L_{cc}(\theta_r) &= L_s + L_m \cos 2\left(\theta_r + \frac{2\pi}{3}\right) & \text{(H)} \end{aligned} \quad (3.4)$$

Equation (3.5) shows the stator mutual inductances of the synchronous machine. In this equation both  $M_s$  and  $L_m$  are constants and  $|M_s| > L_m$  [32]. *With perfectly sinusoidally distributed windings and permeance (assumptions implicit in the dq0 theory), the stator self and mutual inductances have the same peak-to-peak values.* In (3.4) the leakage portion of stator self inductances  $l_s$  is included in  $L_s$ , and

$$L_s - l_s = 2M_s [31].$$

$$\begin{aligned} L_{ab}(\theta_r) &= L_{ba}(\theta_r) = -M_s - L_m \cos 2\left(\theta_r + \frac{\pi}{6}\right) & \text{(H)} \\ L_{bc}(\theta_r) &= L_{cb}(\theta_r) = -M_s - L_m \cos 2\left(\theta_r - \frac{\pi}{2}\right) & \text{(H)} \\ L_{ca}(\theta_r) &= L_{ac}(\theta_r) = -M_s - L_m \cos 2\left(\theta_r + \frac{5\pi}{6}\right) & \text{(H)} \end{aligned} \quad (3.5)$$



- **Mutual inductances between stator and rotor windings:**

Equations (3.6) to (3.8) show the mutual inductances between the stator windings and windings  $F$ ,  $D$  and  $Q$  of the rotor. As can be seen, in these functions, only the fundamental space harmonics are considered and higher space harmonics are ignored. The actual form of these inductances consists of additional *odd* harmonics which will be clarified more in Section 3.4.

$$\begin{aligned}
 L_{aF}(\theta_r) &= L_{Fa}(\theta_r) = M_F \cos(\theta_r) & \text{(H)} \\
 L_{bF}(\theta_r) &= L_{Fc}(\theta_r) = M_F \cos\left(\theta_r - \frac{2\pi}{3}\right) & \text{(H)} \\
 L_{cF}(\theta_r) &= L_{Fb}(\theta_r) = M_F \cos\left(\theta_r - \frac{4\pi}{3}\right) & \text{(H)}
 \end{aligned} \tag{3.6}$$

$$\begin{aligned}
 L_{aD}(\theta_r) &= L_{Da}(\theta_r) = M_D \cos(\theta_r) & \text{(H)} \\
 L_{bD}(\theta_r) &= L_{Db}(\theta_r) = M_D \cos\left(\theta_r - \frac{2\pi}{3}\right) & \text{(H)} \\
 L_{cD}(\theta_r) &= L_{Dc}(\theta_r) = M_D \cos\left(\theta_r - \frac{4\pi}{3}\right) & \text{(H)}
 \end{aligned} \tag{3.7}$$

$$\begin{aligned}
 L_{aQ}(\theta_r) &= L_{Qa}(\theta_r) = M_Q \sin(\theta_r) & \text{(H)} \\
 L_{bQ}(\theta_r) &= L_{Qb}(\theta_r) = M_Q \sin\left(\theta_r - \frac{2\pi}{3}\right) & \text{(H)} \\
 L_{cQ}(\theta_r) &= L_{Qc}(\theta_r) = M_Q \sin\left(\theta_r - \frac{4\pi}{3}\right) & \text{(H)}
 \end{aligned} \tag{3.8}$$

- **Rotor inductances**

Because of the cylindrical structure of the stator (ignoring the effects of slots), the rotor windings (field and damper windings) observe constant permeance. Therefore, self and mutual inductances of the rotor windings do not vary with rotor position. All pairs of windings with  $90^\circ$  displacement have zero mutual inductance. The self inductances of the

rotor windings and the mutual inductances between any pair of these windings are respectively shown in (3.9) and (3.10) .

$$L_{FF}(\theta_r) = L_F \quad L_{DD}(\theta_r) = L_D \quad L_{QQ}(\theta_r) = L_Q \quad (\text{H}) \quad (3.9)$$

$$\begin{aligned} L_{FD}(\theta_r) &= L_{DF}(\theta_r) = M_R & (\text{H}) \\ L_{FQ}(\theta_r) &= L_{QF}(\theta_r) = 0 & (\text{H}) \\ L_{DQ}(\theta_r) &= L_{QD}(\theta_r) = 0 & (\text{H}) \end{aligned} \quad (3.10)$$

### 3.2.1.1 Flux linkage equations in dq0 frame

At the beginning of this chapter it was mentioned that in the dq0 approach, a transformation is used to transfer variables from the stator's frame of reference to the rotor's frame of reference. In this thesis, the transformation  $P$ , as shown in (3.11), is used for this purpose. This is a modified form of the original Park's transformation [15], in that it is an orthogonal transformation (i.e.  $P^{-1}(\theta) = P^T(\theta)$ ). The use of this orthogonal transformation results in a symmetrical inductance matrix in dq0 format.

$$P(\theta_r) = \sqrt{\frac{2}{3}} \begin{pmatrix} \cos \theta_r & \cos\left(\theta_r - \frac{2\pi}{3}\right) & \cos\left(\theta_r - \frac{4\pi}{3}\right) \\ \sin \theta_r & \sin\left(\theta_r - \frac{2\pi}{3}\right) & \sin\left(\theta_r - \frac{4\pi}{3}\right) \\ \frac{1}{\sqrt{2}} & \frac{1}{\sqrt{2}} & \frac{1}{\sqrt{2}} \end{pmatrix} \quad (3.11)$$

This transformation generates the dq0 components of the voltages, currents, and flux linkages as shown in (3.12):

$$\begin{aligned} \underline{v}_{dq0s} &= P(\theta_r) \cdot \underline{v}_{abcs} \\ \underline{i}_{dq0s} &= P(\theta_r) \cdot \underline{i}_{abcs} \\ \underline{\Psi}_{dq0s} &= P(\theta_r) \cdot \underline{\Psi}_{abcs} \end{aligned} \quad (3.12)$$

Applying the transformation  $P$  to the flux linkage equation of (3.2) results in (3.13):

$$\begin{pmatrix} P & 0 \\ 0 & I_3 \end{pmatrix} \begin{pmatrix} \underline{\Psi}_{abc} \\ \underline{\Psi}_{FDQr} \end{pmatrix} = \begin{pmatrix} P & 0 \\ 0 & I_3 \end{pmatrix} \begin{pmatrix} L_{ss} & L_{sr} \\ L_{sr}^T & L_{rr} \end{pmatrix} \begin{pmatrix} P^{-1} & 0 \\ 0 & I_3 \end{pmatrix} \begin{pmatrix} P & 0 \\ 0 & I_3 \end{pmatrix} \begin{pmatrix} \dot{i}_{abc} \\ \dot{i}_{FDQr} \end{pmatrix} \quad (3.13)$$

Using (3.12) and (3.13), the flux linkage equations in dq0 frame are derived and shown in (3.14):

$$\begin{pmatrix} \underline{\Psi}_{dq0s} \\ \underline{\Psi}_{FDQr} \end{pmatrix} = \begin{pmatrix} P \cdot L_{ss} \cdot P^{-1} & P \cdot L_{sr} \\ L_{sr}^T \cdot P^{-1} & L_{rr} \end{pmatrix} \begin{pmatrix} \dot{i}_{dq0s} \\ \dot{i}_{FDQr} \end{pmatrix} \quad (3.14)$$

Equation (3.15) shows the expanded version of (3.14) and the new inductance matrix of the machine in dq0 frame. As shown, the inductance matrix in dq0 frame is much simpler than the inductance matrix in the phase-domain formulation and is independent of the rotor position.

$$\begin{pmatrix} \Psi_d \\ \Psi_q \\ \Psi_0 \\ \Psi_F \\ \Psi_D \\ \Psi_Q \end{pmatrix} = \begin{pmatrix} L_d & 0 & 0 & kM_F & kM_D & 0 \\ 0 & L_q & 0 & 0 & 0 & kM_Q \\ 0 & 0 & L_0 & 0 & 0 & 0 \\ kM_F & 0 & 0 & L_F & M_R & 0 \\ kM_D & 0 & 0 & M_R & L_D & 0 \\ 0 & kM_Q & 0 & 0 & 0 & L_Q \end{pmatrix} \begin{pmatrix} i_d \\ i_q \\ i_0 \\ i_F \\ i_D \\ i_Q \end{pmatrix} \quad (3.15)$$

$$L_d = L_s + M_s + \frac{3}{2} L_m \quad L_0 = L_s - 2M_s = l_s$$

$$L_q = L_s + M_s - \frac{3}{2} L_m \quad k = \sqrt{\frac{3}{2}}$$

### 3.2.1.2 Voltage equations in dq0 frame

The voltage equations of (3.3) can also be transferred to dq0 frame using the transformation  $P$  as shown in (3.16) and (3.17). Here,  $I_3$  is the  $3 \times 3$  identity matrix.

$$\begin{pmatrix} P & 0 \\ 0 & I_3 \end{pmatrix} \begin{pmatrix} \underline{v}_{abc} \\ \underline{v}_{FDQr} \end{pmatrix} = \begin{pmatrix} P & 0 \\ 0 & I_3 \end{pmatrix} \begin{pmatrix} r_s & 0 \\ 0 & r_r \end{pmatrix} \begin{pmatrix} P^{-1} & 0 \\ 0 & I_3 \end{pmatrix} \begin{pmatrix} P & 0 \\ 0 & I_3 \end{pmatrix} \begin{pmatrix} \dot{\underline{i}}_{abc} \\ \dot{\underline{i}}_{FDQr} \end{pmatrix} + \begin{pmatrix} P & 0 \\ 0 & I_3 \end{pmatrix} \frac{d}{dt} \begin{pmatrix} \underline{\Psi}_{abc} \\ \underline{\Psi}_{FDQr} \end{pmatrix} \quad (3.16)$$

$$\begin{pmatrix} \underline{v}_{dq0s} \\ \underline{v}_{FDQr} \end{pmatrix} = \begin{pmatrix} P \cdot r_s \cdot P^{-1} & 0 \\ 0 & r_r \end{pmatrix} \begin{pmatrix} \dot{\underline{i}}_{dq0s} \\ \dot{\underline{i}}_{FDQr} \end{pmatrix} + \begin{pmatrix} P \cdot \frac{d}{dt} \underline{\Psi}_{abc} \\ \frac{d}{dt} \underline{\Psi}_{FDQr} \end{pmatrix} \quad (3.17)$$

Evaluation of  $P \cdot \frac{d}{dt} \underline{\Psi}_{abc}$  can be done by recalling the definition of  $\underline{\Psi}_{dq0s}$  in (3.12),

and simple computations of (3.18).

$$\begin{aligned} \frac{d}{dt} \underline{\Psi}_{dq0s} &= \frac{d}{dt} (P \cdot \underline{\Psi}_{abc}) = \left( \frac{d}{dt} P \right) \cdot \underline{\Psi}_{abc} + P \left( \frac{d}{dt} \underline{\Psi}_{abc} \right) \\ \text{therefore: } P \left( \frac{d}{dt} \underline{\Psi}_{abc} \right) &= \frac{d}{dt} \underline{\Psi}_{dq0s} - \left( \frac{d}{dt} P \right) \cdot P^{-1} \cdot \underline{\Psi}_{dq0s} \end{aligned} \quad (3.18)$$

Now the voltage equations in dq0 frame are:

$$\begin{pmatrix} \underline{v}_{dq0s} \\ \underline{v}_{FDQr} \end{pmatrix} = \begin{pmatrix} r_s & 0 \\ 0 & r_r \end{pmatrix} \begin{pmatrix} \dot{\underline{i}}_{dq0s} \\ \dot{\underline{i}}_{FDQr} \end{pmatrix} + \frac{d}{dt} \begin{pmatrix} \underline{\Psi}_{dq0s} \\ \underline{\Psi}_{FDQr} \end{pmatrix} - \begin{pmatrix} \left( \frac{d}{dt} P \right) \cdot P^{-1} \cdot \underline{\Psi}_{dq0s} \\ 0 \end{pmatrix} \quad (3.19)$$

After expansion, the voltage equations of the machine are obtained in a simple dq0

format shown in (3.20):

$$\begin{pmatrix} v_d \\ v_q \\ v_0 \\ v_F \\ 0 \\ 0 \end{pmatrix} = \begin{pmatrix} r_s & 0 & 0 & 0 & 0 & 0 \\ 0 & r_s & 0 & 0 & 0 & 0 \\ 0 & 0 & r_s & 0 & 0 & 0 \\ 0 & 0 & 0 & r_F & 0 & 0 \\ 0 & 0 & 0 & 0 & r_D & 0 \\ 0 & 0 & 0 & 0 & 0 & r_Q \end{pmatrix} \begin{pmatrix} i_d \\ i_q \\ i_0 \\ i_F \\ i_D \\ i_Q \end{pmatrix} + \frac{d}{dt} \begin{pmatrix} \Psi_d \\ \Psi_q \\ \Psi_0 \\ \Psi_F \\ \Psi_D \\ \Psi_Q \end{pmatrix} + \omega_r \begin{pmatrix} \Psi_q \\ -\Psi_d \\ 0 \\ 0 \\ 0 \\ 0 \end{pmatrix} \quad (3.20)$$

### 3.2.1.3 Derivation of the synchronous machine equivalent circuit in the dq0 frame

By combining (3.15) and (3.20), and re-arranging rows and columns of matrices with respect to the d-, q- and 0- axes, (3.21) is derived. The inductance matrix in this equation is a block diagonal matrix in which each block matrix is the inductance matrix of sets of windings in d-, q- and 0- axes respectively. As predicted, there is no mutual inductance between windings from different axes. This form of equations simplifies the analysis of synchronous machines. Furthermore, an equivalent circuit can be extracted more easily using this equation.

$$\begin{pmatrix} v_d \\ v_F \\ v_D = 0 \\ v_q \\ v_Q = 0 \\ v_0 \end{pmatrix} = \begin{pmatrix} r_s & 0 & 0 & 0 & 0 & 0 \\ 0 & r_F & 0 & 0 & 0 & 0 \\ 0 & 0 & r_D & 0 & 0 & 0 \\ 0 & 0 & 0 & r_s & 0 & 0 \\ 0 & 0 & 0 & 0 & r_Q & 0 \\ 0 & 0 & 0 & 0 & 0 & r_s \end{pmatrix} \cdot \begin{pmatrix} i_d \\ i_F \\ i_D \\ i_q \\ i_Q \\ i_0 \end{pmatrix} + \begin{pmatrix} L_d & kM_F & kM_D & 0 & 0 & 0 \\ kM_F & L_F & M_R & 0 & 0 & 0 \\ kM_D & M_R & L_D & 0 & 0 & 0 \\ 0 & 0 & 0 & L_q & kM_Q & 0 \\ 0 & 0 & 0 & kM_Q & L_Q & 0 \\ 0 & 0 & 0 & 0 & 0 & L_0 \end{pmatrix} \frac{d}{dt} \begin{pmatrix} i_d \\ i_F \\ i_D \\ i_q \\ i_Q \\ i_0 \end{pmatrix} + \omega_r \begin{pmatrix} \Psi_q \\ 0 \\ 0 \\ -\Psi_d \\ 0 \\ 0 \end{pmatrix} \quad (3.21)$$

Windings ( $F, D$  and  $Q$ ) have different turns compared to stator windings.

Therefore, the mutual inductances between each of the windings ( $F, D$  and  $Q$ ) and stator windings have much different values compared to the magnetizing inductances of stator d- and q-axes ( $L_{md} = L_d - l_s$ ,  $L_{mq} = L_q - l_s$ ). Hence, to extract the equivalent

circuit of the synchronous machine from (3.21), the *turns-ratio* of these windings must be taken into account [34]. This method of normalizing machine equations is adopted in this thesis and results in an equivalent circuit with physical parameters (not per unit). The resulting equivalent circuit can be per-unitized later if needed. Equation (3.22) shows the normalized values of the parameters of the windings ( $F, D$  and  $Q$ ). After this normalization, the equivalent circuit of the synchronous machine in dq0 frame can be extracted which is shown in Figure 3.2. Leakage and magnetization inductances of the synchronous machine's equivalent circuit are also defined in (3.22).

Field/Stator	Damper(D)/Stator	Damper(Q)/Stator
$a_F = \frac{kM_F}{L_{md}}$	$a_D = \frac{kM_D}{L_{md}}$	$a_Q = \frac{kM_Q}{L_{mq}}$
$v'_F = \frac{v_F}{a_F}$	$v'_D = \frac{v_D}{a_D} = 0$	$v'_Q = \frac{v_Q}{a_Q} = 0$
$i'_F = a_F \cdot i_F$	$i'_D = a_D \cdot i_D$	$i'_Q = a_Q \cdot i_Q$
$r'_F = \frac{r_F}{(a_F)^2}$	$r'_D = \frac{r_D}{(a_D)^2}$	$r'_Q = \frac{r_Q}{(a_Q)^2}$
$L'_F = \frac{L_F}{(a_F)^2}$	$L'_D = \frac{L_D}{(a_D)^2}$	$L'_Q = \frac{L_Q}{(a_Q)^2}$
$L'_F = \frac{L_F}{(a_F)^2}$	$L'_D = \frac{L_D}{(a_D)^2}$	$L'_Q = \frac{L_Q}{(a_Q)^2}$
Leakage Inductances:		
$l'_{DF} = M'_R - L_{md}$	$l'_F = L'_F - M'_R$	
$l'_D = L'_D - M'_R$	$l'_Q = L'_Q - L_{mq}$	

(3.22)

The inductance  $l'_{DF}$  in the d-axis of the equivalent circuit represents the mutual flux linkage path, which links the field and damper windings on the d-axis, but which does not link the armature winding on the d-axis [30], [33]. The existing synchronous machine model in RTDS [26] is based on the ladder model presented in [33], which includes the inductance  $l'_{DF}$ .

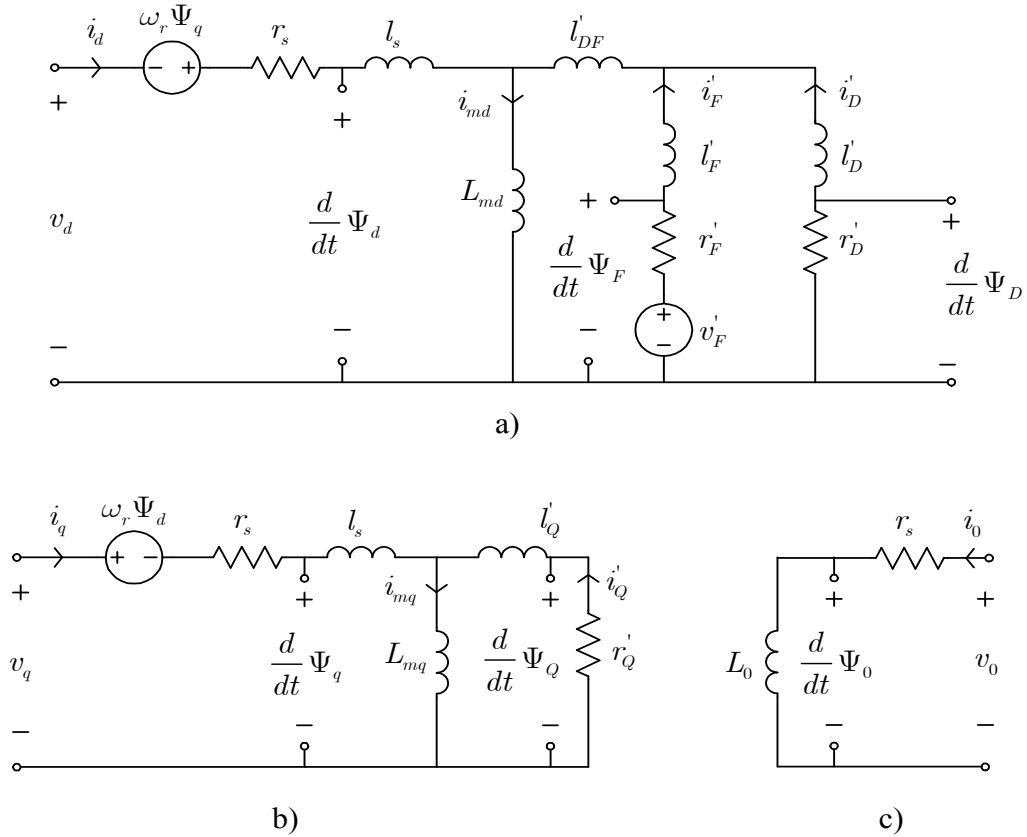


Figure 3.2: Dq0 equivalent circuit of a synchronous machine: (a) d-axis, (b) q-axis, (c) 0-axis

### 3.2.2 Application of the Dq0 Theory in the Modeling of Permanent Magnet Synchronous Machines

Two types of synchronous machines are considered in this thesis: conventional synchronous machines with the field winding and a *permanent magnet synchronous machine* (PMSM). This section begins with an introduction to the physical characteristics of permanent magnets; it then describes the magnetic and electric models of a magnet. Finally it presents the manner in which a permanent magnet synchronous machine can be modeled using a dq0 equivalent circuit. Methods of incorporating this model of PMSM into electromagnetic transients programs are discussed in Chapter 4.

#### 3.2.2.1 Characteristics of permanent magnet materials

Permanent magnet materials are those magnetic materials which can produce a magnetic flux outside the material and maintain it in spite of a large externally applied field intensity [35]. Similar to other magnetic materials, *B-H characteristics* of permanent magnets follows the path of a *hysteresis loop*; however permanent magnets have a much larger B-H hysteresis loop compared to *soft magnetic materials* [35]. Permanent magnet materials are therefore characterized by very high values of *coercive force* ( $H_c$ ) [35].

The first and the second quadrants of a typical B-H hysteresis loop of a permanent magnet are shown in Figure 3.3. The permanent magnet is formed by applying a large external magnetic field intensity ( $H$ ) to an un-magnetized sample of material (shown as *initial magnetization* in Figure 3.3), then shutting it off [36]. This allows the material to relax or *recoil* along the upper curve [36] as shown in Figure 3.3. The recoil region of the B-H characteristics in Figure 3.3 is a straight line with a slope of  $\mu = \mu_r \mu_0$  which is called the *recoil permeability* of the magnet. As a reminder,  $\mu_0 = 4\pi \times 10^{-7} \text{ (Wb/A.m)}$  is the



permeability of free space and  $\mu_r$  is the *relative permeability* of the magnetic material. For Alnico magnets [35], the recoil permeability is in the range of  $3-5 \mu_0$ , whereas for ferrite magnets it is typically between  $1.0 \mu_0$  and  $1.1 \mu_0$  [35]. If the two ends of a magnet are shorted by an infinite permeance, the magnetic field intensity ( $H$ ) will be zero and the magnetic flux density leaving the magnet will be equal to the remanence (shown by  $B_r$  in Figure 3.3).

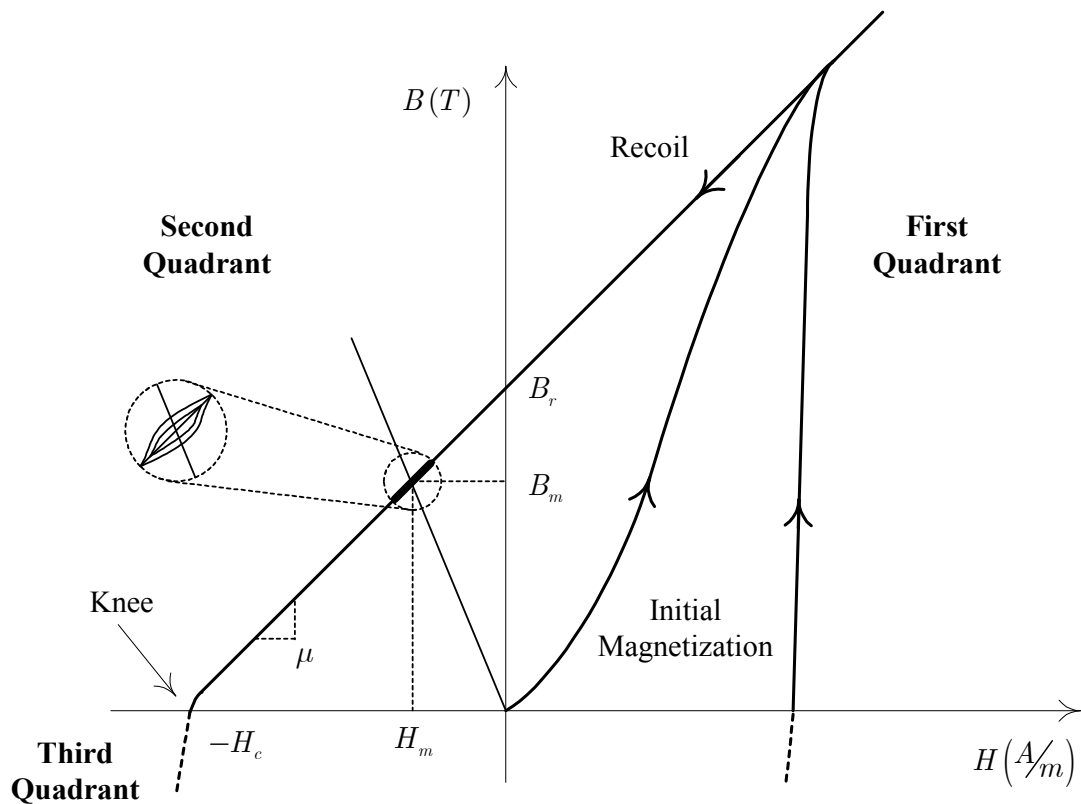


**Figure 3.3:** The B-H loop of a permanent magnet

The second quadrant of the hysteresis loop is the operating region of a magnet in permanent magnet machines. When the magnet is being utilized around an operating point, it is in fact operating along some minor hysteresis loops (shown in Figure 3.3) which can often be estimated by a straight line. With the load increase, the operating

point moves towards the knee point of the B-H characteristics. In practical operations of machines, the excessive load on the magnet, which pushes the operating point to the nonlinear part in the third quadrant, is avoided as it may demagnetize and damage the magnet [36], [37].

### 3.2.2.2 Linear models for permanent magnets

The fact that the operating locus of a permanent magnet is on the straight line of the second quadrant in Figure 3.3, suggests that the magnet can be represented by a linear model. Such a model facilitates calculations, particularly in complex systems that include permanent magnets.

As an example, for the simple rectangular magnet shown in Figure 3.4 with the length of  $l_m$  and cross-section area of  $A_m$ , the relationship between operating flux density ( $B_m$ ) and magnetic field intensity ( $H_m$ ) of the magnet is shown in (3.23).

$$B_m = B_r + \mu_r \mu_0 H_m \quad (3.23)$$

Equation (3.23) is re-written in the form of (3.24). In this equation, the term  $l_m H_m$  is the magnetomotive force along the magnet, also shown by  $\mathcal{F}_m$ , and the term  $A_m B_m$  is equal to the magnetic flux of the magnet ( $\Phi_m$ ).

$$\mathcal{F}_m = l_m H_m = \frac{l_m}{\mu_r \mu_0 A_m} (A_m B_m) - \frac{l_m}{\mu_r \mu_0} B_r \quad (3.24)$$

Thus, the relation between the MMF and flux of the magnet is as shown in (3.25). In this equation, the magnet is represented by a source of magnetomotive force ( $\mathcal{F}_0$ ) in

series with a reluctance  $\mathcal{R}_m$ . The magnetic equivalent circuit of this representation is shown in Figure 3.5a.

$$\mathcal{F}_m = \mathcal{R}_m \cdot \Phi_m - \mathcal{F}_0 \quad (3.25)$$

where:  $\mathcal{R}_m = \frac{l_m}{\mu_r \mu_0 A_m}$ ,  $\mathcal{F}_0 = \frac{l_m}{\mu_r \mu_0} B_r$

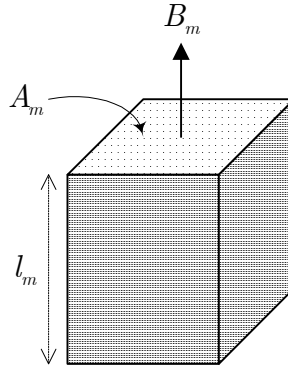


**Figure 3.4:** A simple rectangular magnet

The magnetic equivalent circuit of a device is most useful in analysis and design of that device, however in circuit analysis it is desirable to have the electric equivalent circuit of the element under study [35]. The electric equivalent circuit can be derived directly and uniquely from the magnetic equivalent circuit using the theory of *dual circuits*, where current and voltage correspond respectively to magnetomotive force and flux [35]. The electric equivalent of the magnetic circuit, shown in Figure 3.5a, is a coil with  $N_m$  turns in parallel with a current source. This electric equivalent circuit is shown in Figure 3.5b, with parameters defined in (3.26).

$$i_0 = \frac{\mathcal{F}_0}{N_m} = \frac{l_m}{\mu_r \mu_0 N_m} B_r, \quad L_m = \frac{(N_m)^2}{\mathcal{R}_m} = \mu_r \mu_0 \frac{(N_m)^2 A_m}{l_m} \quad (3.26)$$

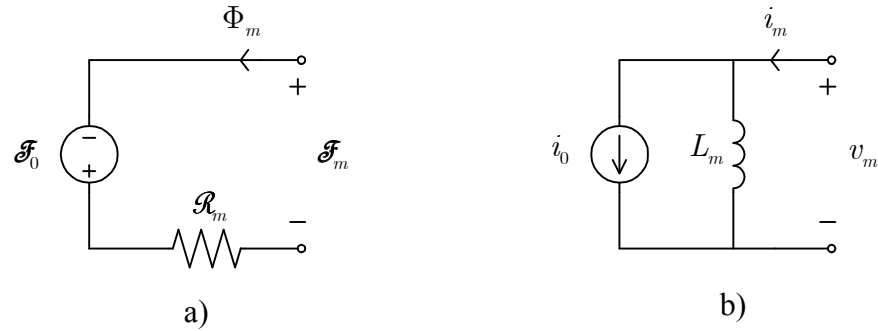


**Figure 3.5:** Equivalent circuits of a magnet: (a) magnetic circuit, (b) electric circuit

### 3.2.2.3 *Dq0* equivalent circuit for a permanent magnet synchronous machine

A PMSM is a synchronous machine which uses permanent magnets on the rotor to create flux in the air-gap instead of a field winding. Similar to a synchronous machine, the stator of a PMSM holds a three-phase winding, which produces an almost sinusoidally distributed magnetomotive force rotating at synchronous speed.

The cross-sectional layouts of two permanent magnet synchronous machine types with their different parts are shown in Figure 3.6.

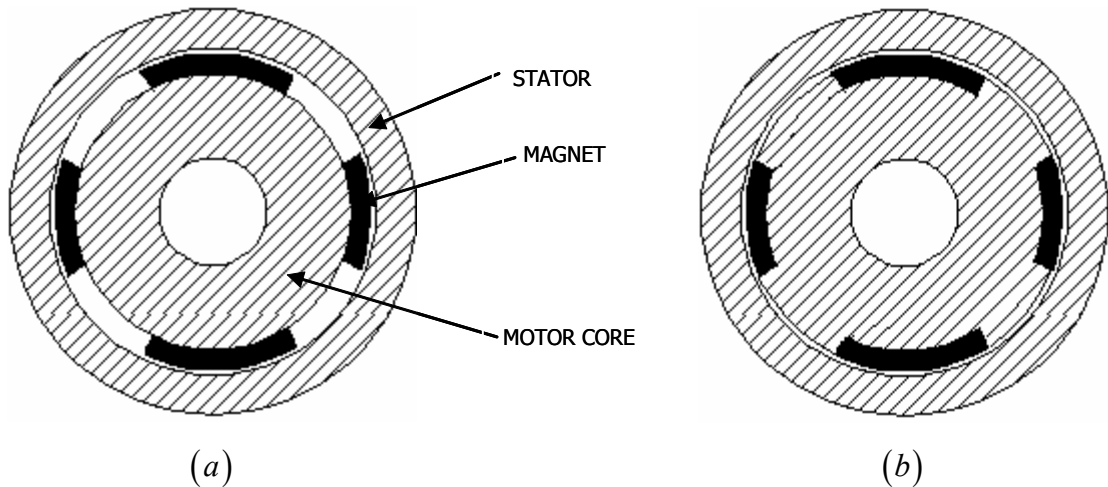


**Figure 3.6:** Simple structure of permanent magnet synchronous machine, (a) surface-mounted PMSM, (b) buried-magnet PMSM.

In a PMSM, if the magnets are mounted on the rotor as shown in Figure 3.6 (a), the machine is called a *surface-mounted* PMSM. However, if the magnets are buried inside the iron (Figure 3.6 (b)), the term *buried-magnet* PMSM is used [35]. These two machines have some differences with respect to the inductances of d- and q- axes, which will be discussed later in this section.

The dq0 equivalent circuit of a PMSM [38] ignoring damper windings is shown in Figure 3.7. The representation of armature windings is identical to the ones belonging to synchronous machines shown in Figure 3.2. If present, damper windings can also be represented in a manner similar to that used for synchronous machines. The magnet is modeled as a current source  $i_m$  in parallel to the magnetizing inductance  $L_{md}$  [38]. The value of this current source is calculated such that the induced flux linkage on the armature windings is equal to the flux linkage induced by the actual magnet [38]. The power loss as the result of eddy currents in the magnet is modeled by the resistance  $R_m$ . The circuit parameters  $i_m$  and  $R_m$  can be computed using dimensions and physical properties of the magnet as explained in [38].

As discussed previously in this section, permeability of magnets is in the range of permeability of the air; therefore in a surface-mounted PMSM, magnetizing inductances on the d- and q-axis ( $L_{md}$  and  $L_{mq}$ ) are almost equal. Because of the large length of air-gap in this machine type, the effects of saturation in the iron are rarely experienced. In a buried-magnet PMSM, because of shorter length of air-gap in the q-axis,  $L_{mq}$  is larger than  $L_{md}$ .

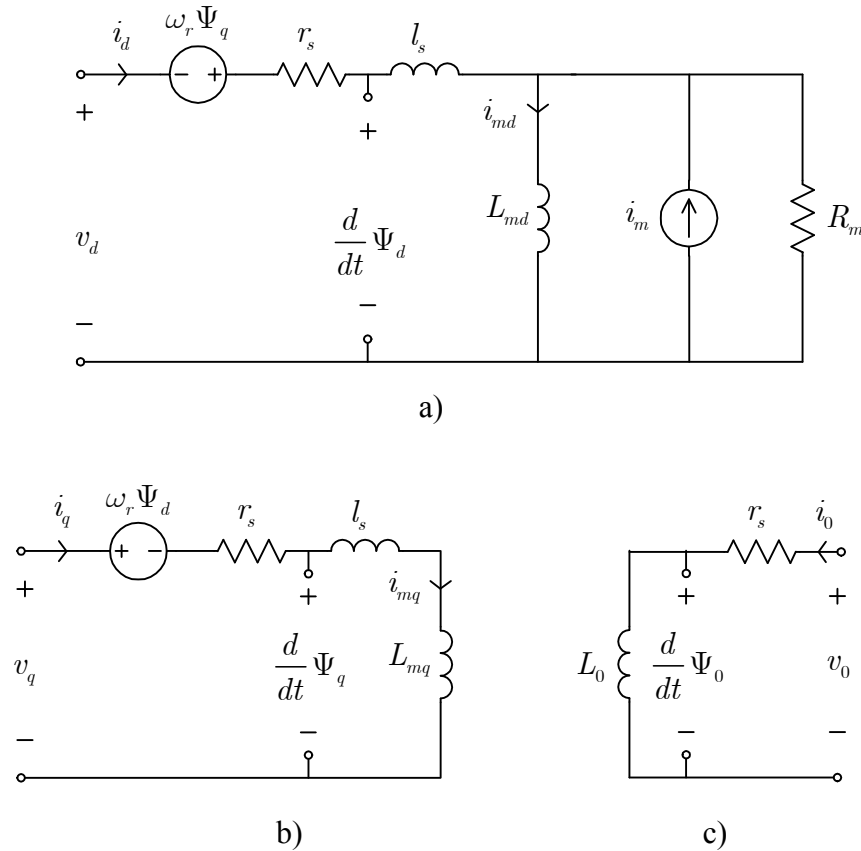


Figure 3.7: Dq0 equivalent circuit of a synchronous machine: (a) d-axis, (b) q-axis, (c) 0-axis.

### 3.2.3 Advantages and Disadvantages of Modeling Machines Using Dq0 Theory

Application of the dq0 theory for analyzing synchronous machines is discussed in previous sections. In this section, the advantages and drawbacks regarding the use of this theory in modeling synchronous machines are discussed.

- **Advantages**

As shown in (3.21), the differential equation of the machine in dq0 frame has a relatively simple form; and the inductance matrix in dq0 frame is a block diagonal matrix and is independent of rotor position. Additionally, the existence of an equivalent circuit in dq0 frame simplifies the analysis of synchronous machines. This approach also facilitates a better physical understanding of the performance of synchronous machines.

Incorporation of a synchronous machine model into electromagnetic transients programs has a lower computational burden if it is done directly in dq0 mode. This is due mostly to the fact that the inductance matrix of the machine in dq0 frame is not changing with time and therefore, it is not required to invert the inductance matrix in every time-step. Normally a dq0 model of a synchronous machine is *interfaced* into electromagnetic transients programs; in the interfaced approach the machine model is external to the transient program, and the machine elements are not included in the *admittance matrix* of the transient solution. This, in turn, means a simpler model and fewer computational operations.

The other advantage of dq0 models is the wide application of these models in the power industry and amongst electrical engineers. Almost every electric power utility identifies its synchronous generators by their dq0 parameters.

- **Disadvantages**

The dq0 models also have some shortcomings listed as follows. It is not feasible to model internal faults directly in dq0 frame. Although some internal fault models may have used the dq0 theory to calculate the approximate values of faulted inductances, the actual solutions of differential equations are performed in the phase-domain [39]-[41]. Furthermore, using the above method, the error in the calculation of faulted winding inductances becomes larger as the fault point approaches the end of the winding [40], [41].

The dq0 models of synchronous machines essentially assume a sinusoidal distribution for the windings, thus they cannot account for the space harmonics of the machine windings and permeance distributions. This matter shows its importance in some

protection schemes based on the harmonic content of voltage and/or the current signals of the machine. One such scheme is the *stator-ground fault* protection, which is based on the level of the third harmonic voltage in the neutral and terminals of synchronous machines [44]. Application of the new model, developed in this thesis, and the shortcomings of dq0 models regarding this protection scheme are explained in Chapter 6.

Finally, in the dq0 models, the saturation effects are modeled by modifying the values of magnetizing inductances on d- and/or q- axes. In this approach, the effect of MMF distribution on the saturation of local pole-arc portions is ignored.

### **3.2.4 Calculation of Approximate Phase-Domain Inductances from the Dq0 Equivalent Circuit**

Some authors [7]-[8], [12], [45]-[46], have performed time-domain modeling of synchronous machines directly in the phase domain, i.e., the final differential equations are in the form of equation (3.1), which uses the phase currents instead of d-q transformed currents as state variables. In this approach, the inductances are changing with time. The phase-domain approach is adapted in [45] as an initial effort to model internal faults in synchronous machines. In [7]-[8], [12], [46], the phase-domain approach is used for the purpose of improving the numerical stability of machine models developed in the electromagnetic transients programs. Some authors modified the phase-domain dq0-based models of synchronous machines to simulate internal faults [39]-[41], [47]-[52].

Although the time-domain solution in all of the above machine models is in terms of phase quantities, the inductance matrix of the machine in phase-domain is actually extracted from the inductance matrix of the machine in dq0 frame. This is because, as



discussed earlier, the electric data for the majority of machines is available only in the dq0 format, due to the pervasiveness of the dq0 based models.

The above machine models consider equations (3.4)-to-(3.15) as functions of phase-domain inductances with parameters that can be calculated using (3.27). Parameters  $L_s, L_m$  and  $M_s$  in (3.27) are evaluated by performing simple algebraic operations on the expressions of  $L_d, L_q$  and  $L_0$  in (3.15). Parameters of normalized mutual inductances between stator and rotor (i.e.  $M'_F, M'_D$  and  $M'_Q$ ) are also evaluated from the expressions of these mutual inductances in dq0 frame as shown in (3.15). These phase domain machine models are algebraically identical to dq0 frame models, therefore the transient response of a dq0-based machine model and an equivalent phase-domain model are expected to be identical [12], [18]. Some differences may arise due to the numerical stability and accuracy of these models [12]-[13], [18]-[19].

$$\begin{aligned}
 L_s &= \frac{1}{3}(L_0 + L_d + L_q) & M_s &= -\frac{1}{3}\left(-\frac{L_d + L_q}{2} + L_0\right) \\
 L_m &= \frac{1}{3}(L_d - L_q) & M'_F = M'_D &= \sqrt{\frac{2}{3}}L_{md} & M'_Q &= \sqrt{\frac{2}{3}}L_{mq}
 \end{aligned} \tag{3.27}$$

### 3.3 Application of the Finite Element Method in Obtaining the Inductances of Electric Machines

As mentioned earlier, usually the dq0 data are the only available electrical parameters of electric machines. The models developed in this thesis are intended to simulate internal faults and winding- and permeance-based time harmonics. The dq-based models are not suitable for these objectives; therefore alternative methods such as the *finite element method* (FEM) and the winding function approach (WFA) are also discussed.

In this section, a brief review is done on obtaining electric machine parameters using the finite element method (FEM). The advantages and shortcomings of this method for such applications are also mentioned. Since the finite element method itself is not the focus of this research, the descriptions are very brief.

The finite element method (FEM) (sometimes referred to as finite element analysis) is a numerical technique for solving relevant field equations for a specific study. This method is based on solving an equation by approximating continuous quantities as a set of quantities at discrete points, often spaced into sub-regions called mesh (Figure 3.8).

Because the finite element method can be adapted for problems of great complexity and unusual geometry, it is an extremely powerful tool in the solution of important problems in heat transfer, fluid mechanics, mechanical systems, and electromagnetism. The availability of fast and inexpensive computers allows problems which are intractable using analytic methods to be solved using finite element methods.

A significant amount of research has been done to study electric machines using the *finite element method* (FEM) [54]-[64]. The main purpose of FEM related research activities is mostly designing electric machines. Such studies are usually performed by

detailed calculation of the inductances of a machine using finite element programs [61]-[64]. Because FEM considers details of machine materials, geometry, saturation level, etc., it has the capability of providing extremely detailed plots of the functional variation of inductances with rotor position etc. FEM is used in Section 3.4 to obtain the inductances of an experimental machine, and to verify the inductance values calculated by the *modified winding function approach* (MWFA).

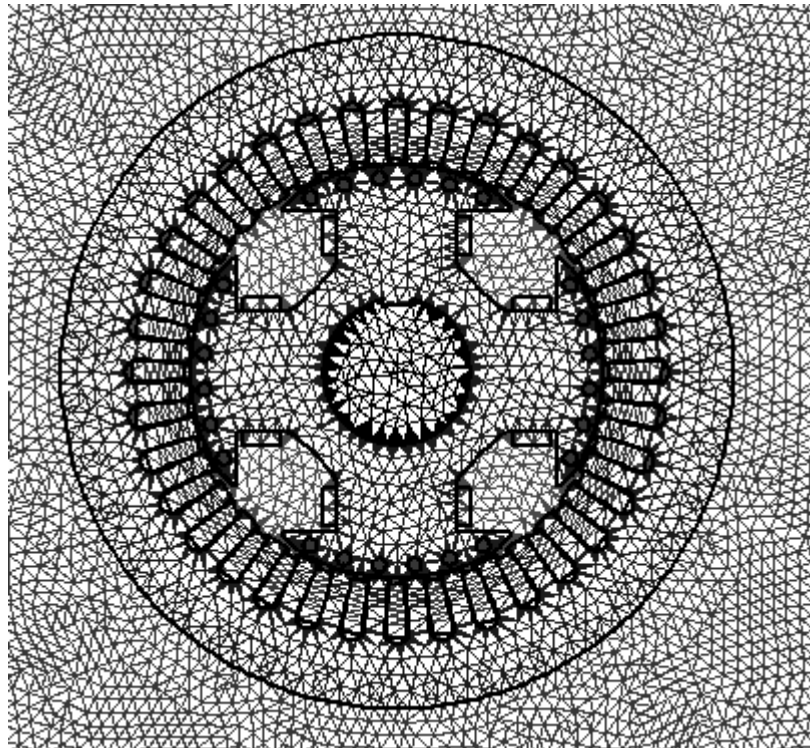


**Figure 3.8:** A triangular mesh pattern used to model a synchronous machine using FEM

For time-domain simulation, these inductances can be used to formulate the machine state space equations; which are then numerically solved to provide the various waveforms of interest. If the focus is on the detailed performance of the machine, rather than on the impact of the machine on a large external network, Faraday's law can be added to the FEM formulation to make a time-domain simulation possible [61]-[62].

However, this process is extremely slow as the resulting problem is a dynamic solution of the field equations, i.e. FEM analysis is run in every time-step of simulation. Therefore, these types of FEM-based simulations are usually limited to the study of a single machine connected to an ideal supply. A better approach is to use the FEM to calculate and store machine inductances and use a separate time-domain simulation program to obtain the transient response.

One of the contributions of this thesis is a new approach of using the finite element method to provide inductance information that is incorporated into a highly detailed real-time formulation of a machine and external network. In this approach, the FEM-based calculated inductances of a synchronous machine are tabulated and used for simulation of the embedded phase domain model developed on the RTDS platform [12], [65]. Such integration results in a time-domain machine model with high accuracy of parameters generated by FEM, combined with the speed of real-time simulation.

- **FEM-based Inductance Calculation versus Winding Function Approach**

The FEM is a very detailed and accurate method of analyzing electric machines. In a FEM analysis, the exact geometry of machine parts such as dimensions of stator, rotor and their slots, precise distribution of the windings and air-gap length are taken into account. The electromagnetic properties of the material used in the machine are considered in a FEM analysis.

Although finite element analysis is a very accurate and detailed method of analyzing electric machines, it is also, at the same time, a very time consuming process. In FEM-based studies, the inductances of machines must be calculated for each rotor position, and

various loading conditions and field excitations. Such analysis, although performed only once, is extremely time-consuming.

The next section discusses the modified winding function approach (MWFA) which is a more direct approach to calculate inductance parameters. This method can provide higher order harmonic representation of inductances (compared to the dq0 theory). The role of the FEM in this thesis is an alternative method that is used to validate and fine tune the MWFA approach, which is the principal approach in this research.

### 3.4 Application of the Modified Winding Function Approach for Obtaining the Inductances of Electric Machines

In previous sections, two methods (dq0 theory and FEM) of computing inductances of electric machines were discussed. This section explains the *modified winding function approach* (MWFA) for this application. Unlike the dq0 theory, the MWFA is capable of taking into account non-sinusoidally distributed windings. Also, this method is computationally more efficient than the finite element method. In this approach, a suitable integration loop is used to determine, using Ampere's law, the resultant air-gap flux density at any given angle. A winding distribution function is used to calculate the Ampere-turns in the integration loop. The results are then processed to determine inductances as described later in Section 3.4.2. The following are the reviews of previous works on the winding function theory and the contributions of the author to this approach.

#### 3.4.1 Background

Early applications of the winding function approach [31] assumed sinusoidal distribution for windings and air-gap length to calculate the inductances in an idealized two-pole synchronous machine. The resulting inductances are in agreement with the format expressed in (3.4)-(3.10); this work relates the parameters of equations (3.4)-(3.10) to the geometrical characteristics of the machine. A great motivation for the application of the winding function approach is its capacity to consider actual distribution of windings rather than idealized sinusoidal distributions. The *winding function approach* (WFA) was introduced in [66] as a new method of modeling induction machines based on the coupled electric circuit approach. In [29], [67] and [68] the winding function

approach was used to model the air-gap dynamic eccentricity in induction machines. In [29] the winding function approach was modified by taking into account *Gauss's law* in addition to *Ampere's law* to calculate the flux density created by each winding. This approach was called the *modified winding function approach (MWFA)* and will be explained briefly in the next section.

In [69] and [70] the MWFA was used for modeling turn-to-turn faults and development of new techniques for detecting turn-to-turn faults in synchronous machine and synchronous reluctance machines. Based on the winding function approach, a synchronous machine model for internal faults was presented in [43]. In this model, the permeance is assumed to be varying sinusoidally as a function of angular position with respect to the rotor.

In this thesis, the *actual distribution of air-gap length*, *effects of slots*, and *MMF drop in the iron* are incorporated into MWFA to calculate the inductances of an experimental synchronous machine. Comparison with the inductance values calculated using FEM shows that the above considerations significantly improve the accuracy of inductances. One way of compensating for these factors, which is introduced in this thesis, is to define an *effective permeance function* based on the physical air-gap function and experimental values of  $L_d$ ,  $L_q$  and  $L_0$ . Incorporation of the *effects of operating-point dependent saturation* into the winding function theory is also one the main contributions of this thesis which will be discussed in Section 4.3.

### 3.4.2 Fundamentals of MWFA

In this section, using a simplified synchronous machine, the fundamentals of the winding function theory [29] are briefly explained. Application of this method to an

experimental machine, and contributions of this thesis to the MWFA are discussed in the following sections.

Consider the elementary salient-pole synchronous machine shown in Figure 3.9. The stator windings of the synchronous machine are embedded in the slots around the inside circumference of the stationary member. Each phase winding of the three-phase stator winding is displaced  $120^\circ$  with respect to the other. A single conductor is threaded back and forth forming a coil. One slot holds the conductors with the flow of current into the plane of the paper shown by  $(\otimes)$  and is assigned as the positive direction. The other slot holds the conductors with the opposite flow of current  $(\odot)$ . The field winding consists of two coils connected in series, and located in the pole-shoe area of the rotor.

Similar to Figure 3.1, the axes  $as$ ,  $bs$ , and  $cs$  indicate the positive direction of the *magneto-motive force* (MMF) produced by phase-A, B, and C of the stator respectively. The *direct-axis* is the direction of MMF produced by the field winding. The angular velocity of rotor, and the angle between the direct-axis and the axis of phase-A are shown by  $\omega_r$ , and  $\theta_r$  respectively. The quantities  $\phi_s$  and  $\phi_r$  are angular positions with respect to the stator axis ( $as$ ) and the rotor axis ( $fd$ ) respectively. Equation (3.28) applies to these quantities:

$$\phi_r = \phi_s - \theta_r \quad (3.28)$$

To calculate the self inductance of a winding, the flux linking a winding due to its own current must be calculated. Similarly, the mutual inductance requires the calculation of the flux linking one winding caused by another winding. The first step in this procedure is to calculate the distribution of flux density due to an energized winding. For example, if only winding A is energized with a current  $i$ , the *magnetic field intensity*  $\vec{H}$



created by this winding can be calculated by applying Ampere's law to the integration path  $C$  shown in Figure 3.9.

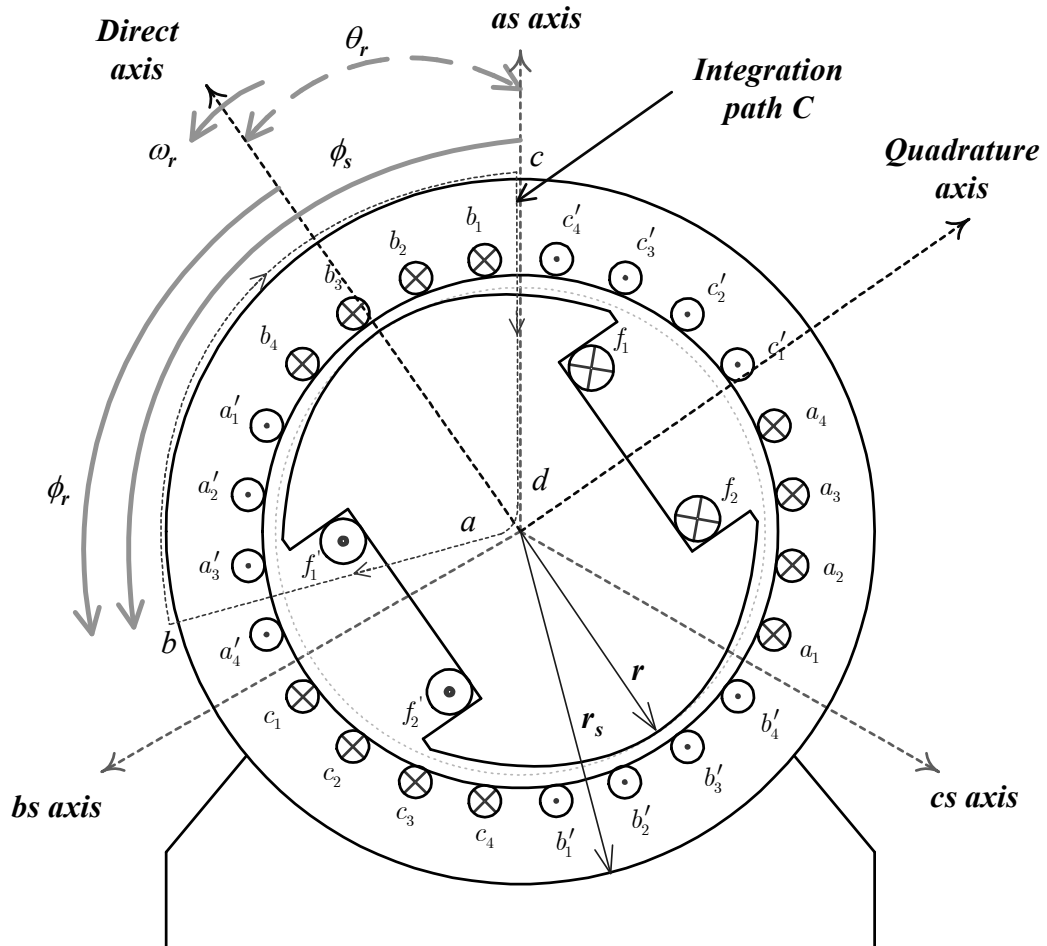


Figure 3.9: An elementary salient-pole synchronous machine with placements of the windings

Such an approach results in the computation of magnetic field intensity in the air-gap as a function of number of turns in the closed path  $C$  and the winding current  $i$  [29]. In previous research conducted using MWFA, the permeability of iron was assumed to be infinite and therefore *only MMF drops along the air-gap were taken into account*. In [29] Gauss's law was also used to determine the correct value of MMF drop at  $\phi_s = 0$

which was not properly estimated in earlier formulations. This ensured that the calculated inductances followed the reciprocity principle.

After the determination of magnetic field intensity in the air-gap, the *flux density* ( $\vec{B}$ ) is determined from the relation between the flux density and the magnetic field intensity ( $\vec{H}$ ) in the air-gap (i.e.  $\vec{B} = \mu_0 \cdot \vec{H}$ ). Finally the inductances are calculated by integrating the flux density over the span of windings and computing the total flux linkage induced in each winding [29].

Equation (3.29) shows the formula used for the calculation of inductances between any two windings for different rotor positions of the machine using this approach. The inductance between windings  $j$  and  $k$  is shown by the symbol  $L_{jk}$ , with the indices  $j$  and  $k$  ranging over the set of stator phases (a, b, c), and the field winding (F). For example,  $L_{aa}$  is the self inductance of stator phase-A, and  $L_{ab}$  is the mutual inductance between phase-A and phase-B. The *stack length* and *rotor radius* are respectively shown by symbols  $l$  and  $r$ . The function  $n_j(\phi_s, \theta_r)$  is called the *turns function* and represents the number of turns of the winding  $j$  enclosed by the path C. In general, the turn function is a function of  $\phi_s$  and rotor position ( $\theta_r$ ), however for a stationary coil, it is only a function of  $\phi_s$ . Turns carrying currents into the page are considered positive while the turns carrying currents out of the page are considered to be negative. In (3.29),  $M_k(\phi_s, \theta_r)$  is called the *modified winding function* which was introduced in [29] by the application of Gauss's law into this theory.

In (3.29),  $\langle g^{-1}(\phi_s, \theta_r) \rangle$  is the *inverse air-gap function* of the machine which shows the variation of air-gap length with respect to angular position in rotor's frame of reference

$\phi_r$ . In (3.29),  $\phi_r$  is replaced by  $\phi_s - \theta_r$  as previously defined in (3.28). The average value of the inverse gap function is shown by  $\langle g^{-1}(\phi_s, \theta_r) \rangle$ . In this equation,  $L_{ls}$  accounts for leakage inductances such as *slot leakages* and *coil end leakages* [72] which are not included in the inductances computed by the winding function theory.

$$L_{j,k}(\theta_r) = L_{ls} + \mu_0 r l \int_0^{2\pi} n_j(\phi_s, \theta_r) M_k(\phi_s, \theta_r) g^{-1}(\phi_s, \theta_r) d\phi_s$$

where

$$M_k(\phi_s, \theta_r) = n_k(\phi_s, \theta_r) - \frac{1}{2\pi \langle g^{-1}(\phi_s, \theta_r) \rangle} \int_0^{2\pi} n_k(\phi_s, \theta_r) g^{-1}(\phi_s, \theta_r) d\phi_s \quad (3.29)$$

$$j, k \in \{a, b, c, F, D, Q\}$$

The MWFA, similar to the other methods of analyzing machines has some advantages and limitations which are as follows:

- **Advantages**

In the winding function theory, the actual distribution of the windings can be easily considered, and the effects of space harmonics on the resulting inductances and machine currents and voltages can be taken into account. The permeance related harmonics also can be taken into analysis of the machine. Analysis of internal faults and rotor eccentricity is also possible using this method. This method is also computationally more efficient than the FEM. Since there is a closed integral formula for the inductances, it is possible to develop an analytical relation between the time-harmonics of the machine voltages and currents and the type of fault in the machine [70].

- **Assumptions and Limitations**

In the winding function theory the permeability of iron is assumed to be infinite, therefore researchers ignored the effects of saturation in the iron. Unlike FEM, it is

difficult to account for *fine geometrical details* of the machine in MWFA. *To address some of these shortcomings, this thesis introduces some techniques into the MWFA which account for the MMF drop in the iron, effects of slots, and non-circular shape of pole-arc. The effects of operating point dependent saturation are also incorporated into the MWFA as discussed in Section 4.3.*

### 3.4.3 Improvements in the MWFA and Validations

In this section, the inductances of an experimental machine are calculated using the MWFA. The inductances are compared with the values computed using a FEM-based software, and also with experimentally measured results. Some modifications are introduced by the author to increase the accuracy and flexibility of the MWFA.

#### 3.4.3.1 Description of the laboratory synchronous machine

A 3kW, 4-pole, 60 Hz, 1800 rpm, 208 V (line to line), star connected salient-pole synchronous machine is considered for this study. The stator and rotor of this machine are shown in Figure 3.10. The stator has a single layer, 3-phase, random-wound concentric winding distributed in 36 stator slots. Each phase of the stator winding has two series-connected coils. There are 16 turns/slot/phase with a total of 96 turns per phase. The salient-pole rotor has 24 damper bars (6 bars/pole-face). The field winding consists of four coils connected in series with 500 turns in each coil. Figure 3.11 shows the layouts for the stator and rotor windings of the laboratory machine. Stator phase-A consists of two *sub-windings* A1 and A2. Series-connected concentric coils  $a_1-a'_1$ ,  $a_2-a'_2$  and  $a_3-a'_3$  form the sub-winding A1 and the coils  $a_4-a'_4$ ,  $a_5-a'_5$  and  $a_6-a'_6$  form the sub-winding A2. The two sub-windings A1 and A2 are 180° apart. Other stator phases, B and

C, also have similar arrangements. The field winding consists of four series-connected coils  $f_1-f'_1$ ,  $f_2-f'_2$ ,  $f_3-f'_3$  and  $f_4-f'_4$  as shown in Figure 3.11.

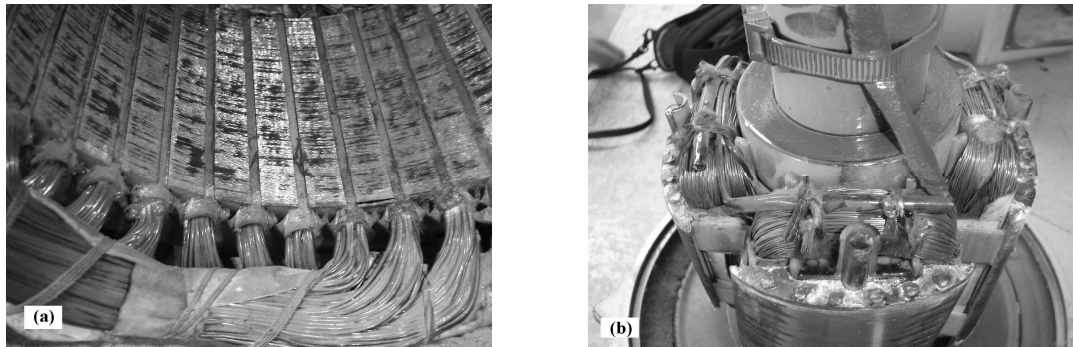


Figure 3.10: The Laboratory synchronous machine: (a) stator, (b) rotor

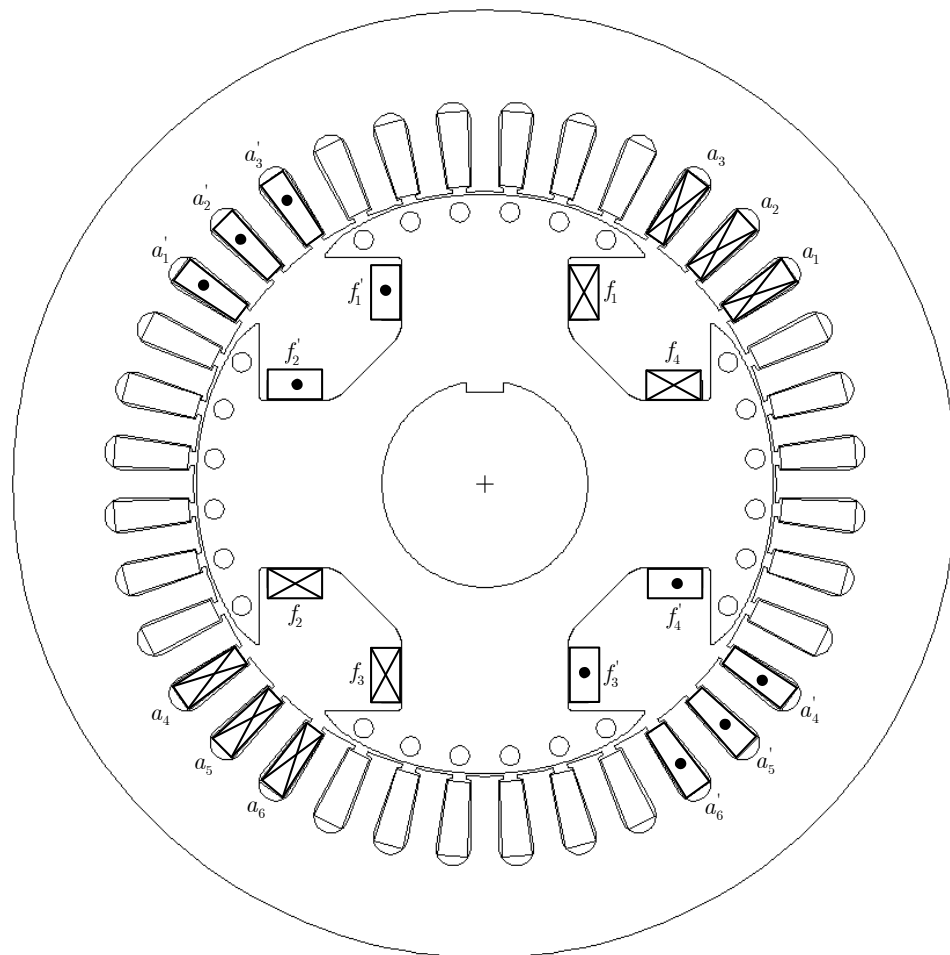


Figure 3.11: Layout of the windings in the stator and rotor of the laboratory machine

The ratings and geometrical specifications of the experimental machine are shown in Table 3.1. In addition to the information about the windings, the table shows the geometrical specifications of the rotor such as stack length, angle of pole-arc, and physical air-gap along d- and q-axes.

A cross-section of the rotor with the position of field windings and rotor damper bars are shown in Figure 3.12-a. To limit the eddy currents, the rotor core is made up of numerous identical rotor laminations. One of these laminations is shown in Figure 3.12-b. As observed in the figure, the rotor pole-arc of the experimental machine is not exactly circular but has different curvatures along the pole-face [71]. This design feature is to make the flux density more sinusoidally distributed.

TABLE 3.1: SPECIFICATIONS OF THE LABORATORY MACHINE

<b>Machine Ratings</b>	
Rated Line-line RMS voltage	208 V
Rated VA	3 kVA
Frequency	60 Hz
Number of phases	3
Field rated volts	120 V
Field rated amps	1.25 A
Number of poles	4
<b>Stator Data</b>	
Stator inner diameter	150 mm
Number of slots	36
Slots/phase/pole	3
Turns/coil	16
Number of layers	1
Number of series coils	2
Turns/phase	96
Coil connection of phase A	1-12, 2-11, 3-10
<b>Rotor Data</b>	
Rotor outer diameter	148.6 mm
Stack length	90 mm
Pole-arc along d-axis	70.5 deg
Physical air-gap along d-axis	0.7 mm
Physical air-gap along q-axis	32.6 mm
Number of damper bars/pole	6
Field turns/coil	500

The actual air-gap function,  $g_a(\phi_r)$ , of the machine is shown in Figure 3.13, on which is also superposed a commonly used circular approximation  $g_c(\phi_r)$  where the air-gap is considered constant along the pole arc. *In this thesis, the actual air-gap distribution is used in the MWFA process to compute the inductances of the experimental machine. These inductances are then compared with the inductances calculated from approximated air-gaps.*

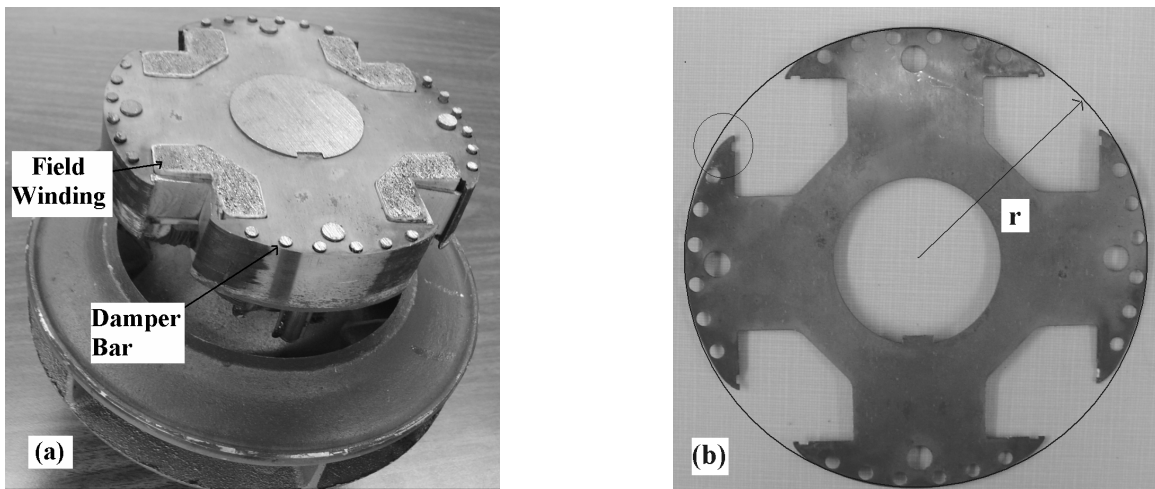


Figure 3.12: Rotor of the laboratory synchronous machine: (a) rotor cross-section, (b) rotor lamination.

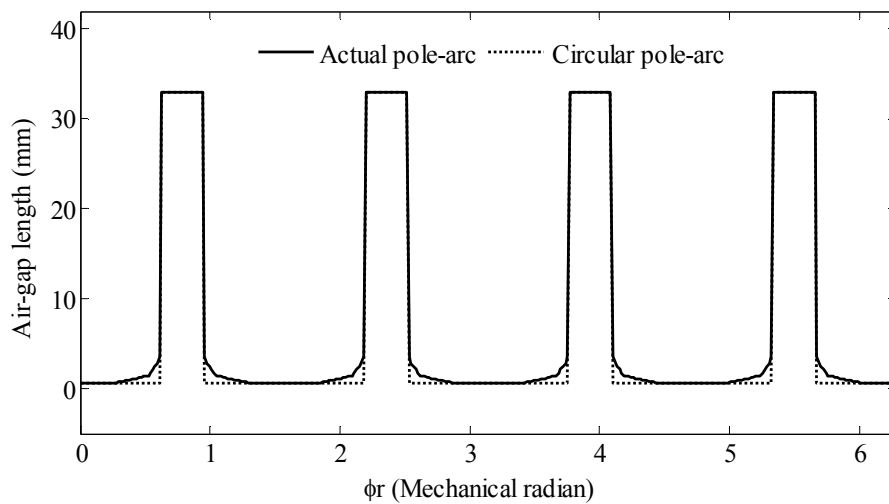
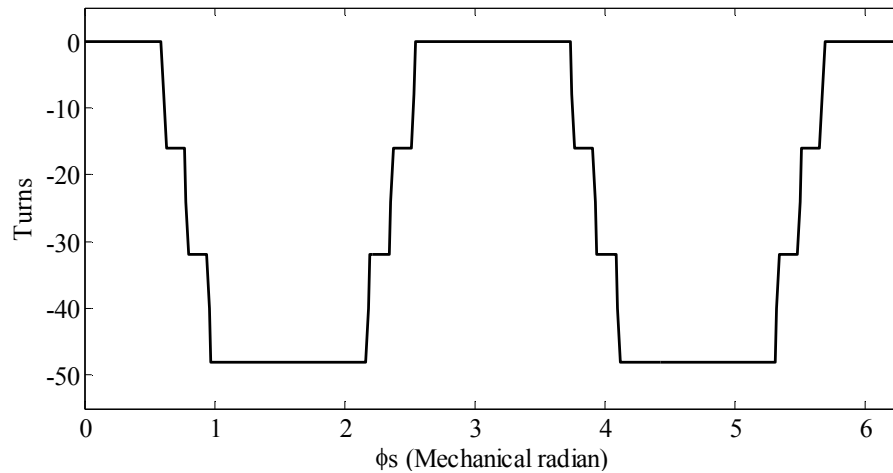
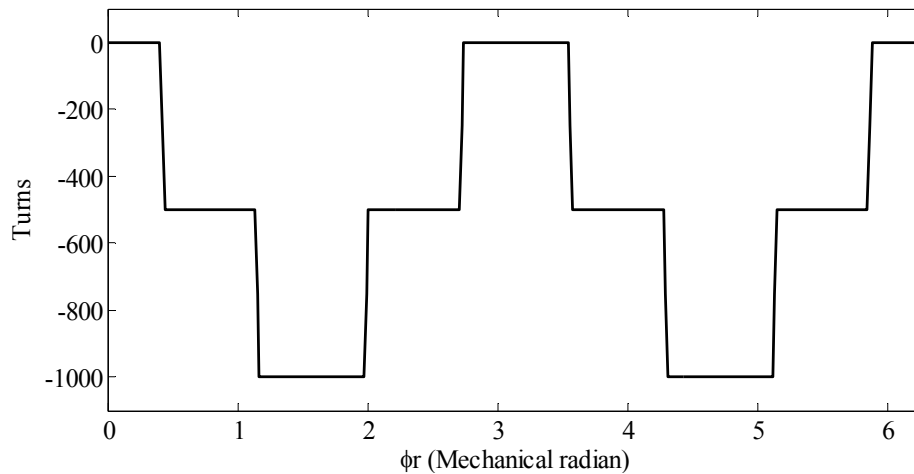


Figure 3.13: The air-gap function considering actual rotor pole-arc

From the arrangements of the stator windings, the turns-function of stator phase-A  $n_a(\phi_s)$  is shown in Figure 3.14. This function represents the number of phase-A turns enclosed in an enclosed path similar to the path C of Figure 3.9. As a reminder, the conductors with the flow of current into the paper are assigned positive values and the ones with the outward flow of the current are considered to be negative values. The turns-functions of phase-B and phase-C can also be obtained in a similar manner. The turns-function of the rotor field winding is shown in Figure 3.15.



**Figure 3.14:** The turns function of the stator phase-A



**Figure 3.15:** The turns function of the field winding



### 3.4.3.2 Incorporating the effects of iron MMF drop and slot fringing into the MWFA

Equation (3.29) is the formula for calculating machine inductances using MWFA.

This equation is re-written in terms of the *permeance function* of the machine,  $P(\phi_s, \theta_r)$ , as shown in (3.30). In this thesis, this change of variable is used to facilitate further improvements by incorporating effects of MMF drop in iron and saturation into MWFA.

$$L_{j,k}(\theta_r) = L_{ls} + \int_0^{2\pi} n_j(\phi_s, \theta_r) M_k(\phi_s, \theta_r) P(\phi_s, \theta_r) d\phi_s$$

where

$$M_k(\phi_s, \theta_r) = n_k(\phi_s, \theta_r) - \frac{1}{2\pi \langle P(\phi_s, \theta_r) \rangle} \int_0^{2\pi} n_k(\phi_s, \theta_r) P(\phi_s, \theta_r) d\phi_s$$

$$j, k \in \{a, b, c, F, D, Q\}$$
(3.30)

As mentioned earlier, the straightforward application of MWFA assumes that the permeability of iron is infinite, and therefore only MMF drops along the air-gap are taken into account. The air-gap function,  $g_c(\phi_s, \theta_r)$ , is also assumed to have a constant value along the pole-arc. With such assumptions the permeance function becomes the function  $P_0(\phi_s, \theta_r)$  as shown in (3.31).

$$P_0(\phi_s, \theta_r) = \frac{\mu_0 r l}{g_c(\phi_s, \theta_r)}$$
(3.31)

In contrast to the above straightforward approach, in this thesis, the accuracy of MWFA is improved by taking into account the actual shape of the pole-arc, MMF drops in the iron, and effects of stator slots. Table 3.2 shows the respective formulae for calculating the permeance function of the machine with such improvements. In this section, the impacts of using each one of these factors will be shown.

In Table 3.2,  $P_1(\phi_s, \theta_r)$  is the permeance function of the machine when the actual shape of pole-arc is considered in the evaluation of air-gap function  $g_a(\phi_s, \theta_r)$ . However,

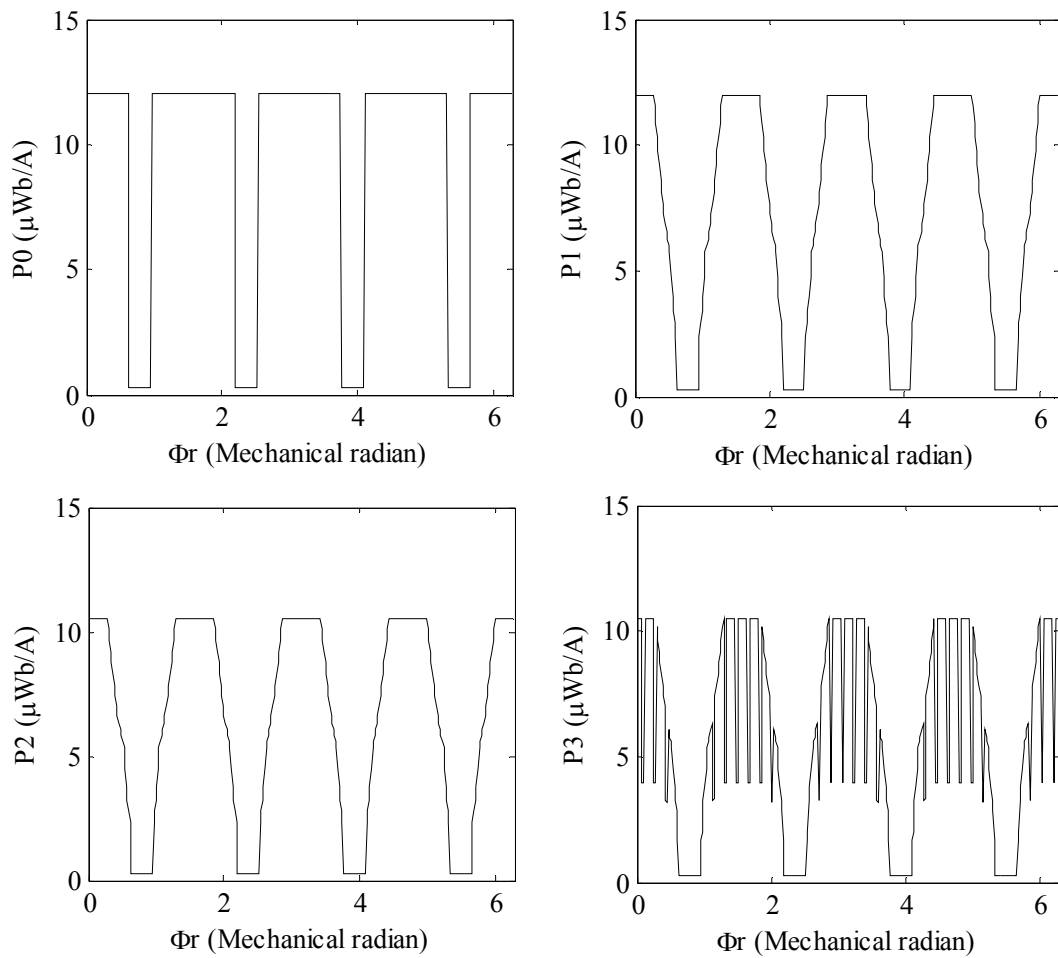
it still ignores the MMF drop in the iron and fringing in the slots. A further improvement is achieved by considering the effects of MMF drop in the iron in the calculation of the permeance function  $P_2(\phi_s, \theta_r)$ . This permeance function is evaluated based on the approximation that the normal component of flux density in the iron is constant along the path C in Figure 3.9, and equal to the flux density in the air-gap. In the equation for  $P_2$ ,  $r_s$  is the outer radius of the stator and  $\mu$  is the *permeability* of iron. Here, the terms  $\frac{g_a(\phi_s, \theta_r)}{\mu_0}$  and  $\frac{r_s - g_a(\phi_s, \theta_r)}{\mu}$  account for the MMF drops in the air-gap and iron, respectively. Finally, to account for the effect of slots, the air-gap function,  $g_s(\phi_s, \theta_r)$ , is generated by considering the effective depth of stator slots using Carter's coefficients [36], [72]. The permeance function  $P_3(\phi_s, \theta_r)$  is generated using this air-gap function.

TABLE 3.2: PERMEANCE FUNCTIONS OF THE MACHINE BY INCORPORATING DIFFERENT DETAILS

Parameters Included in Calculating the Permeance Function	Equation for Calculating the Permeance Function
Air-Gap with the circular pole-arc ( $g_c$ )	$P_0(\phi_s, \theta_r) = \frac{\mu_0 r l}{g_c(\phi_s, \theta_r)}$
Actual gap ( $g_a$ )	$P_1(\phi_s, \theta_r) = \frac{\mu_0 r l}{g_a(\phi_s, \theta_r)}$
Actual gap ( $g_a$ ) + iron MMF drop	$P_2(\phi_s, \theta_r) = \frac{r l}{\frac{g_a(\phi_s, \theta_r)}{\mu_0} + \frac{r_s - g_a(\phi_s, \theta_r)}{\mu}}$
Actual gap considering the slots ( $g_s$ ) + iron MMF drop	$P_3(\phi_s, \theta_r) = \frac{r l}{\frac{g_s(\phi_s, \theta_r)}{\mu_0} + \frac{r_s - g_s(\phi_s, \theta_r)}{\mu}}$

Figure 3.16 shows the variation of the above permeance functions  $P_0 \cdots P_3$  with  $\phi_r$ . Note that,  $\phi_r = \phi_s - \theta_r$  is the angular position in rotor's frame of reference as defined in (3.28). As can be seen,  $P_0$  has a rectangular shape, because the assumed air-gap in this

function is constant along the pole-arc. On the other hand,  $P_1$  varies along the pole-arc as it is generated using the actual air-gap. As the effects of MMF drop in the iron is taken into account in the calculation of the permeance function  $P_2$ , it has smaller values in comparison with  $P_1$ . The effects of stator slots is noticeable in the variation of  $P_3$ . The air-gap function, including effects of slots,  $g_s$ , is a function of both  $\phi_r$  and  $\phi_s$ . Here  $P_3$  has been plotted at rotor position  $\theta_r = 0$ .



**Figure 3.16:** The permeance functions considering different details ( $P_0 \dots P_3$ )

Using (3.30) and permeance functions  $P_0 \dots P_3$ , the self inductance of stator phase-A  $L_{aa}(\theta_r)$  is calculated and shown in Figure 3.17. For the purpose of comparison, this

inductance is also computed using the FEM-based software Maxwell<sup>®</sup> from ANSOFT Corporation [73] and plotted in each graph of Figure 3.17. As can be seen, the more details considered in calculating the permeance function, the more accurate the calculated inductances from MWFA. For example, the computed inductances using  $P_3$  are the best match with the inductances calculated using FEM. In addition, by considering the actual shape of pole-arc in computing the permeance function, the shapes of the resulting inductances are more precise.

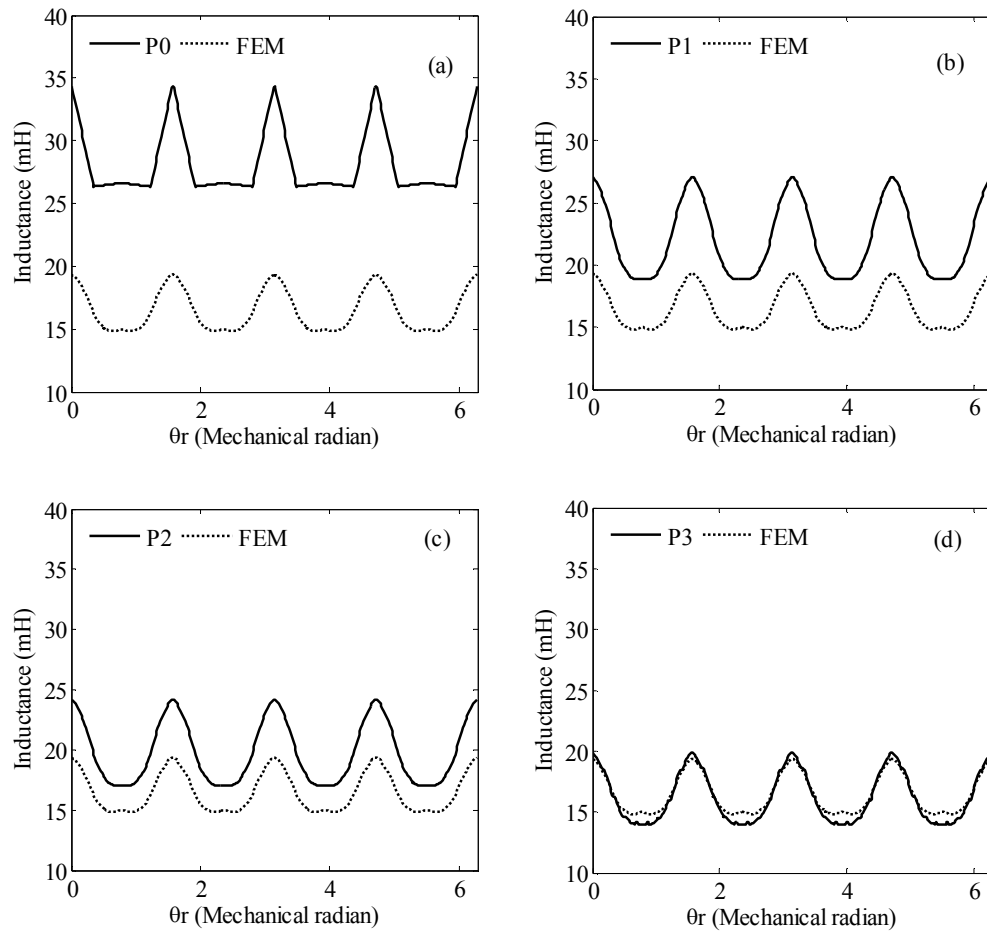


**Figure 3.17:** The stator phase-A self inductance computed using permeance functions  $P_0 \dots P_3$

A similar procedure is followed for calculating the mutual inductance between phase-A and phase-B of the stator. The results are presented in Figure 3.18. As can be seen,

similar to Figure 3.17, better results are obtained when more details are considered in calculating the permeance function.

These observations show that inductance values comparable to those obtained from FEM can be generated by proper application of MWFA in which several additional details are considered. The FEM program, however, takes close to one hour to compute the entire inductance matrix of a synchronous machine on a 1.73 GHz dual core processor. The computational time for MWFA is a small fraction of the above time and is in the range of seconds.

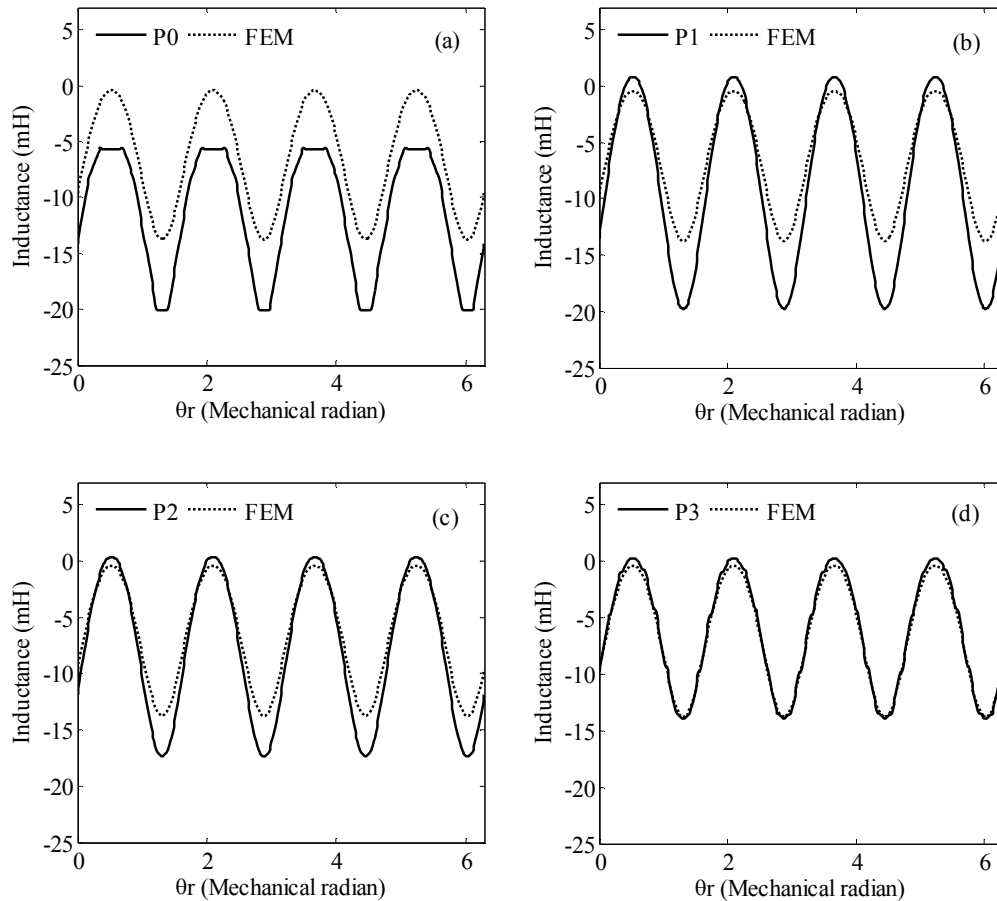


**Figure 3.18:** The mutual inductance between stator phase-A and phase-B computed using permeance functions  $P_0 \dots P_3$ .

### 3.4.3.3 Adjusting the permeance function using experimental values of $L_d$ , $L_q$ and $L_0$

As observed in the previous section, the inductances calculated using either the circular (Figure 3.17-a) or even the physical air-gap (Figure 3.17-b) are significantly different from the actual inductances. The cause of this discrepancy is the change in the permeance due to the presence of factors such as the rotor pole-shoe, stator slots, and the MMF drop in the iron. The accuracy is improved by taking into account the actual shape of pole-arc and effects of stator and rotor slots in the calculation of permeance. However, such calculations assume detailed knowledge of the machine geometry.

More commonly, the dq0 inductances of the machine ( $L_d$ ,  $L_q$  and  $L_0$ ) are known. In this thesis, an MWFA approach is used that modifies the permeance function so that the resultant  $L_d$ ,  $L_q$  and  $L_0$  parameters agree with experimentally obtained values. Earlier authors [69] used an effective air-gap function to achieve a similar objective; which substituted the physical air-gap function. Their approach assumed a circular pole-arc.

For increased accuracy, the proposed method in this thesis defines an *effective permeance function* (ignoring saturation) using the experimental values of  $L_d$ ,  $L_q$ ,  $L_0$  and the actual shape of pole-arc. The first step is accomplished by comparing the MWFA computed values of  $L_d$ ,  $L_q$  and  $L_0$  with their corresponding experimental values, shown in Table 3.3, and modifying the average and the peak-to-peak values of  $P(\phi_s, \theta_r)$  as shown in (3.32). The method of incorporating saturation effects will be discussed later. In (3.32), the subscripts *exp* and *MWFA* are used for the parameters measured from the experiment and computed using the MWFA respectively. Inductances  $L_d$ ,  $L_q$  and  $L_0$  originally arose from the conventional dq0 theory in which the winding distribution are

assumed to be sinusoidal. In that theory, inductances  $L_d, L_q$  and  $L_0$  are constants and they are not varying with a change in rotor position. However, when Park's transformation is applied to the phase-domain inductance matrix  $[L(\theta_r)]$ , with individual elements  $L_{aa}(\theta_r), L_{ab}(\theta_r), \dots$  of the actual machine (i.e. with shapes such as those in Figures 3.17 and 3.18), the resulting inductances  $L_{d-MWFA}, L_{q-MWFA}$  and  $L_{0-MWFA}$  oscillate slightly with rotor position. The parameters  $L_{d-MWFA}, L_{q-MWFA}$  and  $L_{0-MWFA}$  in (3.32) are the average values of the actual inductances computed using MWFA. A detailed derivation of equation (3.32) is provided in Appendix A.

$$\begin{aligned}
 P_{eff}(\phi_s, \theta_r)_{ave} &= \frac{L_{d-exp} + L_{q-exp} - 2L_{0-exp}}{L_{d-MWFA} + L_{q-MWFA} - 2L_{0-MWFA}} P(\phi_s, \theta_r)_{ave} \\
 P_{eff}(\phi_s, \theta_r)_{p-p} &= \frac{L_{d-exp} - L_{q-exp}}{L_{d-MWFA} - L_{q-MWFA}} P(\phi_s, \theta_r)_{p-p}
 \end{aligned} \tag{3.32}$$

TABLE 3.3: THE DQ0 PARAMETERS OF THE LABORATORY SYNCHRONOUS MACHINE

Per-Unit bases	Value		
Voltage base value = Rated line-neutral RMS voltage	120.09 V		
Current base value = Rated line RMS current	8.33 A		
Impedance base value	14.42 $\Omega$		
Inductance base value	38.25 mH		
Parameter	Measurement		MWFA
	Per-unit value	Physical value	Per-unit value
D-axis inductance	0.89	34.1 mH	1.16
Q-axis inductance	0.48	18.4 mH	0.51
Zero sequence inductance	0.11	4.2 mH	0.12
Stator leakage inductance	0.048	1.8 mH	
Field leakage inductance	0.066	2.5 mH	
D-axis damper leakage inductance	0.055	2.1 mH	
Q-axis damper leakage inductance	0.050	1.9 mH	
Stator resistance	0.039	0.56 $\Omega$	
Field resistance	0.011	0.16 $\Omega$	
D-axis damper resistance	0.037	0.53 $\Omega$	
Q-axis damper resistance	0.024	0.34 $\Omega$	

Note that the effective permeance function  $P_{eff}(\phi_s, \theta_r)$  is a scalar multiplication of the originally calculated permeance, and does not change the harmonic content of the function. This can also be seen from Figure 3.19. Also, note that these functions correct for any mismatch between MWFA results and the measurement.

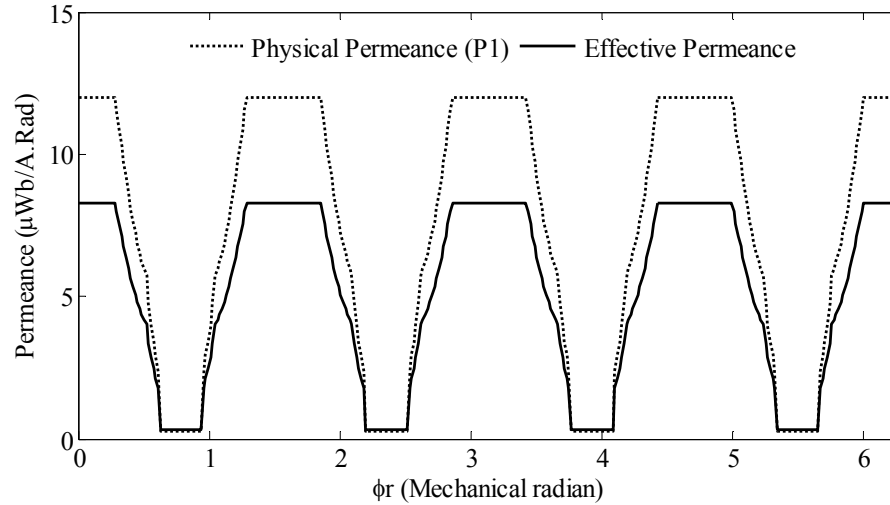


**Figure 3.19: Comparison of physical and effective permeance functions of the machine**

As mentioned earlier, the permeance adjustment formulation in (3.32) ensures that the resulting inductances  $L_{d-MWFA}$ ,  $L_{q-MWFA}$  and  $L_{0-MWFA}$  will be equal to the experimentally measured d-, q-, 0- axis inductances respectively. If any of the permeance functions ( $P_1 \dots P_3$  in Figure 3.16) are used in this adjustment procedure, the resulting effective permeance function will contain the information regarding the shape of pole-arc, and also the correct inductance values will be achieved. Among the permeance functions in Table 3.2,  $P_1$  requires the least amount of information, and therefore it seems to be the most suitable permeance function to be used in the adjustment process of (3.32). Although minimal data is needed to generate this permeance function, the adjustment in (3.32) has the capability of compensating for the initial error. In Figure 3.19, the effective



permeance function, obtained by this adjustment, is compared with the permeance function determined using physical data. The unsaturated self and mutual inductances of the stator are calculated using the modified winding function approach and compared with the inductances computed by FEM as shown in Figure 3.20.

Two different values are shown for the inductances calculated using MWFA; one with the physical permeance function ( $P_1$ ) and the other with the effective permeance function. It can be seen that the stator inductances computed using the effective permeance function are very close to the results of FEM calculations, whereas the inductances calculated from the physical permeance function have noticeable errors.

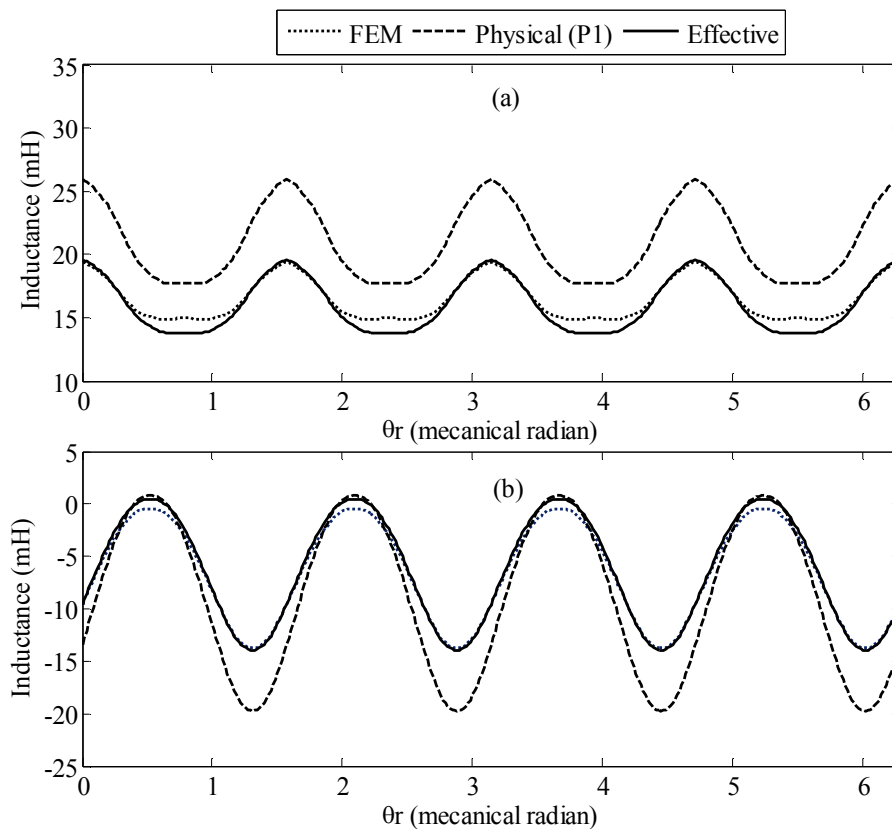


**Figure 3.20: Stator inductances using  $P_1(\phi_s, \theta_r)$ ,  $P_{eff}(\phi_s, \theta_r)$  and FEM, (a) self inductance of stator phase-A, (b) mutual inductances between stator phase-A and phase-B**

It must be noted that the comparison carried out above is mainly for establishing confidence in the approach and does not imply that the FEM-calculated results are the absolute template. Indeed, the effective permeance function approach makes the resulting  $L_d, L_q$  and  $L_0$  values match the experimentally measured ones. The FEM approach used here is a two-dimensional analysis, and effects such as rotor skewing and end winding leakages cannot be considered, which may account for the slight differences. Note that, if the permeance adjustment procedure is carried out using the  $L_d, L_q$  and  $L_0$  from FEM, the resulting inductance plots become almost identical as shown in Figure 3.21.

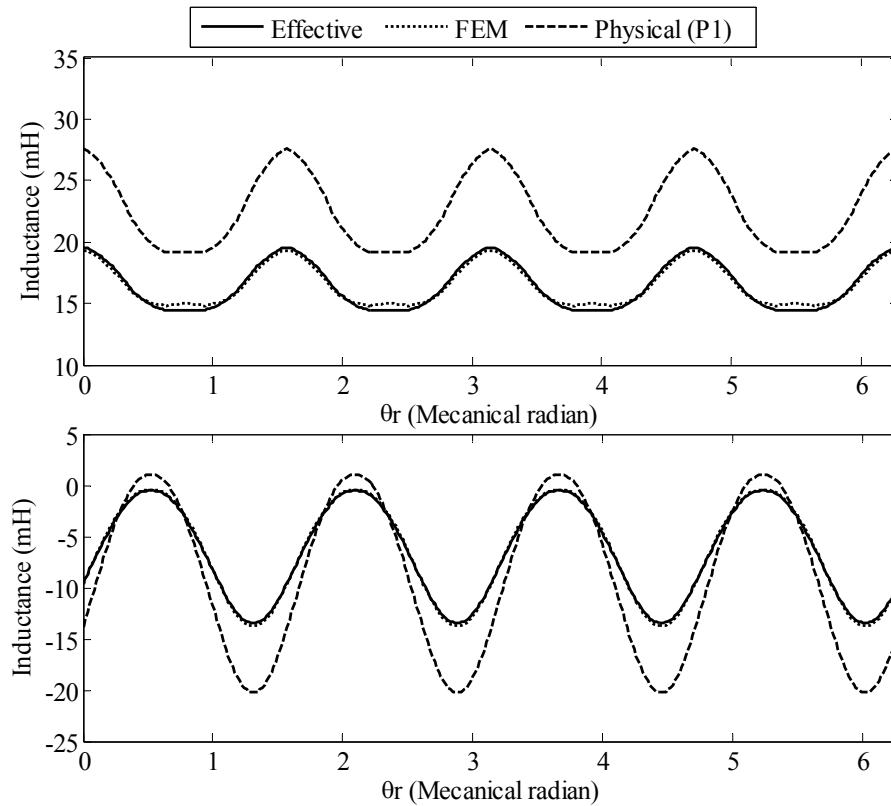


**Figure 3.21:** Stator inductances using  $P_1(\phi_s, \theta_r)$ ,  $P_{eff}(\phi_s, \theta_r)$  and FEM. The permeance is adjusted using the  $L_d, L_q, L_0$  from FEM (a) self inductance of stator phase-A, (b) mutual inductances between stator phase-A and phase-B.

### 3.4.4 Calculation of Faulted Winding Inductances using MWFA

As mentioned in Section 3.4.3.1, every stator phase of the laboratory machine consists of two series connected sub-windings. The inductances of these windings or other portions of a winding can also be computed using the MWFA. These inductances can be used to model internal faults in the machine (as discussed later in Chapter 6).

Similar to the above procedure, the MWFA can be used to compute the inductances of faulted windings of a synchronous machine. Figures 3.22-a, and 3.22-b, respectively, show the self inductance of winding A2 and the mutual inductance between this winding and the field winding.

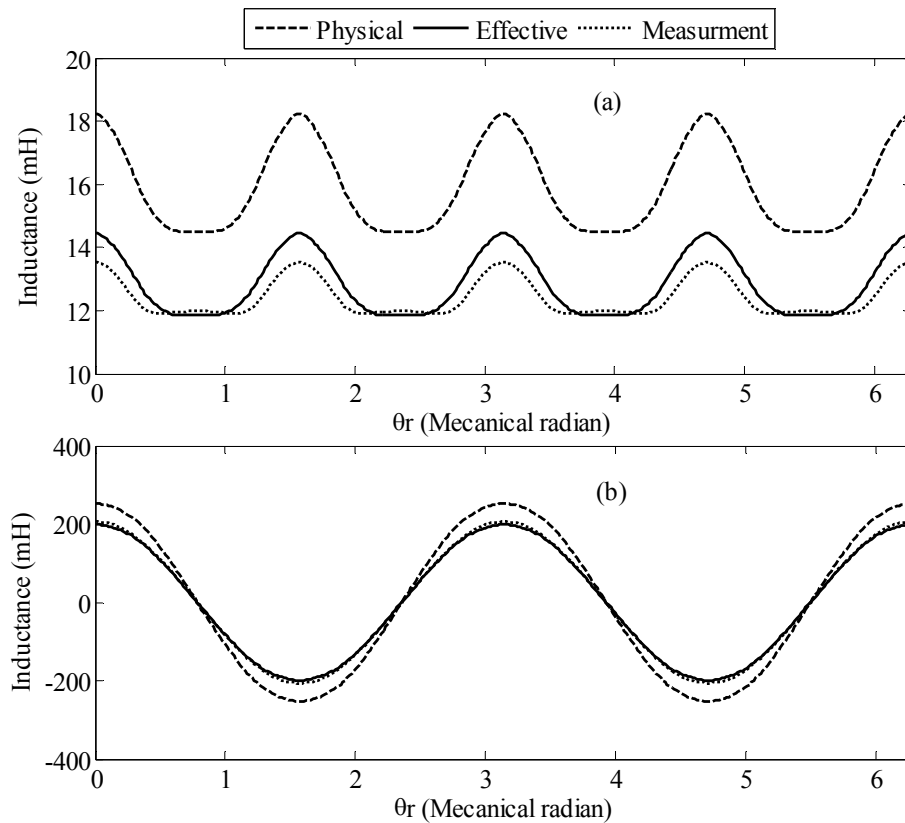


**Figure 3.22:** Inductances of sub-winding A2 using  $P_1(\phi_s, \theta_r)$ ,  $P_{eff}(\phi_s, \theta_r)$  and measurement, (a) self inductance of A2, (b) mutual inductances between A2 and the field winding

Similar to Figure 3.20, the MWFA-based inductances are calculated using both the physical permeance function ( $P_1$ ) and the effective permeance function ( $P_{eff}$ ). In Figures 3.22, the MWFA-based computed inductances are compared with the measured values for these quantities. These inductances were measured in the laboratory using the *inductance bridge method* [74] for various rotor positions. It can be seen that the inductance values computed using the effective permeance function are in good agreement with the measured values, whereas the inductances calculated from the physical permeance function have considerable error.

### 3.5 Chapter Contributions and Conclusions

Three known methods of obtaining inductances of electric machines were reviewed in this chapter; the *dq0 theory*, the *finite element method* (FEM), and *the modified winding function approach* (MWFA). The fundamentals of the dq0 theory were discussed and the dq0 equivalent circuit of synchronous machines was extracted using this theory. In this thesis the orthogonal Park's transformation of (3.11) was used which generates a symmetrical dq0 inductance matrix. The details of using the dq0 theory to analyze permanent magnet synchronous machines were also discussed in this chapter.

The finite element method as a tool of analyzing and evaluating the inductance matrices of machines was also reviewed.

Finally the modified winding function approach (MWFA) was introduced and suitably modified. These *modifications*, include taking into *account the actual shape of pole-arc* and iron MMF drop in computing the permeance function of the machine; and

*adjusting the permeance function* with the help of experimentally measured  $L_d, L_q$  and  $L_0$ .

The relative merits for each of these approaches as to the level of modeling detail and accuracy of results and complexity were discussed. The MWFA (along with the modifications described in this thesis) is adopted in the thesis as the main tool for computing synchronous machine inductances for the purpose of time-domain simulation in the environment of the real-time digital simulator (RTDS<sup>®</sup>). This assessment is based on the flexibility and speed of this routine and its capacity to represent the effects of space harmonics.

# Chapter 4: Inclusion of Saturation Effects in Evaluating Synchronous Machine Inductances

---

So far, in the process of computing inductances using the MWFA, the effects of iron saturation were ignored. *Incorporation of these effects in the winding function approach, which is one of the main contributions of this thesis, is explained in Section 4.3.*

Magnetic saturation in synchronous machines can influence the steady-state loadings as well as the transient waveforms in a simulation. Although the effect of saturation is stronger and hence more relevant in transformer studies than in electric machines (as there is typically an air-gap in a machine), there are nevertheless situations where saturation in machines must be taken into account. This chapter reviews treatment of saturation in calculating inductances and then proposes a new approach to accurately incorporate saturation effects in the MWFA-based models.

## 4.1 Incorporation of Saturation in the Dq0 Approach

In the dq0 theory, the effects of iron saturation in synchronous machines are modeled by adjusting the values of d-axis magnetizing inductance ( $L_{md}$ ) and q-axis magnetizing inductance ( $L_{mq}$ ) of the synchronous machine's equivalent circuit shown in Figure 3.2.

This adjustment is based on the magnitude of magnetizing currents  $i_{md}$  and  $i_{mq}$ . The following assumptions are usually made in representing the magnetic saturation for synchronous machines using dq0 theory [75]:

1. The leakage inductances are independent of saturation. The leakage fluxes flow in the air for a considerable portion of their path so that they are not significantly affected by saturation of the iron portion. As a result the only elements of the equivalent circuit that saturate are magnetizing inductances  $L_{md}$  and  $L_{mq}$ .
2. It is also assumed that, saturation does not deform the sinusoidal distribution of the magnetic field over the face of a pole, and all the inductances therefore maintain their sinusoidal dependence on rotor position.
3. Hysteresis is ignored, while eddy currents are sometimes approximated by inclusion of additional windings on the d- and q-axes or by modifying the parameters of the existing windings.

Given the above assumptions, the effect of saturation can be represented by (4.1). In this equation,  $L_{mdu}$  and  $L_{mqu}$  are the unsaturated values of  $L_{md}$  and  $L_{mq}$  respectively.

$K_{sd}$  and  $K_{sq}$  are called the saturation factors and identify the level of saturation in the d- and q- axes respectively. These factors are functions of d- and/or q- axis magnetizing fluxes (or currents) referred to as *saturation indices*. In unsaturated conditions these factors are equal to 1.

$$\begin{aligned} L_{md} &= K_{sd} \cdot L_{mdu} \\ L_{mq} &= K_{sq} \cdot L_{mqu} \end{aligned} \tag{4.1}$$

Minor differences between various approaches of modeling saturation in dq0 theory arise from the manner in which the dependency of these saturation factors on magnetizing fluxes (or currents) is represented:

One method [1], [75] assumes that both the d- and q-axes magnetizing inductances  $L_{md}$  and  $L_{mq}$  vary with saturation. Also  $K_{sd}$  and  $K_{sq}$  are both functions of total air-gap flux linkage ( $\Psi_{at}$ ) which is defined in (4.2). These functions are identified by the saturation characteristics of d- and q- axes [1].

$$\Psi_{at} = \sqrt{\Psi_{md}^2 + \Psi_{mq}^2}$$

where: (4.2)

$$\Psi_{md} = L_{md} \cdot i_{md}, \quad \Psi_{mq} = L_{mq} \cdot i_{mq}$$

Transient stability programs like PSSE [76] and electromagnetic transients programs like EMTP [75] use this approach to implement the effects of saturation in the synchronous machine models. Although this approach considers different saturation curves for the d- and q- axes, it uses only one saturation index ( $\Psi_{at}$ ) for both axes. This assumption ignores the angular displacement of MMF peak from the d-axis and therefore is more appropriate for non-salient pole synchronous machines.

Other methods assume that saturation takes place on both the d- and q-axes, and  $K_{sd}$  is a function of  $\Psi_{md}$  and  $K_{sq}$  is a function of  $\Psi_{mq}$ . The relation between  $K_{sd}$  and  $\Psi_{md}$  is identified from the d-axis saturation characteristics, and the relation between  $K_{sq}$  and  $\Psi_{mq}$  is defined based on the saturation characteristics of the q-axis. Existing models in the current commercial release of programs like EMTDC [11] and RTDS [26] use this approach of realizing saturation in synchronous machines. These programs, in addition to the above assumptions, introduce an approximation by ignoring the effects of q-axis saturation (i.e.  $K_{sq} = 1$ ). This assumption is based on the existence of a relatively large



air-gap on the q-axis which is not accurate particularly for non-salient pole synchronous machines.

#### 4.1.1 The Cross-Magnetization Phenomenon in Saturated Synchronous Machines

The above methods assume that the d-axis magnetizing flux does not affect the saturation on the q-axis and vice versa. Research [77], [78] has shown that due to nonlinearities introduced by saturation, the permeability pattern is not symmetric around the d-axis. This results in asymmetry in flux linkages; that is, d-axis currents produce q-axis flux linkage and vice versa. This phenomenon is known as *cross-magnetization effect* which is briefly explained in this section. Incorporating the effects of this phenomenon into MWFA in calculating the phase-domain inductances is explained in Section 4.3.

Consideration of the cross-coupling effect in saturated synchronous machines is a result of analyzing machines using a more microscopic technique. Here the actual distribution of magnetomotive force in the air-gap space is taken into account to calculate the flux density in each location of the air-gap. The d- and q-axis components of the flux linkage are then determined by suitable integrations.

For the purpose of simplicity consider a synchronous machine with constant air-gap length along the pole-face area. The unsaturated permeance function of this machine is shown as  $P$  in Figure 4.1 (the same as  $P_0$  in Figure 3.16). The distribution of magnetomotive force for a balanced operating condition is also presented in Figure 3.16. The MMF distribution with respect to rotor frame of reference is approximately a sinusoidal function (as the windings may not be perfectly sinusoidally distributed). Its magnitude and angle depend on the loading conditions and the level of field excitation. The

saturated permeance function,  $P_{sat}$ , is also plotted in Figure 4.1. This calculation is performed by taking into account the intensity of magneto-motive force in each angular position of the rotor space; i.e. when the absolute value of MMF is higher, higher saturation levels are experienced and therefore the value of permeance is reduced more in that particular angular position. Figure 4.1 shows that the saturated permeance is not symmetric on the sides of the d-and q-axis; this results in asymmetry in the generated flux density which is interpreted as *cross-coupling effect* in the dq0 theory.

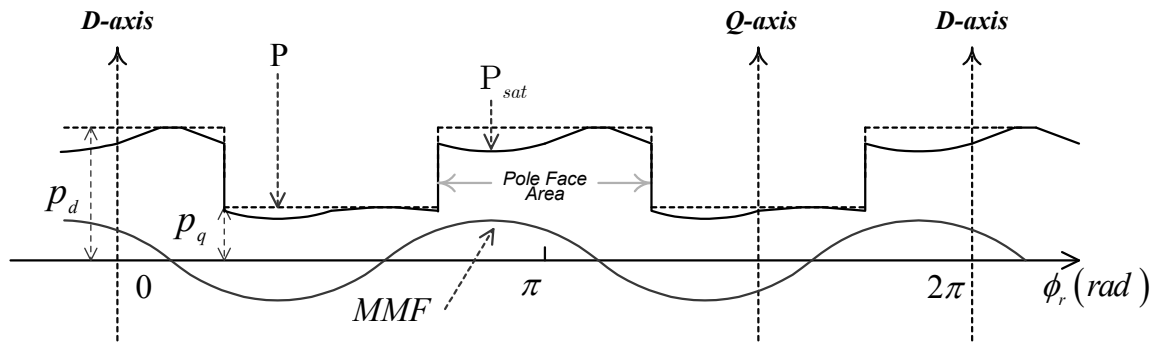


**Figure 4.1:** The effect of MMF distribution on saturated permeance function

The saturated permeance,  $P_{sat}$ , can be computed using the formulae presented in (4.3). In this equation,  $S_d$  and  $S_q$  are known as multiplicative *saturation factors* of the pole-face area and interpole area respectively. These saturation factors are functions of  $\mathcal{F}(\phi_r)$ , the MMF at that particular angle, and have a value in the range of [0 1]. These factors are close to unity for small values of MMF and they decrease in value with the increase in MMF. The saturation factors vary with the ratio of iron to air for each slice of the machine at angle  $\phi_r$  of width  $d\phi_r$ . For example, because of the small air-gap length on the d-axis area,  $S_d$  is smaller than  $S_q$  for the same value of MMF.

$$P_{sat}(\phi_r) = \begin{cases} P(\phi_r) \cdot S_d(\mathcal{F}(\phi_r)) & \text{in the pole face area} \\ P(\phi_r) \cdot S_q(\mathcal{F}(\phi_r)) & \text{in the interpole region} \end{cases} \quad (4.3)$$

The saturation factors ( $S_d$  and  $S_q$ ) can be computed using the saturation characteristic along the d- and q-axes using a least-square fitting approach as explained in [79], [80]. In this approach the saturation factors are approximated by polynomials and the least-square fitting ensures that the measured d and q open-circuit saturation characteristics match those calculated using saturation factor method. The precise shapes of  $S_d$  and  $S_q$  will be shown later; they typically assume the profile shown later in Figure 4.5. In [79], [80] the air-gap flux density at angle  $\phi_r$  is computed using (4.4), where  $k_B$  is a constant that depends on the machine dimensions.

$$B(\phi_r) = k_B \cdot P_{sat}(\phi_r) \cdot \mathcal{F}(\phi_r) \quad (4.4)$$

Equation (4.4) is then integrated to calculate the d- and q- axes flux linkages ( $\Psi_d$  and  $\Psi_q$ ) [79], [80]. The computed  $\Psi_d$  and  $\Psi_q$  are functions of both magnitude and angle of the magnetomotive force. At the magnetomotive force angle of  $0^\circ$ , the relation between  $\Psi_d$  and magnetomotive force magnitude is essentially the computed open-circuit characteristics of the machine ( $\Psi_d$  versus the field current with the stator open circuited). If the saturation factors are selected properly, this computed open-circuit characteristics can be made to match the experimental one. The same procedure can be repeated for the q-axis saturation characteristics. The author of [80] concluded that a fourth-order polynomial is an adequately accurate approximation to represent saturation functions.

The relations between the magnitude and angle of the total MMF in pu ( $I_{mag}$  and  $\xi$ ) and the magnetizing currents on the d- and q- axes (in pu) are shown in (4.5). These, ( $i_{md}$  and  $i_{mq}$ ) can be obtained by transforming winding currents for all three phase windings into d-and q components and summing the currents in all the resulting d and q windings respectively as shown in (4.5).

$$\begin{aligned}\mathcal{F}(\phi_r) &= I_{mag} \cdot \cos(\phi_r + \xi) \\ I_{mag} &= \sqrt{i_{md}^2 + i_{mq}^2}, \quad \xi = \tan^{-1}(i_{mq} / i_{md}) \\ i_{md} &= \sum_{n=1,2,..} i_{d_n}, \quad i_{mq} = \sum_{n=1,2,..} i_{q_n}\end{aligned}\quad (4.5)$$

This equation can be used to extract the d- and q- axes flux linkages ( $\Psi_d$  and  $\Psi_q$ ) and magnetizing reactances ( $X_{md}$  and  $X_{mq}$ ) as functions of  $i_{md}$  and  $i_{mq}$ . As an example, the variation of  $X_{md}$  and  $X_{mq}$  with d- and q- axes magnetizing currents for a generator unit, with the parameters and experimental d- and q-axes saturation curves given in [1], are computed and shown in Figures 4.2 and 4.3. These figures show the dependence of d- and q- axis magnetizing reactances ( $X_{md}$  and  $X_{mq}$ ) on both magnetizing currents  $i_{md}$  and  $i_{mq}$ .

Although the above method originally was developed for dq-based models, it can be directly applied to a phase-domain MWFA-based model as explained in Section 4.3. This is because the approach is used primarily to represent the permeance function as a function of saturation (Equation(4.3)). Once, the saturated permeance is known, (3.29) can be used to calculate the full set of machine inductances.

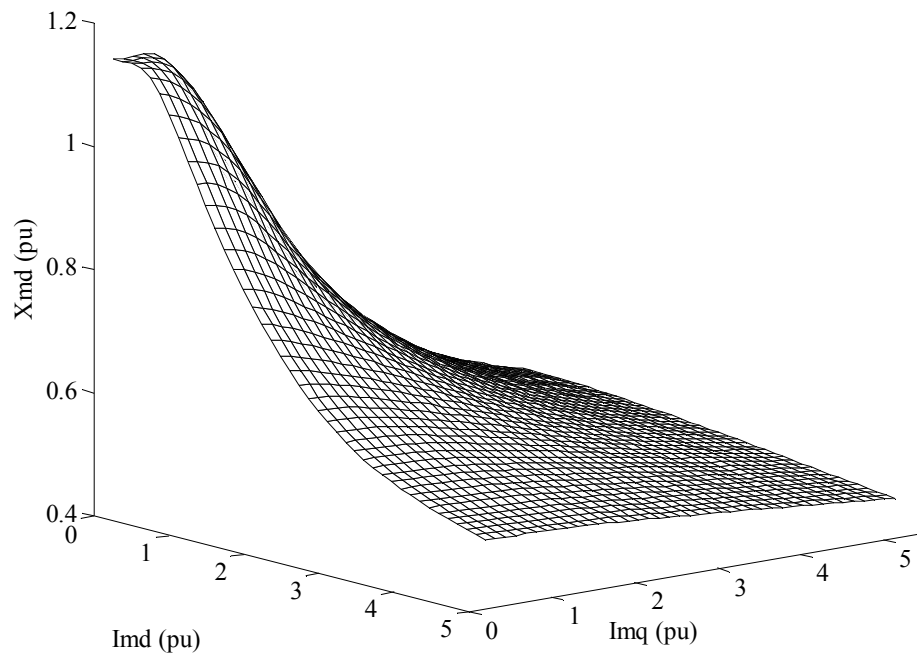


**Figure 4.2:** Variation of direct axis magnetization inductance with d- and q- axes magnetization currents

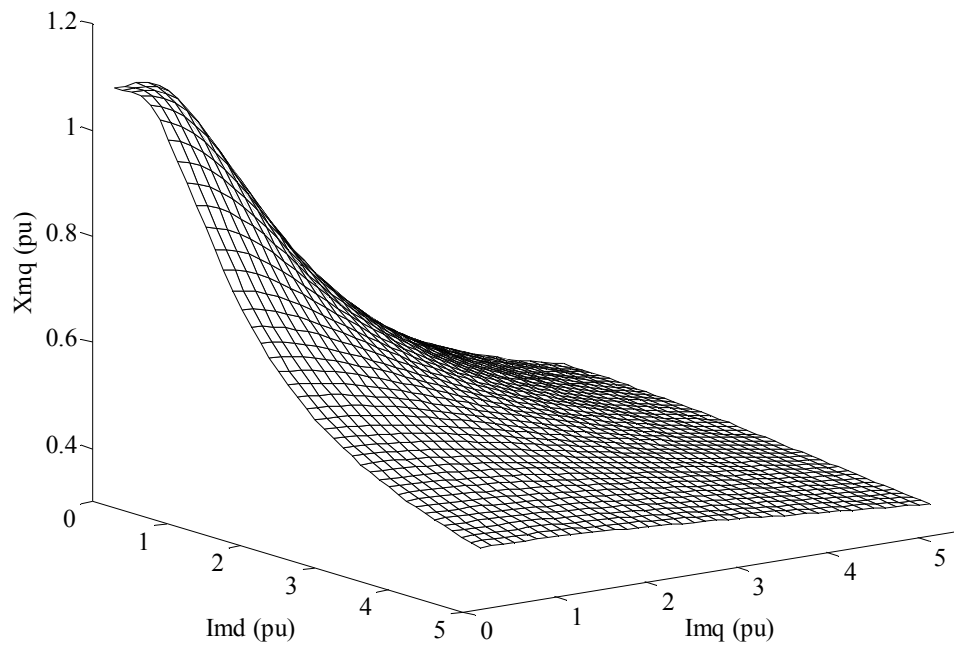


**Figure 4.3:** Variation of quadrature axis magnetization inductance with d- and q- axes magnetization currents

## 4.2 Modeling of Saturation in the FEM

Application of the finite element method (FEM) in analyzing electric machines was briefly introduced in Section 3.3. Fine details including local saturation in the teeth, actual shape of the rotor and stator parts can be included in such analysis.

In [54]-[57], [60], [77] finite element analysis is used to evaluate the saturated d- and q- axis impedances of synchronous machines. In some results [56] it is found that the actual saturated impedances and load angles determined from comprehensive magnetic field solutions have significant differences compared to the values calculated according to the classical methods described in the previous section. Some of these researchers [56], [60], [77] point out that the magnetizing current in one of the d- or q- axis affects the flux in the other axis; i.e. the use of FEM in analyzing the saturation in synchronous machines provides evidence of the presence of cross-magnetization phenomenon.

In [59], [62] the finite element analysis is used to compute the phase-domain inductances of electric machines under saturated conditions. It is reported in [62] that a change in loading condition can cause a phase shift in the calculated phase-domain inductance waveforms which is a result of inherent inclusion of 'cross-magnetization effect' in the FEM analysis.

As mentioned in Section 3.3, the procedure of using FEM to evaluate the saturated phase-domain inductances of a machine is very time-consuming as the magnetic field calculations must be repeated for each loading condition. Therefore in this thesis, for practical reasons, saturation is incorporated into the MWFA to compute the inductances of synchronous machines as described in the next section.

### 4.3 Incorporation of Saturation in the MWFA

This section introduces a new approach in which saturation effects are incorporated into a MWFA formulation for the purpose of calculating inductances of synchronous machines. The MMFs are calculated as function of winding currents, and the saturated permeance is then evaluated based on the magnitude of MMF at each angular position in the rotor frame of reference. Once this permeance variation is determined, (3.30) is used to calculate all phase-domain inductances for any loading condition. *Such treatment is one of the main contributions of this thesis.* The full machine model resulting from this treatment is later (in Chapter 7) shown to be vitally important in representing ambient harmonic conditions in synchronous machines. This factor is vital for closed-loop testing of some protection relays which use these harmonics as a signature to detect faults in synchronous machines.

As mentioned in Section 3.4.3, previous researchers assumed infinite permeability for the iron and therefore only MMF drops along the air-gap were taken into account in the MWFA. With this assumption, it is not feasible to take into account the effects of iron saturation on the inductances calculated from the MWFA. In previous research in this field [69] the effect of saturation in reducing the permeance was approximated by reducing the rotor pole-arc span. This treatment was performed at only one operating point, and any effect of operating-point dependent saturation was ignored.

In contrast, in this thesis, by introducing the permeance function in (3.30) and by incorporating the technique of modifying the permeance function, discussed in Section 4.1.1 the effects of operating-point dependent saturation are incorporated into MWFA. This treatment automatically takes into account the so called ‘cross-magnetizing

phenomenon' into the computation of machine inductances. Inherent in this treatment is the simplification that the spatial distribution of total MMF is sinusoidal. Although this is an approximate treatment, it is validated in Section 6.2 by comparison with experiment.

The following assumptions are made in the incorporation of the effects of magnetic saturation into the MWFA:

1. The leakage inductances are independent of saturation. The leakage inductance ( $L_{ls}$ ) is simply added to the magnetizing portion of the inductance.
2. Hysteresis effects are ignored.

In this section the experimental machine of Section 3.4 is used again as an example to demonstrate the process of incorporating the effects of saturation into MWFA.

#### 4.3.1 Derivation of saturation factors ( $S_d$ and $S_q$ ) from the experimental open-circuit characteristics of the machine

As mentioned in Section 4.1.1, the saturation factors can be derived from the d- and q- axis saturation curves as explained in [79], [80] (see Appendix D for more details). The open-circuit characteristic of the laboratory machine is shown in Figure 4.4. From this curve, using the saliency factor (ratio of d- and q- axis magnetizing inductances) and assuming a quadratic characteristics for the portion of MMF which contributes to saturation [81] the q-axis saturation curve is also obtained [81]. In this method, the needed applied magnetomotive force ( $\mathcal{F}$ ), for a certain magnetic flux in the saturated region, is assumed to consist of two components: one component ( $\mathcal{F}_{ag}$ ) corresponding to the air-gap line (unsaturated condition) and an additional component ( $\mathcal{F}_{sat}$ ), which is needed in addition to  $\mathcal{F}_{ag}$ , to produce the same flux under saturated conditions. This



additional magnetomotive force ( $\mathcal{F}_{sat}$ ) is assumed to have the quadratic form [82] shown in (4.6). In (4.6),  $\Phi$  is the magnetic flux at the operating point and  $\Phi_0$  is the magnetic flux at the knee point at which the saturation characteristic starts to be nonlinear.

$$\begin{aligned}\mathcal{F}_{sat} &= k_{sat} \cdot (\Phi - \Phi_0)^2 & \Phi > \Phi_0 \\ &= 0 & \Phi \leq \Phi_0\end{aligned}\tag{4.6}$$

The values of the d- and q-axis knee point magnetic flux ( $\Phi_{d0}$  and  $\Phi_{q0}$ ) are different:  $\Phi_{d0}$  is known from the open circuit characteristics, and  $\Phi_{q0}$  can be calculated in terms of  $\Phi_{d0}$ , saliency ratio, and angular span of the pole-arc [81]. This value corresponds to a particular MMF where the edges of the pole-arc start saturating. The constant  $k_{sat}$  is assumed to be the same for both d- and q-axes [82]. Its value can be evaluated from the open-circuit characteristics, angular span of the pole-arc and ratio of permeability in the pole-arc region and interpole region[81].

The q-axis saturation curve for the laboratory machine in this thesis is extracted using the above method and shown in Figure 4.4. Using the saturation characteristics along the d- and q-axes, the saturation factors ( $S_d$  and  $S_q$ ) are computed with a least-square fitting approach [79], [80] as mentioned in Section 4.1.1. The resulting variation of saturation factors for the machine as functions of magneto-motive force are shown in Figure 4.5.

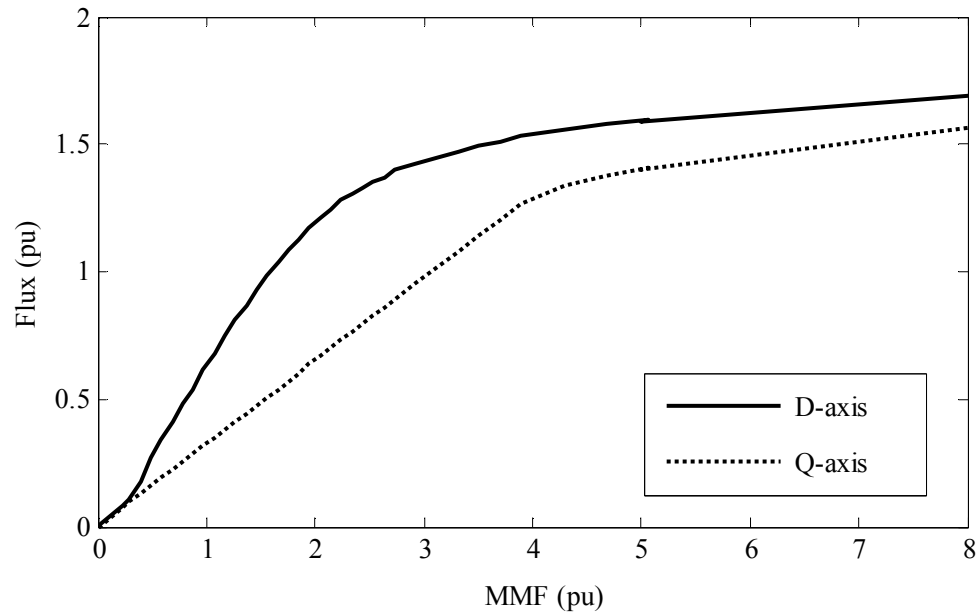


**Figure 4.4:** D- and Q-axis saturation curves generated from the open-circuit characteristics of the experimental machine

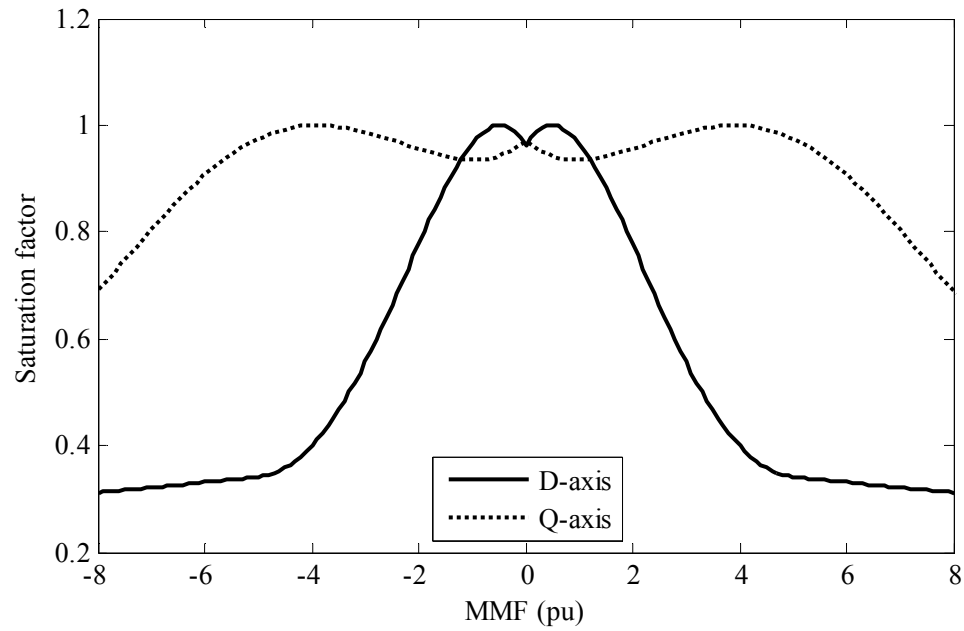


**Figure 4.5:** Direct- and quadrature-axis saturation factors ( $S_d$  and  $S_q$ ) of the experimental machine

### 4.3.2 Generating the saturated permeance function ( $P_{sat}$ ) for each operating point using the saturation factors ( $S_d$ and $S_q$ )

As the loading of the machine varies, the resulting MMF distribution changes in magnitude and phase as mentioned earlier in Section 4.1.1. At each operating point (loading condition) of the machine the total magnetomotive force has an approximate sinusoidal distribution which can be computed using the total magnetizing currents on the d- and q- axis ( $i_{md}$  and  $i_{mq}$ ) as shown in (4.5). Using the function of total MMF and the saturation factors ( $S_d$  and  $S_q$ ) the effective permeance function ( $P_{eff}$ ), evaluated in (3.32), can be modified to derive the saturated permeance function ( $P_{sat}$ ) for that particular operation point. This modification is done by replacing  $\phi_r$  with  $\phi_s - \theta_r$  in (4.3) as shown in (4.7):

$$P_{sat}(\phi_s, \theta_r) = \begin{cases} P_{eff}(\phi_s, \theta_r) \cdot S_d(\mathcal{F}(\phi_s, \theta_r)) & \text{in the pole face area} \\ P_{eff}(\phi_s, \theta_r) \cdot S_q(\mathcal{F}(\phi_s, \theta_r)) & \text{in the interpole region} \end{cases} \quad (4.7)$$

Now the saturated values of inductances for that particular operation point can be obtained by using the saturated permeance function,  $P_{sat}(\phi_s, \theta_r)$ , in (3.30).

As an example, the saturated permeance functions,  $P_{sat}(\phi_s, \theta_r)$ , for two different operating points are computed and shown in Figure 4.6. At the first operating point which is shown by ‘Sat1’, the total magnetizing currents in the d- and q- axis are respectively  $i_{md} = 1.8$  pu and  $i_{mq} = 0$ , which correspond to an open-circuit condition. At this operating point the saturated permeance function has a dip in the middle of the pole-arc as the total MMF peaks in the middle of the pole-arc (as  $i_{mq} = 0$ ). The second operating point, identified by ‘Sat2’ in Figure 4.6, corresponds to a loaded condition with

$i_{md} = 1.2$  pu and  $i_{mq} = 1.4$  pu. For this case, the total MMF is more oriented towards the q- axis and hence one side of the rotor pole-arc is more saturated than the other side; as a result  $P_{sat}$  is lower in that side as seen in Figure 4.6.

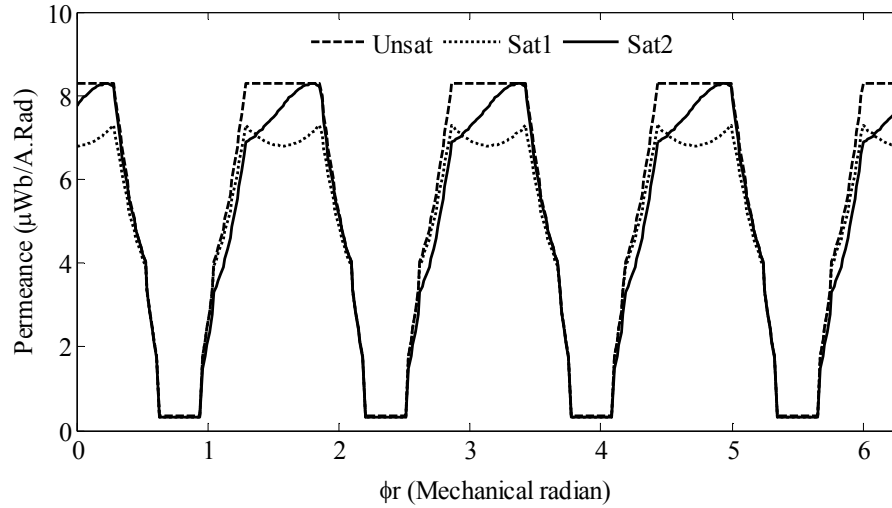


**Figure 4.6:** Change in the permeance function due to change in operating condition

The corresponding saturated stator inductances are shown in Figure 4.7. The saturated inductances have different magnitudes compared to the unsaturated ones, and the inductance variations in the ‘Sat2’ loading condition also show a slight advancement in angular displacement. This angular displacement of the inductance with loading under saturated conditions has also been reported by other authors [62] who used the FEM to evaluate inductances of a synchronous machine.

The proposed method of incorporating saturation, presented here, inherently includes the “cross-magnetization effect” which is at the root of such inductance variation.

It should be noted that, the d-q quantities used in the above derivations are used only to determine the permeance variation with saturation. The MMFs are calculated as functions of winding currents according to (4.5), and the saturated permeance functions

are then calculated using (4.7). Once this permeance variation has been determined, (3.30) can be used to calculate all phase-domain inductances for any loading condition.

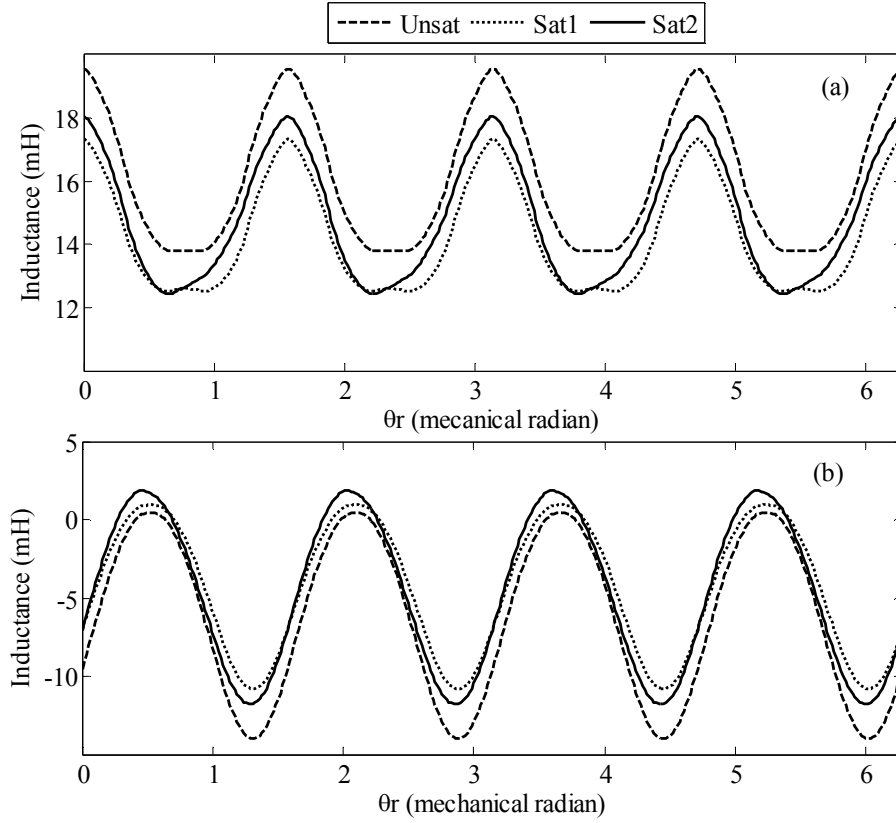


**Figure 4.7:** Change in the stator inductances due to saturation, (a) self inductance of stator phase-A, (b) mutual inductances between stator phase-A and phase-B.

All self and mutual inductances of the machine are calculated using (3.30), (4.5) and (4.7). Note that these inductances are functions of rotor position  $\theta_r$ , and magnetizing currents  $i_{md}$  and  $i_{mq}$ . To indicate that the inductances in (3.30) now are saturation dependent, the vector of currents  $\underline{i}$  is explicitly added to the list of function arguments in (3.30), and thus the inductance matrix of the machine becomes:

$$[L(\theta_r, \underline{i})] = L_{j,k}(\theta_r, \underline{i}), \text{ where } j, k \in \{a, b, c, F, D, Q\} \quad (4.8)$$

To save on-line computation time, these calculations are done in advance and the values of the inductances are stored in tables for look-up during simulation. An efficient technique for this task is discussed further in Section 5.4.

Detailed procedural steps of computing the machine inductances are shown in Figure 4.8. An off-line program is written to automatically calculate the inductances, including saturation effects, based on this flowchart.

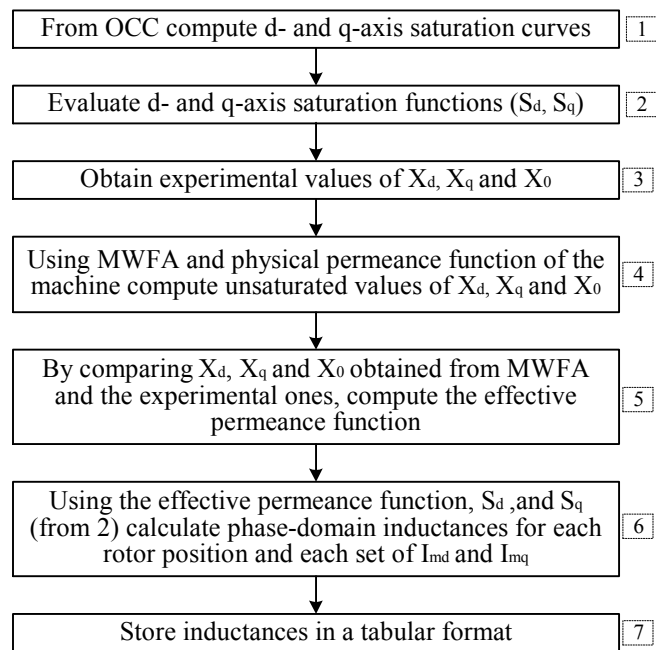


**Figure 4.8: Procedure for computing machine inductances using MWFA**

#### 4.4 Chapter Contributions and Conclusions

Earlier in Chapter 3, three known methods of obtaining electric machine inductances were reviewed; the dq0 theory, the finite element method (FEM), and the winding function approach (MWFA). The relative merits for each of these approaches as to the level of modeling detail and accuracy of results and complexity were discussed, and the MWFA was adopted as the main tool of computing synchronous machine inductances in this thesis.

Here in Chapter 4, the effects of *operating-point dependent saturation* are incorporated into the MWFA routine. In this new approach, the total magneto-motive force is calculated as a function of winding currents, and the saturated permeance function is then evaluated based on the magnitude of the MMF at each angular position with respect to the rotor frame of reference. The unsaturated effective permeance function, defined in Section 3.4.3.3, and the open-circuit saturation characteristic are the inputs for this procedure.

Chapters 4 and 5 described the methods in which the inductances of synchronous machines are evaluated. The next chapter is dedicated to time-domain simulation of electric machines with particular emphasis on electromagnetic transient programs and real-time digital simulators.

# **Chapter 5: Development of an Embedded Approach for Time-Domain Simulation of Electric Machines in Electromagnetic Transients Programs**

---

Earlier chapters describe the manner in which conventional machine inductances are determined and how they vary with rotor position and level of saturation. This chapter shows the manner in which the set of machine differential equations (i.e. (3.1)), resulting from the calculated inductance values, can be integrated into a generalized model of the network external to the machine to solve the full power system equations. The chapter begins with a brief description of the conventional approach of interfacing machine models into electromagnetic transients programs. Subsequently, the embedded approach of incorporating machine models into electromagnetic transients programs is introduced and explained with more details. *Implementation of this approach in the real-time simulator (RTDS) is one of the main contributions of this thesis.*

## **5.1 Introduction**

As discussed in Chapter 2, usually the sophisticated components such as electric machines are *interfaced* into electromagnetic transients programs (shown schematically in Figure 2.2). That means that the machine is modeled as an external component which receives the node voltages from the network solution of the EMTP-type program and, using the differential equation of the machine, it calculates the currents and communicates them back into the network solution [11]. The interfaced machine model has relatively low computational burden as this model is external to the transients



program, and the machine elements are not included in the admittance matrix of the transient solution.

This technique allows smaller and more manageable sub-systems that can be easily simulated in parallel for real time purposes. The advantage of this approach is that the machine model is external to the transients program, and the machine elements are not included in the admittance matrix of the transient solution. This, in turn, means that a new admittance matrix does not need to be calculated (and factorized) for each rotor position. However, the interfaced models may show numerical instability in some network configurations [11] or high operating frequencies (e.g. 400 Hz in [12]). As indicated by Figure 2.2, there is necessarily a time delay of one time-step introduced by the interface. The time-step delay in the procedure of interfacing is believed to be the main reason behind the instability problem. In real time simulation the importance of this problem is more significant, because the models are required to run in practice for long simulations at the actual speed of the physical phenomenon.

In this chapter, the *embedded* approach of incorporating electric machines into EMTP-type programs is introduced which absorbs the machine time-varying inductances into the network solution in the manner of other passive elements like capacitors, inductors and resistors. As will be shown in Section 6.1.4., this approach tends to show significantly improved numerical stability compared to the interfaced model.

## **5.2 Traditional Approach of Interfacing Electric Machines in Electro-Magnetic Transient Programs**

In Section 3.2, the dq0 theory was applied to the differential equations of synchronous machines (3.1) to transform them into dq0 frame. The dq0 format of

machine equations in (3.21) is much simpler than the original equations in  $abc$  frame, and it is commonly used in the analysis of synchronous machines. Therefore, to solve the synchronous machine equations inside the network solution programs of EMTTP type programs like EMTTP, EMTDC and RTDS, the dq0 format of machine equations are used [11]. The conceptual diagram of solving machine equations inside the EMTDC network solution loop [11] is shown in Figure 5.1. In each time-step, the program receives the node voltages  $v_a, v_b$  and  $v_c$  from the EMTDC network solution. These node voltages are computed by solving the nodal equation of the external network as in (2.7) for the previous time-step. Using Park's transformation,  $P(\theta_r)$  defined in (3.11), it then computes the dq0 components of the node voltages  $v_d, v_q$  and  $v_0$ . The derivatives of the flux linkages are obtained using  $v_d, v_q$  and  $v_0$  and the machine equations in (3.20). By integrating the state space variables (i.e. flux linkages) over time, the new values of flux linkages are computed as shown in Figure 5.1. Using the inductance matrix of the machine as in (3.15), the new values of winding currents in dq0 frame are computed. Finally the inverse of Park's transformation,  $P^{-1}(\theta_r)$ , is used to evaluate the abc frame currents  $i_a, i_b$  and  $i_c$ . These currents are then communicated back into the network solution of EMTDC.

The method of interfacing the machine model into the network solution of EMTDC is shown by Figure 5.2. In this figure each phase of the machine is modeled as a current source with the values computed using the above procedure. To improve the numerical stability of the machine, the model is terminated to the network through a resistance [11]. The value of this resistance is  $r'' = 2 \frac{l_c}{\Delta t}$ , where  $l_c$  is called the characteristics inductance

of the machine, and usually is chosen as sub-transient inductance of the machine [11].

The current source  $I_c(t)$  compensates for the current of resistance  $r''$ .

Electromagnetic transients programs have additional state variable based models for multi-mass inertia systems, excitation systems and so on, that are solved externally. The machine model interfaces via excitation voltage, electrical torque, and mechanical speed to these components [11].

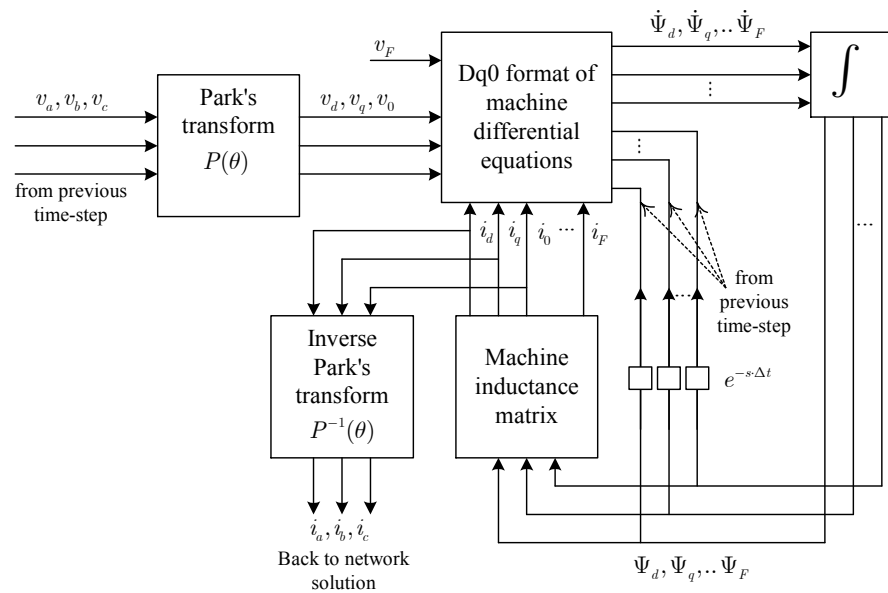


Figure 5.1: Conceptual diagram of solving the machine equations

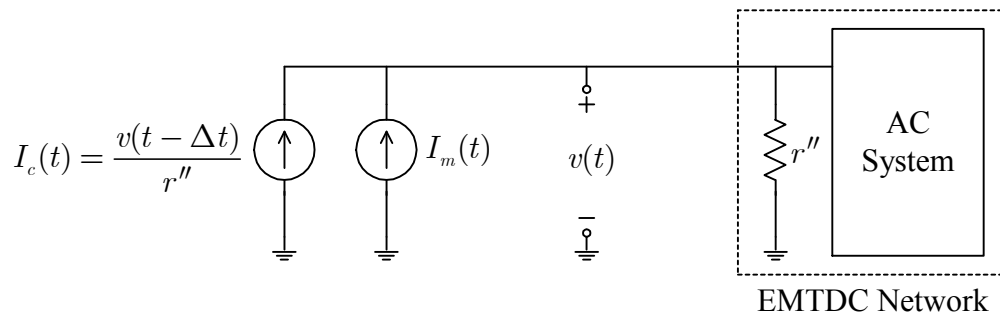


Figure 5.2: Interfacing the machine model to the network solution

### 5.2.1 Methods of Integrating Differential Equations of Electric Machines

As mentioned earlier, numerical integration is used in the process of discretizing the differential equations of a machine and interfacing it to the network solution of the electromagnetic transients programs. In this section, different methods of integrating the machine equations are explained. The effects of using different integration methods on the numerical stability of the model will be discussed later in Section 6.1.4.

One method of integration used in the past is a predictor corrector method. The second order Runge-Kutta method [83] is used to directly integrate the flux linkages in the conceptual diagram of Figure 5.1. However, it is not recommended for reasons discussed later in Section 6.1.4.

Another method is discretizing the differential equations of a machine using the trapezoidal method of integration. One significant advantage of trapezoidal integration is that it is stability preserving for linear systems [2]. This means that if the original system is stable, then so is the simulation of the discretized system. Likewise, if the original system is unstable, so is the case for the discretized system. See Appendix B for more details.

Although, typical real-world power networks modeled in electromagnetic transients programs are not linear, they consist mostly of linear elements. Hence, even though, a stability preserving algorithm (for linear systems) cannot guarantee the stability of non-linear systems, it has nevertheless been observed to exhibit excellent numerical performance in comparison with non-stability preserving algorithms [75].

Here, the trapezoidal method is directly applied to discretize (3.20) which is the differential equation of a machine in the dq0 frame. This differential equation in a more

compact format can be written as in (5.1). In (5.1),  $\underline{\Psi}$ ,  $\underline{v}$  and  $\underline{i}$  are the vectors of fluxes, voltages and currents in dq0 frame.  $[L]$  and  $[R]$  represent the inductance and resistance matrices of the machine in the dq0 frame.

$$\underline{v}(t) = [R]\underline{i}(t) + \frac{d}{dt}\underline{\Psi}(t) + [\omega]\underline{\Psi}(t)$$

where :

$$\underline{\Psi}(t) = [L]\underline{i}(t)$$

$$[\omega] = \omega \begin{pmatrix} 0 & 1 & \dots & 0 \\ -1 & 0 & \dots & \vdots \\ \vdots & \vdots & \ddots & \vdots \\ 0 & \dots & \dots & 0 \end{pmatrix} \quad (5.1)$$

Note that Figure 5.1 shows that flux linkages  $\Psi_d, \Psi_q, \dots$  are the state variables.

Sometimes it is more convenient to use currents as state variables particularly when developing an admittance matrix based model as will be discussed in Section 5.3.

By expressing  $\underline{\Psi}(t)$  as  $[L]\underline{i}(t)$  in (5.1), the differential equation of (5.2) can be obtained. Equation (5.2) is a first order differential equation with  $\underline{i}(t)$  as the independent variable.

$$\underline{v}(t) = [L]\frac{d}{dt}\underline{i}(t) + \underbrace{([R] + [\omega][L])}_{[A]}\underline{i}(t) \quad (5.2)$$

Equation (5.2) is integrated for the time interval  $[t - \Delta t \quad t]$  using trapezoidal integration to obtain the discretized form of this equation as shown in (5.3). In (5.3)  $\underline{v}(t)$  and  $\underline{i}(t)$  are respectively the vectors of winding voltages and currents for the present time-step, and  $\underline{v}(t - \Delta t)$  and  $\underline{i}(t - \Delta t)$  are these quantities for the previous time-step.

$$\frac{\Delta t}{2}(\underline{v}(t) + \underline{v}(t - \Delta t)) = [L](\underline{i}(t) - \underline{i}(t - \Delta t)) + \frac{\Delta t}{2}[A](\underline{i}(t) + \underline{i}(t - \Delta t)) \quad (5.3)$$

By expressing  $\underline{i}(t)$  in terms of other quantities in (5.3), equation (5.4) is obtained which can directly be used to update the dq0 components of currents and prepare them for injection using the conceptual diagram of Figures 5.1.

$$\begin{aligned} \underline{i}(t) = & \frac{\Delta t}{2} \left( [L] + \frac{\Delta t}{2} [A] \right)^{-1} \underline{v}(t) + \frac{\Delta t}{2} \left( [L] + \frac{\Delta t}{2} [A] \right)^{-1} \underline{v}(t - \Delta t) \\ & + \left( [L] + \frac{\Delta t}{2} [A] \right)^{-1} \left( [L] - \frac{\Delta t}{2} [A] \right) \underline{i}(t - \Delta t) \end{aligned} \quad (5.4)$$

In (5.4),  $\underline{i}(t)$  is computed using  $\underline{v}(t)$ , the vector of the node voltages at each time instant ( $t$ ), whose value is assumed to be known. In the interfaced approach used here, these voltage values are calculated by the external system as per the approach depicted in Figure 2.2. Therefore,  $\underline{v}(t)$  is not actually known yet, but  $\underline{v}(t - \Delta t)$  is. To estimate  $\underline{v}(t)$  for use in (5.4), projection methods [14], [26] can be used, which attempt to estimate  $\underline{v}(t)$  based on voltages in previous time-steps.

### **5.3 The Embedded Approach for Integrating Machine Models in Electro-Magnetic Transient Programs**

Since the interface-based model of the machine, discussed in Section 5.2, uses a current source to interface the machine to the network solution, it may show numerical instability and inaccuracy in some cases. Principally these difficulties occur because the decoupled solution approach introduces additional delays. If the machine is integrated into the network solution of electromagnetic transients programs such as EMTDC and RTDS in the same manner as passive elements like inductors and capacitors, interface delays are eliminated and it is expected that the numerical problem will be minimized. This approach is called the *embedded* approach. Later sections will confirm that this ‘embedded model of the machine’ is indeed numerically superior.

Rather than immediately dealing with the detailed set of coupled inductances as in (3.1) for a full machine, this method is first explained by a simple example of a time-varying inductor embedded into an external network. *Additionally, special techniques developed in this thesis for speeding up the procedure, and considerations for real-time simulation are also introduced.*

#### **5.3.1 An Example of the Embedded Approach: Modeling a Time-Varying Inductor in Electromagnetic Transients Programs**

The machine model is essentially a set of mutually coupled time-varying inductors. To address the issues relevant to the embedded machine model, the example of a single time-varying inductor interfaced to an external network is presented below.

The method of discretizing the differential equation of a simple constant inductor using trapezoidal integration was briefly mentioned in Chapter 2. At first glance, it

appears that the straightforward approach to incorporate a time-varying inductor would be to use the model of the fixed inductor of Section 2.1, but make  $g_L$  and  $I_h$  in (2.4) functions of the time-varying inductor  $L(t)$ . However, this approach will be shown later to cause errors in the simulation results. Equation (5.5) shows the general differential equation for a time-varying inductor including the non-linearity of the inductance. In (5.5),  $\Psi(t)$  is the time-varying flux linkage and  $L(t)$  is the time-varying inductance of the inductor.

$$v(t) = \frac{d}{dt}(\Psi(t)) = \frac{d}{dt}(L(t) \cdot i(t)) \quad (5.5)$$

Equation (5.5) is integrated for the time interval  $[t - \Delta t \quad t]$  as shown in (5.6)

$$\int_{t-\Delta t}^t v(t)dt = \int_{t-\Delta t}^t \frac{d}{dt}(L(t) \cdot i(t))dt \quad (5.6)$$

For numerical evaluation of this integral, the trapezoidal rule is applied to the left side of (5.6) as shown in (5.7).

$$\frac{1}{2} \Delta t (v(t) + v(t - \Delta t)) = (L(t) \cdot i(t) - L(t - \Delta t) \cdot i(t - \Delta t)) \quad (5.7)$$

The current  $i(t)$  can be expressed in terms of other parameters as shown in (5.8). This equation is similar to the discretized representation of a constant inductor in (2.4). The difference is that, the conductance value  $g_L(t)$  in (5.8) is time-varying and the history current  $I_h$  has the extra term  $\frac{L(t-\Delta t)}{L(t)}$  as a multiplier to  $i(t - \Delta t)$ . Note that for simple inductors, (5.8) degenerates into (2.4), the discretized equations for a simple inductor.



$$i(t) = g_L(t) \cdot v(t) + I_h$$

where :

$$g_L(t) = \frac{\Delta t}{2L(t)} \quad (5.8)$$

$$I_h = \frac{\Delta t}{2L(t)} v(t - \Delta t) + \frac{L(t - \Delta t)}{L(t)} i(t - \Delta t)$$

Equation (5.8) shows the relation between the voltage across the inductor and the current of the inductor. The electromagnetic transients program solves for **node voltages** using **nodal current injections**, and so (5.8) must be transformed into a node voltage form. The voltage across the inductor is the difference between voltages of the two nodes of the inductor; and current of the inductor is equal to the current of node 1. This relation between node quantities and winding quantities of the inductor is shown in (5.9) where  $v_1(t)$  and  $v_2(t)$  are the voltages between the two ends of the inductor and ground.

$$\begin{aligned} v_1(t) - v_2(t) &= v(t) \\ i_1(t) = -i_2(t) &= i(t) \end{aligned} \quad (5.9)$$

Using (5.8) and (5.9), the discretized form of the inductor equation in nodal format is derived and shown in (5.10).

$$\begin{bmatrix} i_1(t) \\ i_2(t) \end{bmatrix} = \underbrace{\begin{bmatrix} g_L(t) & -g_L(t) \\ -g_L(t) & g_L(t) \end{bmatrix}}_{[G_{inductor}(t)]} \cdot \begin{bmatrix} v_1(t) \\ v_2(t) \end{bmatrix} + \underbrace{\begin{bmatrix} I_h \\ -I_h \end{bmatrix}}_{\underline{I}_{inductor}} \quad (5.10)$$

The equivalent circuit of equation (5.10) is shown in Figure 5.3, where the history terms are represented as current sources and  $[G_{inductor}(t)]$  as a conductance network.

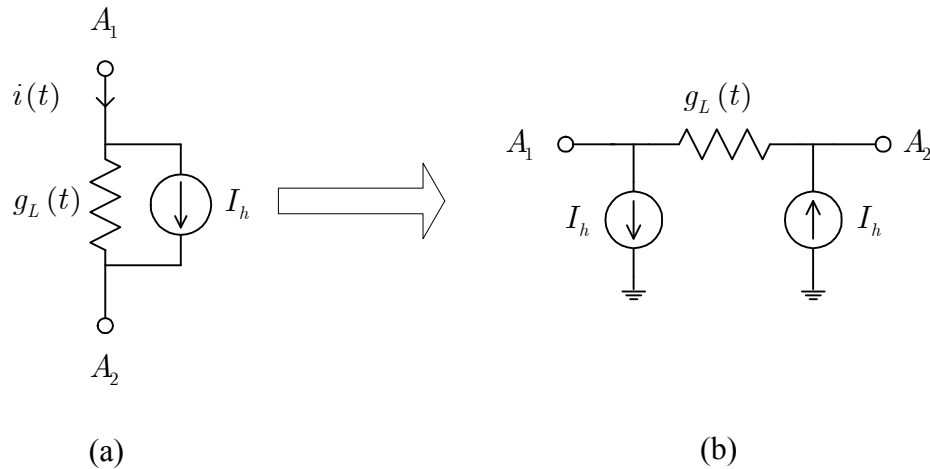


**Figure 5.3:** Discretized equivalent circuit of a time-varying inductor: (a) for branch quantities, (b) for nodal quantities.

This equivalent circuit is similar to the one for a constant inductor which was discussed in Chapter 2. The distinction is that the conductance matrix of Figure 5.3 is changing in each time-step, but the conductance matrix is constant for the discrete model of a constant inductor. This model can be implemented in EMTP-type programs by adding the history terms to the nodes  $A_1$  and  $A_2$  injected currents; and adding the elements of matrix  $[G_{inductor}(t)]$  to the corresponding elements of the network admittance matrix in each time-step of the simulation.

### 5.3.1.1 A simulation example of implementing a time-varying inductor in PSCAD/EMTDC

This example presents modeling of a time-varying inductor in PSCAD/EMTDC. The variation of inductance with time is selected such that the solution for the implemented example circuit can be analytically derived. The results show that the discretizing method can provide an accurate simulation result which is essentially identical to the theory. The PSCAD circuit diagram for modeling a time-varying inductor is shown in Figure 5.4.

Three different approaches are used: a) the correct approach discussed in the above

section, b) the approach that simply changes the inductance  $L$  with time in the formulation of a constant inductor as discussed at the beginning of Section 5.3.1, and c) the analytical solution.

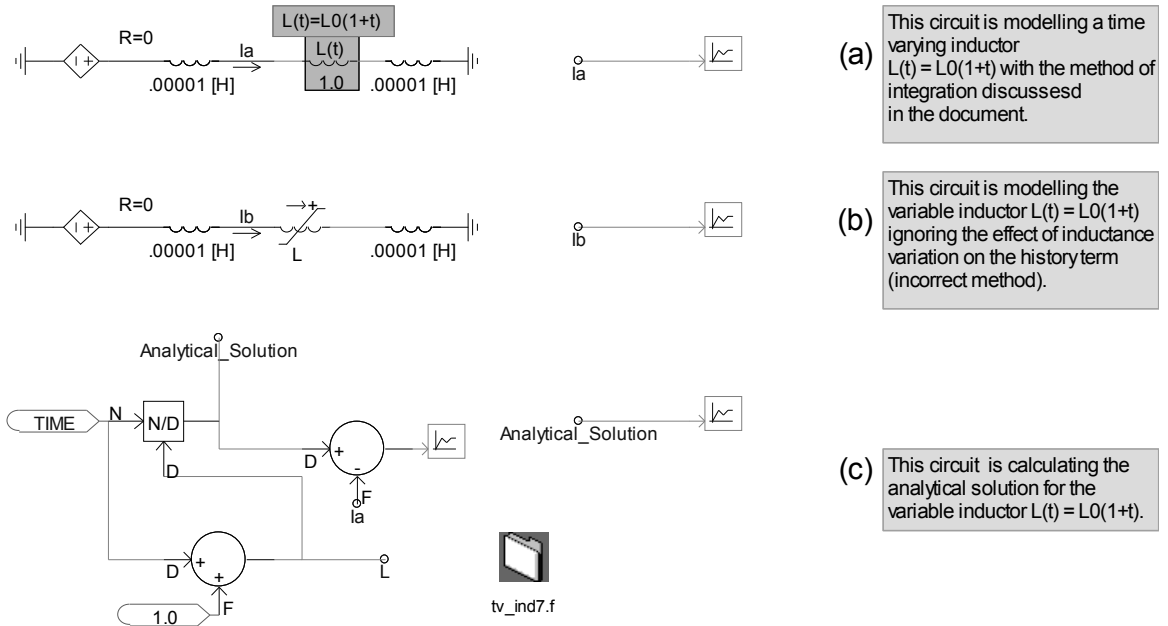


**Figure 5.4: Modeling a time-varying inductor in PSCAD/EMTDC, three different ways**

The time-varying inductance is changed according to  $L(t) = L_0(1 + t)$  with  $L_0 = 1.0(H)$ . It is connected to a DC source with negligible series resistance. Figure 5.4-c contains another circuit which computes the analytical solution of this problem. The simulation case also includes a circuit containing a constant inductance model which models the variable inductor by simply changing the value of inductance in every time-step, as discussed at the beginning of Section 5.3.1. This component ignores the term  $\frac{L(t-\Delta t)}{L(t)}$  in computing the history term in (5.8). The current of this inductor is labeled as  $I_b$  in Figure 5.4.

The analytical solution for this case can be computed as follows:

$$v(t) = d \frac{(L(t) i(t))}{dt} = L(t) \frac{di(t)}{dt} + i(t) \frac{dL(t)}{dt} \quad (5.11)$$

Assuming a constant voltage source  $V$  connected to the inductor with the inductance of  $L_0(1 + \alpha t)$ , (5.11) can be written as:

$$V = L_0(1 + \alpha t) \frac{di(t)}{dt} + i(t) \alpha L_0 \quad (5.12)$$

As can be verified by substituting into (5.12), the analytical solution for this differential equation is shown in (5.13):

$$i(t) = \frac{V}{L_0 \alpha} \left( 1 - \frac{1}{(1 + \alpha t)} \right) \quad (5.13)$$

For the special case of the circuit in Figure 5.4 in which  $V = 1.0(V)$ ,  $L_0 = 1.0(H)$ , and  $\alpha = 1.0(s^{-1})$ , the analytical solution of inductor current can be calculated with the formula shown in (5.14).

$$i_a(t) = 1 - \frac{1}{(1 + t)} \quad (5.14)$$

The simulated current in the time-varying inductor  $I_a(t)$  and the analytical solution of the circuit are shown in Figure 5.5a. The error of simulation is shown in Figure 5.5b. As can be seen, although the simulation is run with the fairly large time-step of  $200\mu S$ , the simulation results are very accurate. Further reduction in the simulation time-step will result in more accurate results.

When the more simplistic approach, in which the representation of a fixed inductor is modified to model a time-varying inductor, is used, significant errors result as shown by the plots of Figure 5.6. This large error is the result of ignoring the term  $\frac{L(t-\Delta t)}{L(t)}$  in the

formulation of a fixed inductor. For this particular inductor, the term  $\frac{L(t-\Delta t)}{L(t)}$  is always smaller than 1.0, and acts as a correction factor.

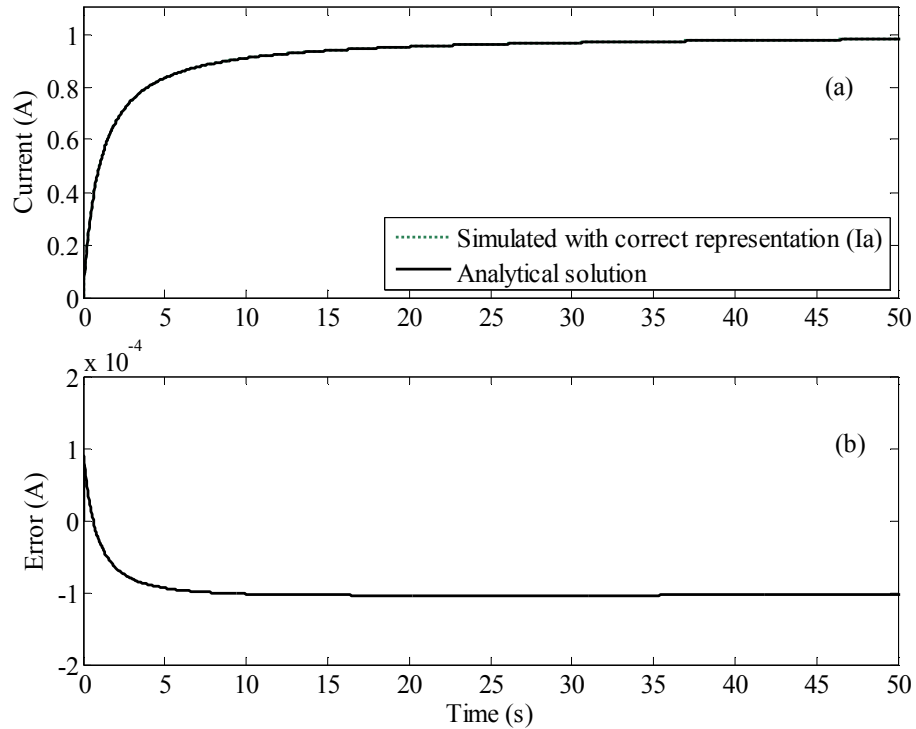


**Figure 5.5:** Comparison of the simulated current and analytical solution of a time-varying inductor in the circuit shown in Figure 5.4 : (a) comparison, (b) error

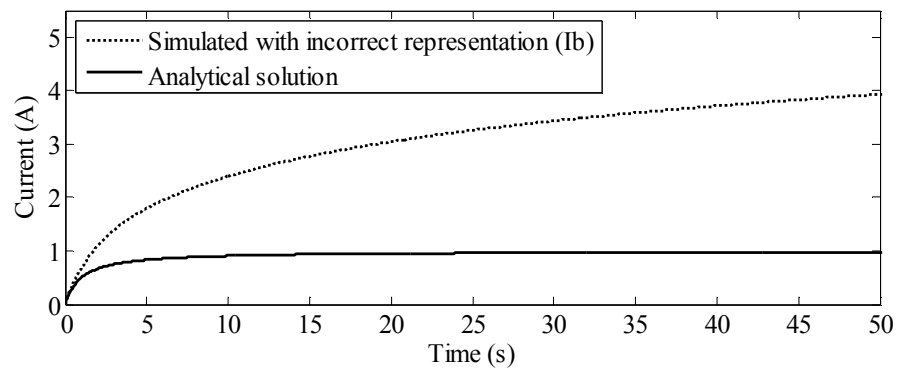


**Figure 5.6:** Simulated current of a time-varying inductor using the representation of a constant inductor and comparison with analytical solution

### 5.3.2 Discretizing Machine General Differential Equations

As discussed in Chapter 3, every electric machine can be considered as a set of mutually coupled inductances. The conceptual configuration for this representation is shown in Figure 5.7. This set has self and mutual inductances that change in value with the rotor position and level of saturation in the iron, and the resulting differential equations are as shown in (3.1).

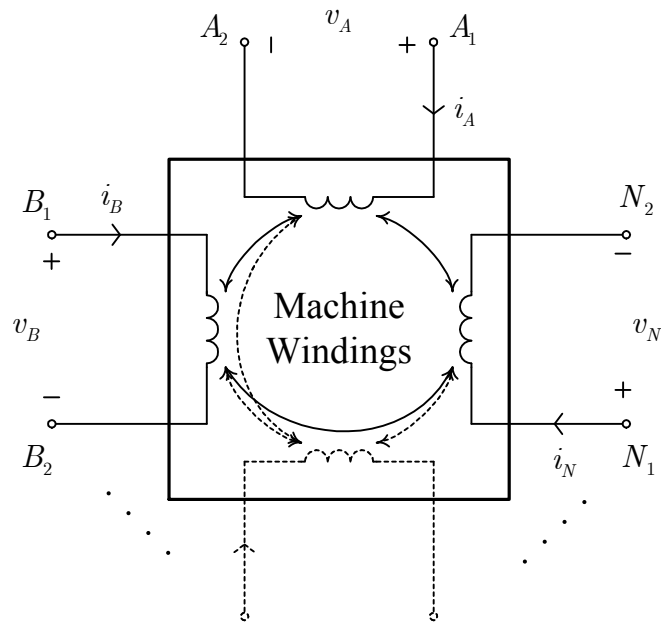


**Figure 5.7:** Representing the machine as a set of time-varying mutually coupled inductances

In Section 5.2, the common traditional interfaced approach was presented, where (3.1) (with suitable expressions for the inductance and resistance matrices) was implemented in electromagnetic transients programs as interfaced current sources. At the beginning of Section 5.3, it was mentioned that the interfaced approach can have numerical problems and the embedded approach is superior. The embedded approach was first demonstrated with a simple example of a time-varying inductor in Section 5.3.1.

This section discusses the implementation of (3.1) in general form for a set of mutually coupled inductors using the embedded approach.

In the embedded approach of modeling machines, trapezoidal integration is applied to the phase-domain differential equations of the machine (3.1) to form the discretized format of machine differential equations. To discretize the differential equation of the machine, (3.1) is integrated for the time interval of  $[t - \Delta t \quad t]$  as shown in (5.15). For numerical evaluation of this integral, the trapezoidal rule is applied to the left side of (5.15) and also to the term  $\int_{t-\Delta t}^t [R]\underline{i}(t)$  in the right side, and the results are shown in (5.16). The term  $\int_{t-\Delta t}^t \frac{d}{dt}([L(t)]\underline{i}(t))dt$  has an analytical solution  $\{[L(t)]\underline{i}(t) - [L(t - \Delta t)]\underline{i}(t - \Delta t)\}$  as shown in (5.16). Here,  $\underline{v}(t)$  and  $\underline{i}(t)$  are, respectively, the vectors of winding voltages and currents for the present time-step, and  $\underline{v}(t - \Delta t)$  and  $\underline{i}(t - \Delta t)$  are these quantities for the previous time-step.

$$\int_{t-\Delta t}^t \underline{v}(t)dt = \int_{t-\Delta t}^t \frac{d}{dt}([L(t)]\underline{i}(t))dt + \int_{t-\Delta t}^t [R]\underline{i}(t)dt \quad (5.15)$$

$$\begin{aligned} \frac{\Delta t}{2}(\underline{v}(t) + \underline{v}(t - \Delta t)) = \\ [L(t)]\underline{i}(t) - [L(t - \Delta t)]\underline{i}(t - \Delta t) + \frac{\Delta t}{2}[R](\underline{i}(t) + \underline{i}(t - \Delta t)) \end{aligned} \quad (5.16)$$

In [7],[8] this equation was used to express  $\underline{v}(t)$  in terms of other quantities and therefore the discrete equivalent circuit of the machine was developed in the form of voltage sources in series with resistances.

In this thesis, the discrete equivalent circuit of the machine is extracted as a Norton form; which is consistent with the discretized form for elements such as inductors and

capacitors (see Section 2.1), and permits direct application of the nodal analysis method.

In (5.17),  $\underline{i}(t)$ , the resulting winding currents in each time-step are expressed in terms of

voltages across the windings in the same time-step  $\underline{v}(t)$  via a conductance matrix

$[G_{eq}(t)]$  and vector of history terms  $\underline{Ih}$  containing the information from the previous

time-step. This representation is similar to representation of simple inductors [2] for

electromagnetic transients programs as explained in Section 2.1. The difference is that,

the machine inductances are changing with rotor position and level of saturation therefore

the conductances  $[G_{eq}(t)]$  are also changing in each time-step.

$$\underline{i}(t) = [G_{eq}(t)]\underline{v}(t) + \underline{Ih}$$

where:

$$\begin{aligned} [G_{eq}(t)] &= [R_{eq}(t)]^{-1} = \left( \frac{2}{\Delta t} [L(t)] + [R] \right)^{-1} \\ \underline{Ih} &= [G_{eq}(t)] \left( \underline{v}(t - \Delta t) + [R'_{eq}(t - \Delta t)] \underline{i}(t - \Delta t) \right) \\ [R'_{eq}(t - \Delta t)] &= \frac{2}{\Delta t} [L(t - \Delta t)] - [R] \end{aligned} \quad (5.17)$$

In (5.17) the vector  $\underline{v}(t)$  represents the voltages across the machine windings.

Electromagnetic transients programs solve for **node voltages** using **nodal current injections**, and so (5.17) must be expressed by node voltages instead of winding voltages.

Every winding has two nodes so the vectors of voltages and currents of the nodes of the machine are divided into two groups identified by indices 1 and 2. The voltage across a winding is the difference between voltages of nodes 1 and 2 of that winding; and the current of that winding is equal to the current of node 1 and negative of the current of node 2. This relation between node quantities and winding quantities is shown in (5.18).



$$\begin{aligned}\underline{v}_1(t) - \underline{v}_2(t) &= \underline{v}(t) \\ \underline{i}_1(t) &= -\underline{i}_2(t) = \underline{i}(t)\end{aligned}\tag{5.18}$$

Using (5.17) and (5.18) the relation between the node currents and node voltages of the machine in the discretized format is shown in (5.19). In this equation the matrix  $[G_{set}(t)]$  is called the *equivalent admittance matrix* of the machine, and  $\underline{Ih}_s$  is the vector of history terms in nodal form. Note that  $\underline{v}_1(t)$  and  $\underline{v}_2(t)$  are node voltages and not branch voltages; and these nodes are also nodes of the combined machine and external network system.

$$\begin{bmatrix} \underline{i}_1(t) \\ \underline{i}_2(t) \end{bmatrix} = \underbrace{\begin{bmatrix} [G_{eq}(t)] & -[G_{eq}(t)] \\ -[G_{eq}(t)] & [G_{eq}(t)] \end{bmatrix}}_{[G_{set}(t)]} \cdot \begin{bmatrix} \underline{v}_1(t) \\ \underline{v}_2(t) \end{bmatrix} + \underbrace{\begin{bmatrix} \underline{Ih} \\ -\underline{Ih} \end{bmatrix}}_{\underline{Ih}_s}\tag{5.19}$$

Equation (5.19) can be presented in the form of an equivalent circuit with history terms as current sources and  $[G_{set}(t)]$  as a conductance network as shown in Figure 5.8. This circuit is called the *discretized Norton equivalent circuit* of the machine.

The method of incorporating this Norton equivalent circuit into the network solution of electromagnetic transients programs will be shown in the next section.

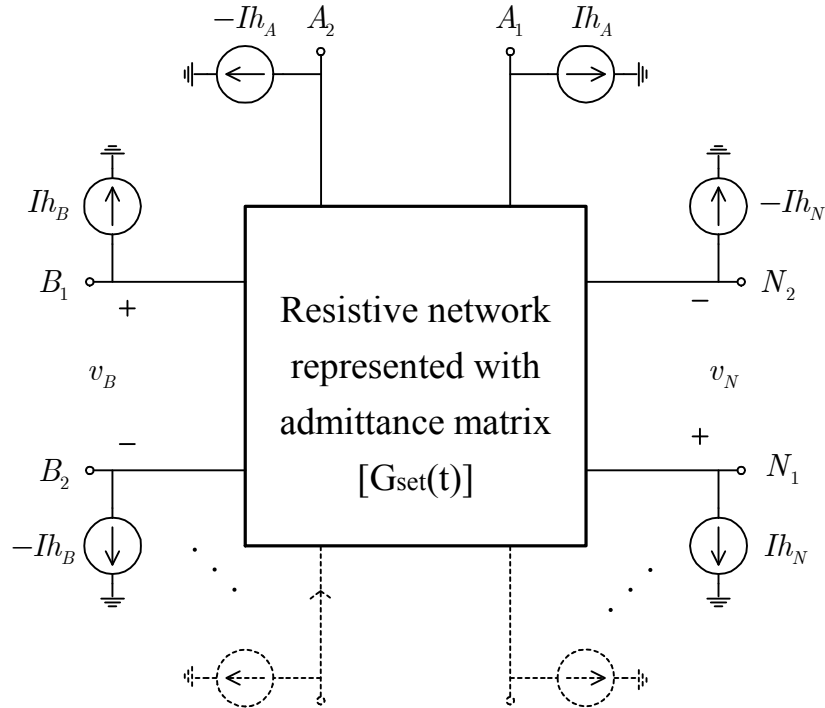


Figure 5.8: Discretized Norton equivalent circuit of the machine

### 5.3.3 Incorporating the Discretized Equivalent Circuit of the Machine in EMTP-Type Programs

It was discussed in Chapter 2 that, off-line (i.e. EMTP, PSCAD/EMTDC) as well as real time electromagnetic transient simulators (i.e. RTDS), use a formulation in which all elements, including dynamic elements such as inductors, capacitors and transmission lines, are converted to an equivalent circuit form consisting only of current sources and resistances [2]. This network representation allows the calculation of network quantities at the end of a time-step with the knowledge of sources and network quantities at the beginning of the time-step. The network history is embedded in the history current source values. The resulting network can be solved by nodal admittance matrix based techniques as shown in (2.7). Equation (2.7) is solved for the unknown voltages using  $LU$  factorization techniques [83]. Once these node voltages are known, all other voltages and

currents can be calculated. By starting with known (or assumed) values at  $t = 0$ , the entire voltage and current history can be determined.

To include the discretized Norton equivalent circuit of the machine (shown in Figure 5.8) into EMTP-type programs, and thus achieve the embedded model of the machine; it is necessary to add the elements of the equivalent admittance matrix of the machine,  $[G_{set}(t)]$ , to the elements of the admittance matrix of the network,  $[Y(t)]$ , at the terminal nodes of the machine as in (5.20)-a. In (5.20)  $p$  and  $q$  identify typical machine terminal nodes. The external network is typically large and has several additional nodes, and its own numbering system. Let the indices  $m$  and  $n$  represent these connection nodes  $p$  and  $q$  in the full network numbering scheme. This process of adding the machine's admittance formulation, shown in (5.19), to that of the external network is referred to as *overlaying*.

Similarly, the history current injection at machine node  $p$   $\underline{Ihs}_p$  must be added to the node injection at the corresponding renumbered node  $m$   $\underline{I}_m$  as shown in (5.20)-b.

$$\begin{aligned}
 [Y(t)]_{m,n} &= [Y(t)]_{m,n} + [G_{set}(t)]_{p,q} & (a) \\
 \underline{I}_m &= \underline{I}_m + \underline{Ihs}_p & (b) \\
 p, q &\in \{1, 2, \dots, 2N\} \\
 N &= \text{number of machine windings}
 \end{aligned}
 \tag{5.20}$$

The network solution equation, (2.7) described earlier, calculates the network voltages  $\underline{V}$ , which now includes the nodes of the embedded machine model, from which the winding voltages  $\underline{v}(t)$  are readily determined. Then, using the first line of (5.17), currents in the machine windings  $\underline{i}(t)$  are determined.

### 5.3.4 Validation Test for the Model of Mutually Coupled Inductances in PSCAD/EMTDC

Unlike the earlier case for the single inductor (Section 5.3.1.1), no easy theoretical solutions are available for validation of a set of time-varying mutually coupled inductances. Hence to validate the model of the set of mutually coupled inductors, the model is compared against a theoretical solution of a circuit with constant mutually coupled inductors (i.e. a multi-winding transformer). This set of mutually coupled inductors is implemented in PSCAD/EMTDC. Figure 5.9 shows a test circuit that is used to verify this model. There are four inductors that are mutually coupled and are connected to four impedances and one voltage source  $v_s = V_m \sin(2\pi \cdot 60 \cdot t)$  as shown in the circuit.

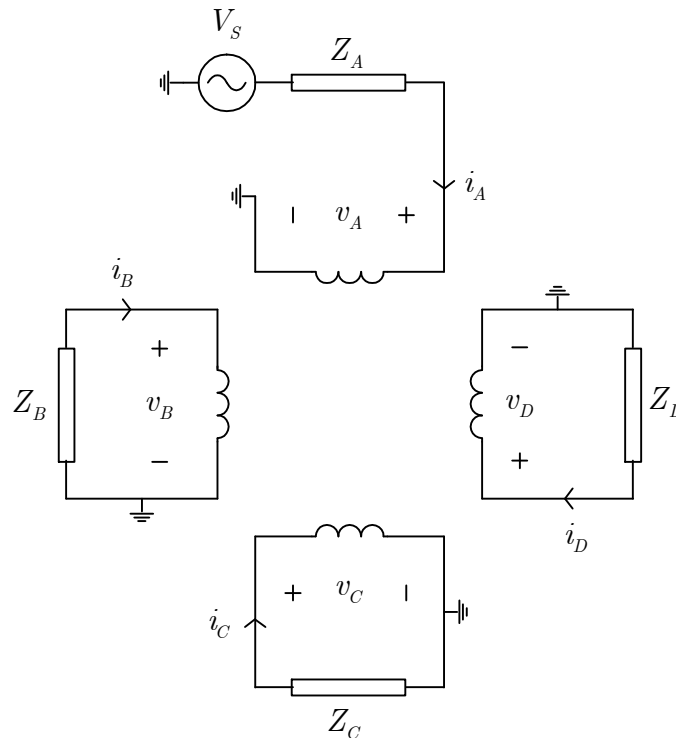


**Figure 5.9:** Test circuit for modeling a set of mutually coupled constant inductors

The phasor solution used for validation is described below. In steady state, the relationship between voltage and current phasors of the inductors considering the inductance matrix is shown by (5.21).

$$\begin{bmatrix} V_A \\ V_B \\ V_C \\ V_D \end{bmatrix} = j\omega \cdot \underbrace{\begin{bmatrix} L_{AA} & L_{AB} & L_{AC} & L_{AD} \\ L_{BA} & L_{BB} & L_{BC} & L_{BD} \\ L_{CA} & L_{CB} & L_{CC} & L_{CD} \\ L_{DA} & L_{DB} & L_{DC} & L_{DD} \end{bmatrix}}_{[X]} \begin{bmatrix} I_A \\ I_B \\ I_C \\ I_D \end{bmatrix} \quad (5.21)$$

Kirchhoff's voltage law (KVL) can also be written for the circuit in Figure 5.9 as shown in (5.22):

$$\begin{bmatrix} V_A \\ V_B \\ V_C \\ V_D \end{bmatrix} + \underbrace{\begin{bmatrix} Z_A & 0 & 0 & 0 \\ 0 & Z_B & 0 & 0 \\ 0 & 0 & Z_C & 0 \\ 0 & 0 & 0 & Z_D \end{bmatrix}}_{[Z]} \begin{bmatrix} I_A \\ I_B \\ I_C \\ I_D \end{bmatrix} = \begin{bmatrix} V_s \\ 0 \\ 0 \\ 0 \end{bmatrix} \quad (5.22)$$

By substituting the voltage vector from (5.21) into (5.22), (5.23) is obtained.

$$\underbrace{([X] + [Z])}_{[Z_{eq}]} \cdot \begin{bmatrix} I_A \\ I_B \\ I_C \\ I_D \end{bmatrix} = \begin{bmatrix} V_s \\ 0 \\ 0 \\ 0 \end{bmatrix} \quad (5.23)$$

And finally the current phasors in the windings are evaluated as shown in (5.24).

$$\begin{bmatrix} I_A \\ I_B \\ I_C \\ I_D \end{bmatrix} = [Z_{eq}]^{-1} \cdot \begin{bmatrix} V_s \\ 0 \\ 0 \\ 0 \end{bmatrix} \quad (5.24)$$

Figure 5.10 shows the comparison between the steady state analytical solution for the currents using (5.24) and the simulation results using PSCAD/EMTDC. At the start of simulation, there is a difference between these two results as expected due to the start-up transients. Once the transient has converged to a steady state, no discernable difference is observed between the results of the theoretical phasor solution and the simulated transient simulation. This validates the accuracy of the embedded approach.

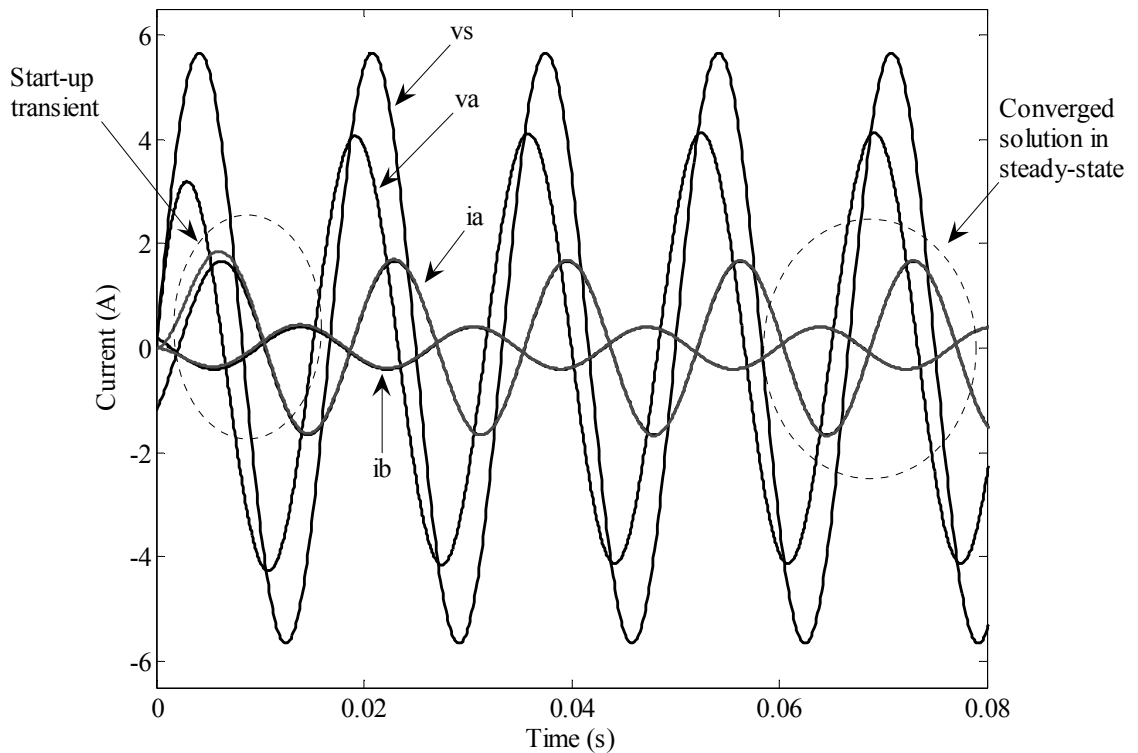


**Figure 5.10:** Comparison of the simulation results with analytical steady state solutions of the test circuit in Figure 5.9

In Section 5.3, the procedure of creating the embedded model of the machine in EMTP-type programs was explained. The method was validated using a single time-varying inductor and a set of mutually coupled constant inductances. In the next section, the technical challenges of implementing the full procedure for the time-varying

inductance matrices of machines in an EMTP-type program, techniques for speeding up the procedure, and special considerations for real-time digital simulations are discussed.

## **5.4 Techniques for Speeding up the Procedure and Special Considerations for Real-Time Implementation of the Embedded Model**

In the course of implementing the embedded model of the machine for EMTP-type programs, a few new techniques are developed in this thesis which speed up the procedure and in some cases are critical for addressing the limited available capacity for computation and communication in real-time digital simulation. These techniques are outlined in this section.

### **5.4.1 Rapid Updating of the Synchronous Machine Inductance Matrix**

The elements of the inductance matrix of the machine change in every time-step as the position of the rotor changes. Moreover as discussed in Section 4.3, if the effects of saturation are considered, the inductance matrix is not only a function of rotor position  $\theta_r$ , but also is a function of the magnetizing currents  $i_{md}$  and  $i_{mq}$ . Hence, the inductance matrix of the machine changes with rotor position and level of saturation, and has to be evaluated and inverted in each time-step. To speed up the updating procedure of the inductance matrix, the following techniques are applied.

#### ***5.4.1.1 Embedded phase-domain machine model with dq0 theory-based inductances; updating the inductance matrix***

Note that, the embedded approach can be used with the dq-based phase-domain model of the machine as well as more sophisticated models such as MWFA-based or FEM-based models discussed in Chapter 3. For dq-based phase-domain models a fast

routine is presented in this section to update the inductance matrix of the machine in every time-step. A more general procedure is proposed in Section 5.4.1.2 which can be applied to MWFA and FEM-based inductances as well.

Equations (3.4)-(3.10) of Section 3.2 can be used to update the phase-domain inductances of a synchronous machine if the dq0 theory is used to analyze the machine. The dq0 parameters of the machine are usually provided by the manufacturer. These dq0 parameters can also be obtained using tests [85]. The abc frame parameters of the inductances ( $L_s, M_s, \dots$ ) can be expressed in terms of dq0 frame parameters ( $L_d, L_q, \dots$ ) as shown in (3.27). The self and mutual inductances of rotor windings are the same in dq0 and abc frame.

Hence, the instantaneous values of the abc frame inductances are obtained by multiplying the inductance coefficients  $L_s, M_s, \dots$  by trigonometric functions of the new rotor position  $\theta_r$ . To consider the effects of saturation in updating the inductance matrix, the saturated values of magnetizing inductances  $L_{md}$  and  $L_{mq}$  must be computed based on the new values of magnetizing currents  $i_{md}$  and  $i_{mq}$ , then the saturated values of the abc frame parameters are evaluated using (3.27). These updated inductance values are used to generate new values of  $[G_{eq}]$  and  $\underline{Ih}$  (shown in (5.17)) for each time-step in the embedded approach.

#### **5.4.1.2 Updating the inductance matrix when the inductances are computed using MWFA or FEM**

It is not realistic to use MWFA or FEM to compute machine inductances in each time-step of an electromagnetic transients program due to the excessive computation



requirements. A workaround is to pre-compute, the inductance values as functions of rotor position and magnetizing currents and store these in a tabular form, amendable to quick look-up during the simulation. However, the size of this table becomes excessively large, particularly when a fine granularity in stored values is desired. For example for even a simple synchronous machine with 3 stator windings and one field winding, each element of the inductance matrix must be tabulated as a function of 4 winding currents and also the rotor position. This requires a 5 dimensional table for each inductance. This problem is critical for real-time simulation as the amount of storage on the simulator's hardware could be limited, and also accessing such a complex table could be time consuming. The approach used in this thesis is based on the recognition that the inductance variation is periodic in  $\theta_r$  and so is expressible as Fourier series. Hence, storing only the most dominant (i.e. lower order) Fourier series coefficients of the inductance functions, as tables of magnetizing currents  $i_{md}$  and  $i_{mq}$  greatly reduces the amount of storage. As shown earlier in Figure 4.7 of Section 4.3, saturation not only changes the magnitude of inductances but also may cause angular displacement in the inductance waveforms in some loading conditions. For any harmonic order, both the Fourier cosine and Fourier sine coefficients are stored as separate tables. This approach guarantees that variations of both the magnitude and angular displacement of the inductances as functions of the d- and q- axis magnetizing currents are properly represented. The real-time simulation implementation, looks-up the appropriate Fourier coefficients in each time-step corresponding to the instantaneous values of  $i_{md}$  and  $i_{mq}$ . These Fourier coefficients are then used to reconstruct the instantaneous inductance values from the known rotor position  $\theta_r$ . By experimentation, the first three Fourier

coefficients are adequate to reconstruct the inductance profile, although it is possible to consider more Fourier coefficients in the reconstruction of inductances.

As the d- and q- axis magnetizing currents are continuous functions of time, their variation within a simulation time-step (a few tens of microseconds) is relatively small. The program therefore calculates saturated inductances from the magnetizing current values in previous time-steps. This is done to avoid iteration as the need to stay in synchronism with a real-world clock puts severe limitations on the number of possible computations in a time-step in real time simulators.

If the effects of operating-point dependent saturation are ignored, the inductances will be only functions of rotor position, and therefore it is possible to store inductances in the forms of arrays [69]. This is useful for example when the details of slots and very high order harmonics are the subject of study and the finite element approach is applied to compute the inductances.

#### 5.4.2 Continuous Inversion of the Matrix $[R_{eq}(t)]$

One of the constraints of models in real-time simulation is that only a limited number of algebraic operations can be executed in each time-step due to the requirement of keeping in synchronism with a real world clock. Therefore a considerable amount of effort must be made to limit the number of operations in the routine. As shown in (5.17), the discretization of machine equations requires the inversion of matrix

$[R_{eq}(t)] = (\frac{2}{\Delta t}[L(t)] + [R])$  in every time-step. This matrix inversion is perhaps the most time-consuming part of the mathematical operation which is executed on the simulator's hardware. Generally there is no analytical formula for the inverse of this matrix.

Therefore, the matrix  $[R_{eq}(t)]$  must be numerically inverted in each time-step. In this thesis, the numerically-efficient Cholesky decomposition routine [83], [84] is implemented in real-time for this purpose. This routine is used to factorize the matrix  $[R_{eq}]$ , and then the equation  $[R_{eq}] \cdot \underline{x}_i = \underline{b}_i$ ,  $i = 1 \dots N$  is solved, where each  $\underline{b}_i$  is the  $i^{th}$  column of the unity matrix. The resulting  $\underline{x}_i$  is the  $i^{th}$  column of the matrix  $[R_{eq}]^{-1}$ .

A necessary condition for using the Cholesky decomposition routine is that matrix  $[R_{eq}(t)]$  must be positive definite and symmetric. This condition is satisfied for the inductance matrices of electric machines as shown below:

It is shown that for every set of mutually coupled inductors, even for nonlinear systems, mutual inductances between any two windings  $\alpha$  and  $\beta$  follow the reciprocity theorem (i.e.  $L_{\alpha\beta} = L_{\beta\alpha}$ ) [86]. Therefore, the machine inductance matrix  $[L(t)]$  and consequently  $[R_{eq}(t)]$  are symmetric matrices.

Further, according to definition [83], a matrix  $[A]$  is positive definite if  $(\underline{x}^T \cdot [A] \cdot \underline{x}) > 0$  for every non-zero vector  $\underline{x}$ . This definition applies to a set of mutually coupled inductances with the inductance matrix  $[L]$  as the stored energy in the set can be expressed as  $E_{stored} = \frac{1}{2}(\underline{i}^T \cdot [L] \cdot \underline{i})$ , where  $\underline{i}$  is the vector of arbitrary branch currents in the set of mutually coupled inductances. The stored energy in a natural inductance system is always positive therefore the inductance matrix  $[L]$  for this system is always positive definite. Simple algebraic operation shows that if  $[L]$  is positive definite then  $[R_{eq}]$  is also positive definite as  $[R]$  is a diagonal matrix with positive elements.

### 5.4.2.1 Analytical inversion of $[R_{eq}(t)]$ when the phase-domain inductance matrix is extracted using dq0 theory

There is no general analytical formula for the inverse of the general inductance matrix of a machine as the inductances of the machine contain various space harmonics.

However, if the phase-domain inductances of the machine are directly extracted from the inductance matrix in dq0 frame, then there will be an analytical inversion for the phase-domain inductance matrix as will be shown in this section. ***This analytical inversion is one of the contributions of this thesis.*** It should be noted that, this can only be done for cases where a dq-based model is adequate, and does not apply when more complex MWFA or FEM generated inductances are used. Analytical inversion of the machine inductance matrix can significantly reduce the number of operations in each time-step.

Recalling (3.13), the relation between the inductance matrix in abc and dq0 frame is:

$$[L_{abc-frame}] = T^{-1} \cdot [L_{dq-frame}] \cdot T \quad (5.25)$$

The resistance matrices in abc and dq0 frames are diagonal and equal:

$$[R_{abc-frame}] = T^{-1} \cdot [R_{dq-frame}] \cdot T = [R_{dq-frame}] \quad (5.26)$$

The matrix  $[R_{eq}]$  in (5.17) now can be expressed as shown in (5.27)

$$\begin{aligned} [R_{eq}] &= \frac{2}{\Delta t} [L_{abc-frame}] + [R_{abc-frame}] \\ &= T^{-1} \cdot \frac{2}{\Delta t} [L_{dq-frame}] \cdot T + T^{-1} \cdot [R_{dq-frame}] \cdot T \\ &= T^{-1} \cdot \left( \frac{2}{\Delta t} [L_{dq-frame}] + [R_{dq-frame}] \right) \cdot T \end{aligned} \quad (5.27)$$

The inverse of the matrix  $[R_{eq}(t)]$  can be calculated as:

$$\begin{aligned}
[R_{eq}]^{-1} &= T^{-1} \cdot \left( \frac{2}{\Delta t} [L_{dq\_frame}] + [R_{dq\_frame}] \right)^{-1} \cdot T \\
&= \frac{\Delta t}{2} \cdot T^{-1} \cdot \left( [L_{dq\_frame}] + \frac{\Delta t}{2} [R_{dq\_frame}] \right)^{-1} \cdot T
\end{aligned} \tag{5.28}$$

The matrices  $[L_{dq\_frame}]$  and  $[R_{dq\_frame}]$  do not change with rotor position. Therefore the matrix  $[L_{dq\_frame}] + \frac{\Delta t}{2} [R_{dq\_frame}]$  can be inverted and stored before the time-domain simulation starts, and the inverse of the matrix  $[R_{eq}]$  can be evaluated using (5.28) in each time-step.

This problem can be simplified even further by expanding  $[L_{dq\_frame}] + \frac{\Delta t}{2} [R_{dq\_frame}]$  as shown in (5.29). In (5.29),  $[L_{dq\_frame}]$  is the dq0 frame block diagonal inductance matrix introduced in (3.21).

$$\begin{aligned}
& \left[ L_{dq\_frame} \right] + \frac{\Delta t}{2} \left[ R_{dq\_frame} \right] = \\
& \begin{pmatrix} L_d & kM_F & kM_D & 0 & 0 & 0 \\ kM_F & L_F & M_R & 0 & 0 & 0 \\ kM_D & M_R & L_D & 0 & 0 & 0 \\ 0 & 0 & 0 & L_q & kM_Q & 0 \\ 0 & 0 & 0 & kM_Q & L_Q & 0 \\ 0 & 0 & 0 & 0 & 0 & L_0 \end{pmatrix} + \frac{\Delta t}{2} \begin{pmatrix} r_s & 0 & 0 & 0 & 0 & 0 \\ 0 & r_F & 0 & 0 & 0 & 0 \\ 0 & 0 & r_D & 0 & 0 & 0 \\ 0 & 0 & 0 & r_s & 0 & 0 \\ 0 & 0 & 0 & 0 & r_Q & 0 \\ 0 & 0 & 0 & 0 & 0 & r_s \end{pmatrix} = \\
& \underbrace{\begin{pmatrix} L'_d & kM_F & kM_D & 0 & 0 & 0 \\ kM_F & L'_F & M_R & 0 & 0 & 0 \\ kM_D & M_R & L'_D & 0 & 0 & 0 \\ 0 & 0 & 0 & L'_q & kM_Q & 0 \\ 0 & 0 & 0 & kM_Q & L'_Q & 0 \\ 0 & 0 & 0 & 0 & 0 & L'_0 \end{pmatrix}}_{[L'_{dq\_frame}]} \quad \text{where} \quad \begin{cases} L'_d = L_d + \frac{\Delta t}{2} r_s \\ L'_F = L_F + \frac{\Delta t}{2} r_F \\ L'_D = L_D + \frac{\Delta t}{2} r_D \\ L'_q = L_q + \frac{\Delta t}{2} r_s \\ L'_Q = L_Q + \frac{\Delta t}{2} r_Q \\ L'_0 = L_0 + \frac{\Delta t}{2} r_s \end{cases} \tag{5.29}
\end{aligned}$$

In (5.29), the matrix  $[L'_{dq\_frame}]$  is a block matrix which can be inverted in the form of another block matrix as shown in (5.30)-(5.31).

$$[L'_{dq\_frame}]^{-1} = [B_{dq\_frame}] = \begin{pmatrix} B_d & B_{dF} & B_{dD} & 0 & 0 & 0 \\ B_{dF} & B_F & B_{FD} & 0 & 0 & 0 \\ B_{dD} & B_{FD} & B_D & 0 & 0 & 0 \\ 0 & 0 & 0 & B_q & B_{qQ} & 0 \\ 0 & 0 & 0 & B_{qQ} & B_Q & 0 \\ 0 & 0 & 0 & 0 & 0 & B_0 \end{pmatrix} \quad (5.30)$$

where:

$$\begin{bmatrix} B_d & B_{dF} & B_{dD} \\ B_{dF} & B_F & B_{FD} \\ B_{dD} & B_{FD} & B_D \end{bmatrix} = \begin{bmatrix} L'_d & kM_F & kM_D \\ kM_F & L'_F & M_R \\ kM_D & M_R & L'_D \end{bmatrix}^{-1} \quad (5.31)$$

$$\begin{bmatrix} B_q & B_{qQ} \\ B_{qQ} & B_Q \end{bmatrix} = \begin{bmatrix} L'_q & kM_Q \\ kM_Q & L'_Q \end{bmatrix}^{-1}, \quad B_0 = L'_0^{-1}$$

The structure of  $[B_{dq\_frame}]$  in (5.30) is identical to that of  $[L_{dq\_frame}]$  in (5.29). When  $[B_{dq\_frame}]$  is transformed to phase (abc-frame) quantities, the resultant expressions must be analogous to (3.4)-to-(3.10) applicable to  $[L_{dq\_frame}]$ , as given by (5.32)-(5.37).

Analogous to (3.27), the coefficients  $B_s, B_m, P_s, P_F, P_D$  and  $P_Q$  in (5.32)-(5.37) are given by (5.38). For stator self elements:

$$\begin{aligned} B_{aa}(\theta_r) &= B_s + B_m \cos 2(\theta_r) \\ B_{bb}(\theta_r) &= B_s + B_m \cos 2\left(\theta_r - \frac{2\pi}{3}\right) \\ B_{cc}(\theta_r) &= B_s + B_m \cos 2\left(\theta_r + \frac{2\pi}{3}\right) \end{aligned} \quad (5.32)$$

For stator mutual elements:

$$\begin{aligned}
 B_{ab}(\theta_r) &= B_{ba}(\theta_r) = -P_s - B_m \cos 2\left(\theta_r + \frac{\pi}{6}\right) \\
 B_{bc}(\theta_r) &= B_{cb}(\theta_r) = -P_s - B_m \cos 2\left(\theta_r - \frac{\pi}{2}\right) \\
 B_{ca}(\theta_r) &= B_{ac}(\theta_r) = -P_s - B_m \cos 2\left(\theta_r + \frac{5\pi}{6}\right)
 \end{aligned} \tag{5.33}$$

For mutual elements between stator and rotor:

$$\begin{aligned}
 B_{aF}(\theta_r) &= B_{Fa}(\theta_r) = P_F \cos(\theta_r) \\
 B_{bF}(\theta_r) &= B_{Fb}(\theta_r) = P_F \cos\left(\theta_r - \frac{2\pi}{3}\right) \\
 B_{cF}(\theta_r) &= B_{Fc}(\theta_r) = P_F \cos\left(\theta_r - \frac{4\pi}{3}\right)
 \end{aligned} \tag{5.34}$$

$$\begin{aligned}
 B_{aD}(\theta_r) &= B_{Da}(\theta_r) = P_D \cos(\theta_r) \\
 B_{bD}(\theta_r) &= B_{Db}(\theta_r) = P_D \cos\left(\theta_r - \frac{2\pi}{3}\right) \\
 B_{cD}(\theta_r) &= B_{Dc}(\theta_r) = P_D \cos\left(\theta_r - \frac{4\pi}{3}\right)
 \end{aligned} \tag{5.35}$$

$$\begin{aligned}
 B_{aQ}(\theta_r) &= B_{Qa}(\theta_r) = P_Q \sin(\theta_r) \\
 B_{bQ}(\theta_r) &= B_{Qb}(\theta_r) = P_Q \sin\left(\theta_r - \frac{2\pi}{3}\right) \\
 B_{cQ}(\theta_r) &= B_{Qc}(\theta_r) = P_Q \sin\left(\theta_r - \frac{4\pi}{3}\right)
 \end{aligned} \tag{5.36}$$

Finally for rotor elements:

$$\begin{aligned}
 B_{FF}(\theta_r) &= B_F & B_{DD}(\theta_r) &= B_D & B_{QQ}(\theta_r) &= B_Q \\
 B_{FD}(\theta_r) &= B_{DF}(\theta_r) & & & & \\
 B_{FQ}(\theta_r) &= B_{QF}(\theta_r) & B_{DQ}(\theta_r) &= B_{QD}(\theta_r) & & = 0
 \end{aligned} \tag{5.37}$$

$$\begin{aligned}
B_s &= \frac{1}{3}(B_0 + B_d + B_q) & B_m &= \frac{1}{3}(B_d - B_q) \\
P_s &= -\frac{1}{3}\left(-\frac{B_d + B_q}{2} + B_0\right) & P_F &= \sqrt{\frac{2}{3}}B_{dF} \\
P_D &= \sqrt{\frac{2}{3}}B_{dD} & P_Q &= \sqrt{\frac{2}{3}}B_{qQ}
\end{aligned} \tag{5.38}$$

Using (5.32) to (5.37) the number of operations needed to invert the inductance matrix of a machine can be reduced significantly. This is because the factors  $B_s$ ,  $B_m$ ,  $P_s$ ,  $P_F$ ,  $P_D$  and  $P_Q$  do not vary with rotor position, and the elements of the matrix  $[B_{abc-frame}]$  can be generated merely by multiplying these factors and appropriate trigonometric functions of the rotor position.

It should be noted that, if saturation is modeled,  $[L'_{dq-frame}]$ , though not a function of rotor position, it is a function of magnetizing currents, and could require repeated inversion if the saturation state of the machine changes. This matrix inversion is required even if the machine is modeled directly in dq0 domain. As this matrix has block structure this inversion process is not computationally expensive.

### 5.4.3 Amortisseur Winding Representation in Real-Time Machine Modeling

The damper grid of a synchronous machines consists of damper bars brazed to the copper segments at the end of each pole [71]. Conventionally the damper grid is modeled as equivalent windings along the d-axis and q-axis only [30], [31], [87], [88]. Multiple windings on the d- or q-axis are used to incorporate deep bar and solid rotor effects [89].

Increasing the complexity of the model brings it closer to the computational limit for real-time implementation. Further, the computational complexity increases enormously if the damper grid with individual damper bars are modeled [56], [67]. Hence, in order to achieve real-time computing speeds with a time-step in the order of 20 $\mu$ s-50 $\mu$ s, the



phase-domain machine model in this thesis represents the damper grid in the conventional manner with d- and q-axis amortisseur windings. This is even the case, when the MWFA is used in computing machine inductances. For the small experimental machine in this thesis, only one damper winding in each axis was required to achieve the desired accuracy. The field-test comparison in Chapter 6 validates this simplification. For machines with a solid rotor or deep bars [89] the model has been dimensioned to accommodate inclusion of up to two additional windings for each axis. For a simulation in real-time with the time-step of  $50\mu\text{s}$ , the total number of machine windings is limited to ten windings. This damper windings representation is also used for simulating turn-turn faults. The accuracy of this assumption is discussed further in Chapter 6.

#### 5.4.4 Technical Consideration for Overlaying the Equivalent Admittance Matrix of the Machine $[G_{set}(t)]$ onto the Admittance Matrix of the Main Network Solution

It was discussed in Section 5.3.3 that to achieve the embedded model of the machine, it is necessary to add the elements of  $[G_{set}(t)]$ , the equivalent admittance matrix of the machine, to the elements of admittance matrix of the network  $[Y(t)]$  at the terminal nodes of the machine. This process was referred to as *overlaying*.

For a machine with 6 windings ( 3 stator, 1 field , and 2 dampers) the equivalent admittance matrix  $[G_{set}(t)]$  will be a  $12 \times 12$  matrix. Note that the network solution and solution of machine equations (including calculation of  $[G_{set}(t)]$ ) are carried out on separate processor cards of RTDS hardware. To overlay  $[G_{set}(t)]$  onto the network admittance matrix  $[Y(t)]$ , elements of  $[G_{set}(t)]$  must be passed over a communication conduit to the network solution processor. It takes approximately  $60ns$  for each of these

elements to be passed over this communication channel [26]. It would be theoretically possible to transfer all the elements of the admittance matrix  $[G_{set}(t)]$  of dimensions  $12 \times 12$  to the network solution in each time-step. However, if too much information is transferred, the real-time nature of the solution would be in jeopardy due to the time required for the transfers.

Generally, the windings of a synchronous machine are connected in a particular manner. For example, as shown in Figure 5.11, the laboratory machine has a Y-connected stator and short-circuited d- and q-axis damper windings. Rather than bringing all 12 nodes out to the external network solution, only the resulting connection points (i.e.  $A1$ ,  $B1$ ,  $C1$ ,  $N$ ,  $F1$ , and  $F2$ ) need to be connected to the external network. This, results in a  $6 \times 6$   $[G'_{set}(t)]$  matrix derived from the original  $12 \times 12$  matrix  $[G_{set}(t)]$  to be overlaid. The rows and columns of  $[G_{set}(t)]$  corresponding to the grounded nodes  $D1$ ,  $D2$ ,  $Q1$  and  $Q2$  are eliminated. To form the corresponding elements of the neutral node  $N$ , rows and columns corresponding to the nodes  $A2$ ,  $B2$  and  $C2$  are added together to form a single row and a single column [9]. Figure 5.12 shows the procedure of deriving  $[G'_{set}(t)]$  from the original  $12 \times 12$  matrix  $[G_{set}(t)]$ .

The number of conductance values to be transmitted reduces from 66 (for the  $12 \times 12$  matrix) to 15 (for the  $6 \times 6$  matrix). Note that, because the conductance matrices are symmetric and the sum of the elements in each row is equal to zero, only the upper diagonal elements need to be transferred.

It is obvious that the history current injection for node  $N$  will be the sum of current injections for nodes  $A2$ ,  $B2$  and  $C2$ .

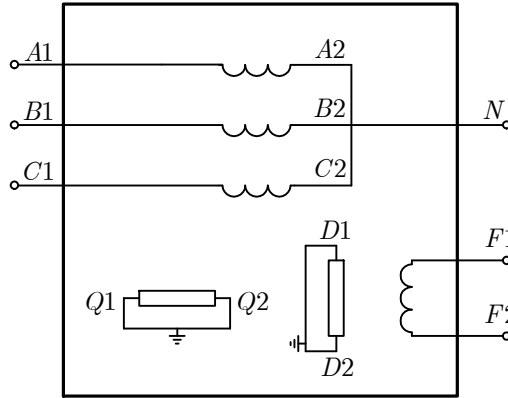


**Figure 5.11:** Connection of winding nodes in an embedded model of a synchronous machine in electromagnetic transients programs

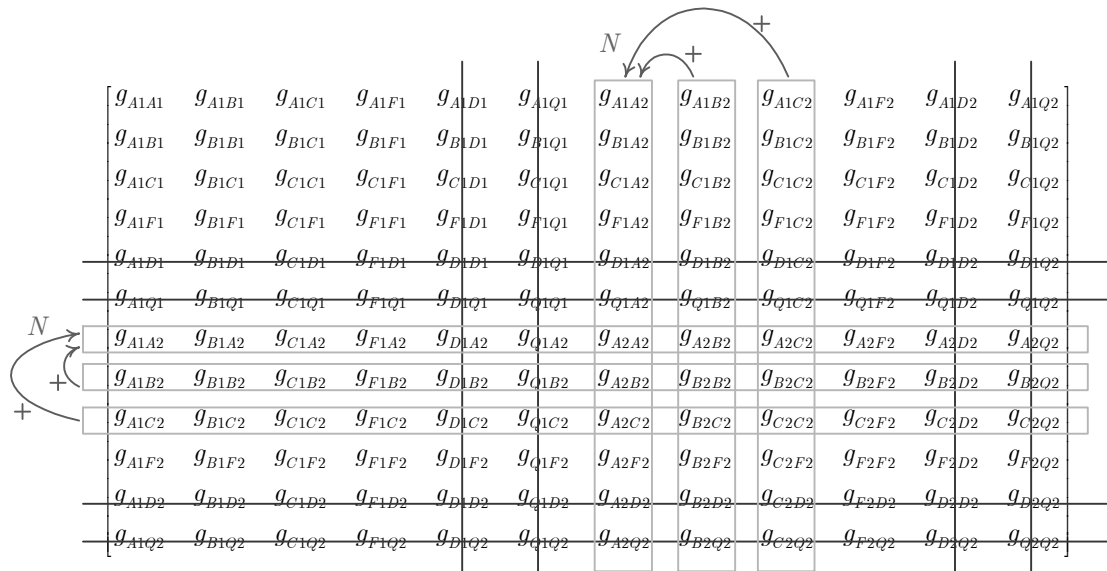


**Figure 5.12:** Treatment of the equivalent admittance matrix of the machine for the node connection in Figure 5.11

Figure 5.13 shows the detailed procedural steps for implementing the real-time routine for the embedded approach of modeling machines.

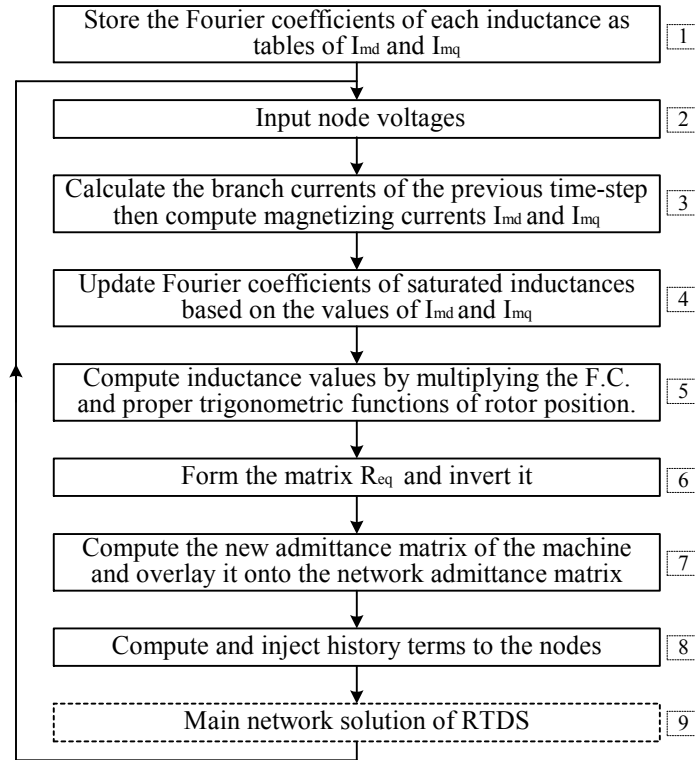


Figure 5.13: Procedure for incorporating the embedded machine model into the network solution of RTDS

## 5.5 Electric Torque Calculation in ABC and DQ0 Frames and Interfacing External Mechanical and Control Systems

Electrical torque in synchronous machines must be calculated to observe the effects of the network on the rotor speed. The general equation for the torque is the rate of change of co-energy  $T_e = \frac{\partial}{\partial \theta} W_m'(\theta_r, \underline{i})$  (see Appendix C). For the non-saturated conditions, (5.39) is a direct representation of this formula and therefore is an accurate expression for the torque [92], [93]. In this thesis, this equation is used for calculating the electric torque in the phase-domain machine model. In (5.39),  $[L(\theta_r, \underline{i})]$  is the inductance

matrix in abc coordinates calculated in (4.8), and the derivative is calculated by taking differences of the quantities in the present and previous time-steps.

$$T_e(t) = \frac{1}{2} \underline{i}(t)^T \frac{\partial}{\partial \theta} [L(\theta_r, \underline{i})] \underline{i}(t)$$

where:

$$\frac{\partial}{\partial \theta} [L(\theta_r, \underline{i})] \approx \frac{[L(\theta_r(t), \underline{i}(t))] - [L(\theta_r(t - \Delta t), \underline{i}(t - \Delta t))]}{\theta_r(t) - \theta_r(t - \Delta t)}$$
(5.39)

As  $\underline{i}(t)$  is the instantaneous current and  $[L(\theta_r, \underline{i})]$  includes space harmonics, (5.39) accurately models torque components due to time harmonics in currents and winding space harmonics. Also, as discussed in Section 4.3,  $[L(\theta_r, \underline{i})]$  is the matrix of saturated inductances. Hence (5.39) is also affected by saturation, and therefore torque components due to saturation and saturation related harmonics do appear in this formulation. However, their values are not entirely accurate as (5.39) is mathematically derived from the rate of change of co-energy in linear conditions. Nevertheless, due to the constraint of real-time simulation, the calculation has to be completed in the time-step used, which is typically  $20\mu s$ -  $50\mu s$ , and therefore any errors resulting from this partial treatment of saturation-related torque are neglected.

Equation (5.40) is used to calculate the electric torque in the dq-based synchronous machine models. This expression is equivalent to the one in (5.39) for synchronous machines with sinusoidal distribution of the windings and permeance, i.e. if the inductances are in the form of (3.4)-(3.10) (see Appendix C). Equation (5.40) is widely used to calculate the electric torque in dq based synchronous machine models in electromagnetic transients programs [5], [11], [75].

$$T_e = \Psi_q i_d - \Psi_d i_q$$
(5.40)

The electrical coupled-inductance based model of the machine is directly embedded within the main network solution of the RTDS, i.e., it is similar to any other resistor or transformer in the network, the difference is that its parameters change with time. However, additional state variable based models such as multi-mass inertia and governor are interfaced via electrical torque, and mechanical speed to the main network solution [5] [11], as shown in Figure 5.14.

The mechanical equations are solved external to the electrical solution. Torque calculated from the electrical model (i.e. (5.39) for phase domain models and (5.40) for dq0 models) is fed as an input to the state-variable model of the mechanical system. One of the state-variables of the mass-inertia model is the rotor angle which is fed to the electrical model as an input. The rotor angle  $\theta_r$  is required for updating the values of the inductance matrix elements. Note that, this approach introduces a one time-step delay [11], because the latest values available to the electric and mechanical models respectively were calculated in previous time-steps. However, as the time constants associated with the mechanical models are very large, this error is not important.

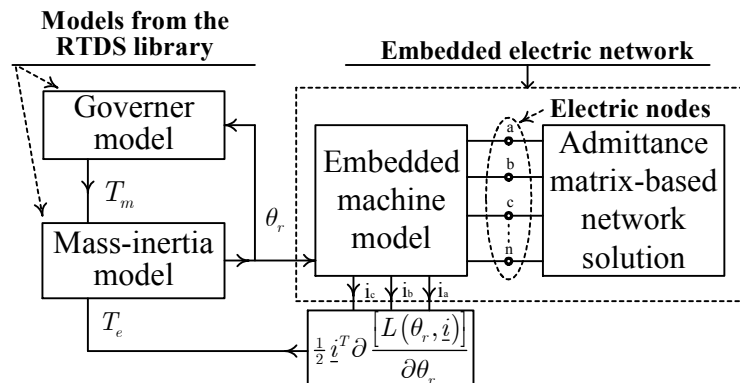


Figure 5.14: Interfacing control and mechanical systems to the main network solution

## 5.6 Chapter Contributions and Conclusions

The conventional *interfaced-based* approach of modeling electric machines for electromagnetic transients programs was briefly introduced in this chapter. In addition, methods of *integrating* differential equations of machines, and techniques of *projecting* node voltages were discussed.

The procedure of developing the new *embedded phase-domain machine model* was explained in detail. Special techniques were established to *speed up* the time-domain simulation of the model, and *special considerations* were introduced for the *real-time* implementation of this model.

The following chapter will discuss validation of the developed model through comparison with other simulation approaches and laboratory experiments.

# Chapter 6: Validation of the New Embedded Phase-Domain Machine Model

---

The new embedded phase-domain machine model has been implemented in both EMTDC and RTDS using the procedure explained in Chapter 5. In this chapter, the model is validated through comparison with other simulation approaches and laboratory experiments. The numerical stability of the model is also assessed in this chapter.

## 6.1 Embedded Phase-Domain Models Algebraically Equivalent to Dq0 Models

In this section, the inductances of the synchronous machines under study are computed using the dq0 theory as functions of rotor position as discussed in Section 5.4.1.1. The time-domain simulation results of the new embedded phase-domain model for these machines are compared against the results of the conventional dq-based interfaced model from the RSCAD library. Since these two models both use dq0 theory, they are *algebraically equivalent*, and theoretically must show identical results in time-domain simulation. Hence, comparing their results helps in validating the capability of the new phase-domain model in accurately solving differential equations of machines<sup>1</sup>. Note that, the dq0-based models of synchronous machines are widely used and their performance in fundamental frequency steady state and transient situations are validated [15],[16],[30],[33],[88]. The model in the RSCAD library is a standard dq0-based model in electromagnetic transients programs and it has already been validated [11].

---

<sup>1</sup> Note that the phase-domain approach used in this thesis is primarily intended for non-sinusoidally distributed windings and arbitrary geometry, which cannot be handled in a dq-based model.



### 6.1.1 Modeling a Synchronous Machine Based on the Data in Dq Frame

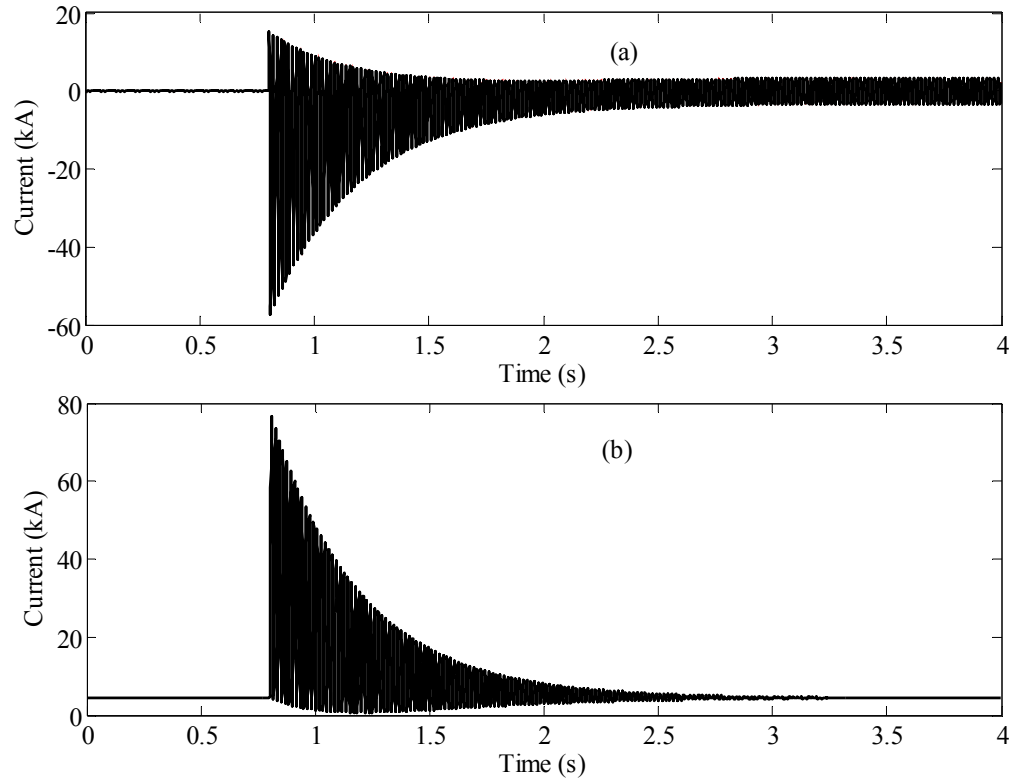
The synchronous machine data shown in Table 6.1 is taken from [90], and initially is used in a benchmark model for the study of subsynchronous resonance. It belongs to a 60 Hz, 100 MVA, 13.8 kV, 3 phase synchronous machine. This data is used to simulate the synchronous machine using both the dq-based interfaced model from the RSCAD library and the new embedded phase domain model in the RTDS environment. For the purpose of simplicity, damper windings and effects of saturation are not included in this example as the purpose is only to establish the mathematical equivalence of the proposed approach with the conventional approach.

TABLE 6.1: THE DQ PARAMETERS OF THE SIMULATED SYNCHRONOUS MACHINE

Parameter	Value		
Voltage base value = Rated line-neutral RMS voltage	7.97	(kV)	
Power base value = Rated MVA	100	(MVA)	
Current base value = Rated stator RMS current	4184	(A)	
Excitation voltage	1	(norm)	
D-axis inductance	1.79	(pu)	9.04 (mH)
Q-axis inductance	1.71	(pu)	8.37 (mH)
Zero sequence inductance	0.13	(pu)	0.66 (mH)
Field inductance	1.722	(pu)	8.70 (mH)
Stator leakage inductance	0.13	(pu)	0.13 (mH)
Stator resistance	0.002	(pu)	3.81 (mΩ)
Field resistance	0.001407	(pu)	2.70 (mΩ)

During the real-time simulation, the machine is operating in open-circuit and its field voltages is adjusted such that the terminal voltage of 1 pu is achieved (1 norm field voltage). The simulation time-step is 50 micro-seconds. After reaching steady state conditions, a sudden three phase short-circuit is applied to the terminals of the machine. Variations of stator phase A current and the field current of the machine during the short circuit is shown in Figure 6.1a and Figure 6.1b respectively. In each figure there are two curves, one corresponding to the new embedded phase domain model and the other to the

model from the RSCAD library. Figure 6.2 shows the stator phase A currents of both models for the first ten cycles of the short circuit facilitating a better comparison between the two signals.



**Figure 6.1:** Short circuit currents in windings of the two synchronous machine models: a) stator phase A, b) field winding

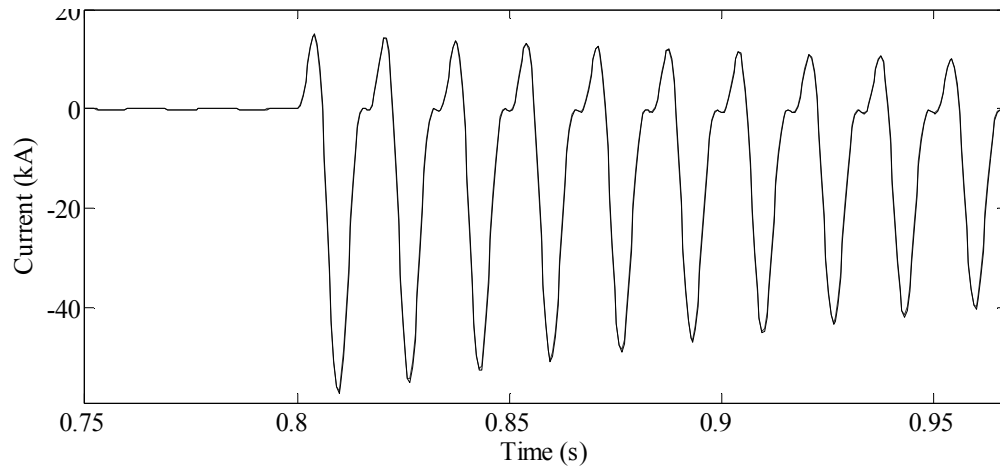


**Figure 6.2:** First ten cycles of the short circuit currents in stator phase A of the two synchronous machine models (curves are overlapping and indistinguishable.)

As shown, the two curves are indistinguishable, establishing the fact that the phase domain machine model is equivalent to the dq-based model when sinusoidal distribution is assumed for the windings and permeance.

### 6.1.2 Incorporation of Saturation in the Dq-equivalent Embedded Phase Domain Approach

The dq-based synchronous machine model from the RSCAD library, incorporates saturation effects only on the d-axis, i.e.  $L_{md}$  varies with the change in the value of the d-axis magnetizing current [26]. Although inclusion of more points for accurate modeling of the saturation curve is feasible, for the purpose of simplicity, the saturation curve is approximated by only two straight line segments as shown in Figure 6.3.

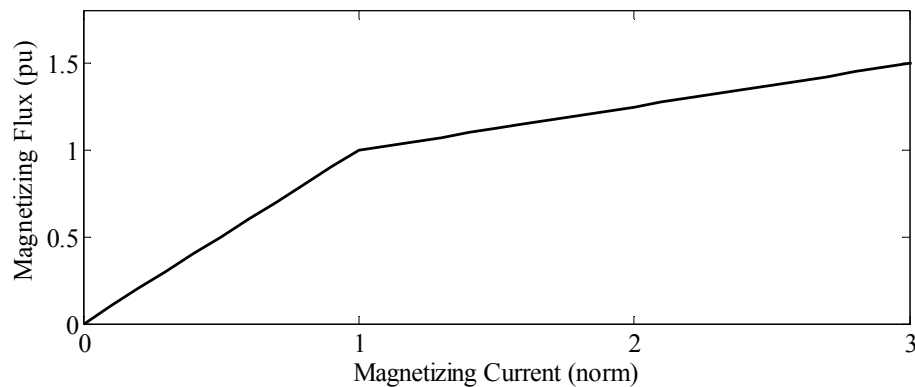


**Figure 6.3:** Assumed saturation characteristics of the synchronous machine under study

Again the purpose for this simplified representation is to validate the mathematical approach by comparing it with earlier established approaches. As discussed in Section 4.3, the complete developed model in this thesis uses the MWFA-based advanced treatment of saturation based on the actual distribution of magnetomotive force. This detailed representation will be validated later Section 6.2.

To incorporate the effects of saturation in the dq-equivalent phase-domain machine model, the saturated phase-domain inductances of the synchronous machine are calculated based on the saturated values of  $L_{md}$  and  $L_{mq}$ , in every time-step, using on the method discussed in Section 5.4.1.1.

In the time-domain simulation, both synchronous machine models (data in Table 6.1) are connected to identical 3 phase 13.8 kV voltage sources. The field voltage for both models is adjusted to  $0.5 E_{fd0}$  (where  $E_{fd0}$  is the field voltage required for 1 pu terminal voltage in open circuit). During a manual transient, the field voltage increased from  $0.5 E_{fd0}$  to  $2.5 E_{fd0}$ . This increase in the field voltage changes the total magnetizing MMF in the d-axis and consequently changes the level of saturation in the machines. The simulation results are shown in Figure 6.4.

Figure 6.4-a and 6.4-b, respectively, show the variation of stator phase A current and the field current in both models. The waveforms show that the two models are in a very good agreement and saturation has been implemented properly. Figure 6.4-c shows the variation in the d-axis magnetization inductance  $L_{md}$  during this transient.

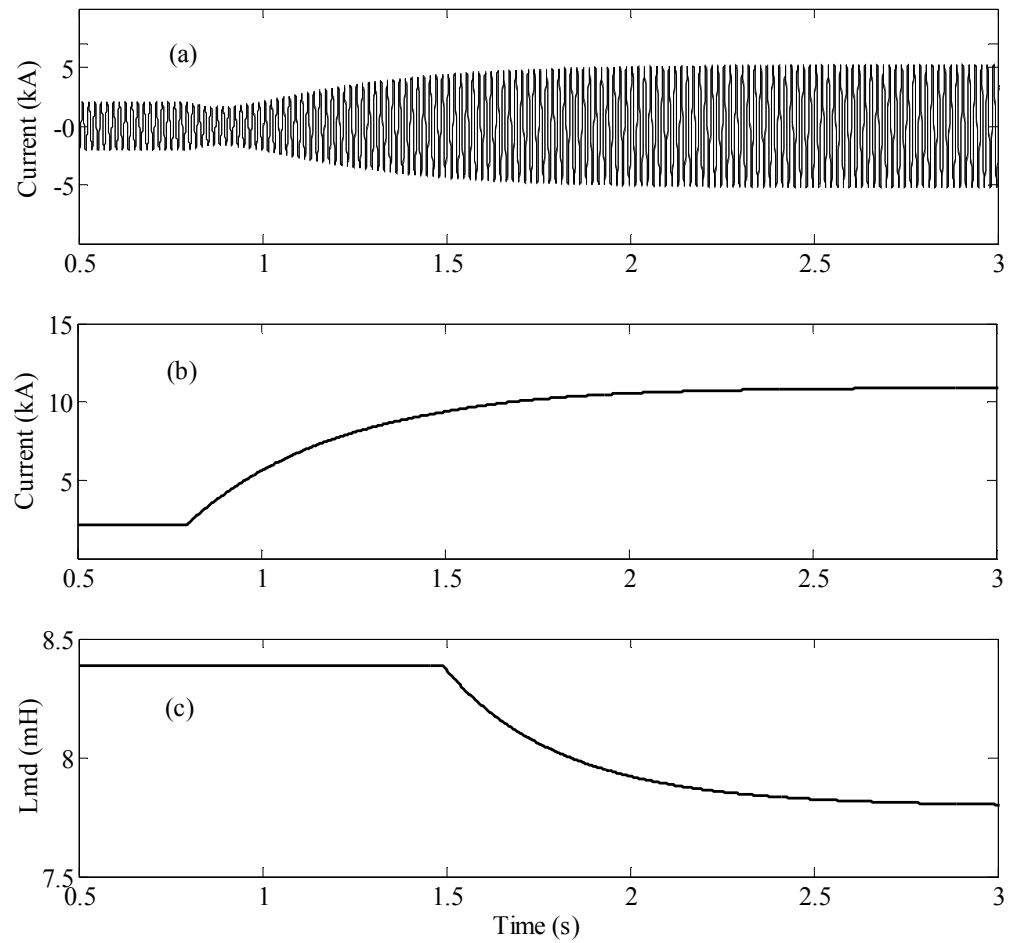


**Figure 6.4:** Transient behaviour of the synchronous machines during a step-increase in the field voltage, a) Phase A currents of the machines, b) Currents of the field windings c) Variation of d-axis magnetization inductance  $L_{md}$  with time (curves are indistinguishable).

### 6.1.3 Modeling a Permanent Magnet Synchronous Machine

The second example of modeling synchronous machines based on the dq0 theory is developed for a permanent magnet synchronous machine (PMSM). This section is a detour in the main flow of this work. Its purpose is to show that the proposed embedded approach can be used with other types of machines. Also, this PMSM model is used in Section 6.1.4 for comparing the numerical stability of different approaches. The reader may skip this section and review it independently at a later time.

The dq0 equivalent circuit of a permanent magnet machine is shown in Figure 3.7. As mentioned in Chapter 3, this equivalent circuit is very similar to that of a synchronous machine. Table 6.2 shows the dq parameters of the 3-phase 208 V, 6 kW PMSM under study [27]. The per-unit system used here is explained in Section 3.1.

TABLE 6.2: THE DQ PARAMETERS OF THE SIMULATED PMSM

Parameter	Symbol	Value	
Rated line-neutral RMS voltage = Voltage base value	$V_{ll\_rms}$	120.09 (V)	
Rated stator RMS current = Current base value	$I_{l\_rms}$	16.7 (A)	
Rated power	$P_{rated}$	6016 (W)	
D-axis inductance	$L_d$	0.249 (pu)	4.76 (mH)
Q-axis inductance	$L_q$	0.249 (pu)	4.76 (mH)
Stator leakage inductance	$l_s$	0.109 (pu)	2.09 (mH)
Stator resistance	$r_s$	0.059 (pu)	0.423 (Ohm)
Magnet resistance	$R_m$	1.94 (pu)	13.92 (Ohm)
Equivalent magnet current	$i_m$	5.47 (pu)	91.35 (A)

Using the dq parameters of Table 6.2 and based on the procedure discussed in Section 5.4.1.1 the phase-domain inductances of the PMSM are computed and an embedded phase-domain model for this PMSM is developed. Based on the conventional approach of modeling machines, discussed in Section 5.2, an interfaced-based model for this PMSM is also developed. For the purpose of simplicity damper windings are ignored. The

PMSM has a large air-gap [38], and it is assumed that the magnet is operating in the linear region of the B-H curve shown in Figure 3.3, therefore saturation is not modeled.

Figure 6.5 shows a test circuit used for comparing the two models. Both machines are connected to a 60 Hz three-phase voltage source with the line-line voltage of 208 V and the initial phase angle of  $\varphi_s = 60^\circ$ . Both machine models (embedded phase-domain and conventional dq0) are operating at rated constant speed with the initial rotor angle of  $\delta = 0^\circ$ . As shown in Figure 6.5 and discussed in Chapter 3, the magnet in the PMSM is represented by the current source  $i_m$  connected to the field winding.

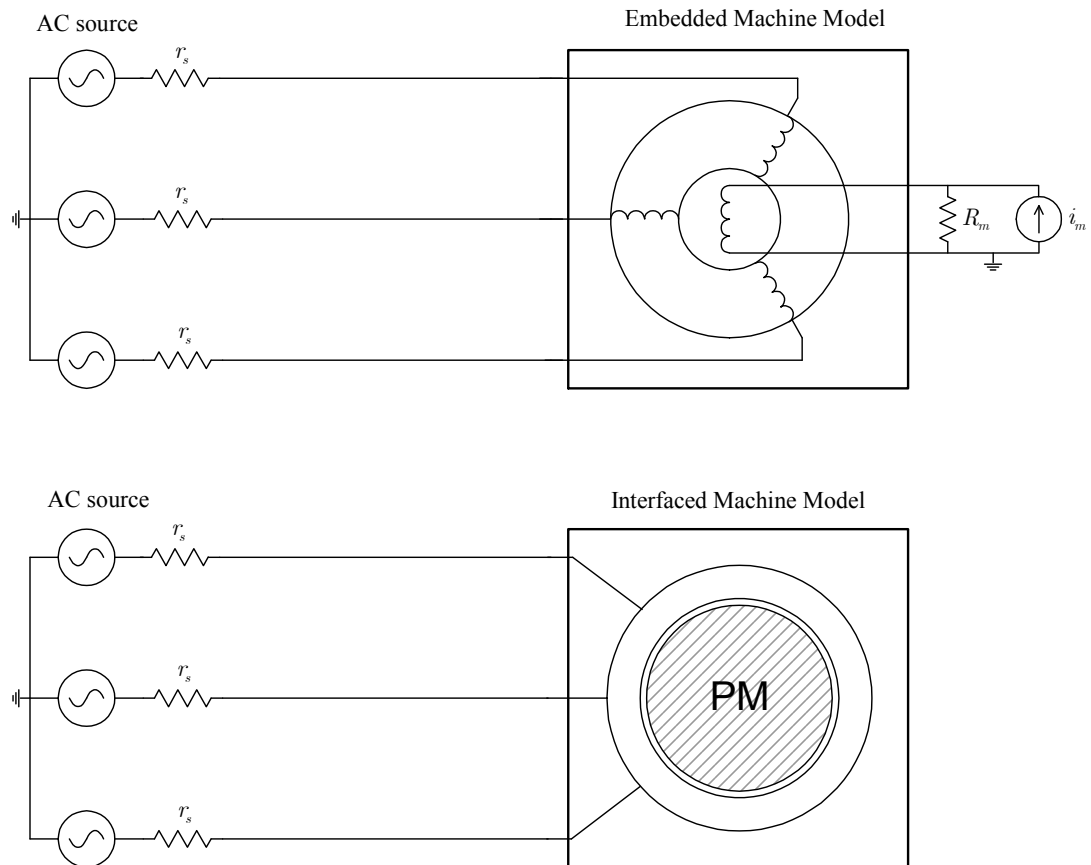


**Figure 6.5:** Test circuit for comparing the embedded and interfaced models of the PMSM

### 6.1.3.1 Steady state performance of the PMSM

Figure 6.6 shows the phase A voltage and stator currents of the above machine models in steady-state. The currents of the two machines are essentially identical. Superimposed on the currents of these two approaches, is a third curve obtained by modifying the parameters of the synchronous machine in the RTDS library so that it represents a permanent magnet synchronous machine. This curve is essentially in complete agreement with the other two curves.

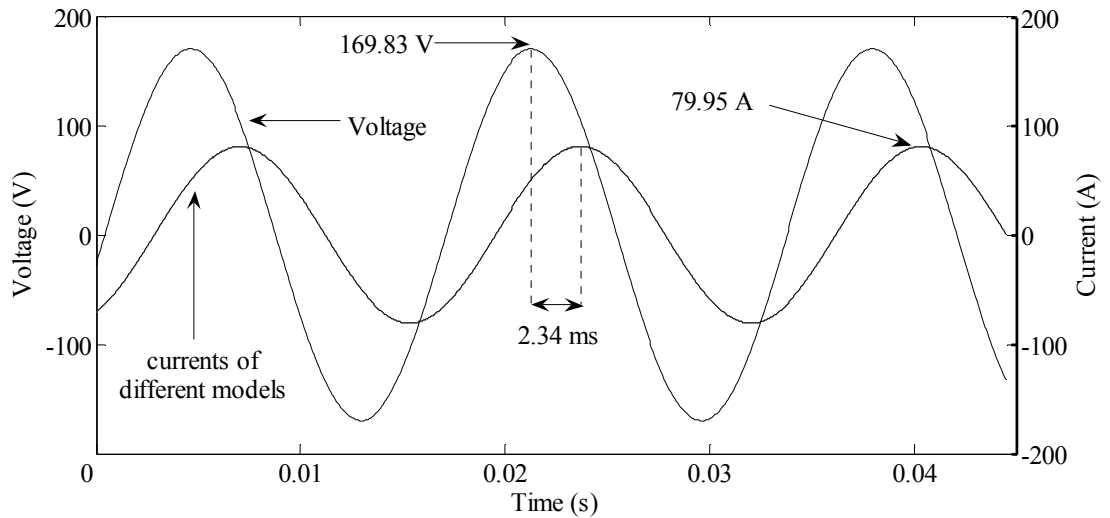


**Figure 6.6:** Steady-state performances of the permanent magnet machines

It is relatively easy to obtain a theoretical solution for the steady state current of the machine. This analytical solution can be used to validate the PMSM models. Figure 6.7 shows the steady-state equivalent circuit for the permanent magnet synchronous machine. This circuit is obtained from the dq equivalent circuit of the PMSM in Section 3.2.2 [38].

Using this circuit, the peak value of armature current in the above example can be easily calculated as shown in (6.1).

$$I_{a,peak} = \frac{V_{a,peak} \angle \varphi_s - \sqrt{\frac{2}{3}} \cdot \omega \cdot L_{md} \cdot i_m \angle \delta}{jX_d + r_s} = 79.95 \angle 9.44^\circ \text{ (A)} \quad (6.1)$$



This calculation verifies the magnitude of simulated current shown in Figure 6.6. Equation (6.1) also shows that the angle between the phase A current and voltage is  $50.5^\circ$  which is equivalent to  $2.34 \text{ ms}$  as shown in Figure 6.6.

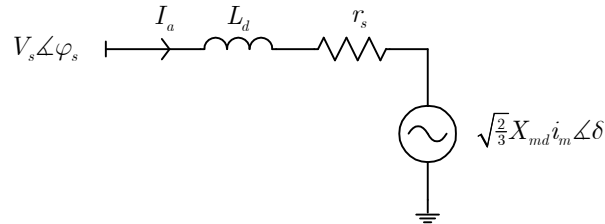


**Figure 6.7:** Steady state equivalent circuit for the PMSM

### 6.1.3.2 Analyzing the transient short circuit current in the PMSM

While the above permanent magnet synchronous machine is operating at the rated speed and rated voltage, a sudden symmetrical three phase short circuit is applied to the terminals of the machine at the instant where the point-of-wave angle of the phase A voltage is  $25.5^\circ$ . The simulated phase A currents from the two models during the short circuit are shown in Figure 6.8. A third curve corresponding to the commercial RTDS model is also superposed in this figure. As can be seen, similar to the steady-state situation, the three models have identical performance. The results may appear peculiar because the pre-fault current is larger than the fault current. This is because, in this example, the phase and magnitude of the applied voltage were such that the machine was initially loaded beyond its rated current. The steady state and transient components of the short circuit current are also shown in Figure 6.8. For *analytical* validation of the simulated short circuit current, the steady-state and transient parts of this waveform are validated separately. By solving the dq equivalent circuit of the PMSM in Section 3.2.2 in steady state short circuit conditions (i.e.  $\Psi_d = \Psi_q = \Psi_0 = 0$  and  $v_d = v_q = v_0 = 0$ ),

the peak value of the short circuit current in the steady state can be analytically calculated as shown in (6.2). The analytically calculated and simulated values of the steady-state short circuit current are in good agreement.

$$I_{sc,peak} = \sqrt{\frac{2}{3}} \cdot i_m \frac{\omega L_{md}}{\omega^2 L_d L_q + r_s^2} \sqrt{(\omega L_q)^2 + r_s^2} = 40.72 \quad (\text{A}) \quad (6.2)$$

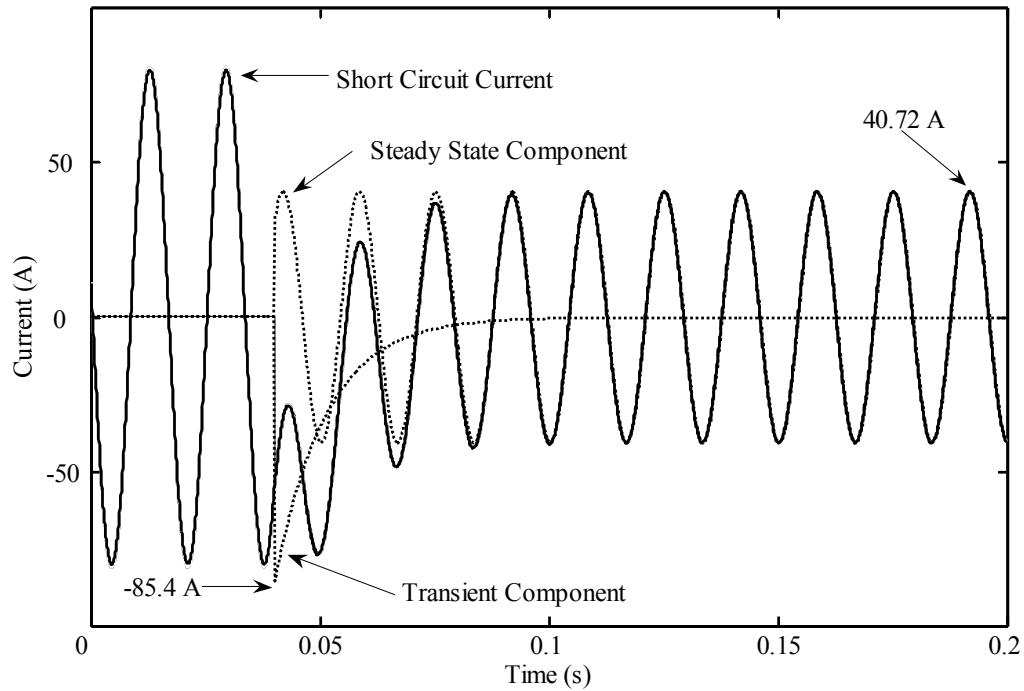


**Figure 6.8:** Stator phase A short circuit currents of the PMSM models (the transient simulated curves for the two approaches lie exactly on each other)

The transient part of the short circuit current contains three components: steady state AC current, transient exponentially damping AC current with the time constant  $T_d'$  (known as unsaturated direct axis transient short-circuit time constant [30]), and the transient exponentially damping DC component with the initial value of  $I_{DC0}$  and time constant  $T_a$  (known as the armature time constant [30]). For the PMSM under study the

values of  $T_d'$  and  $T_a$  are shown in (6.3). Parameters of this machine are shown in Table

6.2

$$\begin{aligned}
 T_d' &= \frac{l_s \parallel L_{md}}{R_m} = 0.084 \text{ (ms)} \\
 T_a &= \frac{1}{\frac{r_s}{2} \left( \frac{1}{L_d'} + \frac{1}{L_q'} \right)} = 11.25 \text{ (ms)} \quad \text{here : } (L_d' = L_q' = L_d) \quad (6.3) \\
 I_{DC0} &= -\frac{V_{a,peak}}{2} \left( \frac{1}{X_d''} + \frac{1}{X_q''} \right) \cos(\gamma_0) = -85.4 \text{ (A)} \quad \text{here : } (X_d'' = X_q'' = X_d)
 \end{aligned}$$

Equation (6.3) demonstrates that, in this PMSM, the direct axis time constant  $T_d'$  is very small, therefore the transient AC component of the short circuit current damps very quickly, and is not noticeable. Therefore, the short circuit current essentially contains a steady state AC current and a transient exponentially damping DC component only. In Figure 6.8 the transient and steady state components of the simulated armature short circuit current has been extracted from the short circuit waveform. No AC component can be noticed in the transient part of short circuit current as was predicted before. The transient component is, in fact, an exponential function with the time-constant of  $T_a = 11.25 \text{ (ms)}$ . This analysis shows that even permanent magnet type machines can be modeled using the proposed phase-domain approach.

#### 6.1.4 Assessing the Numerical Stability of the New Embedded Machine Model

In this section, the numerical stability of the embedded phase-domain machine model is examined and compared to that of the interfaced machine models. The effects of different integration methods (Section 5.2.1) on the stability and accuracy of the interfaced machine model are also discussed. So far it has been shown that the

conventional interfaced and the proposed embedded approach are essentially equivalent as long as the inductances of the phase-domain model are extracted using dq0 theory. However, in this section it will be shown that the embedded approach is numerically more robust compared to the interfaced approach.

The permanent magnet synchronous machine models of Section 6.1.3 were used in this study. Numerical stability of the models is examined by performing two tests: in the first test, every machine model is connected to an inductive voltage source and the time-step of the simulation is increased until the sinusoidal waveforms of the armature currents diverge. This time-step is called the *critical time-step*  $\Delta t_c$ . The inductive source is used instead of a resistive source, because it provides a bigger numerical challenge. The resistive source damps the errors built up by the numerical operations and gives optimistic results. The value of the inductance in the voltage source is normally a fraction of the base inductance of the machine (0.2-0.3 pu). In the second test, the machine is connected to a non-linear circuit, such as a voltage source converter bridge (VSC). In the RTDS simulator this particular VSC bridge component, similar to the interface machine model, is modeled as a current source. In electro-magnetic transient programs such a situation where two components both replaced by current sources are connected to each other, is often numerically unstable. The connection of two current sources at a common point of coupling is also a challenging situation for the numerical stability of the algorithm [94]. The purpose of this test is to observe the interaction of two injection-based (interfaced) models and the effect of this interaction on their numerical stability. Similar to the first test, this analysis is performed by increasing the simulation time-step and observing the divergence of the waveforms.

In this study, in addition to the new embedded machine model and the synchronous machine model from the library of RSCAD, the human-machine interface for the RTDS simulator [26], another interfaced model is developed in which different integrating methods (discussed in Section 5.2.1) are tried out. This interfaced model is shown by the *modified interfaced model* in Table 6.3. The critical time-step ( $\Delta t_c$ ) in which different machine models become numerically unstable is shown in Table 6.3.

As can be seen, the embedded machine model shows excellent numerical stability in both the inductive source case and the VSC source case. This model can be used in a simulation with a time-step in excess of  $30\text{ ms}$ , without becoming unstable. Needless to say, the accuracy with such a time-step is totally unacceptable since it is much larger than the period of  $16.667\text{ ms}$  for a  $60\text{ Hz}$  AC waveform. However it makes the point that the numerical stability of the algorithm is very good. The RTDS synchronous machine model from the RSCAD library is stable with time-steps smaller than  $167\text{ }\mu\text{s}$ . Table 6.3 also shows that, in the modified interfaced model, generally the numerical stability is affected by the integration method. Machine models implemented by the use of trapezoidal integration show significantly better numerical stability.

With the typical simulation time-step of  $50\text{ }\mu\text{s}$  and operational frequency of  $60\text{ Hz}$  all of the above machine models generate accurate results in steady-state. However the interfaced model shows some errors and delays when the case is dealing with transients and switching operations or when the frequency of the operation increases. ***With further increase in the frequency of operation, interfaced machine models can experience numerical instabilities even with a simulation time-step of  $50\text{ }\mu\text{s}$ .***

TABLE 6.3: NUMERICAL STABILITY OF DIFFERENT MACHINE MODELS

		<b>Inductive source</b>	<b>VSC source</b>
<b>Embedded Model</b>		$\Delta t_c \simeq 36000(\mu s)$	$\Delta t_c \simeq 36000(\mu s)$
<b>RTDS Synchronous Machine</b>		$\Delta t_c \simeq 167(\mu s)$	$\Delta t_c \simeq 167(\mu s)$
<b>Modified Interfaced Model</b>	<b>Predictor Corrector Integration</b>	$\Delta t_c \simeq 106(\mu s)$	$\Delta t_c \simeq 167(\mu s)$
	<b>Trapezoidal Integration</b>	$\Delta t_c \simeq 6500(\mu s)$	$\Delta t_c \simeq 1638(\mu s)$

## 6.2 Validation of the MWFA-based Embedded Phase-Domain Machine Model

The capability of the new embedded phase-domain model in solving the differential equations of mutually coupled inductors (3.1) was verified in Section 5.1. In that section, machine inductances were sinusoidal functions in the form of (3.4)-(3.10), therefore the steady-state waveforms of simulated voltage and current were purely sinusoidal.

In this section, the MWFA is used to calculate inductances of the experimental wound rotor synchronous machine (introduced in Section 3.4). The new embedded phase-domain machine model is incorporated into the real-time digital simulator (RTDS<sup>®</sup>). Laboratory experiments are conducted to validate the model. Figure 6.9 shows the configuration of this model in the RTDS environment: the machine has three stator windings, one field winding, one damper winding on the d-axis and one damper winding on the q-axis. In addition, stator phase A is divided into two sub-windings  $A1$  and  $A2$  and the electric node  $AJ$  provides the possibility of simulating internal faults. This node is left open-circuited for situations where modeling internal faults is not intended. Electric nodes  $A$ ,  $B$ ,  $C$ ,  $AJ$ ,  $N$ ,  $F1$  and  $F2$  can be connected to any of the power system components in the RSCAD Library [26]. The electric torque  $T_e$  is calculated using (5.39) and is available for external measurements. The mechanical speed signal  $\omega$  is the input for the machine model. This machine speed  $\omega$  is externally specified, and could be the output of additional state-variable based models such as multi-mass inertia and governor models as described in Section 5.5.

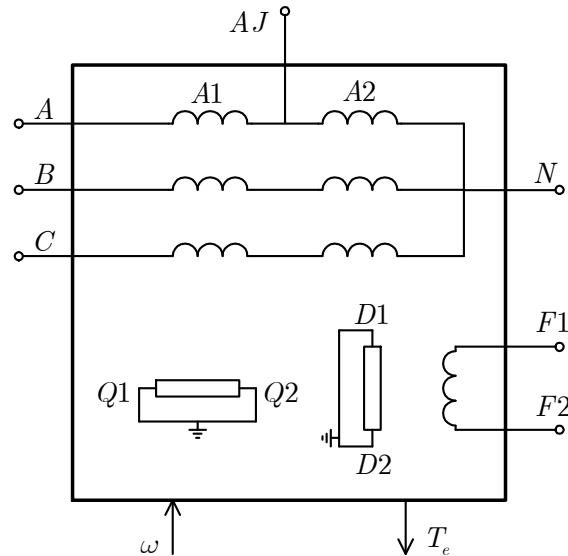


**Figure 6.9:** Configuration of the embedded synchronous machine model developed in the RTDS environment

In order to validate the model, its transient performance is compared with the corresponding experimental results under healthy and faulted conditions. In this thesis, the focus of the model is the electrical part and accurate comparisons can be made if both the model and the experimental machine were running at exactly the same speed at any time. Therefore, the experimental machine is driven by an external prime mover (motor) whose speed is manually adjusted to the rated speed. Hence, the test machine runs nominally at rated speed, but does experience slight speed transients on the application of faults and loads. For comparison with field tests, the speed signal recorded in the experiment as a function of time is fed back through the speed input of the model ( $\omega$  in Figure 6.9).

### 6.2.1 Validation of the Model in Healthy Conditions

As the incorporation of saturation into MWFA is an important contribution of this thesis, some of the tests consider conditions where the effects of saturation are



significant. These include a resistive load switching and a switching on of a leading power factor load; both result in over-voltage and consequently drive the machine into saturation. These tests clearly demonstrate the additional accuracy gained by considering winding distribution, rotor geometry and detailed representation of saturation.

### 6.2.1.1 Simulation and experimental results for the R-C load switching

This interesting scenario is switching of a  $\Delta$ -connected series R-C load (1.05 pu, at 0.5 pf) onto a synchronous machine as shown in Figure 6.10. The data related to this load is shown in Table 6.4. The machine is initially operating in open circuit at the rated speed and 84% of rated voltage. The machine data is as in Table 3.3.

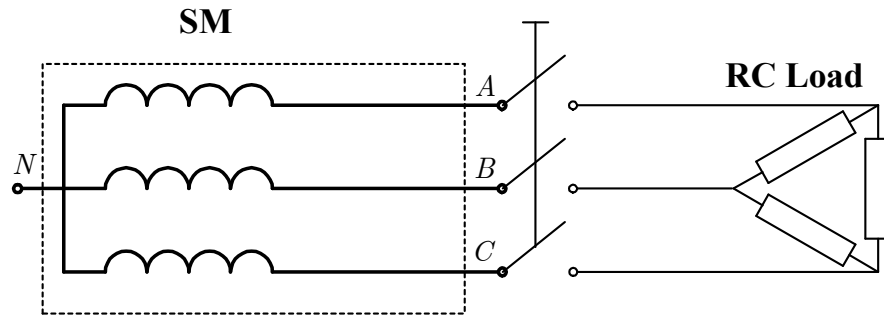
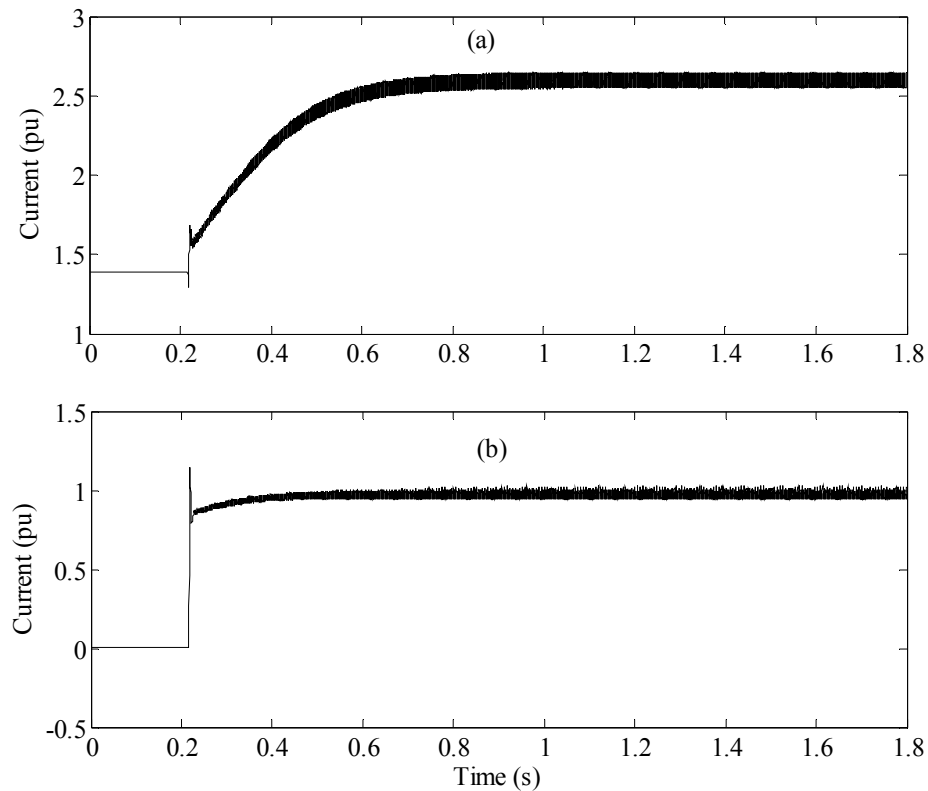


Figure 6.10: Circuit diagram of the synchronous machine connected to an R-C load.

TABLE 6.4: SPECIFICATION OF THE LOADS IN LABORATORY EXPERIMENTS

R-C Load		
Parameter	Symbol	Value
Load capacitance	$C_L$	74.5 $\mu$ F
Load resistance	$R_L$	20.5 $\Omega$
Field voltage	$V_f$	32.37 V
Resistive Load		
Parameter	Symbol	Value
High load resistance	$R_H$	15.2 $\Omega$
Low load resistance	$R_L$	40.0 $\Omega$
Field voltage	$V_f$	56.0 V

An R-C load was selected because the switching on a capacitor increases the d- and q-axis magnetizing currents, and hence exercises the proposed saturation modeling feature. Figure 6.11 shows the simulated per-unit magnetizing currents in the d- and q-axis, clearly indicating an increase of MMF. In particular, the iron is significantly saturated along the d-axis ( $I_{md} = 2.6$  pu).



**Figure 6.11:** Simulated variation of the total magnetizing currents along d and q-axis of the generator with R-C load switching: a)  $i_{md}$ , b)  $i_{mq}$

The field current transient is presented in Figure 6.12 which shows a) the experimental result; b) the result from simulation with the full model and; c) the result from simulation with saturation ignored. The full model agrees closely with the experiment. When saturation is ignored, the rise-time of the field current is considerably (incorrectly) larger.

The steady-state ripple in the simulated waveforms is not due to numerical error, but due to the presence of harmonics of order  $6k$ ,  $k \in 1, 2, \dots$  as a result of stator winding space harmonics [70]. The ripple in the measured current (Figure 6.12a) is due not only to winding space harmonics but also due to measurement noise and not-modeled factors such as structural asymmetries. Note that the comparisons of Figures 6.12-b and 6.12-c with Figures 6.12-a should be made on the basis of the field current DC transient and not on the basis of ripple.

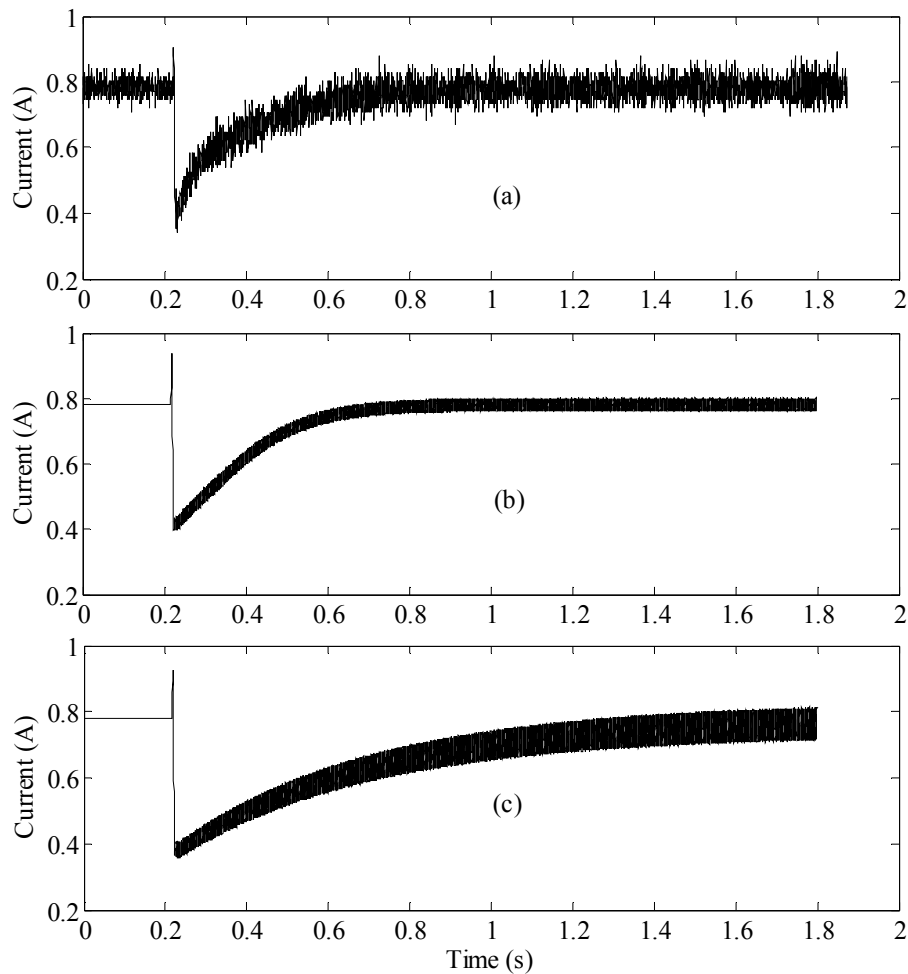


**Figure 6.12:** Experimental and simulated variation of the field current during the switching of the generator on the R-C load: a) experiment b) simulation incorporating saturation c) simulation ignoring saturation

Figures 6.13 and 6.14 show the simulated phase-neutral voltage and phase current, ignoring and including saturation respectively, together with the experimental results for the two-cycle interval just after the switching instant. The simulation results with saturation incorporated (Figure 6.14-a) are only marginally closer to the experimental results than those with saturation ignored (Figure 6.13-a). Both are in good agreement with the experiment. This is because the machine was initially operating at a low level of saturation (open circuit with 84% rated voltage) and so the inclusion of saturation in the model makes only a small improvement. Later experiments that exercise the saturation behaviour more strongly are presented later in this section.

The results from the model also contain the time harmonic in the waveform. The existence of these time harmonics can be explained using space and permeance related harmonics resulting from the non-sinusoidal distribution of the windings and saliency of the machine [70]. These would have been absent in the conventional dq0 representation.

Figures 6.15 and 6.16 show the same comparisons after the post-switching steady state is attained. At this time, the machine is highly saturated and therefore ignoring saturation makes significant errors as seen in Figure 6.15. On the other hand the comparison with the full model including saturation is very close as seen in Figure 6.16.

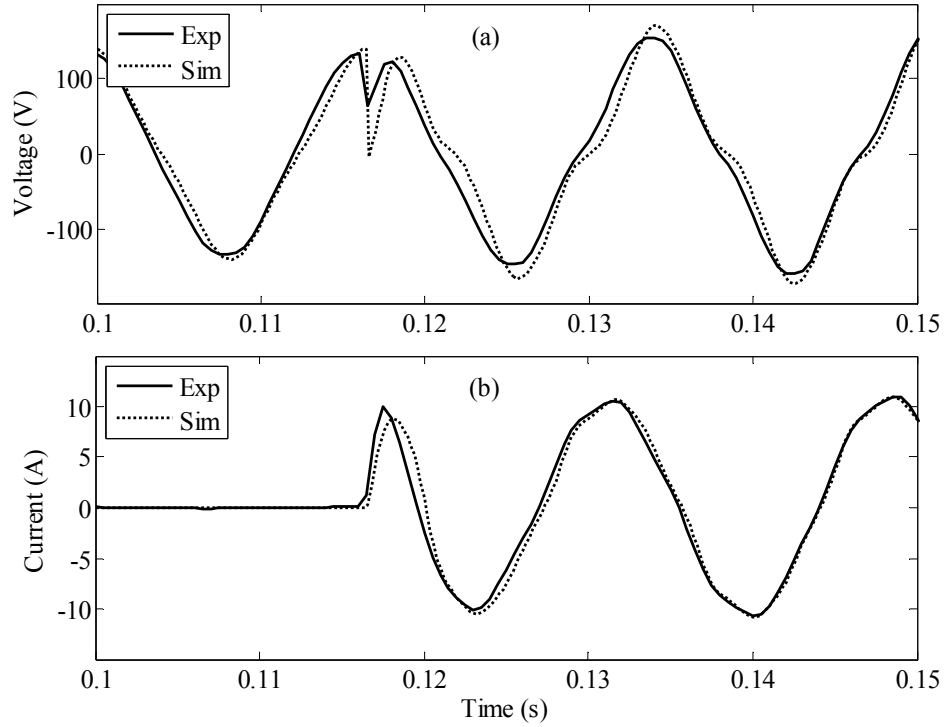


**Figure 6.13:** Experimental and simulated R-C switching transient ignoring saturation, a) phase-neutral voltage, b) phase current

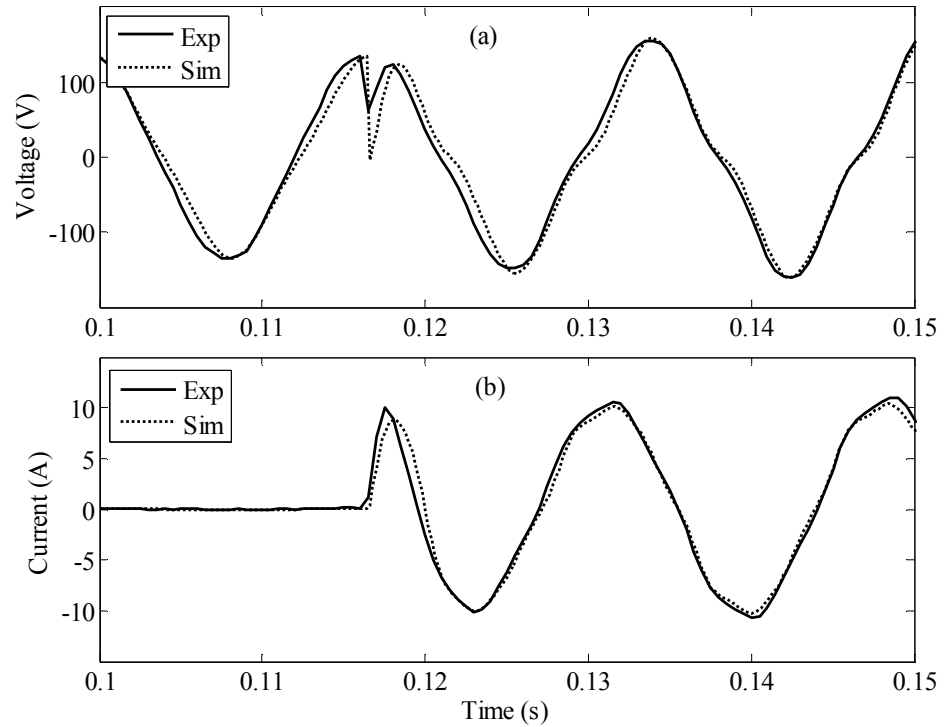


**Figure 6.14:** Experimental and simulated R-C switching transient including saturation, a) phase-neutral voltage, b) phase current

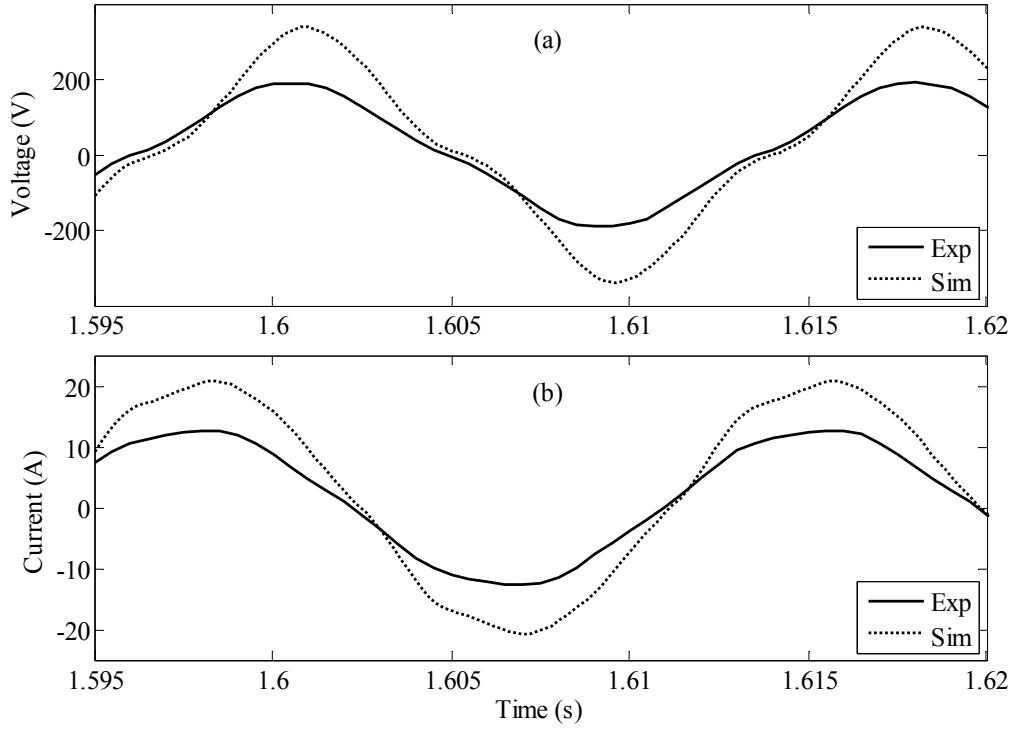


**Figure 6.15:** Experimental and simulated steady-state waveforms with R-C load ignoring saturation, a) phase-neutral voltage, b) phase current

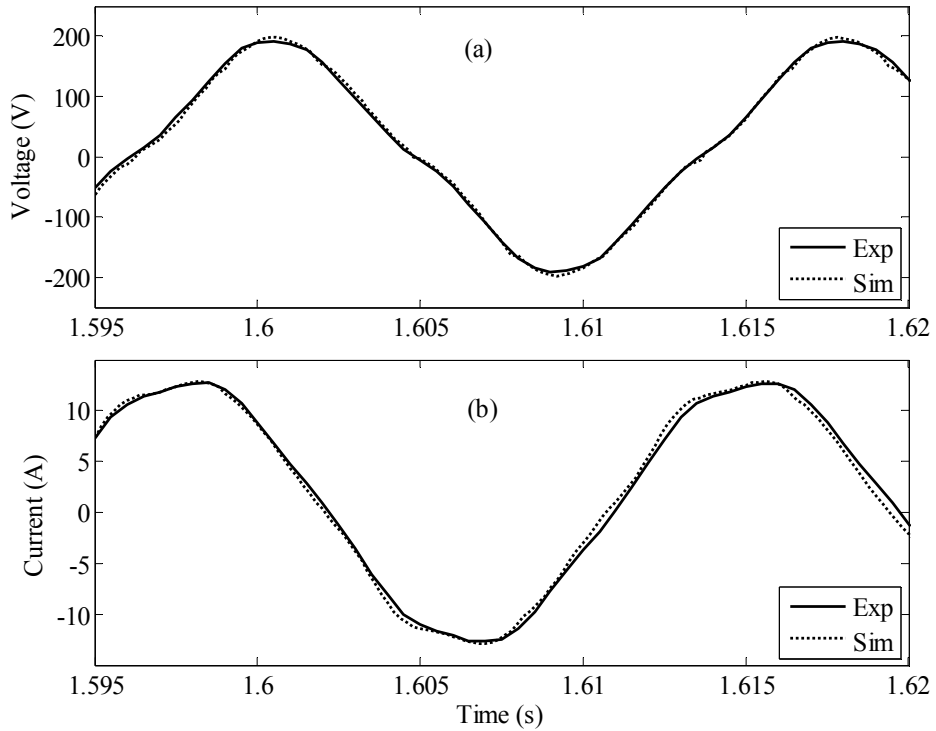


**Figure 6.16:** Experimental and simulated steady-state waveforms with R-C load including saturation, a) phase-neutral voltage, b) phase current

### **6.2.1.2 Simulation and experimental results for the resistive load switching**

The synchronous machine was operated as a generator in the steady state at the rated speed and 109 % of rated voltage with a 0.95 pu resistive load (resistance of  $15.2 \Omega$ ). A portion of the load was then switched off resulting in a much reduced load of 0.36 pu (resistance of  $40 \Omega$ ). A resistive load has de-magnetizing effect; therefore reducing the load (i.e. increasing the resistance) increases the saturation level and results in over-voltage. Data related to this experiment is also shown in Table 6.4.

The steady-state pre- and post-switching waveforms of phase voltage were examined to check the impact of the proposed model on the steady state machine performance. Figure 6.17a shows the experimentally obtained phase-to-neutral voltage and the simulation results from the proposed detailed model (including saturation). Figure 6.17b compares the same experimental result with the proposed model, but with saturation ignored; and in this case the comparison is poorer. However, the simulation ignoring saturation still shows time harmonics in the waveform (indicating that the non-sinusoidal windings and actual shape of rotor pole-arc are being considered).

Figure 6.18 shows similar waveforms when steady-state is reached after switching off the load. Again, the comparisons with the detailed model (saturation included) are very good. Also, comparing Figure 6.17a (0.95 pu resistive load) and Figure 6.18a (0.36 pu resistive load), shows that the voltage waveform with higher loading is more distorted.

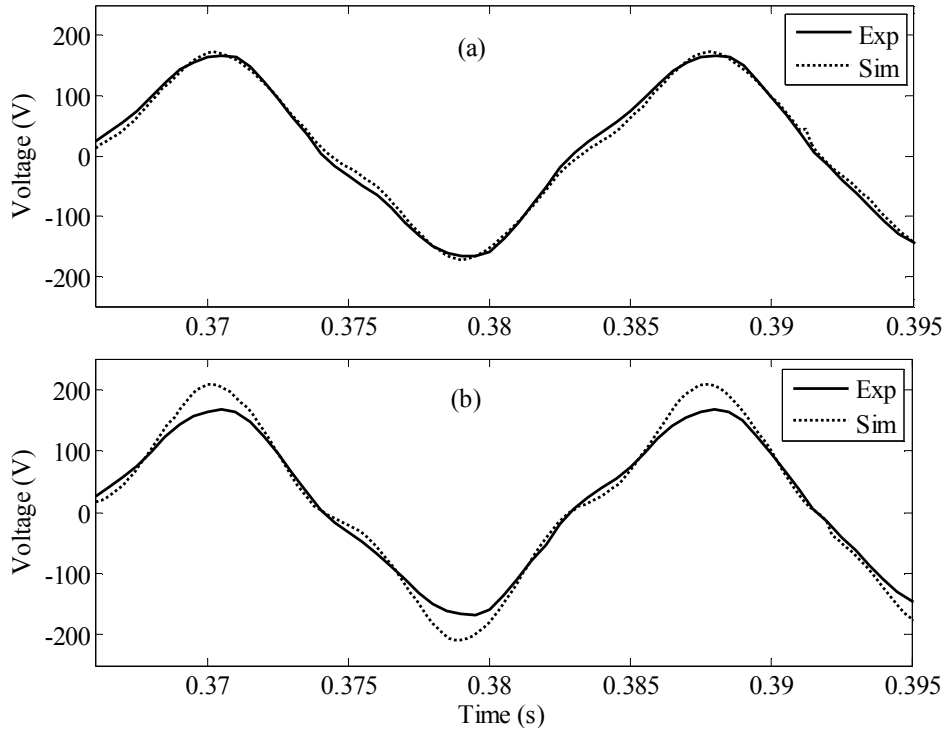


**Figure 6.17:** Experimental and simulated steady-state pre-switching (full-load) phase to neutral voltage: a) saturation modeled b) saturation ignored

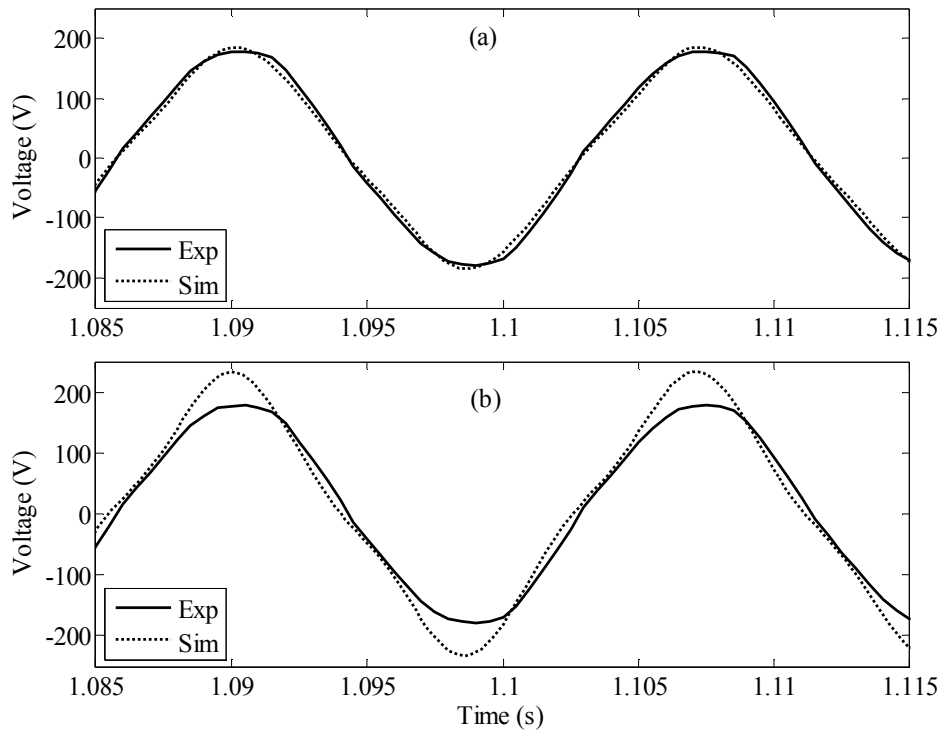


**Figure 6.18:** Steady-state experimental and simulated post-switching (0.36 pu load) phase to neutral voltage: a) saturation modeled b) saturation ignored.



### 6.2.1.3 Comparison of proposed model with conventional d-q based model regarding harmonic generation

The new detailed model was validated through laboratory experiments in Sections 6.2.1.1 and 6.2.1.2. The simulated waveforms are in good agreement with the experimental results with respect to *fundamental components* as well as *time harmonics* of these signals. To demonstrate the difference in results between the proposed detailed model and conventional d-q axis based models, a test is conducted in which the same R-C load as in Section 5.2.1.1 was connected to the machine. The machine is operating at the rated speed, and the field voltage is adjusted to 54% of the rated open-circuit voltage. Figure 6.19 shows the waveform of the experimentally obtained phase current superposed on the results obtained by the detailed and simplified (d-q axis) based modeling [11]. The agreement between the proposed detailed model and the experiment is very close. The magnitude and harmonic profile of the simulated current agrees with the experimentally obtained waveform. However, the d-q based model shows a current which is purely sinusoidal, and the time harmonics are absent. This is because; in dq0 theory a sinusoidal distribution is assumed for the machine windings and its permeance (see Chapter 3).

As can be seen in Figure 6.19, the magnitude of the current generated by the d-q based model is also (incorrectly) larger. The reason for this error is the method of modeling the effects of iron saturation in electromagnetic transients programs (EMTDC and RTDS). In these programs, saturation is modeled by adjusting the value of only d-axis magnetizing inductance  $L_{md}$  as a function of total d-axis magnetizing current  $i_{md}$  (see Section 4.1).

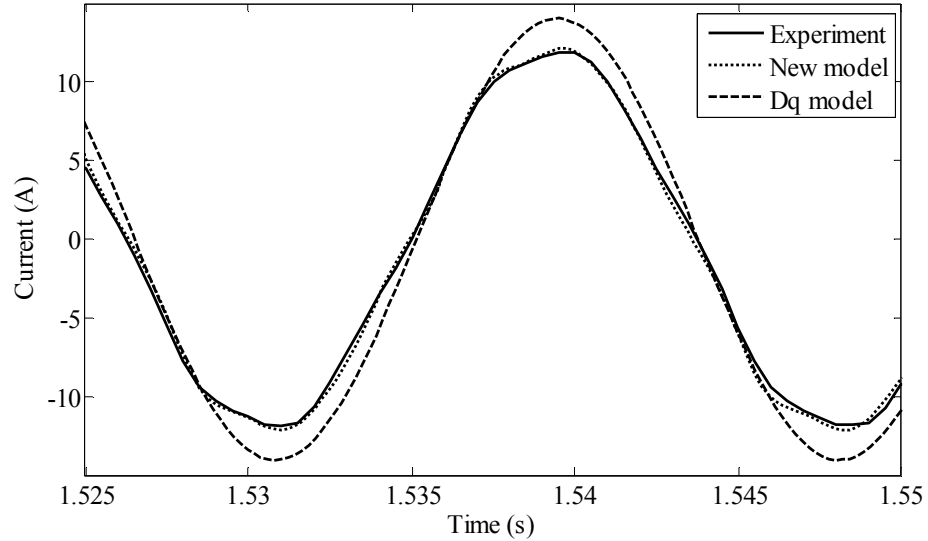


**Figure 6.19:** Experimental and simulated steady-state phase current waveforms with R-C load

Figure 6.20. shows the simulated per-unit magnetizing currents in the d-and q axis for this switching scenario. The steady-state values for these quantities respectively are  $I_{md} = 2.0$  pu and  $I_{mq} = 1.0$  pu. The dq synchronous machine model only considers the d-axis magnetizing current as an index for saturation, therefore based on the open-circuit characteristics (Figure 4.4), it assumes that the machine still operates in the linear region. However, according to (4.5) of Section 4.1.1, the total magnetomotive force in this situation has a sinusoidal distribution with the peak value of  $\sqrt{2.0^2 + 1.0^2} = 5.0$  pu which is deviated from the middle of pole-arc. This means that one side of rotor pole-arc is considerably saturated, and therefore the assumption of operation in the linear region in the dq synchronous machine model is incorrect.

To correct this problem in dq-based synchronous machine models, saturated values of the d- and q-axis magnetizing inductances  $L_{md}$ ,  $L_{mq}$  can be determined based on both d- and q-axis magnetizing currents  $i_{md}$ ,  $i_{mq}$  [78], [79], [91].

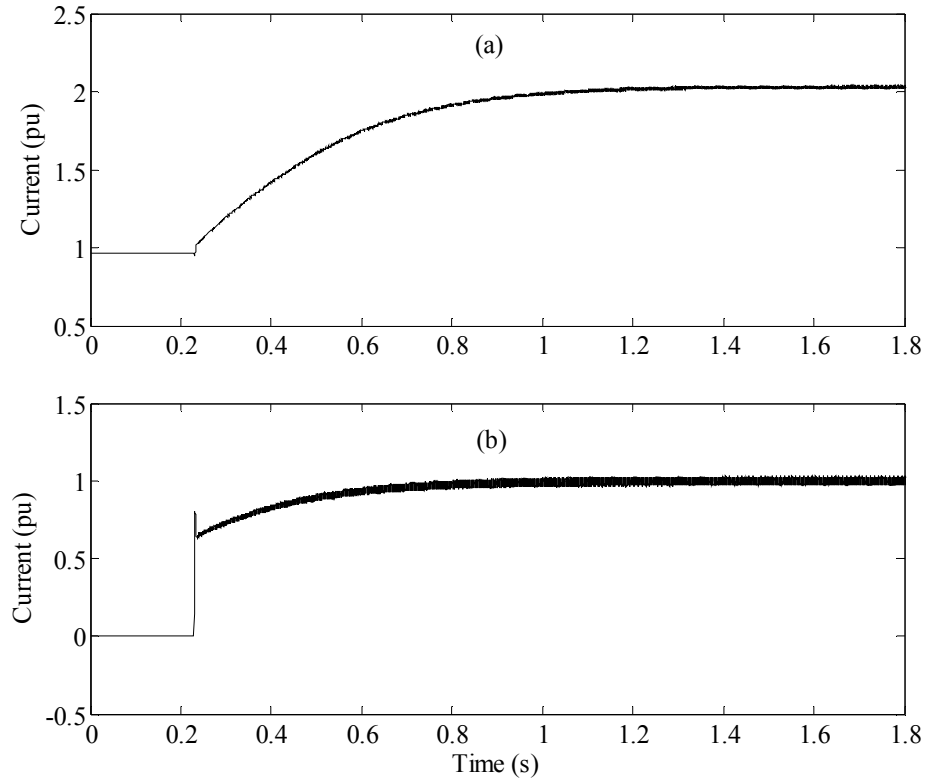


**Figure 6.20:** Simulated variation of total d and q-axis magnetizing currents of the generator with R-C load switching: a)  $i_{md}$ , b)  $i_{mq}$

## 6.2.2 Validation of the Model for Faulted Conditions

To investigate fault simulations, three phase, single phase and internal fault short circuit tests are conducted and the results are compared with the simulation. As shown in Figure 3.11, every stator phase of the experimental machine consists of two sub-windings which are mechanically  $180^\circ$  apart. The sub-windings of each phase are connected in series to form individual phases as shown in Figure 6.21. In this Figure,  $AJ$  is the connection point between two sub-windings of phase A. The node  $N$  identifies the neutral of the Y-connected stator in this synchronous machine.

Symmetrical three phase faults (i.e. solid short circuits between the nodes  $A, B, C$ ) and line-neutral faults (i.e. solid short circuits between the nodes  $A, N$ ) are applied and the results are compared with the simulation in Section 6.2.2.1. In Section 6.2.2.2, the results of an *internal fault* (a solid short circuit between the nodes  $AJ$  and the neutral) are discussed.

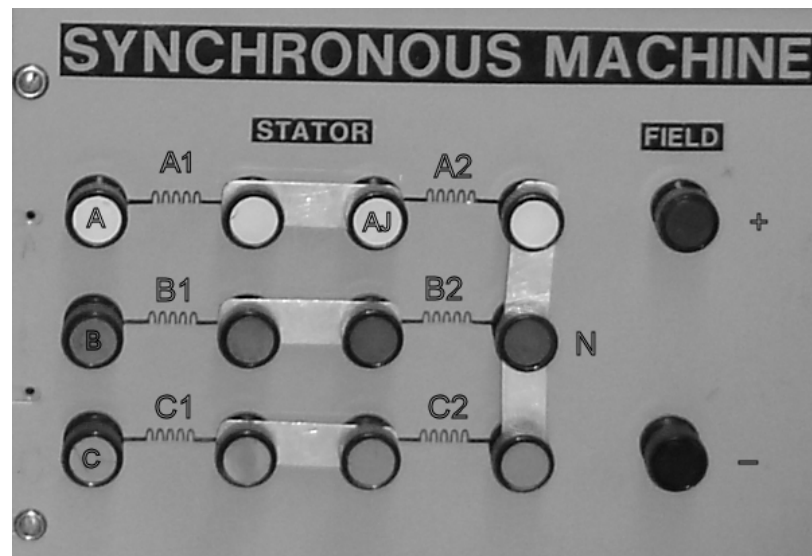
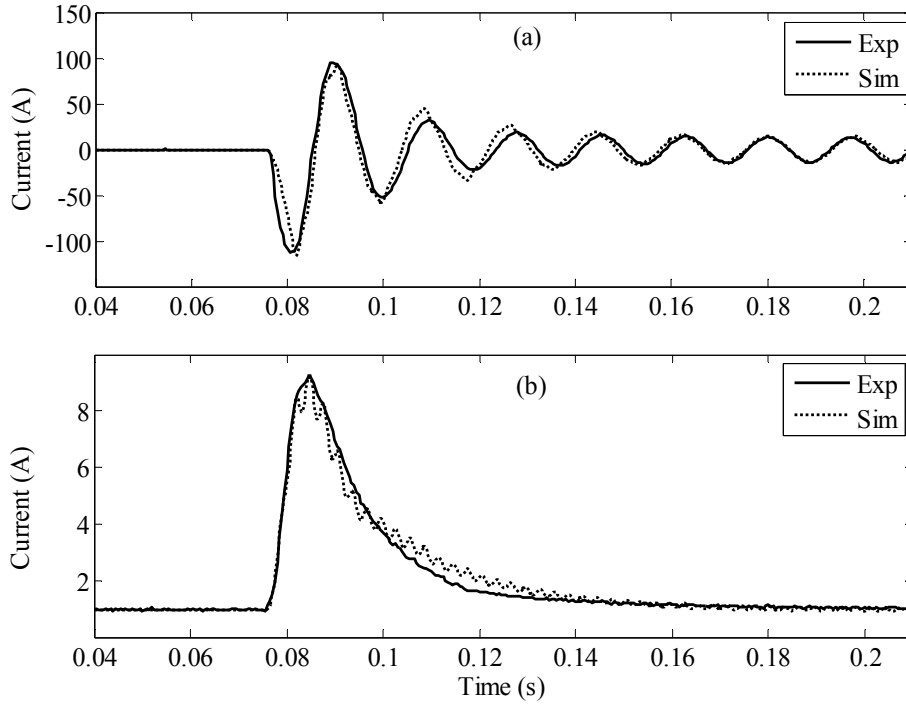


Figure 6.21: Connection of the synchronous machine windings in the laboratory setup

### ***6.2.2.1 Validation of the model for three phase and line-neutral short circuits***

The machine is initially operating in open circuit at the rated speed and 95% of the rated voltage. A three phase short circuit is applied to the stator terminals of the machine, and the resulting field and armature current waveforms are captured and compared with the simulation. Figure 6.22 shows the field and armature currents following a three phase fault. The close comparison demonstrates that the machine time constants have been properly represented in the new model. The short circuit fault occurs at the instant where the point-of-wave angle of the phase A voltage is close to  $90^\circ$  (i.e. at an instant very close to the peak of phase A voltage), therefore the transient short circuit current waveform does not contain considerable amount of DC offset [30].

In another laboratory experiment, the machine is initially operating in open circuit at the rated speed and rated voltage. A sudden short circuit is applied between the phase-A terminal and the neutral of the machine. Figure 6.23 shows the comparison between experimental and simulated waveforms of the field and armature currents for this line-neutral fault. As shown in Figure 6.23-a, there is close agreement between the simulated and experimental stator currents with respect to both magnitude and the harmonic contents (mainly third harmonic) of these waveforms.



**Figure 6.22:** Experimental and simulated transients of a symmetrical three phase short circuit on the initially open circuited generator: a) phase-A current, b) field current

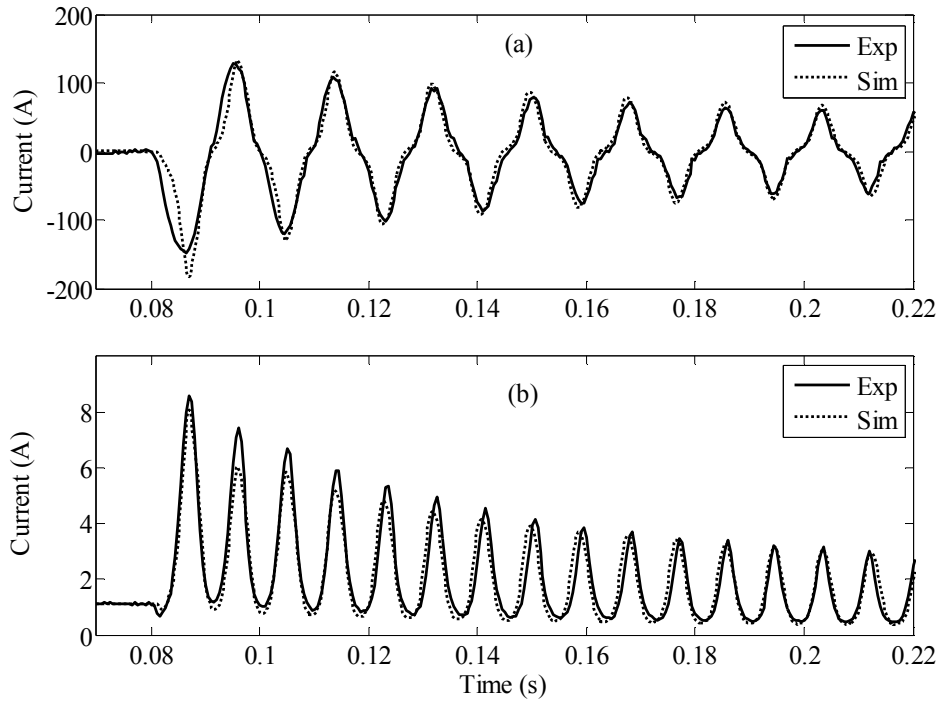


**Figure 6.23:** Experimental and simulated transients of a terminal-to-neutral short circuit on the initially open circuited generator: a) phase-A current, b) field current

### 6.2.2.2 *Performance of the model during internal faults (a turn-to-neutral fault)*

In this experiment, the machine is initially operating in open circuit at the rated speed and 97% of the rated voltage. A solid short circuit is applied between node  $AJ$  and the neutral of the machine (i.e. one of the two series coils of phase A is shorted), and the resulting armature and field current waveforms are captured. Figures 6.24-a and -b, respectively, show the experimental currents of the winding A2 and the field winding for this internal fault. This fault, with the same pre-fault conditions, is also simulated using the embedded phase-domain model and the results from the first attempt in doing so are shown in Figure 6.25. As can be seen, unlike external faults in the previous sub-section, the results from the embedded phase-domain model have very large errors (around 64%). The oscillations of the experimental fault current are much larger than the ones from simulation. The causes of this discrepancy will be discussed in the following pages of this section. ***It will be shown that the conventional modeling of the damper gird as equivalent windings along the d-axis and q-axis is not adequate for modeling these types of faults.*** This indicates that a refinement to the model is necessary for simulating internal faults. Such a modification is introduced later in this section.

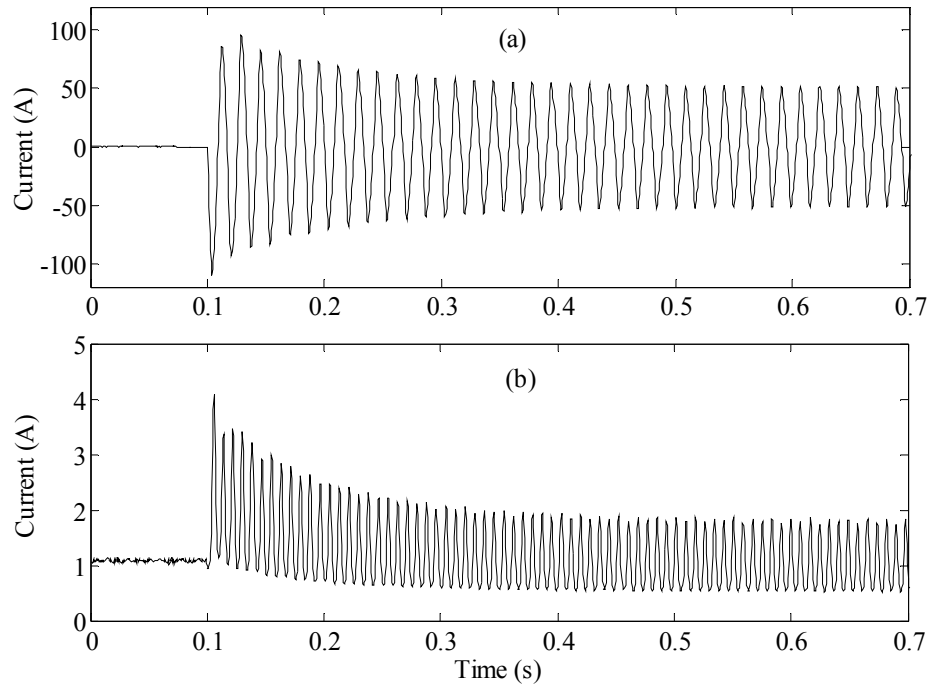


**Figure 6.24:** Experimental transient currents of a short circuit on the stator winding A2: a) faulted winding A2, b) the field winding

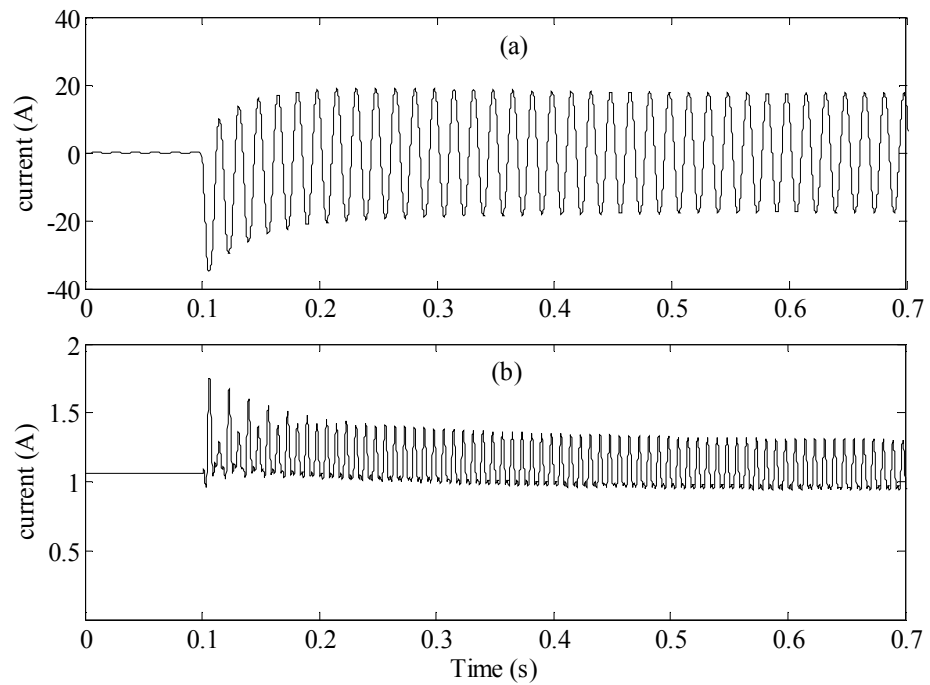


**Figure 6.25:** Simulated transient currents of a short circuit on the stator winding A2 using the new embedded phase-domain model: a) faulted winding A2, b) the field winding



During this internal fault (a short circuit between nodes  $AJ$  and the neutral), only the sub-winding A2 (see Figure 6.21) from the stator is carrying current and the rest of the stator windings are open-circuited. Figure 6.26 shows the cross-section of the machine in this situation at an instant in which the rotor is at  $0^\circ$ . As mentioned in Chapter 3, series-connected concentric coils  $a_1-a'_1, a_2-a'_2$  and  $a_3-a'_3$  form the sub-winding A1 and the coils  $a_4-a'_4, a_5-a'_5$  and  $a_6-a'_6$  form the sub-winding A2. During the internal fault, the flux produced by winding A2 (shown by  $\Phi_{A2}$ ) tends to enter the rotor area from pole 3 (and thus is strongest in magnitude in this pole) and goes out through the poles 1, 2 and 4. In this condition, according to Lenz's law, the flux  $\Phi_{f3}$  created by the coil  $f_3-f'_3$ , of the field winding, is such that it resists  $\Phi_{A2}$  (i.e. it is in a direction opposite to the flow of  $\Phi_{A2}$ ). Therefore  $\Phi_{f3}$  has an outward direction as shown in Figure 6.26. The field coils in all poles are series connected and as a consequence they carry identical currents with the direction identified in Figure 6.26. Hence, the same reactionary current which creates  $\Phi_{f3}$  to oppose  $\Phi_{A2}$ , now flows into coils  $f_1-f'_1, f_2-f'_2$  and  $f_4-f'_4$  to generate fluxes  $\Phi_{f1}, \Phi_{f2}$  and  $\Phi_{f4}$  respectively. As shown, the coils  $f_2-f'_2$  and  $f_4-f'_4$  generate inward-directed fluxes  $\Phi_{f2}$  and  $\Phi_{f4}$ , and the coil  $f_1-f'_1$  generate outward-directed flux  $\Phi_{f1}$ . Hence, MMF produced by coils  $f_2-f'_2$  and  $f_4-f'_4$  appears to be in a direction opposite to that of  $\Phi_{A2}$ , and MMF produced by the coil  $\Phi_{f1}$  is in the same direction that  $\Phi_{A2}$  flows.

The damper grid also reacts to the flow of flux  $\Phi_{A2}$ . The damper grid consists of 6 bars per pole connected through copper laminations at both ends of the bars. Unlike the field winding, the damper bars of each pole have independent performance, and all of

them resist the flow of  $\Phi_{A2}$ . Hence, the damper bars in poles 1,2 and 4 generate inward-directed fluxes  $\Phi_{D1}$ ,  $\Phi_{D2}$  and  $\Phi_{D4}$ , and the damper bars in pole 3 generate the outward-directed flux  $\Phi_{D3}$  as shown in Figure 6.26.

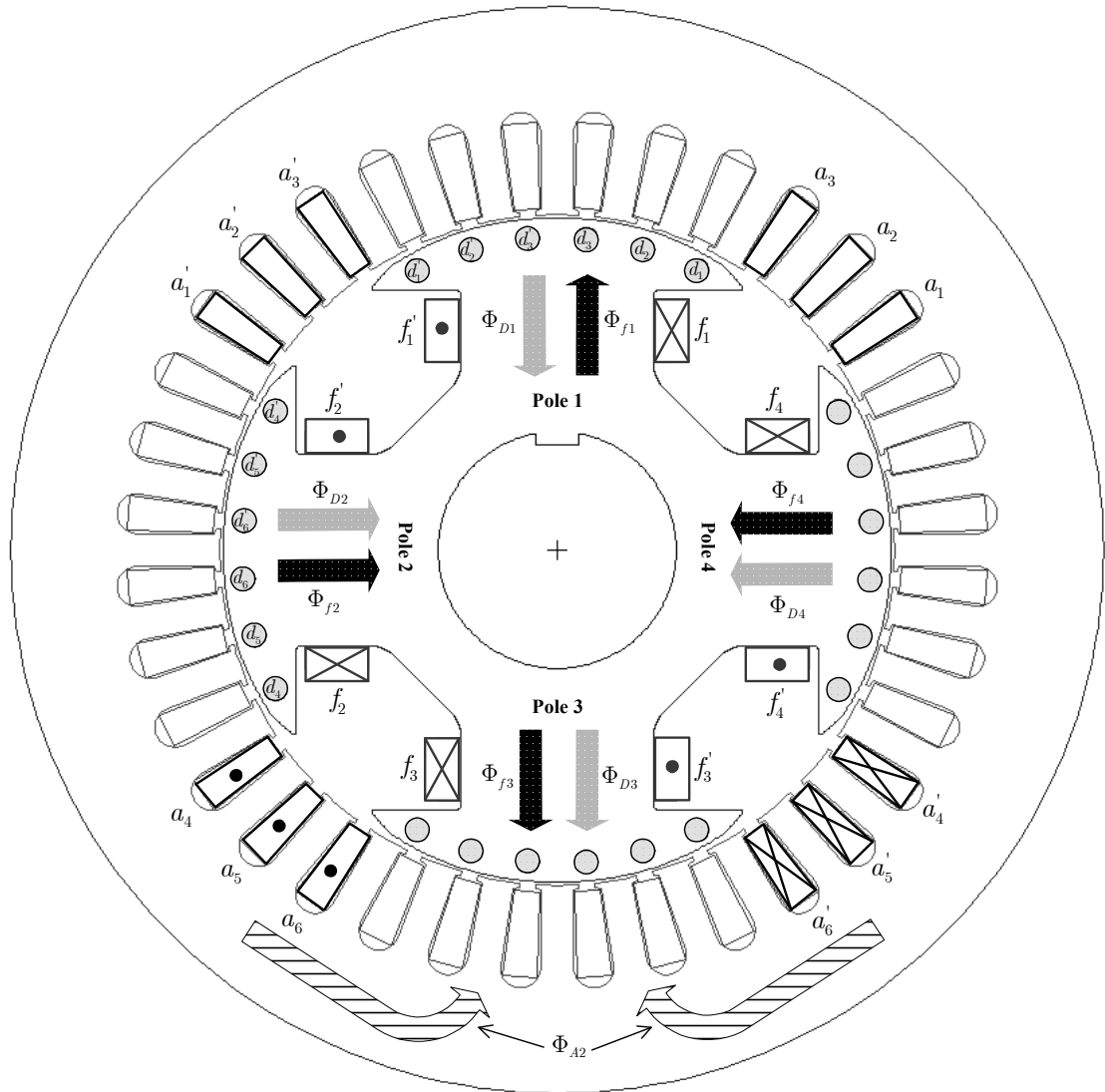


**Figure 6.26:** Direction of fluxes generated by the field winding and damper grid when only winding A2 is energized.

The above analysis shows that the damper grid resists the flow of  $\Phi_{A2}$  in pole 1 whereas the field winding in this pole aids the flow of this flux component. In the

conventional approach of modeling a damper grid as equivalent windings along the d-axis and q-axis [30], [31], [87], [88], the d-axis damper winding consists of coils for each pole which are connected in series in a manner similar to the field winding. The q-axis damper winding also has similar distribution with an electrical angular shift of  $90^\circ$ , and there is no mutual coupling between the d- and q- axis damper windings. Such an arrangement causes the d-axis damper winding to behave like the field winding and aids the flow of  $\Phi_{A2}$  in pole 1, which is contrary to the reaction of the actual damper grid as discussed above. Therefore the arrangement of series connected damper coils does not correctly represent the behaviour of the actual damper grid during situations like a fault between node  $AJ$  and the neutral of the machine.

A better representation of the damper grid for such faults is considering independent d- and q-axis shorted damper windings for each pole: for example in pole 1 the damper bars  $d_1, d_2, d_3$  and  $d'_1, d'_2, d'_3$  can form a concentric shorted d-axis winding ( $D_1$ ); and the set of bars  $d'_1, d'_2, d'_3$  and  $d'_4, d'_5, d'_6$  can form a q-axis damper winding ( $Q_1$ ). Such a representation results in a complex machine model with four d-axis ( $D_1-D_4$ ) and four q-axis damper winding ( $Q_1-Q_4$ ). Every d-axis damper winding is located between two q-axis damper windings having three damper bars (as indicated above) in common with each of these windings, and vice versa.

To take into account the proper coupling of each of these damper windings and all other windings, the MWFA procedure as discussed in Section 3.4 is used to generate the position varying inductance matrix of this 15 winding machine ( 3 stator windings, 1 field winding, 4 d-axis damper windings and 4 q-axis damper windings) . Strictly speaking, as

the windings share common conductances, there are also mutual resistances between these damper windings, and a current flowing in a d-axis damper winding causes the leakage flux of the shared bars to be induced on the neighboring q-axis damper windings [67]. These effects are neglected for now.

With the present technology, the computational capacity of the RTDS hardware does not allow implementation of such a complex machine model with 15 windings. Therefore a stand-alone program is written in MATLAB<sup>®</sup> to model the synchronous machine with a detailed representation of the damper grid as described above. The computational approach of this program is similar to that used in the RTDS formulation of the embedded phase-domain machine model. An EMTP-type program [1] solves the network equations for the full system; i.e. arbitrary external network including RLC elements<sup>1</sup> and voltage and current sources with the machine represented as an embedded set of time-varying coupled coils as described in Section 5.3. ***Development of this program is one of the main contributions of this thesis.***

As shown in Figure 6.27, every terminal of the experimental machine in Figure 6.21 is shown by an electric node in the developed electromagnetic transients program (nodes 1-14). In this electro-magnetic transient program, any two nodes can be connected through arbitrary voltage sources or impedance for applying any kind of fault or energizing windings independently. This level of flexibility will be helpful for future research in this area.

The internal fault on the sub-winding A2 is simulated by connecting nodes 7 and 10 of the electromagnetic transients program through a very small resistor. Figures 6.28-a

---

<sup>1</sup> Resistive, inductive and capacitive elements

and  $-b$ , respectively, show the simulated currents of the faulted winding A2 and the field winding. These results are in better agreement with the experimental results (Figure 6.24) compared to the simulation results obtained from the model with the conventional damper winding representation (Figure 6.25).

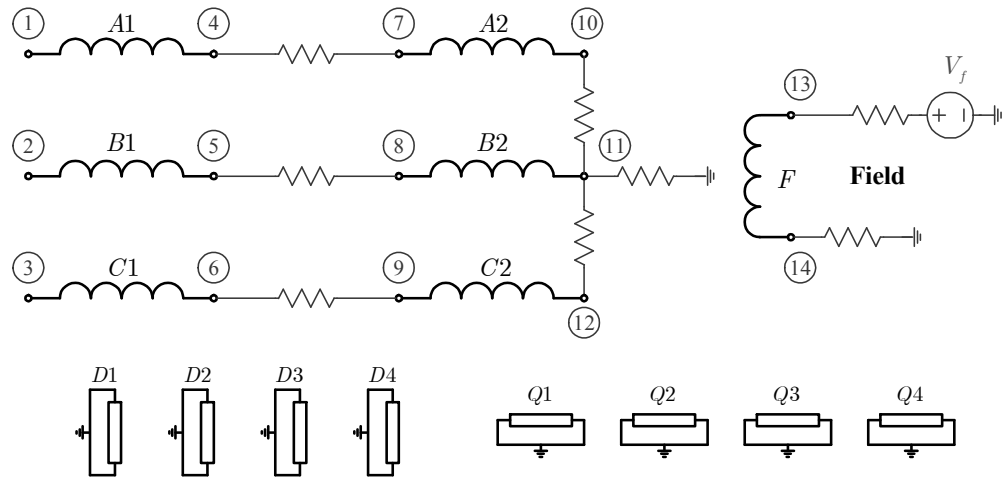


**Figure 6.27:** Diagram of the synchronous machine model with a detailed damper representation embedded in a stand-alone electromagnetic transients program

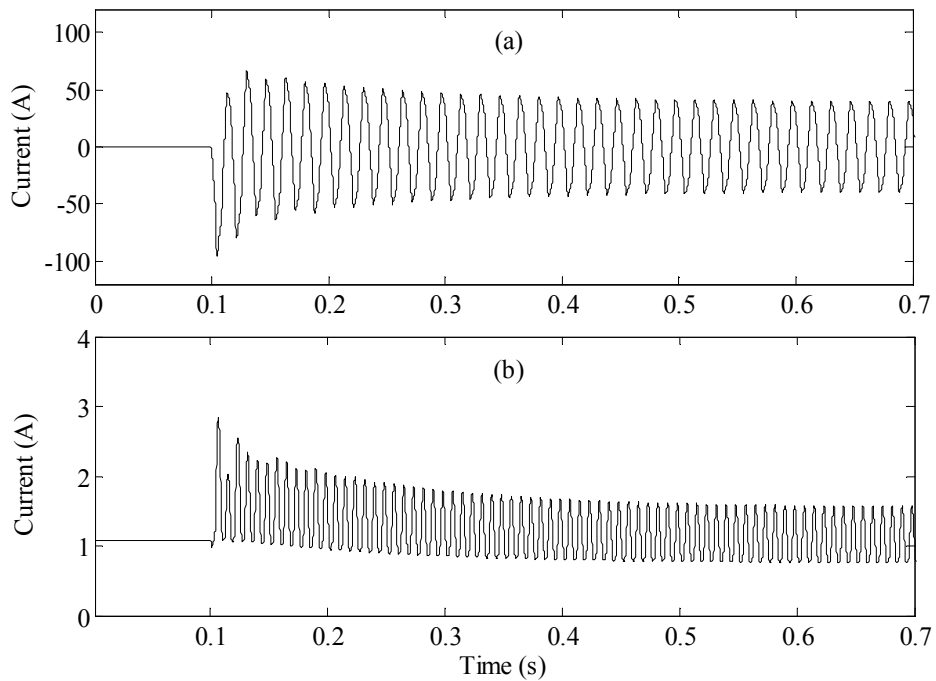


**Figure 6.28:** Simulated transient currents of a short circuit on the stator winding A2 using the model with individual damper windings for each pole: a) faulted winding A2, b) the field winding

Figures 6.29-a and 6.29-b, respectively, show the steady-state simulated current of the faulted winding A2 and currents of the d-axis damper windings. The rotor windings in the model are normalized to the stator and therefore the magnitude of damper currents (Figure 6.29-b) is reflected to the stator side. As can be seen, at any positive or negative peak of the stator current, one of the damper winding currents ( $D_1$ - $D_4$ ) peaks. Also, the current in each of these d-axis damper windings is phase shifted from the current of the neighboring d-axis damper winding, which would not be represented with a single damper winding.

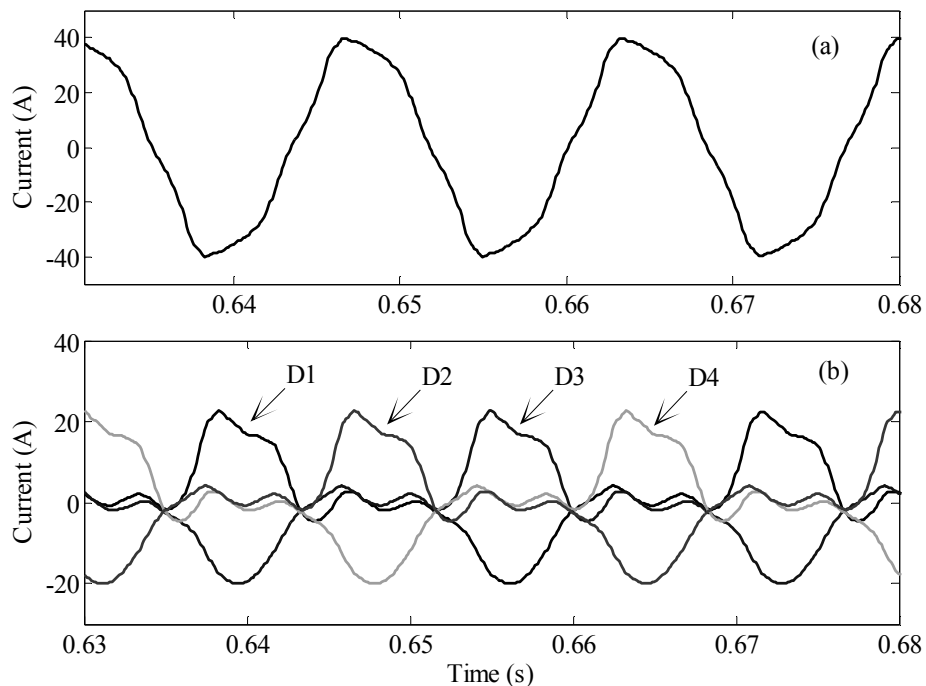


**Figure 6.29:** Steady-state simulated waveforms of a short circuit on the stator winding A2 using the model with individual damper windings for each pole: a) the current in the faulted winding A2, b) currents of the d-axis damper windings (D1-D4) reflected to the stator side.

It should be noted that this detailed machine model (with individual d- and q-axis damper windings for each pole) and the model with the conventional damper representation generate identical stator currents for **external faults** such as **terminal-**

**neutral** and **three-phase** faults. The terminal-neutral fault of Section 6.2.2.1 (i.e. an external fault) is simulated using the machine model with individual d- and q-axis damper windings for each pole with the machine operating at the same pre-fault conditions. Figure 6.30-a shows the steady-state simulated phase A current in this machine model. Comparison of the waveforms in Figures 6.30-a and 6.23-a shows that, consideration of individual d- and q-axis damper windings for each pole does not affect the behaviour of the machine for external faults, and validates the long used conventional approach of modeling the damper grid for such faults. Figure 6.30-b shows the steady-state simulated currents of the d-axis damper windings in this machine model. As can be seen, the four dampers have identical currents contrary to the situation in Figure 6.29-b.

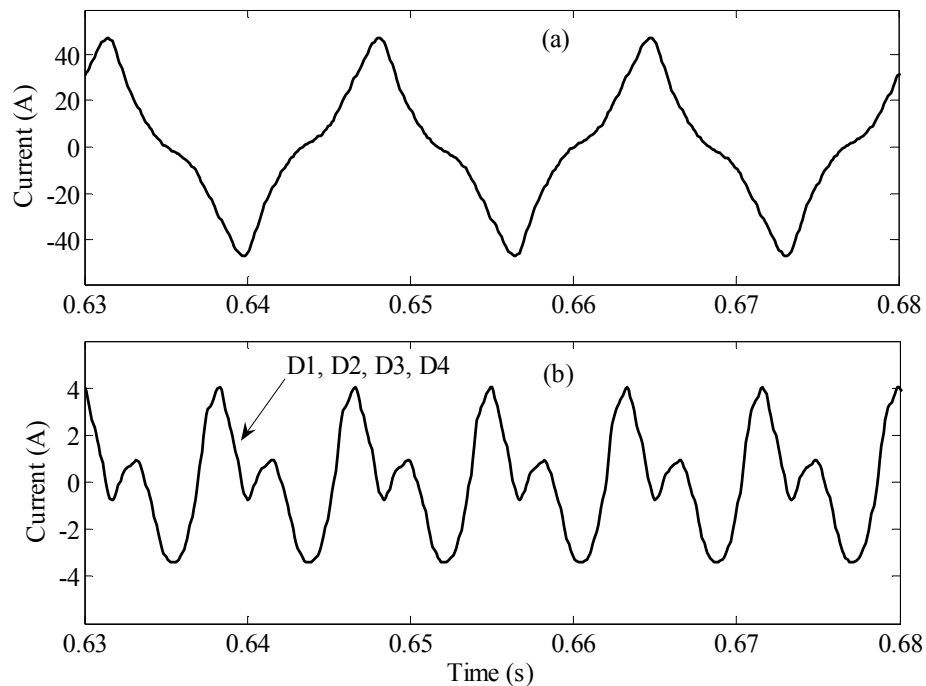


**Figure 6.30:** Steady-state simulated currents of a terminal-to-neutral short circuit using the model with individual damper windings for each pole: a) phase current, b) currents of the d-axis damper windings (D1-D4) reflected to the stator side. (Curves are indistinguishable)

For this internal fault (a solid short circuit on the winding A2) the simulation results can be improved even further by modeling the rotor damper grid in the form of a cage [30], [56], [67]. As explained, every d-axis damper winding is between two q-axis damper windings and shares damper bars with each of these windings. As shown in Figure 6.31, in addition to the effects of mutual inductances, a current flow in a d-axis damper winding causes the leakage flux of the shared bars to be induced on the neighboring q-axis windings. This effect is considered by superposing the leakage inductance of the damper bars to the off-diagonal elements of the rotor inductance matrix [67]. Similar arrangement is done for the resistance matrix of the rotor dampers [67].

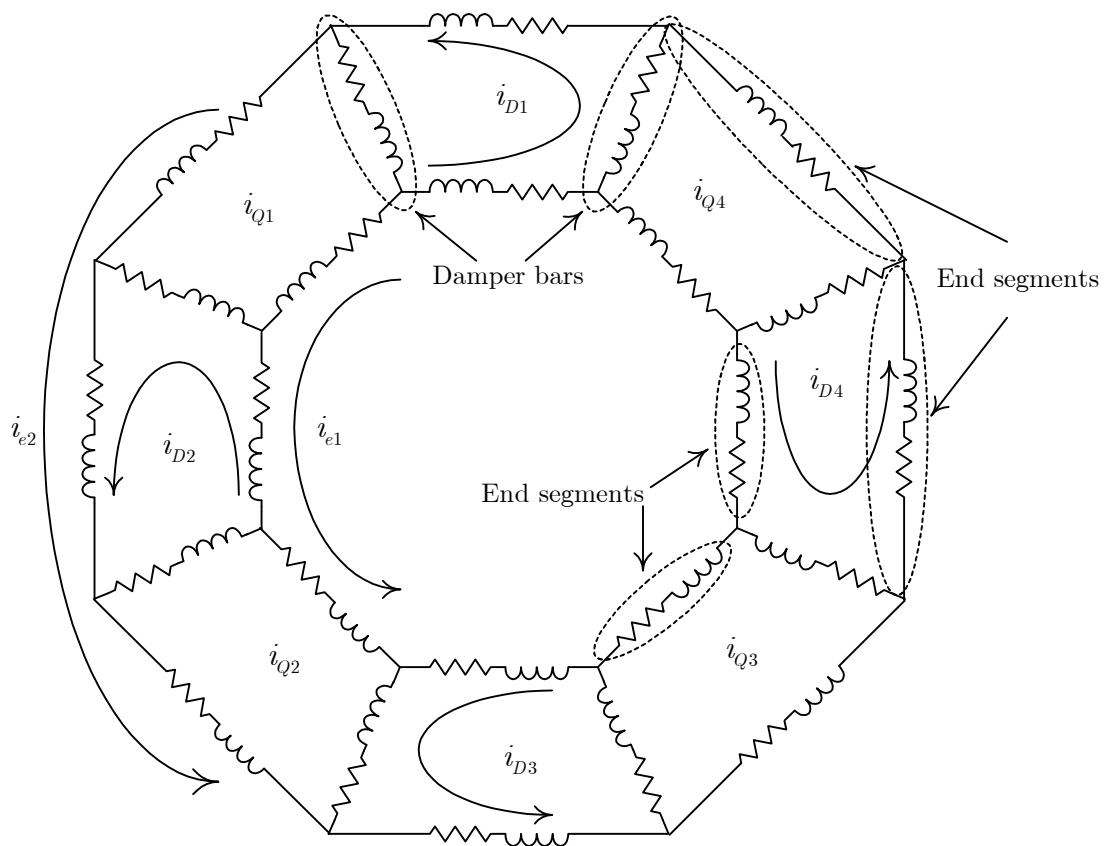


**Figure 6.31:** Equivalent circuit of the rotor damper cage showing rotor loop currents and end ring currents



Figures 6.32-a and 6.32-b, respectively, show the steady-state simulated current of the faulted winding A2 using the machine model with four d-axis and four q-axis damper windings and the one with the damper grid modeled in a form of a cage. Figure 6.32-c shows the current of A2 captured experimentally. As shown, there is good agreement between the experiment and the machine model in which the damper grid is simulated in the form of a cage.

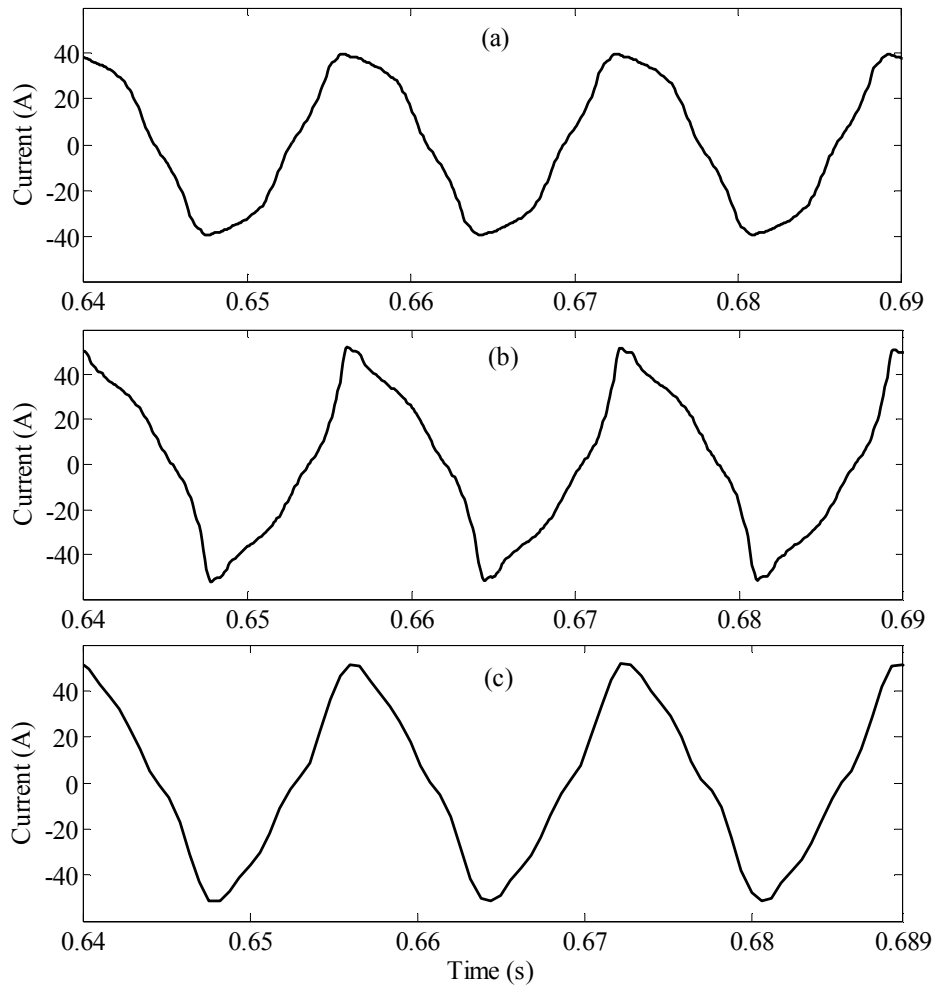


**Figure 6.32:** Experimental and simulated currents of a short circuit on the stator winding A2 in the steady-state: a) simulated using a model with 4 d-axis and 4 q-axis damper winding, b) simulated using a model with damper grid modeled as a cage, c) Experiment

With the present technology, it is not foreseeable that RTDS computational capability will be sufficient for modeling the damper grid as individual dampers for each pole. However, as technology improves, modeling additional damper windings may become possible. The number of these damper windings will be defined by technology and accuracy requirements.

### ***6.2.2.3 Comments on Possible Adaptability of the Machine Model with Conventional Damper Windings for Representing Internal Faults***

It could be argued that the error in the results of the machine model with conventional damper winding representation could be remedied by adjusting some of the parameters of the machine such as leakage inductances of the stator and rotor side. To investigate this possibility, the stator leakage inductances, field winding leakage inductance, and damper windings leakage inductances of this machine model were varied over a range from 0.01 to 10.0 times of the nominal leakages, and the internal fault between nodes  $AJ$  and the neutral was simulated for each set of these leakage inductances. As expected, by decreasing these leakage inductances the current of the faulted winding  $A2$  increases. However this change is relatively small, and the steady-state peak value of the fault current does not exceed  $20 A$ , even with very small leakage inductances (the actual fault current has a peak value of  $50 A$ ). Therefore detailed representation of the damper grid, as discussed in the previous section, is necessary for proper modeling of this internal fault.

## **6.3 Chapter Contributions and Conclusions**

The new real-time embedded machine model was systematically validated using simulations and laboratory experiments. By comparing this new model against the

existing interfaced dq-based models of electromagnetic transients programs, the capabilities of this model in *accurate solving* of the *differential equations* of synchronous machines were confirmed. The *Numerical stability* of the model was also assessed in this chapter.

Laboratory experiments showed that this new model properly represents the effects of *non-sinusoidally distributed windings*, and *the actual shape of the pole-arc*. Also the effects of *operating point dependent saturation* were included correctly in this model.

For modeling some internal faults, it is necessary to consider the *actual damper* grid instead of the conventional representation of *equivalent damper windings* in d- and q-axis. When this is not possible, individual d- and q- damper windings can be considered for each pole, which improves the simulation results significantly. The accuracy of this approach can be improved by considering more windings for each pole and by taking into account the fact that these rotor windings are connected in the form of a cage.

***Generalization of this concept to other synchronous machines with larger number of poles and different winding distribution requires further research.***

# Chapter 7: Application of the New Real-Time Model in Synchronous Generators Protection Studies

---

The new embedded phase-domain machine model is implemented in a real-time digital simulator RTDS. This model was validated as described in Chapter 6 using laboratory experiments. This model is intended to be used in the testing of some stator fault protection schemes in synchronous machines. In this chapter, the capabilities of this machine model in testing the stator-ground fault protection schemes are demonstrated.

## 7.1 Introduction

Stator-ground faults are amongst the most frequent causes of damage to the stator windings of synchronous machines and a direct cause of phase-phase faults [44], [95]. An undetected or non-cleared ground fault could develop into a phase-to-phase fault or into an inter-winding fault if another single-phase-to-ground fault occurs [96]-[98]. This can inflict significant damage to the generator.

The amount of current which flows during a phase-to-ground fault depends on the configuration of grounding in the stator of generators. In many applications, generator neutrals are grounded through an impedance to limit ground fault currents and to provide means to detect ground faults. Two common methods of stator grounding are *low-impedance* and *high-impedance* grounding [96]-[98].

In the low impedance grounding method, a resistor or a reactor is connected between the generator neutral and the ground. In general, this impedance is selected to limit the

generator's contribution to a single-phase-to-ground fault at its terminals to a value up to 150% of rated full-load current [98]. Solid connection of the neutral to ground is not recommended [97], [99] as a stator-ground fault in this case will be equivalent to a turn-turn fault causing a large amount of current to flow in the faulted winding. In this type of grounding, a stator-ground fault provides sufficient current for differential relaying systems. The capabilities of the new real time machine model for *testing differential protection schemes* of stator-ground fault are explained briefly in Section 7.2.

In the high-impedance grounding method, a distribution transformer is connected between the generator neutral and ground, and a resistor is installed across the transformer secondary. The resistor limits the ground fault current, and the transformer's secondary voltage can be used to detect ground faults. The high impedance normally limits the fault current to levels considerably below the practical sensitivity of the differential relay [96]. Therefore, differential relaying will not detect stator ground faults in high-impedance grounded generators. One of the protection schemes which is used in case of high impedance grounding is based on the existence of the third harmonic voltage on the neutral and terminals of synchronous machines. Section 7.3 explains the procedure for using the new machine model in the setting and testing of such relays.

## **7.2 Differential Protection for Stator-Ground Faults**

As stated in the introductory section of this chapter, in the low impedance grounding method for synchronous generators, a stator-ground fault provides sufficient current for differential relaying systems. Figure 7.1 shows the fundamental technique of using the differential scheme for stator-ground fault protection [97]. For each phase, during normal operation, the current flowing in essentially equals the current flowing out. However,

during a fault between a stator winding and ground the flow of fault current  $I_f$  causes an unbalance between the incoming and outgoing currents of that winding. This difference between the currents of the two sides of a winding enables the differential relay to detect the stator-ground fault.

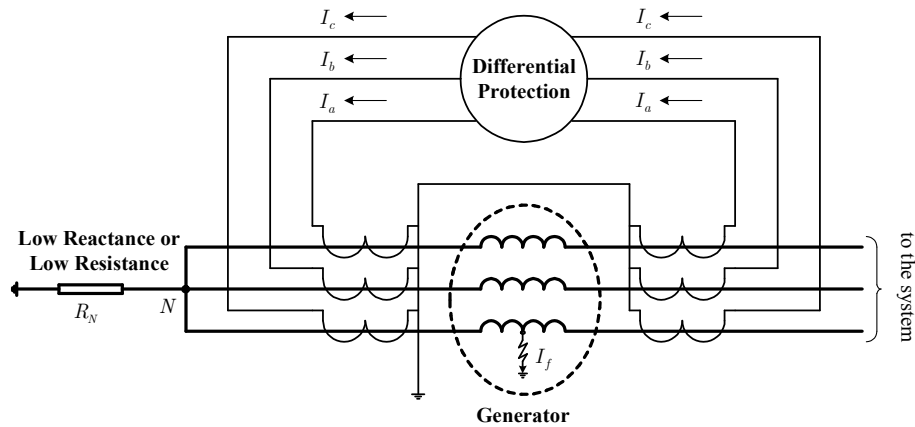


**Figure 7.1:** Basic current differential scheme for the generator stator-ground fault protection

Because the new synchronous machine model for a real-time simulator (RTDS), developed in this thesis, allows application of internal faults, it is useful for closed-loop testing of differential relays designed to protect synchronous generators against stator-ground faults. As mentioned in Section 1.2, in closed-loop testing the actual relay is connected to the real-time simulator, and is therefore subject to waveforms similar to those that it would experience in a field application. Furthermore any trip signal provided by the relay can operate circuit-breaker models in the simulation. Hence, this type of simulation is a very realistic representation of the true field experience that the relay would be subject to.

In this model as shown in Figure 6.9, the stator phase A is divided into two sub-windings  $A1$  and  $A2$  and the electric node  $AJ$  can be connected to the ground to simulate a stator-ground fault. The computed currents of sub-windings  $A1$  and  $A2$  in the RTDS

model are converted to analog signals using D/A converters and suitably amplified to conform to the input requirements of the differential relays under test [26].

As discussed in Section 6.2.2.2, due to computational speed limitations, the detailed damper grid, required for accurate modeling of internal faults, cannot be included in the RTDS model. Also, the more simplified machine model with conventional amortisseur winding representation causes an underestimation of the magnitude of the fault current. However, as industrial differential protection schemes are triggered by differential currents as low as 10% of the rated current [99], this model is still reasonable to use for such applications.

Additionally, as stated in the introductory section of this chapter, in the low impedance grounding method the grounding impedance is selected such that the terminal-ground fault will be limited to a value up to 150% of rated full-load current [98]. This means that, the grounding impedance is large enough to be a more important factor in determining the magnitude of fault current than the machine model itself. For the experimental machine in this thesis, a grounding resistance of  $5.3 \text{ Ohms}$  limits the terminal-ground fault to the above stated value. Using this grounding resistance, a fault between node  $AJ$  and the ground is simulated. The same pre-fault conditions as in Section 6.2.2.2 (rated speed and 97% of rated voltage) are applied here. Figure 7.2-a shows the simulated fault current from the custom model developed in Section 6.2.2.2, which represents the damper grid as equivalent windings along the d- and q-axis. This simulation is repeated using the machine model which considers the detailed damper cage, the results are shown in Figure 7.2-b. As verified in Section 6.2.2.2, this detailed machine model accurately generates the internal fault currents. A comparison between

Figures 7.2-a and -b shows that the error of the machine model with conventional damper winding representation is a more acceptable value of 21%. This error is much smaller in comparison with the 64% error for the solidly grounded stator (see Section 6.2.2.2).

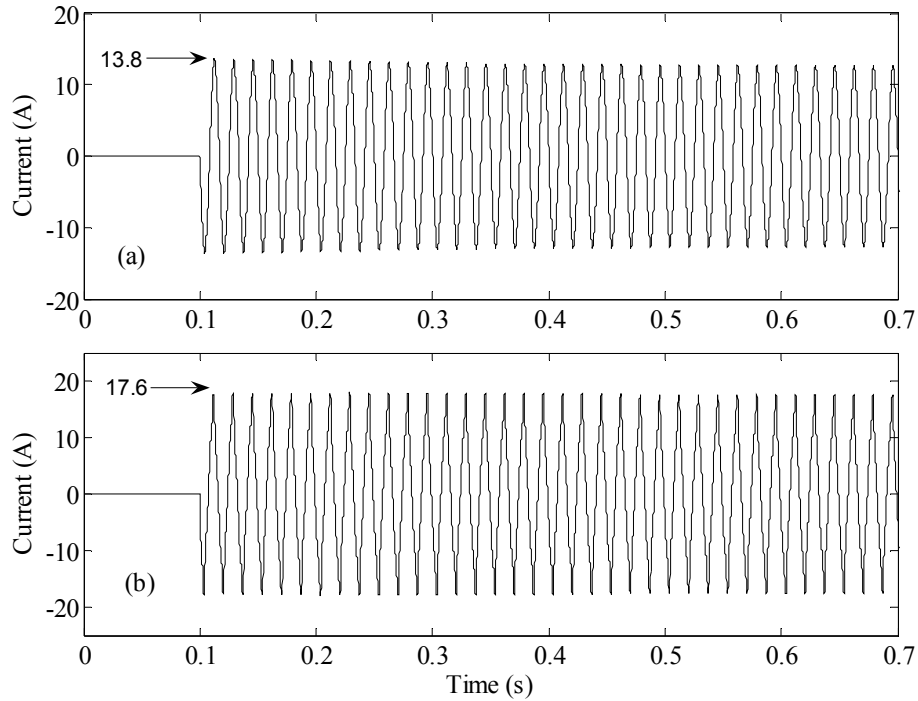


**Figure 7.2:** Simulated transient currents of a stator-ground fault (node *AJ*-to-ground) with a grounding resistance of 5.3 Ohm, a) conventional representation of the damper grid as d- and q-axis windings, b) damper grid modeled as a cage.

### 7.3 100% Stator-Ground Fault Protection Scheme

Synchronous generators produce some amount of third-harmonic voltage. These harmonic voltages are generated due to space harmonics of windings and non-sinusoidal permeance of the machine [70]. Figure 7.3 is a conceptual circuit diagram of a synchronous machine with the neutral connected to the ground through a resistance  $R_N$ . In this figure,  $C_N$  represents the equivalent lumped charging capacitance-to-ground of the stator winding at the ground end of the winding, and  $C_T$  represents the equivalent lumped capacitance-to-ground at the stator terminal (windings, cables, etc.) [95], [96].



When no fault is present, the voltages across the stator windings of the synchronous machine contain the fundamental component in addition to the odd harmonics [70]. As the machine is balanced, only the harmonics of order  $3k, k \in 1, 3, \dots$  are present in the neutral-ground voltage of the machine,  $v_N$ , whereas the terminal-ground voltage,  $v_T$ , contains the fundamental component and all the odd harmonics. During normal operation, the magnitude of the third harmonic voltage in the neutral and terminal of the machine,  $V_{N3}$  and  $V_{T3}$ , depends on the magnitude of the third harmonic voltage across the winding and impedance values of  $C_N, C_T$  and  $R_N$  [95], [96]. During a stator-to-ground fault, the third harmonic components in the neutral, as well as, on the phase terminals change. This change is used as a signature to detect the ground fault [95]-[98]. This detection method is commonly [96]-[98] referred to as the “**100% stator-ground fault protection scheme**”.

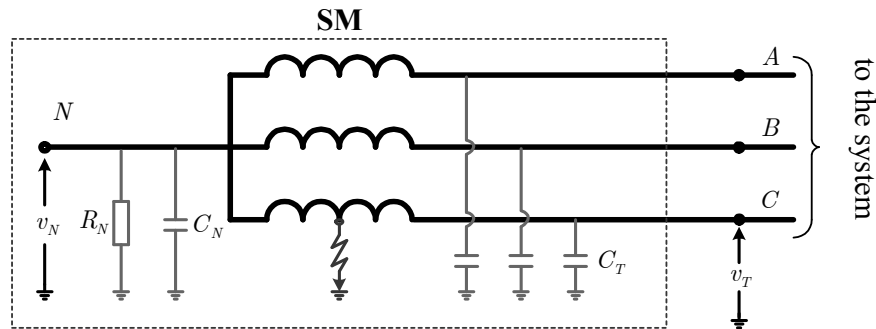


**Figure 7.3:** Circuit diagram of a stator-ground fault in a synchronous machine

As discussed above, the third harmonic voltage on the neutral and terminals exists even without a stator-ground fault. Hence in the industrial commissioning of such relays, one of the requirements is recording these harmonic voltages at different operating points as the loading conditions affect the magnitude of these signals [95], [96], [98].

In the present day industrial practice, this procedure must be carried out individually for each machine type using a laboratory setup. In order to expedite the setting process, relay manufacturers and utilities have expressed the desire to have EMTP-type models that would show this third harmonic behavior. The detailed MWFA-based synchronous machine model developed in this thesis is a good candidate for such applications. The model considers the actual distribution of the windings, the shape of the pole-arc; and the effects of operating point dependent saturation. Therefore correct modeling of harmonics such as the third harmonic voltage across the winding and their variation with loading is ensured. Furthermore, the model is developed for a real-time simulator (RTDS), so it can also be used for on-line closed-loop testing of the relay performance.

### **7.3.1 Shortcomings of the Dq-based Models in this Application**

Some authors have modified the phase-domain dq0-based models of synchronous machines to simulate internal faults [39]-[41], [45], [47]-[53]. These authors calculated the approximate inductances of faulted windings based on the assumption that the inductances of unfaulted windings are in the form of equations (3.4)-to-(3.15). Numerical methods were then employed for time-domain simulation of an isolated case which consists of a synchronous machine and a source.

In [47], [48] the inductances of faulted windings were calculated from the inductances of healthy windings based on the turns ratio of the faulted winding. The symmetrical component approach were used in [49], [50] to compute the internal fault currents of the machine based on the inductances computed in [47], [48].

Synchronous machine armature windings are the combination of coils in different angular positions connected in series and in parallel. In [53], using proper turns ratios and

angular shifts, the inductances of faulted windings of a synchronous machine were calculated.

Authors of [39]-[41] assumed that the faulted portions of armature windings create approximately sinusoidally distributed magnetomotive forces in the stator space. Therefore, a faulted armature winding was divided into two sinusoidally distributed windings in specific angular positions [39]. Using this technique the analytical formulae for the faulted inductances were also presented.

Although these models are developed primarily for simulating synchronous machine internal faults, in healthy conditions such models have identical time-domain responses to dq0-based models and generate no time harmonics. *Therefore, these models cannot be used for the testing of this “100% stator-ground fault protection scheme”.*

### **7.3.2 Validation of the Detailed Phase-Domain Machine Model Regarding the Generation of the 3rd Harmonic Voltage**

As stated above, the “100 stator-ground fault protection scheme” operates based on the 3<sup>rd</sup> harmonic component of winding voltages. In this section, the harmonic contents of winding voltages obtained from the new embedded phase-domain model and laboratory experiment are compared and presented.

In Figures 6.16a, and 6.17a, the steady-state simulated stator phase-to-neutral voltages of the machine are compared against the experimental results for a leading power factor load and a resistive load. Very good agreement between the experiment and simulation was achieved. These curves are re-plotted here in Figures 7.4-a and 7.5-a, respectively. Figures 7.4-b and 7.5-b, respectively, show the harmonic spectrums of the voltage waveforms in Figures 7.4-a and 7.5-a.

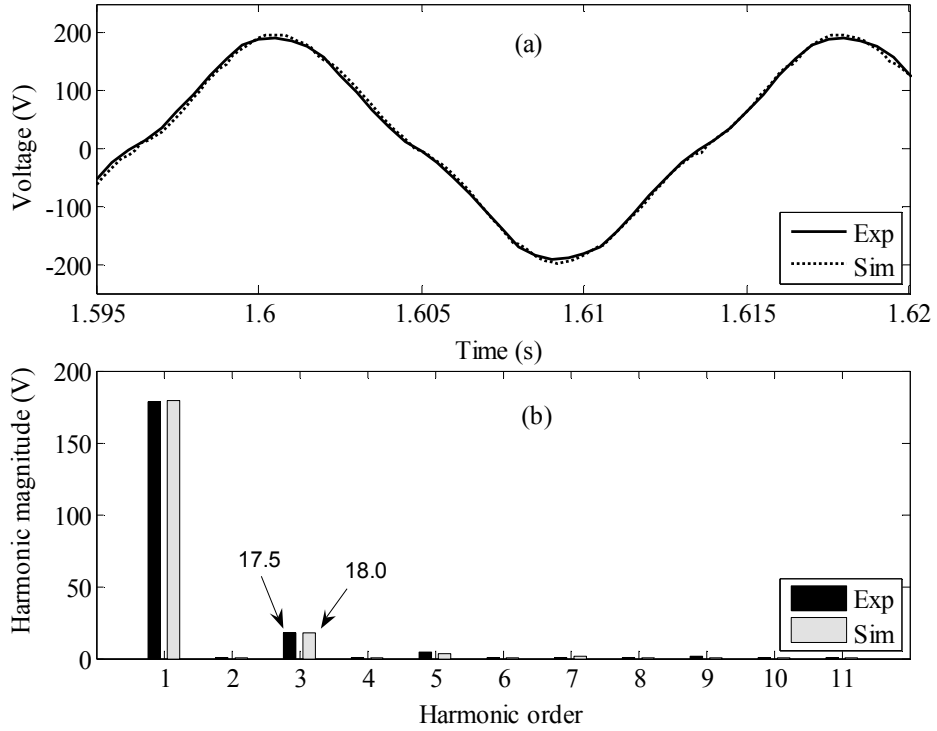


**Figure 7.4:** Experimental and simulated voltage across the stator phase-A with the R-C load a) steady state waveform, b) harmonic spectrum (peak magnitude).

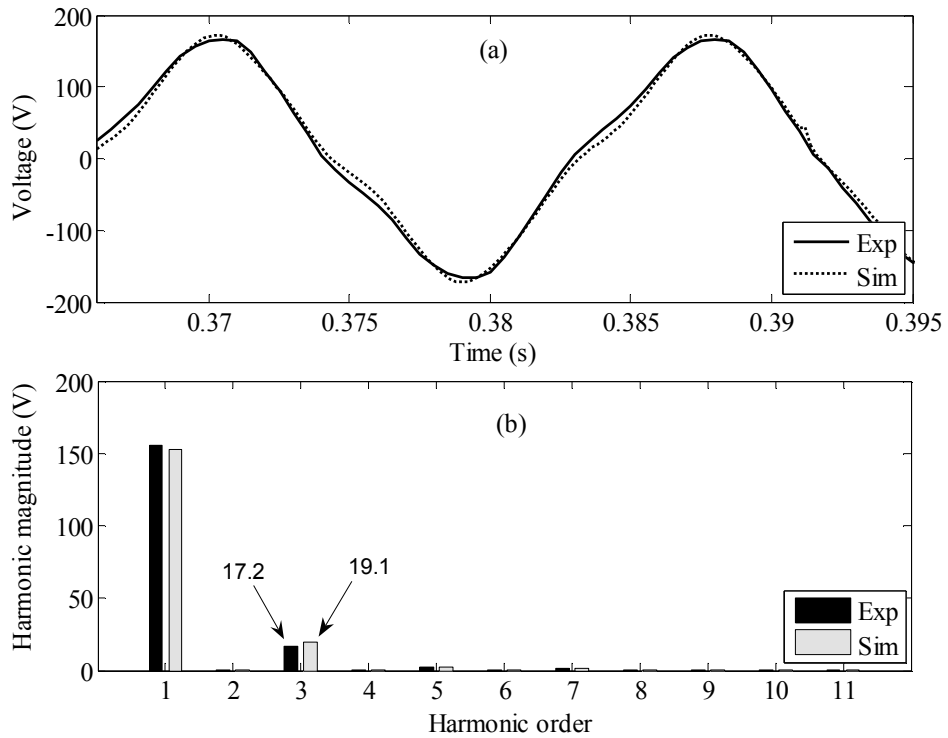


**Figure 7.5:** Experimental and simulated voltage across the stator phase-A with the resistive load: a) steady state waveform, b) harmonic spectrum (peak magnitude).

As can be seen, the third harmonic component in the phase voltage is considerable (17.5 V for the R-C test and 17.2 V for the resistive load). Also, the third harmonic component of the simulated waveforms shows good agreement with the experiment in both tests (18.0 V for the R-C test and 19.1 V for the resistive load).

### 7.3.3 Simulation for the Purpose of Relay Setting Determination

In this section, using the new embedded phase-domain machine model, variation of the third harmonic voltage in the neutral and terminals of the machine is studied. This exercise demonstrates the capability of this new machine model in setting the relays designed to detect stator-ground faults in synchronous machines using the “100% stator-ground fault protection scheme”.

Figure 7.6 shows a part of the simulated circuit as drawn in RSCAD, the human-machine interface for the RTDS simulator [26]. The neutral and terminals are connected to the ground using the neutral resistance and charging capacitances mentioned at the beginning of Section 7.2. The stator terminals are connected to a dynamic load which can be altered during the simulation in *RUN TIME* environment [26]. As mentioned, in the new embedded phase-domain machine model developed in the RTDS environment, the stator phase A is divided into two sub-windings *A1* and *A2*. Node *NAJ* represents a point in the stator phase-A winding which divides phase-A into two sub-windings A1 and A2. This node can be connected to ground through a fault model (externally specified time-dependent impedance) to simulate the effects of a stator-ground fault. The machine is run at rated speed, and excitation voltage is set so that rated terminal voltage is achieved with a 1 pu, 0.8 pf  $\Delta$ -connected series R-L load. The circuit is simulated in *real-time* on the *GPC hardware card* of RTDS [26] with a simulation time-step of  $50\mu\text{s}$ .

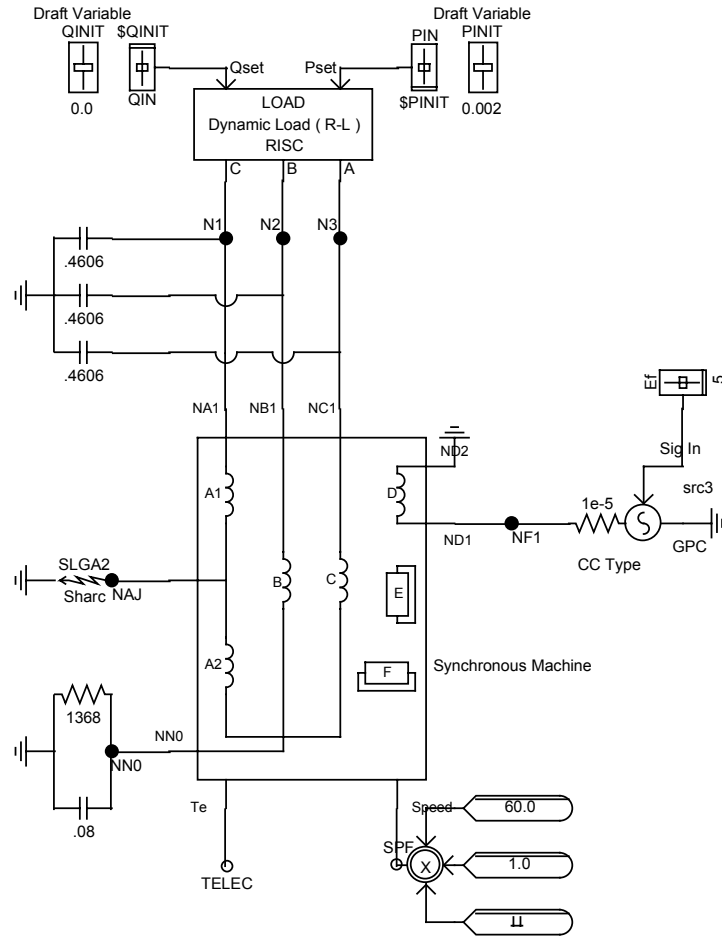


**Figure 7.6:** RSCAD draft circuit used for the simulation of the 3<sup>rd</sup> harmonic voltage

In this example, stator sub-winding A1 has 80 turns and sub-winding A2 contains the remaining 16. Using the procedure discussed in Section 3.4 of this thesis, the inductances of machine windings including faulted windings A1 and A2 can be computed for various operating points and rotor positions.

As an example, the inductances of windings A1 and A2 in a loading condition, where  $i_{md} = 1.2$  pu and  $i_{mq} = 1.4$  pu, are shown in Figure 7.7. The variations of the self inductance of sub-winding A1 ( $L_{A1A1}$ ) and the self inductance of sub-winding A2 ( $L_{A2A2}$ )

with rotor position are shown in Figure 7.7-a. Also Figure 7.7-b shows the mutual inductances between sub-winding A1 and A2 and the field winding ( $L_{A1F}$  and  $L_{A2F}$ , respectively).

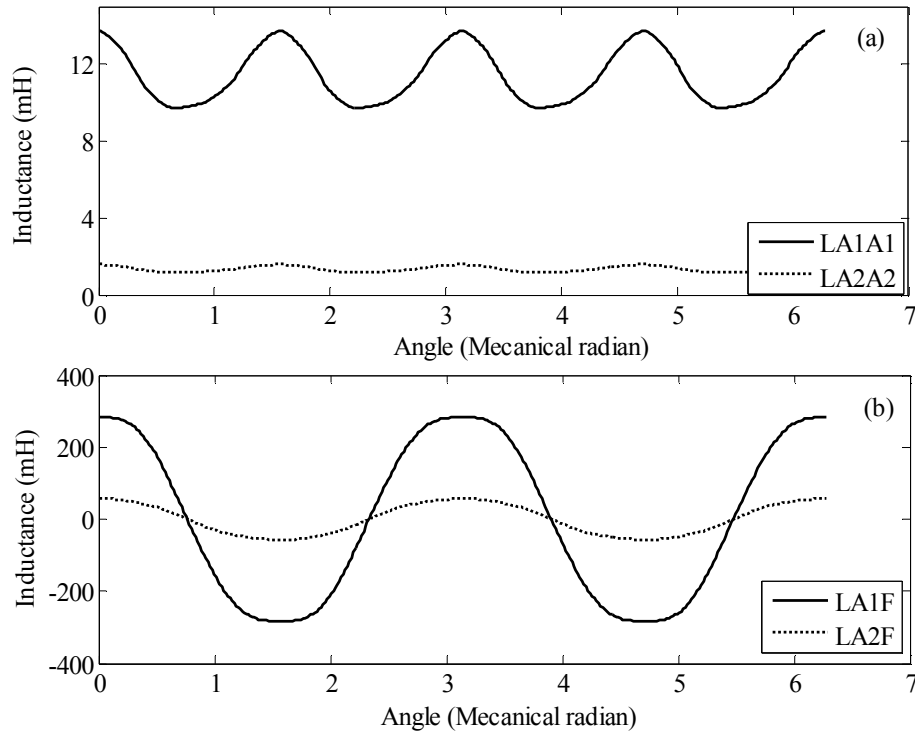


**Figure 7.7:** Saturated inductances of faulted windings generated using MWFA, a) self inductances of windings A1 and A2, b) mutual inductances between the field winding and sub-windings A1 and A2.

Figure 7.8a shows the variation of neutral voltage during a fault between node NAJ and ground. As can be seen, before the fault this signal is mostly the third harmonic with the peak value of 13.1V. After the fault, the neutral voltage contains the fundamental component as well. This is because the machine is operating in an unbalanced condition. The peak value of the third harmonic however is reduced to 2.1 V, as determined from Fourier analysis (not shown). The variation of the neutral voltage during a fault between the terminal node NA1 and the ground (SL-G) is shown in Figure 7.8b, where the peak value of the third harmonic voltage changes from 13.1V to 15.8V. The simulation of the

SL-G fault is repeated with a dq-based machine model and the results are shown in Figure 7.8c. As can be seen, no voltage exists on the neutral of this machine before the fault (which is incorrect), and this voltage contains only the fundamental frequency after the fault. *This clearly shows that a conventional dq-based model would be inadequate for a real time simulator required for testing such protection schemes.*

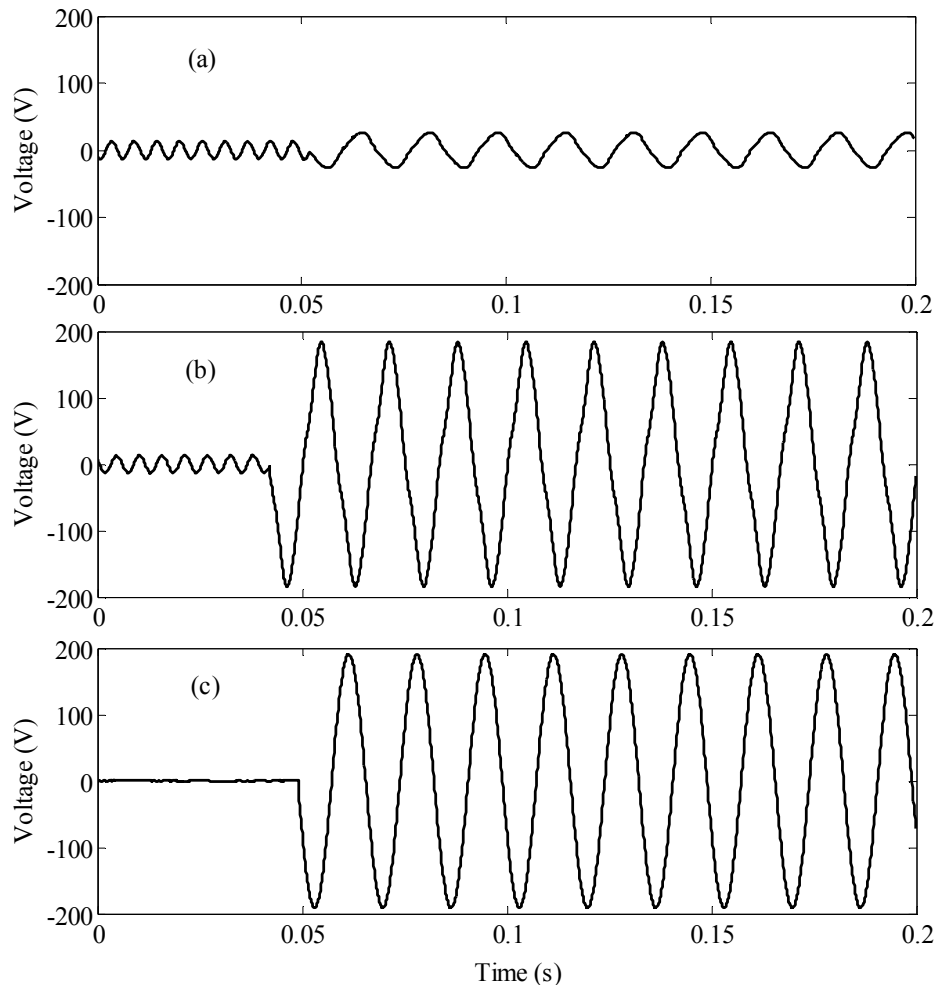


**Figure 7.8: Neutral voltage during a stator-ground fault a) ground fault on node NAJ, b) ground fault on terminal node NA1, c) ground fault on terminal node NA1 in a dq-based machine model.**

As mentioned earlier, in the industrial commissioning of relays designed to detect stator-ground faults based on the “100% stator-ground fault protection scheme”, one of



the requirements is the recording of the third harmonic voltage of terminals and the neutral at different operating points. By running a pre-programmed automated sequence of runs, using the RSCAD's Script feature [26], the circuit in Figure 7.6 is simulated in real-time on the RTDS hardware with the load absorbing various active and reactive powers. In each set of active and reactive powers, the third harmonic component of the neutral and terminal voltages ( $V_{N3}$  and  $V_{T3}$ ) are recorded after the circuit reaches the steady state condition.

Figures 7.9 and 7.10 show the variation of the third harmonic component in the neutral and the terminals respectively. These figures are generated by dynamically changing the resistor and inductances of the load and recording the active and reactive power of the load and the third harmonic component of the neutral and terminals voltages.

As shown, the active power significantly affects the value of the third harmonic voltage, which is also reported in [95], [98]. The variation of the third harmonic voltage with the active power is comparable to the variation of this signal with a stator-to-ground fault. This re-affirms the need to record the pre-fault values of the third harmonic voltage in the neutral and terminals to avoid ambiguity in detecting the fault. Using these pre-determined values for ambient 3<sup>rd</sup> harmonic voltage in stator and neutral terminals, the threshold settings for the relay can later be determined [96].

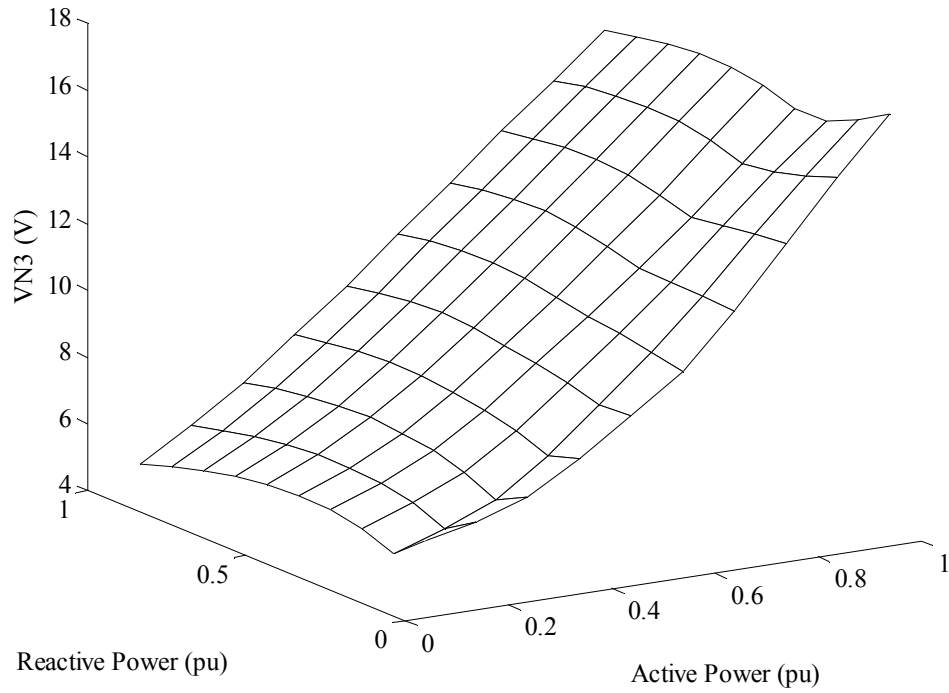


**Figure 7.9:** Neutral voltage 3<sup>rd</sup> harmonic component as a function of active and reactive power loading

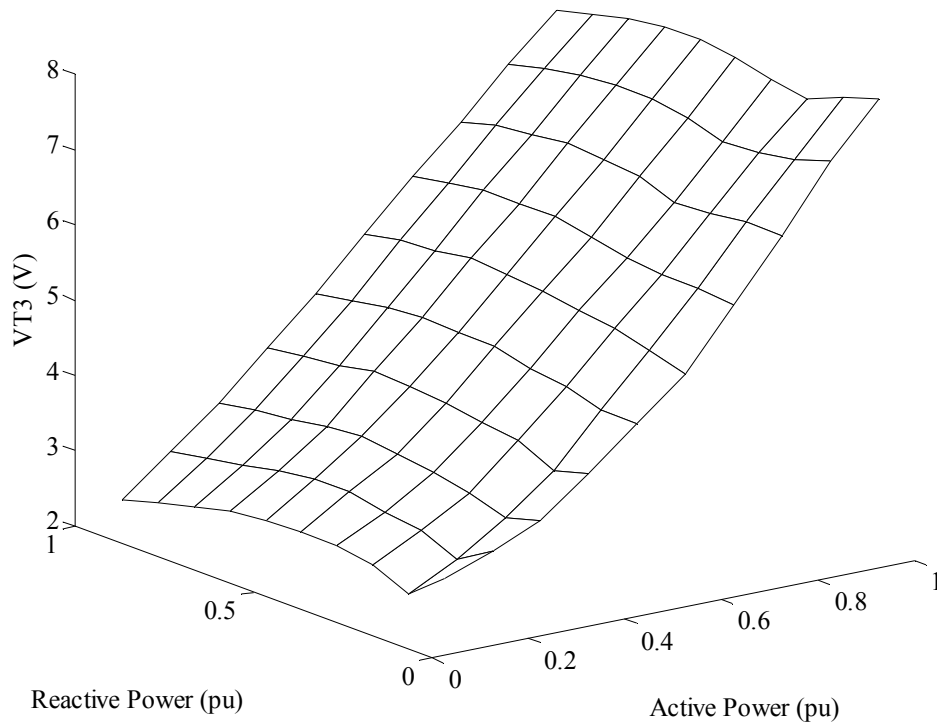


**Figure 7.10:** Terminal voltage 3<sup>rd</sup> harmonic component as a function of active and reactive power loading

## 7.4 Chapter Contributions and Conclusions

The stator-ground fault protection schemes for synchronous generators were briefly introduced in this chapter. The capabilities of the new *real-time* synchronous machine model in the closed-loop testing of a “*differential protection scheme*” and a “*100% stator-ground fault protection scheme*” were demonstrated.

As discussed, in some of the stator-ground fault protection schemes, the *third harmonic voltage in the neutral and terminals* of the machine are utilized to detect a stator-to-ground fault. These harmonics are generated due to the non-sinusoidal distribution of the windings and machine permeance. It was demonstrated that the new machine model properly represents these harmonics and their variation with *fault* and *loading conditions*. This is because, this new model considers effects of winding distribution, rotor geometry and *operating-point dependent saturation*. Therefore it can be used in setting the relays designed to detect stator-ground faults in synchronous machines using such harmonics.

# Chapter 8: Conclusions and Future Directions

---

This thesis has contributed to advances in electric machine models for electromagnetic transient simulation programs and real-time digital simulators. The new tools and techniques, developed in this thesis, expand the application of real-time digital simulators to closed-loop testing of protection relays designed to protect synchronous machines against internal faults. In addition, the effects of magnetic saturation are modeled more accurately compared to previous models in electromagnetic transients programs. Also numerical stability of the machine models has improved significantly.

This chapter summarizes the major contributions of the thesis and also identifies some other related areas where further research may be carried out.

## 8.1 Main Contributions of the Thesis

The followings are considered the main contributions of this thesis:

- To evaluate the inductances of synchronous machines, a winding function approach was developed in this thesis which is capable of taking into account the *actual distribution of windings, shape of the pole-arc*, and effects of *operating point-dependent saturation*. The inductances of an experimental machine were evaluated using this approach and validated using the finite-element method and laboratory measurements.
- An *embedded phase-domain approach* was developed for the *time-domain simulation* of electric machines in off-line and real-time electromagnetic

transients programs. Particular techniques were established to *speed up* the time-domain simulation of the model, and *special considerations* were introduced for the *real-time* implementation of this model. The accuracy and numerical stability of the model were also validated.

- Laboratory experiments were conducted to show the capability of this new synchronous machine model in properly representing the *time-harmonics* generated due to non-sinusoidally distributed windings, and pole-arc. The importance of incorporating the effects of iron saturation into the procedure of calculating inductances was also discussed.
- An off-line EMTP-type program was developed to solve the network equations for an arbitrary external network and an embedded phase-domain machine model. The damper grid of this machine model was represented by considering individual d- and q-axis damper windings for each pole. An internal fault can be applied to any of the stator windings. Effects of *damper grid representations* on simulating *turn-turn faults* were also investigated.
- Capabilities of this new *real-time* synchronous machine model in the closed-loop testing of *protection relays*, designed to protect synchronous machines against *stator-ground faults*, were demonstrated.

## 8.2 Summary of the Conclusions

The following conclusions were obtained during the progress of this thesis:

### 8.2.1 Method of Evaluating Synchronous Machine Inductances for the Purpose of Real-Time Simulation

Three known methods for evaluating electric machines inductances (the dq0 theory, the finite element method, and the modified winding function approach) were discussed. The relative merits for each of these approaches as to the level of modeling detail and accuracy of results and complexity were discussed. Unlike the dq0 approach, the MWFA is capable of taking into account details such as the *actual distribution of windings*. At the same time, the computational burden and input data for this approach is much lower than the finite element method. Consequently, the modified winding function approach is preferred as the main tool for computing synchronous machine inductances for the purpose of real-time digital simulation.

Based on the MWFA, the inductances calculated using the physical data are significantly different from the actual inductances. The cause of this error is the change in the permeance due to the presence of factors such as the rotor pole-shoe, stator slots, and the MMF drop in the iron. Although, the accuracy can be improved by taking into account these details in calculating the permeance function, such calculations need very detailed knowledge of the machine geometry, which may not be readily available.

To compensate for these effects, an *effective permeance function* was defined and used in the process of calculating inductances using MWFA. In this thesis, the effective permeance function was computed based on the *actual shape of the pole-arc* and *experimental* values of *d-, q- and 0-axis inductances*.

Any variation in the loading condition and the level of the synchronous machines field excitation changes the distribution of the magnetic flux and the intensity of saturation in different parts of the iron. Therefore, using a single permeance function to

compute synchronous machine inductances will not be valid for all loading conditions. To incorporate the effects of operating point-dependent saturation into the MWFA, the permeance function was adjusted based on the local magnitude of the magneto-motive force in each loading condition. The saturated inductances were stored in a tabular form as functions of rotor position, and the direct and quadrature axis magnetizing currents.

### **8.2.2 Embedded Phase-Domain Approach for Inclusion of the Machine Model in Electromagnetic Transients Programs**

The procedure of modeling electric machines in electromagnetic transients programs using the new *embedded phase-domain approach* was explained. This method was compared to the conventional *interface-based* approach. Generally the burden of *computation* and *communication* is higher in the embedded phase-domain approach, as the inductance matrix needs to be inverted in each time-step and elements of the equivalent admittance matrix are continuously changing. With the aid of new techniques such as *analytical inversion* of the inductance matrix, *merging electric nodes*, and *Fourier-based storage*, the described computational and computational loads were minimized.

It was shown that, the numerical stability of the embedded phase domain models is higher than the interfaced models. This can be crucial for situations where the operational frequency of the system or the component is higher than usual frequencies (50 or 60Hz).

### **8.2.3 Experimental Validation of the MWFA-Based Embedded Machine Model and Observations**

Inductances of an experimental synchronous machine were computed using the MWFA and the modifications, introduced in this thesis, were applied. Then the embedded phase domain machine model was utilized for time-domain simulation of this

experimental machine in the environment of a real-time digital simulator (RTDS<sup>®</sup>). Laboratory experiments were used to validate this model in healthy and faulted conditions.

It was shown that, even in unfaulted conditions, *time harmonics* exist in voltages and currents of the synchronous machine. The source of these harmonics is the non-sinusoidal distribution of the windings and the air-gap. These harmonics as well as the fundamental components vary with a change in the loading conditions of the machine. ***It was shown that the new MWFA-based phase-domain synchronous machine model shows all of the above effects properly.*** These time-harmonics are absent in the dq-based models as they assume sinusoidal distribution for the windings and permeance. It was also shown that, the inclusion of saturation effects into the MWFA is crucial for correct representation of these time-harmonics as well as the fundamental component in the voltages and currents of the machine.

It was also shown that, the conventional representation of the *damper grid* as equivalent shorted windings along the d- and q- axes is adequate for short circuit faults between external nodes like terminals and the neutral. However, for proper modeling of short circuits that involves a point inside a winding (*internal faults*) it might be necessary to model the damper grid as a detailed network which includes individual damper bars and end segments of each pole. It was shown that, representation of the damper grid by one d-axis damper winding and one q-axis damper winding for each pole is adequate for simulating the internal fault short circuit conducted in this thesis.



### 8.2.4 Application of the New Tool in Testing Protection Schemes of Synchronous Machines

The capabilities of this new real-time synchronous machine model in closed-loop testing of some protection schemes were demonstrated. The procedures of using this tool for closed-loop testing of a “*differential protection scheme*” and a “*100% stator-ground fault protection scheme*” were explained.

Some stator-ground fault protection schemes utilize the *third harmonic voltage in the neutral and terminals* of the machine to detect a stator-to-ground fault. These harmonics vary with a stator-to-ground *fault*, as well as, a change in *loading conditions*. The new machine model developed in this thesis properly represents these effects, and therefore is a good candidate for the testing of such protection schemes.

The use of the new detailed synchronous machine model in testing synchronous machine protection schemes opens new *industrial applications* for real-time digital simulators.

## 8.3 Thesis Publications

The followings are the publications arose during the progress of this thesis:

### 8.3.1 Refereed Journal Papers

1. A. B. Dehkordi, R.W. Menzies, T.L. Maguire, and, A.M Gole “Effects of Damper Grid Representation on Modeling Synchronous Machines Stator Turn-Turn Faults,” IEEE Trans. Energy Conversion, to be submitted for publication.
2. A. B. Dehkordi, P. Neti, A.M Gole, and T.L. Maguire, “Development and Validation of a Comprehensive Synchronous Machine Model for a Real-Time Environment,” IEEE Trans. Energy Conversion, Vol. 25, No. 1, March 2010.

### 8.3.2 Refereed Conference Papers

1. A.B. Dehkordi, D.S. Ouellette, P.A. Forsyth, "Protection Testing of a 100% Stator Ground Fault Scheme Using a Phase Domain Synchronous Machine Model in Real-Time," The 10th International Conference on Developments in Power System Protection (DPSP 2010), Manchester, UK, March-April 2010, submitted for publication.
2. A. B. Dehkordi, P. Neti, A.M Gole, and T.L. Maguire, "Development and Validation of a Comprehensive Synchronous Machine Model for a Real-Time Environment," 2009 IEEE Power & Energy Society General Meeting (PES 09), Calgary, July, 2009.
3. A.B. Dehkordi, A.M Gole, T.L. Maguire, and P. Neti, "A Real-Time Model for Testing Stator-Ground Fault Protection Schemes of Synchronous Machines", International Conference on Power System Transients (IPST 2009), Kyoto, June, 2009.
4. P. Neti, A.B. Dehkordi, and A.M Gole, "A New Robust Method To Detect Rotor Faults in Salient-Pole Synchronous Machines Using Structural Asymmetries", 2008 Industry Applications Society Annual Meeting (IAS 2008), Edmonton, Oct., 2008.
5. A. B. Dehkordi, A.M Gole, and T.L. Maguire, "Real-time Simulation of Internal Faults in Synchronous Machines", International Conference on Power System Transients (IPST 2007), Lyon, June, 2007.
6. R.C. Okonkwo, A. Dehkordi, A.M. Gole, and R. Hanitsch, "Permanent Magnet DC Linear Machine Model for Real Time Simulation", Canadian Conference on Electrical and Computer Engineering (CCECE 05), pp.1509-1512, May 2005.
7. A.B. Dehkordi, A.M Gole, and T.L. Maguire, " Permanent magnet synchronous machine model for real- time simulation", International Conference on Power System Transients (IPST 2005), Montreal, June, 2005.

## 8.4 Recommended Future Directions

The tools and techniques developed in this thesis show great potential for further research in this area both in the development of new advanced tools and applications.

### 8.4.1 Development of Detailed Induction Machine Models and Permanent Magnet Machines Models for Off-Line and Real-Time Electromagnetic Transients Programs

With the rapid expansion of distributed and small-scale generation plants such as wind farms and kinetic hydropower applications, more detailed and sophisticated tools

are needed to analyze these systems and study their interactions with the power system network.

Permanent magnet and induction generators play an important role in these small-scale grids. A permanent magnet machine generates harmonics due to the particular shape of the magnets. These harmonics can interact with power electronics and filters in small-scale grids and also the rest of the network. Development of detailed models of permanent magnet machines for off-line and real-time electromagnetic transients programs capable of representing these harmonics will be a very useful tool to analyze such effects. Similarly, there are interests to develop such detailed models for induction machines.

#### **8.4.2 Exploring New Applications for Real-Time Simulators in Protection Studies**

The capabilities of the new tool developed in this thesis for closed-loop testing of some protection relays were demonstrated. It would be a very useful research activity to explore new applications for the real-time digital simulators in protection studies.

Initially, a comprehensive study could be performed to analyze the common protection schemes of power equipment. In the next step, the feasibility of utilizing the existing models of equipment in closed loop testing of the above schemes can be assessed. It will be necessary in many cases to develop new models to be able to test the performance of other protection schemes using the real-time digital simulators.

#### **8.4.3 Further Study for Proper Representation of Damper Grids for Modeling Internal Faults**

It was shown that, the conventional representation of the *damper grid* as equivalent shorted windings along the d- and q- axes causes large errors in modeling *internal short*

*circuit faults* for the experimental machine considered in this thesis. For accurate modeling of these faults, the damper grid of the experimental machine was represented as a detailed network which considered individual damper bars and end segments of each pole. Such sophisticated representation of damper grids puts a large computational burden on the simulation, and therefore real-time simulation of a machine model with such damper grid representation is currently not feasible.

Further research is needed to investigate the level of detail needed for proper representation of the damper grid when synchronous machines with a higher *number of poles* and different *winding distributions* are subjects of internal faults studies. It will also be useful to find out the amount of error caused by conventional representation of damper windings in the above situations. References

# References:

---

- [1] P.S. Kundur, *Power system stability and control*, New York, McGraw-Hill., 1983, Chapter 3.
- [2] H. W. Dommel, "Digital computer solution of electromagnetic transients in single and multiphase networks," *IEEE Trans. Power Apparatus and Systems*, vol. PAS-88, no. 4, pp. 388-399, April 1969.
- [3] O. Anaya-Lara, E. Acha, "Modeling and analysis of custom power system by PSCAD/EMTDC," *IEEE Trans. Power Delivery*, vol. 17, no. 1, pp. 266-272, January 2002.
- [4] Y. H. Liu, J. Arrillaga, N. R. Watson, "Multi-level voltage sourced conversion by voltage re-injection at six times the fundamental frequency," *IEE Proc.-Electric Power Applications*, vol. 149, no. 3, pp. 201-207, May 2002.
- [5] D. A. Woodford, A. M. Gole and R. W. Menzies, "Digital simulation of dc links and ac machines," *IEEE Trans. Power Apparatus and Systems*, vol. PAS-102, no. 6, pp.1616-1623, June 1983.
- [6] "RTDS Technologies Inc.", Web address: <http://www.rtds.com>.
- [7] J. R. Marti and T. O. Myers, "Phase-domain induction motor model for power system simulators," in Proc. IEEE Conf. Communications, Power, and Computing, vol. 2, pp. 276-282, May 1995.
- [8] J.R. Marti and K.W. Louie, "A phase-domain synchronous generator model including saturation effects," *IEEE Trans. Power Systems*, vol. 12, No.2, pp. 222-229, Feb. 1997.
- [9] N. Balabanian and T. Bickart, *Linear network theory*, Chesterland, *Matrix Publishers, Inc.*, 1981, Chapter 5.
- [10] P.G. McLaren, R. Kuffel, R. Wierckx, J. Giesbrecht, L. Arendt, "A real time digital simulator for testing relays", *IEEE Transactions on Power Systems*, vol. 7, no. 1, pp. 207-213, January 1992.
- [11] A.M. Gole, R.W. Menzies, D.A. Woodford and H. Turanli, "Improved interfacing of electrical machine models in electromagnetic transients programs," *IEEE Trans. Power Apparatus and Systems*, vol. PAS-103, no. 9, pp. 2446-2451, Sept. 1984.
- [12] A.B. Dehkordi, A.M Gole, and T.L. Maguire, "Permanent magnet synchronous machine model for real- time simulation", *International Conference on Power System Transients (IPST 2005)*, Montreal, June, 2005.
- [13] X. Cao, A. Kurita, H. Mitsuma, Y. Tada, and H. Okamoto, "Improvements of numerical stability of electromagnetic transient simulation by use of phase-domain synchronous machine models," *Elect. Eng. Jpn.*, Vol. 128, no. 3, pp. 53-62, Apr. 1999.
- [14] A. M. Gole and V. K. Sood, "Static compensation model for use with electromagnetic transients simulation programs," *IEEE Trans. Power Delivery*, vol.5, no. 3, pp.1398-1407, June 1990.
- [15] R.H. Park, "Two reaction theory of synchronous machines, Part 1," *AIEE Transactions*, vol. 48, pp. 716-730, 1929.

- [16] R. H. Park, "Two reaction theory of synchronous machines, Part 2," *AIEE Transactions*, vol. 52, p 352, 1933.
- [17] V. Brandwajn and H.W. Dommel "A new method for interfacing generator models with an electromagnetic transients program," 1977 PICA Proc., p. 260.
- [18] Y. Cui, H. W. Dommel, and W. Xu, "A comparative study of two synchronous machine modeling techniques for EMTP simulation," *IEEE Trans. Energy Conversion.*, vol. 19, no. 2, pp. 462–463, Jun. 2004.
- [19] L. Wang, J. Jatskevich, and H. W. Dommel, "Re-examination of synchronous machine modeling techniques for electromagnetic transient simulations," *IEEE Trans. Power Systems*, vol. 22, No.3, pp. 1221-1230, Aug. 2007.
- [20] T.Sakaguchi, Y. Sekine, K. Takahashi, "Real-time simulation of power system dynamics", *Electrical Power and Energy Systems*, vol. 16, no.3, pp. 145-156, June 1994.
- [21] G. Carrara, A. Clerici, G. Mazza, A. Taschini, "TNA and laboratory study of the switching-surge behavior of lightning arresters", *IEEE Trans. Power Apparatus and Systems*, vol. PAS-88, No.10, pp. 1449-1462, Oct. 1969.
- [22] L.N. Walker, J.V. Stith,, H. Graham, "dispatch operator training program utilizing the hybrid simulator", *IEEE Trans. Power Apparatus and Systems*, vol. PAS-101, No.9, pp. 3342-3348, Oct. 1982.
- [23] "TransÉnergie Technologies.", Web address: <http://www.transenergie-tech.com/en/produits/description.html>.
- [24] "Opal-RT Technologies Inc.", Web address: <http://www.opal-rt.com>.
- [25] D. Brandt, R. Wachal, R. Valiquette, R. Wierckx, "Closed loop testing of a joint VAR controller using a digital real-time simulator", *IEEE Transactions on Power Systems*, vol. 6, no. 3, pp. 1140-1146, August 1991.
- [26] RTDS Technologies Inc., *RTDS™ User's Manual Set*, Winnipeg, CA, 2009.
- [27] G. R. Slemon, "An equivalent circuit approach to analysis of synchronous machines with saliency and saturation," *IEEE Trans. Energy Conversion*, vol. 5, no. 3, pp. 538–545, Sep. 1990.
- [28] Y. Xiao, G. R. Slemon, and M. R. Iravani, "Implementation of an equivalent circuit approach to the analysis of synchronous machines," *IEEE Trans. Energy Conversion*, vol. 9, no. 4, pp. 717–723, Dec. 1994.
- [29] N.A. Al-Nuaim and H.A. Toliyat, "A novel method for modeling dynamic air-gap eccentricity in synchronous machines based on modified winding function theory," *IEEE Trans. On Energy Conversion*, vol. 13, no.2, pp. 156-162, June 1998.
- [30] B. Adkins and R.G. Harley, *The general theory of alternating current machines*, London, Chapman and Hall, 1975.
- [31] P.C. Krause, O. Wasynczuk, S.D. Sudhoff, *Analysis of electric machinery*, New York, IEEE Press, 1995.
- [32] P.M. Anderson and A.A. Fouad, *Power system control and stability*, New York, IEEE Press, 1994, pp. 83-87.
- [33] I.M. Canay, "modelling of alternating-current machines having multiple rotor circuits," *IEEE Trans. Energy Conversion*, vol. 8, no. 2, pp. 280–296, June 1993.

- [34] W.A. Lewis, "A basic analysis of synchronous machines, Part I, " *AIEE Transactions*, vol. 52, pp. 436-456, 1958.
- [35] G.R. Slemon, *Magnetolectric devices*, New York, John Wiley & Sons, Inc., 1966, pp. 39-64.
- [36] D.C. Hanselman, *Brushless permanent magnet motor design*, New York, McGraw-Hill, Inc., 1994, pp. 13-38.
- [37] L. Xu, L. Ye, L. Zhen, and A. El-Antably, "A new design concept of permanent magnet machine for flux weakening operation," *IEEE Trans. Industry Applications*, vol. 31, No.2, pp. 373-378, March/April 1995.
- [38] T. Sebastian, and G.R. Slemon, "Transient modeling and performance of variable-speed permanent-magnet motors," *IEEE Trans. Industry Applications*, vol. 25, No.1, pp. 101-106, Sep. 1986.
- [39] P. P. Reichmeider, D. Querrey, C. A. Gross, D. Novosel, and S. Salon, "Partitioning of synchronous machine windings for internal fault analysis," *IEEE Trans. Energy Conversion*, vol. 15, no.4, pp. 372-375, Dec 2000.
- [40] P. P. Reichmeider, D. Querrey, C. A. Gross, D. Novosel, and S. Salon, "Internal faults in synchronous machines part I: the machine model," *IEEE Trans. Energy Conversion*, vol. 15, no.4, pp. 376-379, Dec 2000.
- [41] P. P. Reichmeider, D. Querrey, C. A. Gross, D. Novosel, and S. Salon, "Internal faults in synchronous machines part II: model performance," *IEEE Trans. Energy Conversion*, vol. 15, no.4, pp. 380-385, Dec 2000.
- [42] A. B. Dehkordi, A.M Gole, and T.L. Maguire, "Real-time simulation of internal faults in synchronous machines", *International Conference on Power System Transients (IPST 2007)*, Lyon, June, 2007.
- [43] X. Tu, L. Dessaint, M. El Kahel, and A. O. Barry, J. Jatskevich, "A new model of synchronous machine internal faults based on winding distribution," *IEEE Trans. Industrial Electronics*, vol. 135, No.6, pp. 1818-1828, Dec. 2006.
- [44] C. H. Griffin and J. W. Pope, "Generator ground fault protection using overcurrent, overvoltage, and undervoltage relays," *IEEE Trans. Power Apparatus and Systems*, vol. PAS-101, no. 12, pp. 4490-4497, Dec. 1982.
- [45] P. Subramaniam, and O. P. Malik, "Digital simulation of a synchronous generator in direct-phase quantities," *Proc. IEE*, vol. 118, No. 1, pp. 153-160, January 1971
- [46] L. Wang and J. Jatskevich, "A voltage-behind-reactance synchronous machine model for the EMTP-type solution," *IEEE Trans. Power Systems*, vol. 21, no. 4, pp. 1539-1549, Nov. 2006.
- [47] V.A. Kinitsky, "Inductances of a portion of the armature winding of synchronous machines", *IEEE Trans. PAS*, Vol. 84, no.5, pp. 389-396, May 1965.
- [48] V.A. Kinitsky, "Mutual inductances of synchronous machines with damper windings", *IEEE Trans. PAS*, vol. 83, no.10, pp. 997-1001, Oct. 1964.
- [49] V.A. Kinitsky, "Calculation of Internal Fault Currents in Synchronous Machines", *IEEE Trans. PAS*, vol. 84, no.5, pp. 381-389, May 1965.
- [50] V.A. Kinitsky, "Digital computer calculation of internal fault currents in a synchronous machines", *IEEE Trans. PAS*, vol. 87, no.8, pp. 1675-1679, Aug. 1968.

- [51] A.I. Megahed, O.P. Malik, "Synchronous generator internal fault computation and experimental verification" *IEE Proceedings on Generation, Transmission and Distribution*, vol. 145, no. 5, pp. 604-610, Sept. 1998.
- [52] A.I. Megahed, O.P. Malik, "Simulation of internal faults in synchronous generators" *IEEE Trans. Energy Conversion*, vol. 14, no. 4, pp. 1306-1306, Sept. 1999.
- [53] D. Muthumuni, P.G. McLaren, E. Dirks, V. Pathirana, "A synchronous machine model to analyze internal faults," IEEE Conference on the Industry Applications, vol. 3, pp. 1595-1600, 30 Sept.-4 Oct. 2000.
- [54] P. Silvester and, E.M.V.K Chari, "Finite-element solution of saturable magnetic field problems," *IEEE Trans. Power Apparatus and Systems*, vol. PAS-90, pp. 454-464, 1971.
- [55] E.F. Fuchs, E.A. Erdelyi, "Nonlinear theory of turbo-alternators Part I: Magnetic fields and no-load and balanced loads and Part II: Load dependent synchronous reactances," *IEEE Trans. Power Apparatus and Systems*, vol. PAS-91, pp. 583-599, 1972.
- [56] N.A. Demerdash, H.B. Hamilton, "A simplified approach to determination of saturated synchronous reactances of large turbo-generators under load," *IEEE Trans. Power Apparatus and Systems*, vol. PAS-95, No.2, pp. 560-569, March/April. 1976.
- [57] N.A. Demerdash, H.B. Hamilton, and G.W. Brown, "Simulation for design purposes of magnetic fields in turbo-generators with symmetrical and asymmetrical rotors-Part I: model development and solution technique and Part II: Model calibration and application," *IEEE Transaction Power Apparatus and Systems*, vol. PAS-91, pp. 1985-1999, 1972.
- [58] N.A. Demerdash, T.W. Nehl, "Nonlinear three dimensional magnetic vector potential finite element solution of field problems," *IEEE Trans. Magnetism*, vol. MAG-17, No.16, pp. 3408-3410, Nov. 1981
- [59] T.W. Nehl, F.A. Fouad, N.A. Demerdash, "Determination of saturated values of rotating machinery incremental and apparent inductances by an energy perturbation method," *IEEE Trans. Power Apparatus and Systems*, vol. PAS-101, No.12, pp. 4441-4451, Dec. 1982.
- [60] D.C. Macdonald, A.B.J. Reece, and P.J. Turner, "Turbine-Generator steady state reactances," *Proc. IEE (London)*, vol. 132, No.3, pp. 101-108, 1985.
- [61] E. Deng, and N.A.O. Demerdash, "A coupled finite-element state-space approach for synchronous generators. Part I: model development," *IEEE Trans. Aerospace and Electronic Systems*, vol. 32, No.2, pp. 775 - 784, Apr. 1996
- [62] E. Deng, N.A.O. Demerdash, J.G. Vaidya, M.J. Shah, "A coupled finite-element state-space approach for synchronous generators. Part II: Applications," *IEEE Trans. Aerospace and Electronic Systems*, vol. 32, No.2, pp. 785 - 794, Apr. 1996.
- [63] N.A. Demerdash, T.W. Nehl, "Electric machinery parameters and torques by current and energy perturbations from field computations-Part I: Theory and formulation," *IEEE Trans. Energy Conversion*, vol. 14, No.4, pp. 1507 - 1513, Apr. 1999.
- [64] N.A. Demerdash, T.W. Nehl, "Electric machinery parameters and torques by current and energy perturbations from field computations-Part II: Application and results," *IEEE Trans. Energy Conversion*, vol. 14, No.4, pp. 1514 - 1522, Apr. 1999.
- [65] R.C. Okonkwo, A. Dehkordi, A.M. Gole, and R. Hanitsch, "Permanent magnet DC linear machine model for real time simulation", *Canadian Conference on Electrical and Computer Engineering (CCECE 05)*, pp.1509-1512, May 2005.



- [66] Luo, X., Y. Liao, H. Toliyat, A. El-Antably and T.A. Lipo, "Multiple coupled circuit modeling of induction machines," *IEEE Trans. Industry Applications*, vol. 31, No.2, pp. 311-318, Mar. /Apr. 1995.
- [67] H.A. Toliyat, M.S. Arefeen and, A.G. Parlos "A method for dynamic simulation of air-gap eccentricity in induction machines," *IEEE Trans. Industry Applications*, vol. 32, no.4, pp. 910-918, Jul. /Aug. 1996.
- [68] G. M. Joksimovic, M. D. Durovie, J. Penman, and N. Arthur, "Dynamic simulation of dynamic eccentricity in induction machines-winding function approach," *IEEE Trans. Energy Conversion*, vol. 15, no. 2, pp. 143-148, Jun. 2000.
- [69] P. Neti and S. Nandi, "Determination of effective air-gap length of synchronous reluctance motors (SynchRel) from experimental data", *IEEE-Trans. Industry Applications*, Vol. 42, No.2, pp. 454-464, Mar. / Apr. 2006.
- [70] P. Neti, "Stator fault analysis of synchronous machines" Ph.D. Thesis, University of Victoria, 2007. *IEEE Trans. Power Systems*, vol. 22, No.3, pp. 1221-1230, Aug. 2007.
- [71] J.H.Walker, *Large synchronous machines - Design, Manufacture, and Operation*, Clarendon Press Oxford, 1981.
- [72] P.L. Alger, *Induction Machines Their Behavior and Uses*, New York, Gordon and Breach, Science Publishes, 1970.
- [73] "ANSOFT Corporation", Web address: <http://www.ansoft.com>.
- [74] C.V. Jones, *The unified theory of electrical machines*, New York, Plenum Press, 1967.
- [75] H. W. Dommel, *EMTP Theory Book*, Vancouver, Canada, Microtran Power System Analysis Corporation, 1992.
- [76] PSS/E Program Application Guide-Manual, Volume II, Power Technologies, Inc., 2004.
- [77] Minnich, S.H., Schulz, R.P., Baker, D.H. Sharma, D.K., Farmer, R.G. and Fish, J.H., "Saturation functions for synchronous generators from finite elements", *IEEE Transactions on Energy Conversion*, Vol. EC-2, 1987, pp. 680-692
- [78] A.M. El-Serafi, A.S. Abdallah, M.K. El-Sherbiny and E.H. Badawy, "Experimental study of the saturation and the cross-magnetizing phenomenon in saturated synchronous machines", *IEEE Transactions on Energy Conversion*, Vol. EC-3, 1988, pp. 815-823.
- [79] A.M El-Serafi, and E. Demeter, "Cross-magnetization phenomenon in saturated cylindrical-rotor synchronous machines," *Canadian Conference on Electrical and Computer Engineering*, vol. 2, pp. 922 - 926, 7-10 March 2000.
- [80] E. Demeter, "Modeling of saturated cylindrical-rotor synchronous machines", Master's Thesis, University of Saskatchewan, July 1998.
- [81] El-Serafi, A.M. and Kar, "Methods for determining the q-axis saturation characteristics of salient-pole synchronous machines from the measured d-axis characteristics", *IEEE Trans. On Energy Conversion*, vol. 18, no.1, pp. 80-86, Mar 2003.
- [82] F.P. de Mello and L.H. Hannett, "Representation of saturation in synchronous machines," *IEEE Trans. Power Systems*, vol.1, pp. 8-18, Nov. 1986.
- [83] William H. Press, Saul A. Teukolsky, William T. Vetterling & Brian P. Flannery, *Numerical Recipes in C*, Cambridge University Pres., second edition, 1992.

- [84] T.L. Maguire, J. Giesbrecht, "The Implementation of the Cholesky factorization routine in the RTDS real time network solution", ICDS '99, Vasteras, Sweden, May 1999.
- [85] IEEE Guide: Test Procedure for synchronous Machines, IEEE Standard 115-1995, Dec. 1995.
- [86] J.A. Melkebeek, J.L. Willems, "Reciprocity relations for the mutual inductances between orthogonal axis windings in saturated salient-pole machines ", *IEEE Transactions on Industry Applications*, Vol. 26,no. 1, pp. 107-114, Jan./Feb. 1990.
- [87] G. Kron, *Equivalent circuits of electric machinery*, General Electric Series, New York, *John Wiley & Sons, Inc.*, 1951.
- [88] C. Concordia, *Synchronous machines theory and performance*, New York, *John Wiley & Sons, Inc.*, 1951, p. 28.
- [89] F.P. de Mello and L.H. Hannett, "Validation of synchronous machine models and derivation of model parameters from tests," *IEEE Trans. Power Apparatus and Systems*, vol.PAS-100, No.2, pp. 662-672, Feb. 1981.
- [90] IEEE Subsynchronous Resonance Task Force of the Dynamic System Performance Working Group Power System Engineering Committee, "First benchmark model for computer simulation of subsynchronous resonance," *IEEE Transactions on Power Apparatus and Systems*, vol. PAS-96, no. 5, pp.1565-1572, Sep./Oct. 1977.
- [91] Emil Levi and Viktor A. Levi, "Impact of dynamic cross-saturation on accuracy of saturated synchronous machine models," *IEEE Trans. Energy Conversion*, vol. 15, No.2, pp. 224-230, June. 2000.
- [92] D.C. White and H.H. Woodson, *Electromechanical energy conversion*, New York, *John Wiley & Sons, Inc.*, 1959, Chapter 1.
- [93] J. Meisel, *Principles of Electromechanical energy conversion*, New York, *McGraw-Hill, Inc.*, 1966, Chapter 1.
- [94] H.K. Lauw and W.S. Meyer, "Universal machine modeling for the representation of rotating electric machinery in an electromagnetic transients program," *IEEE Trans. Power Apparatus and Systems*, vol.PAS-101, No.6, pp. 1342-1351, Jun. 1982.
- [95] M. Fulczyk, "Voltage 3rd harmonic in generator stator winding at changes in generator load conditions," IEEE International Electric Machines and Drives Conference, pp. 1476–1482, 2003.
- [96] Schweitzer Engineering Laboratories Inc., *SEL-300G Generator Relay [Installation Manuel]*, Pullman, WA, 2006.
- [97] IEEE Guide for Generator Ground protection, IEEE Standard C37.102<sup>TM</sup>-2006, Feb. 2007.
- [98] IEEE Guide for AC Generator Protection, IEEE Standard C37.101<sup>TM</sup>-2006, Nov. 2007.
- [99] J. Lewis Blackburn, "Protective relaying principles and applications", New York, *Marcel Dekker, Inc.*, 1998.

# Appendix A: Calculation of the Effective Permeance Function

---

In this appendix, the theoretical background for the calculation of the effective permeance function shown in (3.32) is explained.

In general, calculation of inductances using the MWFA requires numerical integration methods to evaluate the integral in (3.29). However, due to the inherent periodicity of the machine windings, the turns function a winding can be expressed by a Fourier series of its space harmonics. Based on these Fourier coefficient expressions, it is possible to obtain analytical expressions for the self and mutual inductances of any set of windings. According to [69] the turns functions for the stator windings A, B and C can be expressed as:

$$\begin{aligned}
 n_a(\phi_s) &= N_s \left( a_0 + \sum_{k=1}^{\infty} a_k \cdot \cos(pk\phi_s) \right) \\
 n_b(\phi_s) &= N_s \left( a_0 + \sum_{k=1}^{\infty} a_k \cdot \cos\left(pk\left(\phi_s - \frac{\beta}{p}\right)\right) \right) \\
 n_c(\phi_s) &= N_s \left( a_0 + \sum_{k=1}^{\infty} a_k \cdot \cos\left(pk\left(\phi_s - \frac{2\beta}{p}\right)\right) \right)
 \end{aligned} \tag{A.1}$$

where:  $k = 1, 3, 5 \dots$        $\beta = 2\frac{\pi}{3}$

In (A.1),  $N_s$  is the number of turns in each stator coil and  $p$  is the number of pole-pairs. The permeance function can also be expressed in terms of Fourier coefficients as shown in (A.2). In (A.2),  $P(\phi_s, \theta_r)_{ave}$  and  $P(\phi_s, \theta_r)_{p-p}$  are the average and peak-peak values of the permeance function.

$$P(\phi_s, \theta_r) = P(\phi_s, \theta_r)_{ave} + P(\phi_s, \theta_r)_{p-p} \cdot \sum_{k=1}^{\infty} c_k \cdot \cos(2pk(\phi_s - \theta_r)) \quad (A.2)$$

$$k = 1, 3, 5 \dots$$

Using the (A.1), (A.2) and the MWFA integral in (3.30), the analytical expressions for the self and mutual inductances are evaluated and expressed in [69]. Equation (A.3) shows the expressions for the stator inductances  $L_{aa}$ ,  $L_{ab}$  and  $L_{ac}$  as the function of rotor position  $\theta_r$ .

$$L_{aa}(\theta_r) = L_{ls} + L_{s0} + \sum_{k=1}^{\infty} L_{sk} \cdot \cos(2pk\theta_r)$$

$$L_{ab}(\theta_r) = M_{s0} + \sum_{k=1}^{\infty} M_{sk} \cdot \cos(2pk\theta_r - k\beta)$$

$$L_{ac}(\theta_r) = M_{s0} + \sum_{k=1}^{\infty} M_{sk} \cdot \cos(2pk\theta_r - 2k\beta)$$

$$k = 1, 3, 5 \dots \quad (A.3)$$

In this equation,  $L_{s0}$  and  $M_{s0}$  are functions of all Fourier coefficients of the stator turns function ( $a_k$ ).  $L_{s0}$  and  $M_{s0}$ , however are linearly proportional to the average permeance function  $P(\phi_s, \theta_r)_{ave}$  and do not depend on other Fourier coefficients of the permeance function. In a similar manner,  $L_{sk}$  and  $M_{sk}$ , depend on all Fourier coefficients of the stator turns function and only on the  $k^{th}$  Fourier coefficient of the permeance function. For  $L_{s0}$ ,  $M_{s0}$ ,  $L_{s1}$  and  $M_{s1}$  this relationship is shown in (A.4). Constants  $k_1 \dots k_4$  are functions of Fourier coefficients of the stator turns functions.

$$L_{s0} = k_1 \cdot P(\phi_s, \theta_r)_{ave} \quad L_{s1} = k_3 \cdot P(\phi_s, \theta_r)_{p-p}$$

$$M_{s0} = k_2 \cdot P(\phi_s, \theta_r)_{ave} \quad M_{s1} = k_4 \cdot P(\phi_s, \theta_r)_{p-p} \quad (A.4)$$

The stator inductance matrix can be formed using the expressions in (A.3), and the d-, q- and 0- axis inductances can be obtained by applying the Park's transformation to the

stator inductance matrix in each rotor position. Since the windings are not sinusoidally distributed, the d-, q- and 0- axis inductances are not constant, but varying periodically with the rotor position. However, the average value of these inductance values can be considered as  $L_{d-MWFA}$ ,  $L_{q-MWFA}$  and  $L_{0-MWFA}$  which are related to  $L_{s0}$ ,  $M_{s0}$ ,  $L_{s1}$  and  $M_{s1}$  as shown in (A.5).

$$\begin{aligned} L_{d-MWFA} &= L_{ls} + L_{s0} + M_{s0} + \frac{1}{2} L_{s1} + M_{s1} \\ L_{q-MWFA} &= L_{ls} + L_{s0} + M_{s0} - \frac{1}{2} L_{s1} - M_{s1} \\ L_{0-MWFA} &= L_{ls} + L_{s0} - 2M_{s0} \end{aligned} \quad (\text{A.5})$$

From (A.4) and (A.5) it can be shown that:

$$\begin{aligned} L_{d-MWFA} + L_{q-MWFA} - 2L_{0-MWFA} &= 6M_{s0} = 6k_2 \cdot P(\phi_s, \theta_r)_{ave} \\ L_{d-MWFA} - L_{q-MWFA} &= L_{s1} + 2M_{s1} = (k_3 + 2k_4) \cdot P(\phi_s, \theta_r)_{p-p} \end{aligned} \quad (\text{A.6})$$

Therefore, to adjust the permeance function such that the MWFA generates dq0 inductances equal to the experimentally measured dq0 inductances, the following equation must be used:

$$\begin{aligned} P_{eff}(\phi_s, \theta_r)_{ave} &= \frac{L_{d-exp} + L_{q-exp} - 2L_{0-exp}}{L_{d-MWFA} + L_{q-MWFA} - 2L_{0-MWFA}} P(\phi_s, \theta_r)_{ave} \\ P_{eff}(\phi_s, \theta_r)_{p-p} &= \frac{L_{d-exp} - L_{q-exp}}{L_{d-MWFA} - L_{q-MWFA}} P(\phi_s, \theta_r)_{p-p} \end{aligned} \quad (\text{A.7})$$

In addition to the effective permeance function, the leakage inductance  $L_{ls}$  can also be calculated from the experimental values of  $L_d$ ,  $L_q$  and  $L_0$ . It was mentioned in Chapter 3 that,  $L_{ls}$  accounts for leakage inductances such as *slot leakages* and *coil end leakages* not calculated by the winding function theory. Equation (A.8) is derived by substituting the values of  $L_{s0}$ ,  $M_{s0}$ ,  $L_{s1}$  and  $M_{s1}$  from (A.4) into (A.5):

$$\begin{aligned}
L_{d-MWFA} + L_{q-MWFA} &= 2L_{ls} + 2(k_1 + k_2) \cdot P(\phi_s, \theta_r)_{ave} \\
L_{0-MWFA} &= L_{ls} + (k_1 - 2k_2) \cdot P(\phi_s, \theta_r)_{ave}
\end{aligned} \tag{A.8}$$

This equation shows that the terms  $L_{d-MWFA} + L_{q-MWFA} - 2L_{ls}$  and  $L_{0-MWFA} - L_{ls}$  are proportional to the average value of the permeance function. As shown in (A.9), the ratio between these two terms is a constant term  $k_5$ . This constant term depends on Fourier coefficients of stator turn functions.

$$\frac{L_{d-MWFA} + L_{q-MWFA} - 2L_{ls}}{L_{0-MWFA} - L_{ls}} = \frac{2(k_1 + k_2)}{(k_1 - 2k_2)} = k_5 = \text{constant} \tag{A.9}$$

From (A.9),  $L_{ls}$  is derived as a function of  $L_{d-MWFA}$ ,  $L_{q-MWFA}$ ,  $L_{0-MWFA}$  and  $k_5$  as shown in (A.10).

$$L_{ls} = \frac{L_{d-MWFA} + L_{q-MWFA} - k_5 L_{0-MWFA}}{2 - k_5} \tag{A.10}$$

This leakage inductance must be added to the stator self inductance calculated using MWFA.

# Appendix B: Numerical Stability of a Discretized System Using Rectangular and Trapezoidal Integration

---

In this appendix, stability of a discretized system using different integration methods is analyzed. Consider a system described by the following state-space equation, which is presumed to be stable.  $\underline{X}$ ,  $\underline{U}$ , and  $\underline{Y}$  are vectors of state variables, inputs and outputs.

$$\begin{cases} \dot{\underline{X}} = [A]\underline{X} + [B]\underline{U} \\ \underline{Y} = [C]\underline{X} + [D]\underline{U} \end{cases} \quad (\text{B.1})$$

The discrete form of this set of equations is shown in (B.2). The matrices  $[G]$  and  $[H]$  can be expressed in terms of  $[A]$  and  $[B]$  depending on the method of discretization.

$$\begin{cases} \underline{X}(t) = [G]\underline{X}(t - \Delta t) + [H]\underline{U}(t - \Delta t) \\ \underline{Y}(t) = [C]\underline{X}(t) + [D]\underline{U}(t) \end{cases} \quad (\text{B.2})$$

In Appendix B.1, the rectangular rule of integration is used to discretize (B.1) and subsequently the numerical stability of this discretized system is analyzed. Similar analysis is performed for the method of trapezoidal integration in Appendix B.2.

Since the original system is stable, the eigenvalues of matrix  $[A]$  are located in the left side of the imaginary axis in the complex plane. It will be shown in this appendix that, after applying the trapezoidal integration, the eigenvalues of matrix  $[G]$  will be inside the unity circle regardless of the value of the simulation time-step. This conclusion cannot be made for the eigenvalues of matrix  $[G]$  after application of the rectangular integration.

### B.1 Stability of the System Using Rectangular Integration

The first equation of (B.1) is integrated for the time interval of  $[t - \Delta t \quad t]$ :

$$\underline{X}(t) = \int_{\tau=t-\Delta t}^t ([A]\underline{X}(\tau) + [B]\underline{U}(\tau))d\tau + \underline{X}(t - \Delta t) \quad (\text{B.3})$$

Using the rectangular rule of integration:

$$\begin{aligned} \underline{X}(t) &= [A]\Delta t \cdot \underline{X}(t - \Delta t) + [B]\Delta t \cdot \underline{U}(t - \Delta t) + \underline{X}(t - \Delta t) \\ &= [G] \cdot \underline{X}(t - \Delta t) + [H] \cdot \underline{U}(t - \Delta t) \end{aligned} \quad (\text{B.4})$$

$$\text{where } [G] = I + [A]\Delta t \quad \text{and} \quad [H] = [B]\Delta t$$

Now, the goal is to find out the condition in which all the eigenvalues of matrix  $[G]$  are enclosed in the unity circle. If  $\lambda'$  is one of the eigenvalues of matrix  $[G]$ , (B.5) applies:

$$|\lambda' I - G| = 0 \quad (\text{B.5})$$

Equation (B.5) can be expressed in terms of matrix  $[A]$ :

$$\begin{aligned} &|\lambda' I - (I + [A]\Delta t)| = 0 \\ \Rightarrow &|(\lambda' - 1)I - [A]\Delta t| = 0 \quad (\text{B.6}) \\ \Rightarrow &\Delta t \left| \frac{(\lambda' - 1)}{\Delta t} I - [A] \right| = 0 \end{aligned}$$

or

$$\begin{aligned} &|\lambda I - G| = 0 \\ \text{where } &\lambda = \frac{(\lambda' - 1)}{\Delta t} \quad \text{or} \quad \lambda' = \lambda \cdot \Delta t + 1 \end{aligned} \quad (\text{B.7})$$



According to definition,  $\lambda$  is an eigenvalue of matrix  $[A]$  and its relation with  $\lambda'$  is shown in (B.7). The condition for the discretized set of equations (B.4) to be numerically stable is that the eigenvalues of matrix  $[G]$  must be in the unity circle:

$$|\lambda'| \leq 1 \quad \Rightarrow \quad |\lambda\Delta t + 1| \leq 1 \quad (\text{B.8})$$

Every complex value like  $\lambda$  can be in the form of (B.9):

$$\lambda = a + jb \quad (\text{B.9})$$

From (B.8) and (B.9):

$$\begin{aligned} |(a + bj)\Delta t + 1| &\leq 1 \\ \Rightarrow \sqrt{(a\Delta t + 1)^2 + (b\Delta t)^2} &\leq 1 \end{aligned} \quad (\text{B.10})$$

This means:

$$\Delta t \leq \frac{-2a}{a^2 + b^2} \quad \text{or} \quad \Delta t \leq \frac{-2\text{Re}(\lambda)}{|\lambda|^2} \quad (\text{B.11})$$

Equation (B.11) must be valid for every eigenvalue of matrix  $[A]$ , therefore the maximum simulation time-step which provides a stable discretized system is:

$$\Delta t_c = \min \left( \frac{-2\text{Re}(\lambda)}{|\lambda|^2} \right) \quad (\text{B.12})$$

Based on the complex variable theory, the location of the eigenvalue loci of matrices  $[A]$  and  $[G]$  are evaluated and plotted in Figure B.1. All the eigenvalues of the matrix  $[A]$  are located in a circle on the left hand side of the complex plane. The imaginary axis is tangent to this circle. Multiplying  $[A]$  by  $\Delta t_c$ , maps these eigenvalues into another

circle on the left hand side half plane with the unity radius. Finally, adding the identity matrix  $I$  to  $[A]\Delta t_c$ , transfers the eigenvalues into the unity circle.

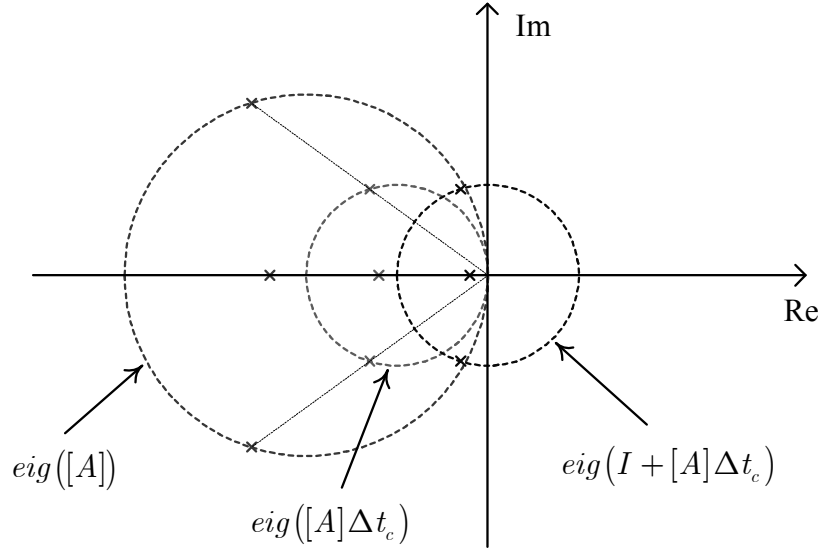


**Figure B.1:** Eigenvalue loci of matrix  $[A]$  and matrix  $[G]$  using rectangular integration

## B.2 Stability of the System Using Trapezoidal Integration

Application of the trapezoidal integration for discretizing the state-space equations results in the following equation:

$$\underline{X}(t) = [G] \cdot \underline{X}(t - \Delta t) + [H] \cdot \underline{U}^*(t)$$

$$\text{where: } \left\{ \begin{array}{l} [G] = \left( I - \frac{\Delta t}{2} [A] \right)^{-1} \left( I + \frac{\Delta t}{2} [A] \right) \\ [H] = \left( I - \frac{\Delta t}{2} [A] \right)^{-1} (\Delta t [B]) \\ \underline{U}^*(t) = \frac{\underline{U}(t) + \underline{U}(t - \Delta t)}{2} \end{array} \right. \quad (\text{B.13})$$

Assuming  $\lambda'$  is one of the eigenvalues of matrix  $[G]$ , (B.14) applies:

$$|\lambda' I - G| = 0 \quad (\text{B.14})$$

Equation (B.14) can be expressed in terms of matrix  $[A]$ :

$$\begin{aligned}
 & \left| \lambda' I - \left( I - \frac{\Delta t}{2} [A] \right)^{-1} \left( I + \frac{\Delta t}{2} [A] \right) \right| = 0 \\
 \Rightarrow & \left| \lambda' \left( I - \frac{\Delta t}{2} [A] \right)^{-1} \left( I - \frac{\Delta t}{2} [A] \right) - \left( I - \frac{\Delta t}{2} [A] \right)^{-1} \left( I + \frac{\Delta t}{2} [A] \right) \right| = 0 \quad (\text{B.15}) \\
 \Rightarrow & \left| \left( I - \frac{\Delta t}{2} [A] \right)^{-1} \cdot \left( \lambda' \left( I - \frac{\Delta t}{2} [A] \right) - \left( I + \frac{\Delta t}{2} [A] \right) \right) \right| = 0
 \end{aligned}$$

The determinant of the product of two matrices is the product of the determinants of the matrices, therefore:

$$\left| \left( I - \frac{\Delta t}{2} [A] \right)^{-1} \right| \cdot \left| \lambda' \left( I - \frac{\Delta t}{2} [A] \right) - \left( I + \frac{\Delta t}{2} [A] \right) \right| = 0 \quad (\text{B.16})$$

This means:

$$\begin{aligned}
 & \left| \lambda' I - I - \lambda' \frac{\Delta t}{2} [A] - \frac{\Delta t}{2} [A] \right| = 0 \\
 \Rightarrow & \left| (\lambda' - 1) I - (\lambda' + 1) \frac{\Delta t}{2} [A] \right| = 0 \\
 \Rightarrow & \left| \frac{(\lambda' - 1)}{(\lambda' + 1)} I - \frac{\Delta t}{2} [A] \right| = 0 \quad (\text{B.17}) \\
 \Rightarrow & \left| \frac{2}{\Delta t} \frac{(\lambda' - 1)}{(\lambda' + 1)} I - [A] \right| = 0
 \end{aligned}$$

Equation (B.17) shows that  $\lambda$ , defined in (B.18), is an eigenvalue of the matrix  $[A]$ .

$$\lambda = \frac{2}{\Delta t} \frac{(\lambda' - 1)}{(\lambda' + 1)} \quad \text{or} \quad \lambda' = -\frac{\frac{\Delta t}{2} \lambda + 1}{\frac{\Delta t}{2} \lambda - 1} \quad (\text{B.18})$$

In the following, it is proven that as long as the eigenvalues of  $[A]$  are in the left side of the imaginary axis in the complex plane, the eigenvalues of matrix  $[G]$  stay in the unity circle. An eigenvalue of matrix  $[G]$  is expressed in terms of real and imaginary parts of an eigenvalue of  $[A]$  ( $\lambda = a + jb$ ).

$$\lambda' = -\frac{\frac{\Delta t}{2}(a + bj) + 1}{\frac{\Delta t}{2}(a + bj) - 1} \quad (\text{B.19})$$

And the magnitude of  $\lambda'$  is evaluated in (B.20)

$$|\lambda'| = \left| -\frac{\frac{\Delta t}{2}(a + bj) + 1}{\frac{\Delta t}{2}(a + bj) - 1} \right| \quad (\text{B.20})$$

*or*

$$|\lambda'| = \sqrt{\frac{\left(a \frac{\Delta t}{2} + 1\right)^2 + \left(b \frac{\Delta t}{2}\right)^2}{\left(a \frac{\Delta t}{2} - 1\right)^2 + \left(b \frac{\Delta t}{2}\right)^2}}$$

The condition for  $\lambda'$  to be in the unity circle is:

$$\begin{aligned} |\lambda'| \leq 1 & \Leftrightarrow \left(a \frac{\Delta t}{2} + 1\right)^2 + \left(b \frac{\Delta t}{2}\right)^2 \leq \left(a \frac{\Delta t}{2} - 1\right)^2 + \left(b \frac{\Delta t}{2}\right)^2 \\ & \Leftrightarrow \left(a \frac{\Delta t}{2} + 1\right)^2 \leq \left(a \frac{\Delta t}{2} - 1\right)^2 \end{aligned} \quad (\text{B.21})$$

Since the eigenvalues of matrix  $[A]$  are on the left hand side of the complex plane (i.e.  $a \leq 0$ ), (B.21) is always correct regardless of the value of the time-step  $\Delta t$ . This proves the stability preserving nature of the trapezoidal integration.

Similar to the previous section, a diagram is shown here (Figure B.2 ) which presents the loci of matrices  $[A]$  and  $[G]$  using the trapezoidal integration.

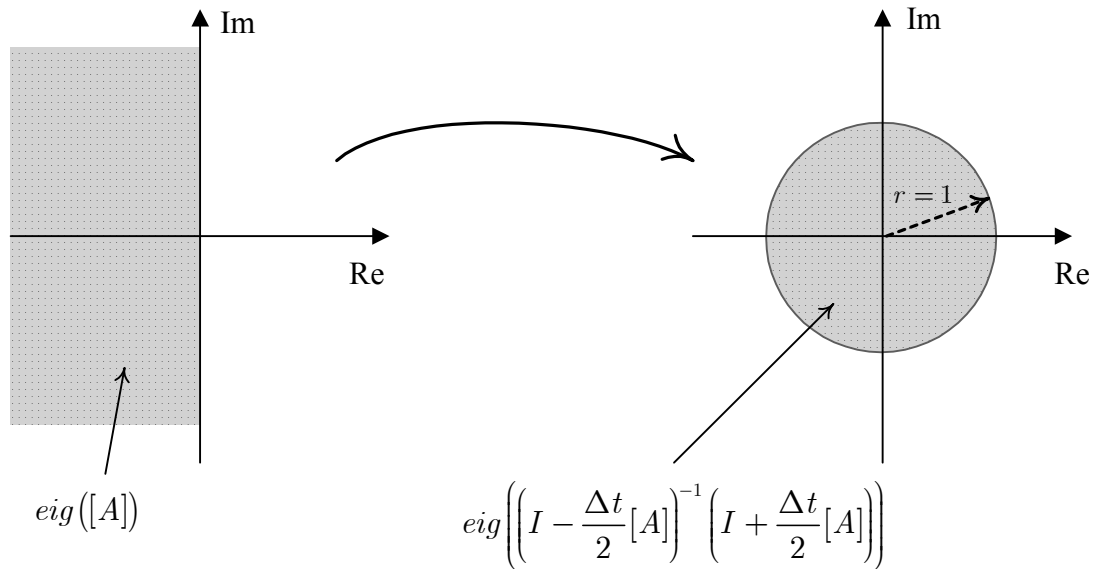


**Figure B.2:** Eigenvalue loci of matrix  $[A]$  and matrix  $[G]$  using the trapezoidal integration

# Appendix C: Electric Torque Calculation in Synchronous Machines

In this appendix, the theoretical background of calculating electric torque in synchronous machines is explained. It is also shown that the formulae for calculating electric torque in dq-based models (5.40) and phase-domain models (5.39) are equivalent.

In an electromechanical energy conversion system, defined by the coordinates  $\underline{\theta}_i$ , currents  $\underline{i}_i$  and flux linkages  $\underline{\Psi}_i$ , the mechanical torque can be calculated [92] using the following set of equations shown in Table C.1.

TABLE C.1: MECHANICAL TORQUE CAUSED BY MAGNETIC COUPLING FIELD

Independent variables	Torque evaluated from stored energy	Torque evaluated from co-energy
Currents $\underline{i}_i$ Coordinates $\underline{\theta}_i$	$\left(\underline{T}_e\right)_k = -\frac{\partial W_m(\underline{i}, \underline{\theta})}{\partial \theta_k} + \sum_{i=1}^n \underline{i}_i \frac{\partial \Psi_i(\underline{i}, \underline{\theta})}{\partial \theta_k}$	$\left(\underline{T}_e\right)_k = \frac{\partial W'_m(\underline{i}, \underline{\theta})}{\partial \theta_k}$
Fluxes $\lambda_i$ Coordinates $\underline{\theta}_i$	$\left(\underline{T}_e\right)_k = -\frac{\partial W_m(\underline{i}, \underline{\theta})}{\partial \theta_k}$	$\left(\underline{T}_e\right)_k = \frac{\partial W'_m(\underline{i}, \underline{\theta})}{\partial \theta_k} - \sum_{i=1}^n \underline{\Psi}_i \frac{\partial \underline{i}_i(\underline{i}, \underline{\theta})}{\partial \theta_k}$

Consider the equation in Table C.1 which calculate torque from the co-energy with the independent variables  $\underline{i}_i$  and  $\underline{\theta}_i$ . From the mathematical point of view, since variables  $\underline{i}_i$  and  $\underline{\theta}_i$  are independent variables, the partial derivative is taken with respect to  $\underline{\theta}_i$ , holding all other  $\theta$ 's and  $i$ 's constant. The holding of the  $i$ 's constant is a mathematical restriction imposed by the selection of the independent coordinates and has nothing to do with the electrical terminal constraints [92]. The mathematical restrictions are often misinterpreted as electrical terminal constraints, and some confusion about the generality of the force expression results.

In a linear system the torque can be calculated as:

$$(T_e)_k = \frac{1}{2} \dot{i}^T \cdot \frac{d}{d\theta_k} [L] \cdot \dot{i} \quad (C.1)$$

Equation (C.1) can be used directly to calculate the electric torque in synchronous machines. For dq-based synchronous machine models this equation can be simplified further. Recalling (3.2), the electric torque for an equivalent two-pole synchronous machine can be expressed as shown in (C.2). Here  $[L_{ss}]$  and  $[L_{rr}]$  are the stator and rotor inductance matrices, and  $[L_{sr}]$  is the matrix of mutual inductances between stator and rotor windings.

$$\begin{aligned} T_e &= \frac{1}{2} \dot{i}^T \cdot \frac{\partial}{\partial \theta_r} [L] \cdot \dot{i} \\ &= \left\{ \begin{aligned} &\frac{1}{2} (\dot{i}_{abc})^T \cdot \frac{\partial}{\partial \theta_r} [L_{ss}] \cdot \dot{i}_{abc} \\ &+ \frac{1}{2} (\dot{i}_{abc})^T \cdot \frac{\partial}{\partial \theta_r} [L_{sr}] \cdot \dot{i}_{FDQ} + \frac{1}{2} (\dot{i}_{FDQ})^T \cdot \frac{\partial}{\partial \theta_r} [L_{sr}] \cdot \dot{i}_{abc} \\ &+ \frac{1}{2} (\dot{i}_{FDQ})^T \cdot \frac{\partial}{\partial \theta_r} [L_{rr}] \cdot \dot{i}_{FDQ} \end{aligned} \right\} \quad (C.2) \end{aligned}$$

According to (3.9) and (3.10), the elements of rotor inductance matrix  $[L_{rr}]$  are independent of rotor position, therefore (C.2) can be simplified to:

$$T_e = \left\{ \frac{1}{2} (\dot{i}_{abc})^T \cdot \frac{\partial}{\partial \theta_r} [L_{ss}] \cdot \dot{i}_{abc} + (\dot{i}_{abc})^T \cdot \frac{\partial}{\partial \theta_r} [L_{sr}] \cdot \dot{i}_{FDQ} \right\} \quad (C.3)$$

The torque equation can be expressed in terms of dq0 variables as shown in (C.4):

$$T_e = \left\{ \begin{aligned} &\frac{1}{2} (\dot{i}_{dq0})^T \cdot P \cdot \frac{\partial}{\partial \theta_r} (P^{-1} \cdot [L_{dq0s}] \cdot P) \cdot P^{-1} \cdot \dot{i}_{dq0} \\ &+ (\dot{i}_{dq0})^T \cdot P \cdot \frac{\partial}{\partial \theta_r} (P^{-1} \cdot [L_{dq0sr}]) \cdot \dot{i}_{FDQ} \end{aligned} \right\} \quad (C.4)$$

Each line of (C.4) is expanded separately to evaluate the expression for torque. For the first line (C.5) applies:

$$\begin{aligned}
& P \cdot \frac{\partial}{\partial \theta_r} \left( P^{-1} \cdot [L_{dq0s}] \cdot P \right) \cdot P^{-1} \\
&= P \cdot \left( \frac{\partial P^{-1}}{\partial \theta_r} \cdot [L_{dq0s}] \cdot P + \underbrace{P^{-1} \cdot \frac{\partial}{\partial \theta_r} [L_{dq0s}] \cdot P}_0 + P^{-1} \cdot [L_{dq0s}] \cdot \frac{\partial P}{\partial \theta_r} \right) \cdot P^{-1} \quad (C.5) \\
&= P \cdot \frac{\partial P^{-1}}{\partial \theta_r} \cdot [L_{dq0s}] + [L_{dq0s}] \cdot \frac{\partial P}{\partial \theta_r} P^{-1}
\end{aligned}$$

The matrices  $P \cdot \frac{\partial P^{-1}}{\partial \theta_r}$  and  $P \cdot \frac{\partial P}{\partial \theta_r}$  are transposed of each other and evaluated in (C.6):

$$P \cdot \frac{\partial P^{-1}}{\partial \theta_r} = \begin{bmatrix} 0 & 1 & 0 \\ -1 & 0 & 0 \\ 0 & 0 & 0 \end{bmatrix}, \quad \frac{\partial P}{\partial \theta_r} P^{-1} = \begin{bmatrix} 0 & -1 & 0 \\ 1 & 0 & 0 \\ 0 & 0 & 0 \end{bmatrix} \quad (C.6)$$

Now (C.5) becomes:

$$\begin{aligned}
& P \cdot \frac{\partial P^{-1}}{\partial \theta_r} \cdot [L_{dq0s}] + [L_{dq0s}] \cdot \frac{\partial P}{\partial \theta_r} P^{-1} \\
&= \begin{bmatrix} 0 & 1 & 0 \\ -1 & 0 & 0 \\ 0 & 0 & 0 \end{bmatrix} \cdot \begin{bmatrix} L_d & 0 & 0 \\ 0 & L_q & 0 \\ 0 & 0 & L_0 \end{bmatrix} + \begin{bmatrix} L_d & 0 & 0 \\ 0 & L_q & 0 \\ 0 & 0 & L_0 \end{bmatrix} \cdot \begin{bmatrix} 0 & -1 & 0 \\ 1 & 0 & 0 \\ 0 & 0 & 0 \end{bmatrix} \quad (C.7) \\
&= \begin{bmatrix} 0 & L_q & 0 \\ -L_d & 0 & 0 \\ 0 & 0 & 0 \end{bmatrix} + \begin{bmatrix} 0 & -L_d & 0 \\ L_q & 0 & 0 \\ 0 & 0 & 0 \end{bmatrix} = \begin{bmatrix} 0 & L_q - L_d & 0 \\ L_q - L_d & 0 & 0 \\ 0 & 0 & 0 \end{bmatrix}
\end{aligned}$$

And:



$$\begin{aligned}
& \frac{1}{2} (\dot{i}_{dq0})^T \cdot P \cdot \frac{\partial}{\partial \theta_r} (P^{-1} \cdot [L_{dq0s}] \cdot P) \cdot P^{-1} \cdot \dot{i}_{dq0} \\
&= \frac{1}{2} \begin{bmatrix} i_d & i_q & i_0 \end{bmatrix} \cdot \left( (L_q - L_d) \cdot \begin{bmatrix} 0 & 1 & 0 \\ 1 & 0 & 0 \\ 0 & 0 & 0 \end{bmatrix} \right) \cdot \begin{bmatrix} i_d \\ i_q \\ i_0 \end{bmatrix} \\
&= (L_q i_q) i_d - (L_d i_d) i_q
\end{aligned} \tag{C.8}$$

For the second line of (C.4), the following applies:

$$\begin{aligned}
& (\dot{i}_{dq0})^T \cdot P \cdot \frac{\partial}{\partial \theta_r} (P^{-1} \cdot [L_{dq0sr}]) \cdot \dot{i}_{FDQ} \\
&= (\dot{i}_{dq0})^T \cdot P \cdot \left( \frac{\partial}{\partial \theta_r} (P^{-1}) \cdot [L_{dq0sr}] + \underbrace{P^{-1} \frac{\partial}{\partial \theta_r} [L_{dq0sr}]}_0 \right) \cdot \dot{i}_{FDQ} \\
&= (\dot{i}_{dq0})^T \cdot \begin{bmatrix} 0 & 1 & 0 \\ -1 & 0 & 0 \\ 0 & 0 & 0 \end{bmatrix} \cdot \sqrt{\frac{3}{2}} \begin{bmatrix} M_F & M_D & 0 \\ 0 & 0 & M_Q \\ 0 & 0 & 0 \end{bmatrix} \cdot \dot{i}_{FDQ} \\
&= \sqrt{\frac{3}{2}} \begin{bmatrix} i_d & i_q & i_0 \end{bmatrix} \cdot \begin{bmatrix} 0 & 0 & M_Q \\ -M_F & -M_D & 0 \\ 0 & 0 & 0 \end{bmatrix} \cdot \begin{bmatrix} i_F \\ i_D \\ i_Q \end{bmatrix} \\
&= (kM_Q i_Q) i_d - (kM_F i_F + kM_D i_D) i_q
\end{aligned} \tag{C.9}$$

Using (C.4), (C.8) and (C.9), the expression for electric torque in terms of dq0 variables is evaluated and shown in

$$\begin{aligned}
T_e &= \left\{ \left( (L_q i_q) i_d - (L_d i_d) i_q \right) + \left( (kM_Q i_Q) i_d - (kM_F i_F + kM_D i_D) i_q \right) \right\} \\
&= \left\{ \underbrace{(L_q i_q + kM_Q i_Q) i_d}_{\Psi_q} + \underbrace{-(L_d i_d + kM_F i_F + kM_D i_D) i_q}_{\Psi_d} \right\} \\
&= \{ \Psi_q i_d - \Psi_d i_q \}
\end{aligned} \tag{C.10}$$

# Appendix D: Derivation of Synchronous Machines Saturation Factors

---

The saturated permeance functions of the laboratory synchronous machine were evaluated using the saturation factors for the pole-arc and the inter-pole regions of the synchronous machine ( $S_d$  and  $S_q$ ). In this appendix, the method of evaluating these saturation factors is explained in detail [80]. Figure D.1 shows the unsaturated permeance function of a two pole salient-pole synchronous machine with the pole-arc expansion of  $2\tau$ . The permeances of the machine in the pole-arc and inter-pole regions are respectively shown by  $P_d$  and  $P_q = \alpha P_d$ .

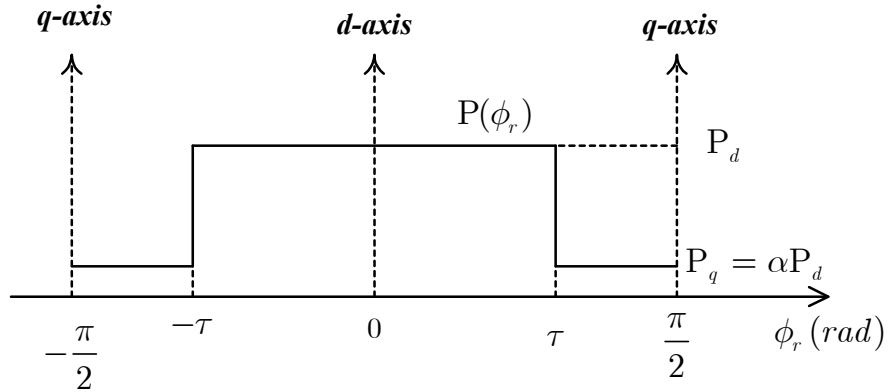


**Figure D.1:** Unsaturated permeance function of a salient-pole synchronous machine

As mentioned in Chapter 4, during the operation a synchronous machine, the total MMF in the air-gap has a sinusoidal distribution with the magnitude of  $I_{mag}$  and angle of  $\xi$  as shown in (D.1).

$$\mathcal{F}(\phi_r) = I_{mag} \cdot \cos(\phi_r + \xi) \quad (\text{D.1})$$

The d-axis component of air-gap flux density can be computed using (D.2). Here,  $k_\Phi$  is a constant that depends on the distribution of stator windings.

$$\begin{aligned}\Phi_d &= k_\Phi B_d \\ &= \frac{2}{\pi} \int_{-\frac{\pi}{2}}^{\frac{\pi}{2}} k_\Phi \cdot k_B \cdot B(\phi_r) \cdot \cos(\phi_r) d\phi_r\end{aligned}\quad (\text{D.2})$$

By expressing  $B(\phi_r)$  in terms of the total magneto-motive force and the saturation factors (Equation(4.4)),  $\Phi_d$  can be evaluated as shown in (D.3).

$$\begin{aligned}\Phi_d &= k_\Phi B_d \\ &= \frac{2}{\pi} \int_{-\frac{\pi}{2}}^{\frac{\pi}{2}} k_\Phi k_B P_{sat}(\phi_r) \mathcal{F}(\phi_r) \cos(\phi_r) d\phi_r \\ &= \frac{2}{\pi} \int_{-\frac{\pi}{2}}^{-\tau} k_\Phi k_B \mathcal{F}(\phi_r) S_q(\mathcal{F}(\phi_r)) \alpha P_d \cos(\phi_r) d\phi_r \\ &= \frac{2}{\pi} \int_{-\tau}^{\tau} k_\Phi k_B \mathcal{F}(\phi_r) S_d(\mathcal{F}(\phi_r)) P_d \cos(\phi_r) d\phi_r \\ &= \frac{2}{\pi} \int_{\tau}^{\frac{\pi}{2}} k_\Phi k_B \mathcal{F}(\phi_r) S_q(\mathcal{F}(\phi_r)) \alpha P_d \cos(\phi_r) d\phi_r\end{aligned}\quad (\text{D.3})$$

Since  $k_\Phi$ ,  $k_B$ , and  $P_d$  are constant values for a given machine, they can be grouped into a single constant value  $k$  as shown in (D.4):

$$k = k_\Phi k_B P_d \quad (\text{D.4})$$

Representing the saturation factors  $S_d(\mathcal{F}(\phi_r))$  and  $S_q(\mathcal{F}(\phi_r))$  as polynomial functions of total MMF:

$$\begin{aligned}S_d(\mathcal{F}(\phi_r)) &= 1 - \sum_{i=1}^n a_{id} |\mathcal{F}(\phi_r)|^i \\ S_q(\mathcal{F}(\phi_r)) &= 1 - \sum_{i=1}^n a_{iq} |\mathcal{F}(\phi_r)|^i\end{aligned}\quad (\text{D.5})$$

By substituting (D.4) and (D.5) in (D.3), the d-axis component of the magnetic flux can be expressed as:

$$\begin{aligned}
\Phi_d &= \frac{2}{\pi} k \alpha \int_{-\frac{\pi}{2}}^{-\tau} I_{mag} \cdot \cos(\phi_r + \xi) \left( 1 - \sum_{i=1}^n a_{iq} |\mathcal{F}(\phi_r)|^i \right) \cos(\phi_r) d\phi_r \\
&= \frac{2}{\pi} k \int_{-\tau}^{\tau} I_{mag} \cdot \cos(\phi_r + \xi) \left( 1 - \sum_{i=1}^n a_{id} |\mathcal{F}(\phi_r)|^i \right) \cos(\phi_r) d\phi_r \quad (D.6) \\
&= \frac{2}{\pi} k \alpha \int_{\tau}^{\frac{\pi}{2}} I_{mag} \cdot \cos(\phi_r + \xi) \left( 1 - \sum_{i=1}^n a_{iq} |\mathcal{F}(\phi_r)|^i \right) \cos(\phi_r) d\phi_r
\end{aligned}$$

Equation (D.6) can be simplified to:

$$\Phi_d = (\alpha I_{0q}^d + I_{0d}^d) I_{mag} - \sum_{i=1}^n (\alpha a_{iq} I_{iq}^d + a_{id} I_{id}^d) I_{mag}^{i+1} \quad (D.7)$$

where:

$$\begin{aligned}
I_{0q}^d &= \frac{2}{\pi} k \int_{-\frac{\pi}{2}}^{-\tau} \cos(\phi_r + \xi) \cos(\phi_r) d\phi_r \\
&\quad + \frac{2}{\pi} k \int_{\tau}^{\frac{\pi}{2}} \cos(\phi_r + \xi) \cos(\phi_r) d\phi_r \\
I_{0d}^d &= \frac{2}{\pi} k \int_{-\tau}^{\tau} \cos(\phi_r + \xi) \cos(\phi_r) d\phi_r \\
I_{iq}^d &= \frac{2}{\pi} k \int_{-\frac{\pi}{2}}^{-\tau} \cos(\phi_r + \xi) |\cos(\phi_r + \xi)|^i \cos(\phi_r) d\phi_r \\
&\quad + \frac{2}{\pi} k \int_{\tau}^{\frac{\pi}{2}} \cos(\phi_r + \xi) |\cos(\phi_r + \xi)|^i \cos(\phi_r) d\phi_r \\
I_{id}^d &= \frac{2}{\pi} k \int_{-\tau}^{\tau} \cos(\phi_r + \xi) |\cos(\phi_r + \xi)|^i \cos(\phi_r) d\phi_r
\end{aligned} \quad (D.8)$$

Similarly the q-axis component of the air-gap magnetic flux can be computed as shown in (D.9) and (D.10).

$$\begin{aligned}
\Phi_q &= \frac{2}{\pi} k \alpha \int_{-\frac{\pi}{2}}^{-\tau} I_{mag} \cdot \cos(\phi_r + \xi) \left( 1 - \sum_{i=1}^n a_{iq} |\mathcal{F}(\phi_r)|^i \right) \sin(\phi_r) d\phi_r \\
&= \frac{2}{\pi} k \int_{-\tau}^{\tau} I_{mag} \cdot \cos(\phi_r + \xi) \left( 1 - \sum_{i=1}^n a_{id} |\mathcal{F}(\phi_r)|^i \right) \sin(\phi_r) d\phi_r \\
&= \frac{2}{\pi} k \alpha \int_{\tau}^{\frac{\pi}{2}} I_{mag} \cdot \cos(\phi_r + \xi) \left( 1 - \sum_{i=1}^n a_{iq} |\mathcal{F}(\phi_r)|^i \right) \sin(\phi_r) d\phi_r \\
&= (\alpha I_{0q}^q + I_{0d}^q) I_{mag} - \sum_{i=1}^n (\alpha a_{iq} I_{iq}^q + a_{id} I_{id}^q) I_{mag}^{i+1}
\end{aligned} \tag{D.9}$$

where:

$$\begin{aligned}
I_{0q}^q &= \frac{2}{\pi} k \int_{-\frac{\pi}{2}}^{-\tau} \cos(\phi_r + \xi) \sin(\phi_r) d\phi_r \\
&\quad + \frac{2}{\pi} k \int_{\tau}^{\frac{\pi}{2}} \cos(\phi_r + \xi) \sin(\phi_r) d\phi_r \\
I_{0d}^q &= \frac{2}{\pi} k \int_{-\tau}^{\tau} \cos(\phi_r + \xi) \sin(\phi_r) d\phi_r \\
I_{iq}^q &= \frac{2}{\pi} k \int_{-\frac{\pi}{2}}^{-\tau} \cos(\phi_r + \xi) |\cos(\phi_r + \xi)|^i \sin(\phi_r) d\phi_r \\
&\quad + \frac{2}{\pi} k \int_{\tau}^{\frac{\pi}{2}} \cos(\phi_r + \xi) |\cos(\phi_r + \xi)|^i \sin(\phi_r) d\phi_r \\
I_{id}^q &= \frac{2}{\pi} k \int_{-\tau}^{\tau} \cos(\phi_r + \xi) |\cos(\phi_r + \xi)|^i \sin(\phi_r) d\phi_r
\end{aligned} \tag{D.10}$$

### D.1 Determination of the Constants $\alpha$ , $k$

The parameters  $\alpha$ ,  $k$  can be determined from the values of unsaturated d- and q-axis magnetizing reactances. The unsaturated value of d-axis magnetizing reactance  $X_{mdu}$  can be computed by substituting  $\xi = 0$ ,  $a_{id} = 0$  (i.e.  $S_d(\mathcal{F}(\phi_r)) = 1.0$ ), and  $a_{iq} = 0$  (i.e.  $S_q(\mathcal{F}(\phi_r)) = 1.0$ ) in (D.6) and dividing the computed magnetic flux by  $I_{mag}$ . This is shown in (D.11).

$$\begin{aligned}
X_{mdu} &= \frac{2}{\pi} k \alpha \int_{-\frac{\pi}{2}}^{-\tau} \cos(\phi_r) \cos(\phi_r) d\phi_r \\
&= \frac{2}{\pi} k \int_{-\tau}^{\tau} \cos(\phi_r) \cos(\phi_r) d\phi_r \\
&= \frac{2}{\pi} k \alpha \int_{\tau}^{\frac{\pi}{2}} \cos(\phi_r) \cos(\phi_r) d\phi_r \\
&= \frac{4}{\pi} k \left( \int_0^{\tau} \cos^2(\phi_r) d\phi_r + \alpha \cdot \int_{\tau}^{\frac{\pi}{2}} \cos^2(\phi_r) d\phi_r \right) \\
&= k \left( (1 - \alpha) \sin(\tau) + (1 - \alpha) \tau + \alpha \pi \right)
\end{aligned} \tag{D.11}$$

Similarly, the unsaturated value of q-axis magnetizing reactance  $X_{mqu}$  can be computed by substituting  $\xi = \frac{\pi}{2}$ ,  $a_{id} = 0$  (i.e.  $S_d(\mathcal{F}(\phi_r)) = 1.0$ ), and  $a_{iq} = 0$  (i.e.  $S_q(\mathcal{F}(\phi_r)) = 1.0$ ) in (D.9) and dividing the computed magnetic flux by  $I_{mag}$ . The resulting magnetizing inductance is shown in (D.12).

$$\begin{aligned}
X_{mqu} &= \frac{4}{\pi} k \left( \int_0^{\tau} \sin^2(\phi_r) d\phi_r + \alpha \cdot \int_{\tau}^{\frac{\pi}{2}} \sin^2(\phi_r) d\phi_r \right) \\
&= k \left( (\alpha - 1) \sin(\tau) + (1 - \alpha) \tau + \alpha \pi \right)
\end{aligned} \tag{D.12}$$

Knowing the values of unsaturated d- and q- axis magnetizing reactances  $X_{mdu}$ ,  $X_{mqu}$  and the span of the pole-arc ( $\tau$ ), the parameters  $\alpha$ ,  $k$  can be determined as shown in (D.13):

$$\begin{aligned}
\alpha &= \frac{(X_{mqu} + X_{mdu}) \cdot \sin(\tau) + (X_{mqu} - X_{mdu}) \cdot \tau}{(X_{mqu} + X_{mdu}) \cdot \sin(\tau) + (X_{mqu} - X_{mdu}) \cdot \tau + (X_{mdu} - X_{mqu}) \cdot \pi} \\
k &= \frac{\pi X_{mqu}}{k \left( (\alpha - 1) \sin(\tau) + (1 - \alpha) \tau + \alpha \pi \right)}
\end{aligned} \tag{D.13}$$

## D.2 Determination of the Saturation Factors Coefficients $a_{id}$ , $a_{iq}$

The coefficients  $a_{id}$ ,  $a_{iq}$  ( $i = 1 \cdots n$ ) of the saturation function are constants for a given machine. They can be obtained from the measured d- and q-axis saturation curves. Substituting  $\xi = 0$  in (D.7) and (D.8), the equation of the d-axis saturation curve can be written as follows:

$$\Phi_d = (c_0^d)I_{mag} - \sum_{i=1}^n (c_{iq}^d a_{iq} \alpha + c_{id}^d a_{id}) I_{mag}^{i+1}$$

where:

$$\begin{aligned} c_0^d &= \frac{2}{\pi} k \alpha \left( \int_{-\frac{\pi}{2}}^{-\tau} \cos^2(\phi_r) d\phi_r + \int_{\tau}^{\frac{\pi}{2}} \cos^2(\phi_r) d\phi_r \right) + \frac{2}{\pi} k \int_{-\tau}^{\tau} \cos^2(\phi_r) d\phi_r \quad (D.14) \\ c_{iq}^d &= \frac{2}{\pi} k \left( \int_{-\frac{\pi}{2}}^{-\tau} \cos^{i+2}(\phi_r) d\phi_r + \int_{\tau}^{\frac{\pi}{2}} \cos^{i+2}(\phi_r) d\phi_r \right) \\ c_{id}^d &+ \frac{2}{\pi} k \int_{-\tau}^{\tau} \cos^{i+2}(\phi_r) d\phi_r \end{aligned}$$

Similarly, for the q-axis magnetizing flux:

$$\Phi_q = (c_0^q)I_{mag} - \sum_{i=1}^n (c_{iq}^q a_{iq} \alpha + c_{id}^q a_{id}) I_{mag}^{i+1}$$

where:

$$\begin{aligned} c_0^q &= \frac{2}{\pi} k \alpha \left( \int_{-\frac{\pi}{2}}^{-\tau} \sin^2(\phi_r) d\phi_r + \int_{\tau}^{\frac{\pi}{2}} \sin^2(\phi_r) d\phi_r \right) + \frac{2}{\pi} k \int_{-\tau}^{\tau} \sin^2(\phi_r) d\phi_r \quad (D.15) \\ c_{iq}^q &= (-1)^i \cdot \frac{2}{\pi} k \int_{-\frac{\pi}{2}}^{-\tau} \sin^{i+2}(\phi_r) d\phi_r + \frac{2}{\pi} k \int_{\tau}^{\frac{\pi}{2}} \sin^{i+2}(\phi_r) d\phi_r \\ c_{id}^q &+ (-1)^i \cdot \frac{2}{\pi} k \int_{-\tau}^0 \sin^{i+2}(\phi_r) d\phi_r + \frac{2}{\pi} k \int_0^{\tau} \sin^{i+2}(\phi_r) d\phi_r \end{aligned}$$

Clearly:

$$\begin{aligned} c_0^d &= X_{mdu} \\ c_0^q &= X_{mqu} \end{aligned} \quad (D.16)$$

The representations of the d- and q-axis saturation curves of (D.14) and (D.15) are polynomials in terms of the magnitude of total MMF  $I_{mag}$ , and can be written in the following form:

$$\Phi_d = b_0^d I_{mag} - \sum_{i=1}^n b_i^d I_{mag}^{i+1}$$

$$\Phi_q = b_0^q I_{mag} - \sum_{i=1}^n b_i^q I_{mag}^{i+1}$$

where:

$$b_0^d = c_0^d = X_{mdu} \tag{D.17}$$

$$b_0^q = c_0^q = X_{mqu}$$

$$b_i^d = c_{iq}^d a_{iq} \alpha + c_{id}^d a_{id}$$

$$b_i^q = c_{iq}^q a_{iq} \alpha + c_{id}^q a_{id}$$

with  $i = 1 \dots n$

Solving (D.17) yields the polynomial coefficients of saturation factors ( $a_{id}$  and  $a_{iq}$ ), hence d- and q-axis saturation factors can be determined. The least square errors fitting technique is used in [80] to determine these coefficients.